UNIVERSITY
OF
JOHANNESBURG

COPYRIGHT AND CITATION CONSIDERATIONS FOR THIS THESIS/ DISSERTATION

- Attribution — You must give appropriate credit, provide a link to the license, and indicate if changes were made. You may do so in any reasonable manner, but not in any way that suggests the licensor endorses you or your use.

- NonCommercial — You may not use the material for commercial purposes.

- ShareAlike — If you remix, transform, or build upon the material, you must distribute your contributions under the same license as the original.

How to cite this thesis

Surname, Initial(s). (2012) Title of the thesis or dissertation. PhD. (Chemistry)/ M.Sc. (Physics)/ M.A. (Philosophy)/M.Com. (Finance) etc. [Unpublished]: University of Johannesburg. Retrieved from: https://ujcontent.uj.ac.za/vital/access/manager/Index?site_name=Research%20Output (Accessed: Date).

MIXED-METAL OXIDE CONDUCTING POLYMER NANOCOMPOSITES FOR THE REMOVAL OF FLUORIDE AND CHROMIUM(VI) FROM AQUEOUS SOLUTION

By

MARKO CHIGONDO

Student number: 201607527

Thesis submitted in fulfilment of the requirement for the degree of

DOCTOR OF PHILOSOPHY

In

CHEMISTRY

In the

FACULTY OF SCIENCE

Of the

UNIVERSITY OF JOHANNESBURG

SUPERVISOR: **PROF. KRIVESHINI PILLAY**

CO-SUPERVISORS : **PROF. ARJUN MAITY**

DR. MADHUMITA BHAUMIK

2018

DECLARATION

I hereby declare that this thesis, which I herewith submit for the research qualification:

DOCTOR OF PHILOSOPHY IN CHEMISTRY

To the University of Johannesburg, Department of Applied Chemistry, is, apart from the recognised assistance of my supervisors, my own work and has not previously been submitted by me to another institution to obtain a research degree.

_____ on this ____25th_ day of __September 2018_____

(Candidate)

_____ on this__25th___ day of _ September 2018_____

(Supervisor)

UNIVERSITY OF JOHANNESBURG

_____ on this ____25th_ day of ___ September 2018_____

(Co-supervisor)

_____ on this __25th___ day of _ September 2018_____

(Co-supervisor)

DEDICATION

I dedicate this work to my wife Rufaro, my children Hillary, Batsirai, Mazvita and Tanatswa for support and encouragement.

UNIVERSITY
OF
JOHANNESBURG

ACKNOWLEDGEMENTS

A sincere, heartfelt gratitude and thanks to:

- My supervisors: Prof. K. Pillay, Prof A. Maity and Dr M. Bhaumik for dedicating their precious time and providing me with continuous inspiration, valuable recommendations and guidance throughout my study.

- My family and friends, notably, my wife Rufaro, my brother Dr Fidelis Chigondo and my friends Lungelo Dhlamini, Liberty Chipise, Tlou Phukubje, Thembisile Mahlangu, Dr Hugues Kamdem Paumo and Dr Nazia Kera for morally and emotionally supporting me through the research.

- The staff and faculty of the University of Johannesburg, Doornfontein Campus.

- The staff of Council for Scientific and Industrial Research (CSIR), South Africa particularly Prof A. Maity, for his kind guidance and relentless attempts to bring excellence in this research project. The characterization unit at the DST-CSIR National Centre for Nanostructured Materials for all their contribution to this project along with the assistance with materials characterization.

- The University of Johannesburg, University Research Committee and Water Research Commission (WRC) for providing me with the financial support in the form of bursaries and other expenses which enabled me to accomplish this research project.

UNIVERSITY OF JOHANNESBURG

PUBLICATIONS

The work presented in this thesis has been published and submitted to peer-reviewed journals of international repute.

Peer-reviewed Publications

Chigondo M., Paumo H.K., Bhaumik, Pillay K., Maity A., Rapid high adsorption performance of hydrous cerium-magnesium oxides for removal of fluoride from water, J. Mol. Liq. 265 (2018) 496–509.

doi.org/10.1016/j.molliq.2018.06.015

Chigondo M., Paumo H.K., Bhaumik, Pillay K., Maity A., Hydrous CeO_2-Fe_3O_4 decorated polyaniline fibers nanocomposite for effective defluoridation of drinking water, J. Colloid Interface Sci. 532 (2018) 500–516.

https://doi.org/10.1016/j.jcis.2018.07.134

Chigondo M., Paumo H.K., Bhaumik, Pillay K., Maity A.,Magnetic arginine-functionalized polypyrrole with improved and selective chromium(VI) ions removal from water, Received positive comments, J. Mol. Liq, MOLLIQ_2018_4103

UNIVERSITY OF JOHANNESBURG

ABSTRACT

Water is an indispensable natural resource for sustaining life which is undoubtedly not free in all places. The chemical composition of surface or underground waters is one of the principal aspects upon which the relevancy of water for domestic, industrial or agricultural purposes hinges upon. Inorganic anions are commonly in existence in water; nonetheless, some of these including oxy-anions, are undesirable and continually accountable for the grave environmental and health problems. Such ions like arsenic (As(V)), hexavalent chromium(Cr(VI)), fluoride (F^-) phosphate (PO_4^{3-}) and nitrate (NO_3^-) when in exceeding maximum limits, constitute some of the most hazardous water pollutants. Fluoride, at low a concentration of 0.8-1.5 mg/L as recommended by World Health Organisation (WHO) can prevent tooth decay and contribute to the development of strong bones, especially in young children. However, at higher concentrations it has catastrophic health effects ranging from dental related problems to debilitating skeletal fluorosis as well as affecting body parts like the muscles, brain, lungs, kidneys, thyroid, reproduction and enzymes. Its high concentration in ground water is primarily owing to the weathering of fluoride rich minerals, high ash volcanic eruptions and many anthropogenic activities. On the other hand, industrial activities such as electroplating, leather tanning, dye production, ferrochrome production, wood preservation, mining and paints manufacture have indirectly led to the discharge of Cr(VI) ions into environmental water. Cr(VI) is one of the most toxic, highly soluble and mobile anions in the environment which causes health problems in the form of dermatitis, damage to the liver, lung and skin cancer, skin irritation and internal haemorrhage. The WHO recommended level of Cr(VI) is 0.1 mg/L in surface waters and 0.05 mg/L in drinking water. Consequently, sustainable technologies have been developed to remove fluoride and Cr(VI) ions from water ranging from chemical precipitation, reverse osmosis, electrochemical methods, adsorption, membrane processes, ion exchange and phytoremediation. Among these techniques, adsorption has shown superiority, attributed to its simplicity in design, low operating costs, efficiency and reversibility. Several adsorbents have been utilised for adsorption successfully. However, some drawbacks such as high cost, low selectivity, narrow pH ranges, low adsorption capacity, slow adsorption and poor mechanical strength have been encountered with some of the adsorbent materials. Nano-metal oxides (NMOs) and conduction polymers have a better potential as adsorbents physical and chemical properties. However they have problems of agglomeration, hence low adsorption capacity and difficult to separate from aqueous media. More studies on modification and

UNIVERSITY OF JOHANNESBURG

combining the advantages offered by mixed NMOs and conduction polymer to produce better composite adsorbents with better adsorption properties and can be isolated from aqueous media were inevitable. Thus, the of synthesis and application of mixed NMOs conducting polymer composites for the removal of fluoride and Cr(VI) ions from aqueous solution was the main focus of this study.

The preparation costs of adsorbents may dictate the overall cost of the water treatment process. In this study, simple co-precipitation synthesis, co-precipitation deposition of hydrous metal oxides on polyaniline fibers and *in situ* polymerisation of magnetic arginine functionalised polypyrrole techniques were used to prepare novel eco-friendly hydrous cerium-magnesium bimetal oxides (HCeMgO1:1), hydrous cerium-iron oxides decorated polyaniline nanofibers (HCeFe NFs-2) as potential adsorbents for fluoride and a magnetic arginine-functionalized polypyrrole (Fe_3O_4@Arg-PPy) nanocomposite as a potential adsorbent for Cr(VI) ions. These materials were comprehensively characterized by various physico-chemical and spectrochemical techniques including Fourier transform infrared spectroscopy (FTIR), X-ray diffraction (XRD), field emission scanning electron microscopy (FE-SEM), high resolution-transmission electron microscopy (HR-TEM), thermogravimetric analysis (TGA), Braunauer-Emmett-Teller (BET) surface area analysis, vibrational sample magnetometry (VSM), X-ray photoelectron spectroscopy (XPS), dynamic mechanical analysis (DMA) and pH at point-of-zero charge measurements. Batch adsorption studies on the effect of various parameters such as adsorbent dosage, contact time, initial concentration, initial pH and effect of co-existing ions were conducted as well as adsorbent regeneration experiments. The concentrations of pollutants in resulting solutions were determined using an ion selective electrode for fluoride ions while UV-vis spectrophotometry and ion chromatography-inductively coupled plasma mass spectrometry (IC-ICP-MS) techniques were employed for Cr(VI) determination and chromium speciation, respectively.

In the first part of this study, a simple co-precipitation method was used to prepare a hydrous cerium-magnesium bimetal oxide composite (HCeMgO1:1) which was applied for water defluoridation. The FTIR, XRD, XPS and TEM confirmed the successful synthesis of the adsorbent. The BET surface area of HCeMgO1:1 was around 34 m^2/g. This adsorbent, not only demonstrated high fluoride adsorption efficiency but also rapid kinetics. A pseudo-second-order model best described the adsorption kinetics and the process was hindered by phosphate and sulphate co-existing ions. The fluoride uptake followed the Langmuir adsorption isotherm

model, with maximum adsorption capacities in the range of 66.23−80.00 mg/g for 25−45 ^{o}C at a pH value of 5.5. Both ion exchange and electrostatic interactions were found to dictate the process of adsorption. The revival study of the fluoride laden HCeMgO1:1 exhibited a high desorption efficiency and up to four adsorption-desorption cycles were possible. Further tests on underground water samples established the potential use of hydrous CeO_2-MgO as suitable material for water defluoridation.

In the second part of this study, hydrous CeO_2-Fe_3O_4 decorated polyaniline nanofibers (HCeFe NFs-2) composite was obtained through a simple co-precipitation deposition of metal oxides on pre-synthesized polyaniline nano-fibers (PANI NFs) and utilised for water defluoridation. FTIR, XRD, XPS and TEM confirmed the successful deposition of hydrous CeO_2 and Fe_3O_4 nano-metal oxides onto PANI NFs to obtain the HCeFe NFs-2 adsorbent. The BET specific surface area of the adsorbent was 66 m^2/g, which was much higher than that of pristine PANI NFs (39 m^2/g). This material exhibited remarkable adsorption efficiency towards fluoride ions *via* both electrostatic interactions and an ion exchange mechanisms. Fluoride adsorption followed the pseudo-second-order rate model and best fitted the monolayer Langmuir isotherm model, with the maximum capacities within 93.46-117.64 mg/g over a broad pH range of 3-10. The regeneration studies and mechanical stability of HCeFe NF-2 adsorbent showed a considerable adsorption-desorption efficiency over three consecutive cycles and resistance to strain, respectively. Eventually, the adsorbent was tested on spiked fluoride containing groundwater at its natural pH and the obtained results demonstrated its potential utility for defluoridation of natural water.

UNIVERSITY OF JOHANNESBURG

Finally, in the third part of this study, a magnetic arginine-functionalized polypyrrole (Fe_3O_4@Arg-PPy) nanocomposite was fabricated by *in-situ* polymerisation of pyrrole monomer in the presence of arginine and Fe_3O_4 nanoparticles for toxic Cr(VI) ions removal from simulated and chromium ores leaching effluent. FTIR, XRD, XPS, TEM and VSM established the successful attachment of arginine and Fe_3O_4 onto the PPy support. The adsorption kinetics study for the removal of Cr(VI) ions using Fe_3O_4@Arg-PPy demonstrated that the process followed a pseudo-second-order model. Isothermal investigation, on the other hand, revealed a monolayer adsorption behaviour following the Langmuir model with a maximum absorption capacity of 322.58 mg/g at 25 °C and pH of 2. The reduction of Cr(VI) to Cr(III) by the active electron rich nanocomposite was established using IC-ICP-MS and XPS analyses. Cr(VI) removal took place *via* electrostatic attractions, reduction and chelation. Also,

even in high salinity conditions, Fe_3O_4@Arg-PPy retained its impressive adsorption efficiency towards Cr(VI) ions. Furthermore, assessment of the adsorbent for Cr(VI) ions removal from chromium ores leaching water samples demonstrated its potential practicability. The described adsorbent was regenerated for four adsorption-desorption cycles and retained up to 64% of its original adsorption efficiency.

The HCeMgO1:1, HCeFe NFs-2 and Fe_3O_4@Arg-PPy nanocomposite adsorbents demonstrated great potential for the removal of fluoride and Cr(VI) ions from water and the adsorption capacities are comparable, if not superior to other adsorbents that have been studied for fluoride and Cr(VI) ions removal from water. However, more studies to determine their potential for long term water treatment such as column studies and large-scale processes are necessary.

UNIVERSITY
OF
JOHANNESBURG

TABLE OF CONTENTS

UNIVERSITY OF JOHANNESBURG

UNIVERSITY OF JOHANNESBURG

UNIVERSITY OF JOHANNESBURG

UNIVERSITY OF JOHANNESBURG

UNIVERSITY OF JOHANNESBURG

UNIVERSITY OF JOHANNESBURG

UNIVERSITY
OF
JOHANNESBURG

LIST OF FIGURES

UNIVERSITY OF JOHANNESBURG

UNIVERSITY OF JOHANNESBURG

UNIVERSITY OF JOHANNESBURG

UNIVERSITY OF JOHANNESBURG

UNIVERSITY OF JOHANNESBURG

LIST OF TABLES

Table ***Description*** ***Page***

UNIVERSITY OF JOHANNESBURG

UNIVERSITY
OF
JOHANNESBURG

LIST OF SCHEMES

UNIVERSITY OF JOHANNESBURG

LIST OF ABBREVIATIONS

WHO	World Health Organization
FTIR	Fourier transform infrared spectroscopy
BET	Brunauer-Emmet-Teller surface area analysis
XRD	X-ray diffraction analysis
SEM	Scanning electron microscopy
FE-SEM	Field emission scanning electron microscopy
EDX	Energy dispersive X-ray spectral analysis
TEM	Transmission electron microscopy
HR-TEM	High resolution transmission electron microscopy
STEM	Scanning transmission electron microscopy
TGA	Thermogravimetric analysis
DTA	Differential thermal analysis
XPS	X-ray photoelectron spectroscopy
NPs	Nanoparticles
CNTs	Carbon nanotubes
SWCNTs	Single walled carbon nanotubes
MWCNTs	Multi walled carbon nanotubes
ICPs	Intrinsic conducting polymers
Py	Pyrrole monomer
PPy	Polypyrrole
ANI	Aniline monomer
PANI	Polyaniline
PANI NFs	Polyaniline nanofibers
NCs	Nanocomposites
IR	Infra-red radiation
TISAB	Total ionic strength adjustment buffer
AR	Analytical reagent
USA	United States of America
EPA	Environmental Protection Agency
VSM	Vibrating Sample Magnetometry
IC-ICP-MS	Ion chromatography- inductively coupled plasma mass spectrometer
DMA	Dynamic mechanical analysis

UNIVERSITY OF JOHANNESBURG

NMOs	Nano-metal oxides
TISAB	Total ionic strength adjustment buffer
HCeMgO	Hydrous cerium-magnesium oxide
$HCeO_2$	Hydrous cerium oxide
HMgO	Hydrous magnesium oxide
$HCeO_2Fe_3\ O_4$	Hydrous cerium-iron oxide
HCeFe NFs-2	Cerium-iron oxide decorated polyaniline fiber
Fe_3O_4@Arg-PPy	Magnetic Fe_3O_4 arginine functionalised polypyrrole
UV	Ultra Violet
ED	Electrodialysis
RO	Reverse Osmosis
NF	Nanofiltration
AC	Activated Carbon
BIS	Bureau of Indian Standards
DNA	Deoxyribonucleic acid
Cr(III)	Trivalent chromium
Cr(VI)	Hexavalent chromium

UNIVERSITY OF JOHANNESBURG

CHAPTER 1

INTRODUCTION

1.1 Background

The demand for clean and pure water has escalated over the years as the world population continues to surge as humans rely on this natural resource for survival. As a result, the global demand for safe drinking water has become one of the critical challenges for this century. Water pollution aggravates the current predicament of fresh water scarcity by contaminating enormous amounts of accessible water [1,2]. This emerges from the rapid population surge, expansion of cities and extensive industrial activity [3,4,5]. Some of the pollutants which threaten water resources and hence present a potential health hazard to humans, flora and fauna include inorganic anions such as arsenic, hexavalent chromium, fluorides, phosphates and nitrates [4].

Among the various inorganic pollutants in water, fluoride (F^-) and hexavalent chromium (Cr(VI)) ions are two of the most prominent water pollutants in South Africa [5]. This is attributed to the serious health implications caused by the two pollutants on people who depend on surface and underground water for their daily domestic and industrial uses [2]. Excess uptake of fluoride can lead to detrimental health effects on the human body [1] depending on the level and duration of exposure to fluoride. As a result, the World Health Organisation (WHO)'s acceptable level of fluoride concentrations in drinking is between 0.5 and 1.5 mg/L [2]. In addition, Cr(VI) is one of the most toxic anions which causes health problems [3]. The WHO' recommends the levels of Cr(VI) ions to be 0.1 and 0.05 mg/L in surface water and drinking water, respectively [4]. As a result, this study focused on the application of adsorption technology for water defluoridation and for the removal of Cr(VI) ions from water and effective adsorbents were developed using hydrous metal oxides and conducting polymer nanocomposites.

1.2 Problem statement

Fluoride is one of the most copious anions existing globally in groundwater and generates a major problem for drinking water sources [1]. Fluorine is the most electronegative and reactive

UNIVERSITY OF JOHANNESBURG

of all the elements in the periodic table [2] and therefore cannot be found naturally as an element but occurs in the form of fluorides in the environment. The fluoride level is less in the tropical areas owing to high rainfall, which have a diluting effect on groundwater chemical composition. However, in arid and semi-arid countries, the problem of high fluoride levels is more severe [1,5]. In South Africa, there is high prevalence of fluoride contaminated water especially in the North West, Northern Cape, Kwazulu Natal and Limpopo provinces [5]. Fluoride may be valuable or calamitous to human health, depending on the concentration and quantities consumed [6]. For example, reasonable levels of fluoride ingestion (0.8-1.0 mg/L) can guard teeth against decay and promote the growth of strong bones, particularly in early childhood [7,8]. Nevertheless, ingestion of excess fluorides leads to adverse health effects, ranging from mild dental diseases to crippling skeletal fluorosis [9]. Fluoride ions can enter into the human body in various ways, such as industrial exposure, food, cosmetics or medicine, municipal water with fluoride from underground drinking water being the principal source of the daily intake [10]. Consequently, the WHO has stipulated acceptable fluoride concentrations in drinking water to be between 0.5 and 1.5 mg/L. [11]. It is estimated that more than 200 million people worldwide consume drinking water containing fluoride ions [12]. Henceforth, fluoride removal from environmental water sources is a top priority. Additionally, Cr(VI) ions are some of the most abundant anionic species, attributed to their high solubility in water across the pH range. The main sources of Cr (VI) ions in water are tanning, electroplating, timber making, manufacturing of alloys, stainless steel welding, chromate production, dye and pigment production, wood preservation and poor storage and incorrect disposal practices by mining industries [13,14,15]. Globally, South Africa has one of the largest ferrochrome industries with 14 ferrochrome smelters and metallurgical industries scattered around the country. The Bushveld Complex of South Africa has the most important chromium and platinum group metals (PGM) deposits globally [16]. Small quantities of Cr(VI) polluted wastewater are inadvertently generated by numerous processing stages applied by the ferrochrome industry. Furthermore, the PGM mining and metallurgical refining industries in South Africa likewise consume noteworthy amounts of chromite ore [16]. Exposure to hexavalent chromium can cause health problems in the form of dermatitis, damage to the liver, lung and skin cancer, skin irritation, cancer and internal haemorrhage [15,17]. The WHO standard for Cr(VI) in surface water is 0.1 mg/L and 0.05 mg/L for drinking water [14]. Henceforth, Cr(VI) removal from the environmental water sources is also a top priority in South Africa.

UNIVERSITY OF JOHANNESBURG

The above challenges highlight the importance of developing effective fluoride and Cr(VI) removal systems that can be utilised to treat contaminated environmental water and wastewater. A variety of remediation technologies have been developed for fluoride and Cr(VI) removal from water including coagulation, precipitation [11], membrane processes [12], electrochemical treatment, ion exchange and adsorption [17]. However, some of the techniques have been found to have inherent weaknesses including relatively high cost [10], low efficiency for the removal of trace levels of pollutants [12], non-selectivity, pH sensitivity, requirement of large amounts of chemicals [13], production of large volumes of secondary pollution, such as sludge, susceptibility to fouling [14] and pre and post-treatment requirements [4,14,19]. A comprehensive review of the literature reveals surface adsorption as a promising alternative method especially for the third world countries because this process is simple, cheap to design and operate, environmentally friendly, less time consuming and efficient [10,19,20]. To identify effective and economic adsorbents, an assortment of adsorbents has been developed and evaluated. These include activated carbon, coal fly ash, chitosan, shells, alumina brick powder, polymers, charcoal, silica, zeolites, agricultural waste and other biosorbents [13,16,19,21]. However, these adsorbents have been reported to generate secondary pollutants, have low adsorption capacities, are nonselective, have narrow pH range and with decreasing ion concentration, a lot of these adsorbents have low efficiences. The preparation cost of adsorbents, selectivity, stability and sensitivity may dominate the overall cost and viability of the treatment process [13,14,19]. Synthetic methods based on relatively expensive reactants or working at high temperatures may not be feasible. Therefore, more research must be carried out to produce, modify and combine the advantages offered by different materials to produce easily prepared adsorbents with high adsorption capabilities that address the above challenges.

UNIVERSITY OF JOHANNESBURG

1.3 Justification

Recently, nanostructured materials have become some of the most popular materials globally due to their diverse properties and applications. The unique properties of these nanomaterials (NPs) [7] have led to their application in a number of fields including environmental pollution control [1,13]. Nano-engineered materials, among all available adsorbents, have demonstrated great potential in water remediation. They might be implemented as a useful strategy to mitigate water scarcity in developing countries. This is ascribed to their unique physical and chemical properties attributed to the increase in surface area with a decrease in particle size [2,4,13,14].

Nano-metal oxides (NMOs) are some of the most promising nanoparticle adsorbents that have been developed over the past decade and have attracted much attention. They have a rock salt crystal structure which result in increased chemical activity, low volume to surface area ratio, high number of easily accessible surface sites, high adsorption capacities, good acidic and basic properties and high chemical activity due to oxygen vacancies. Moreover, they can be regenerated for re-use, are amenable to doping, mimic natural soil systems and are applicable to poor communities as they are relatively less expensive [1,3,4]. The available nano-sized metal oxides include nano-sized ferric, manganese, aluminium, titanium, calcium, magnesium, zirconium and rare earth metal oxides [3,4]. There has been considerable interest on the application of (NMOs) for the removal of water contaminants with much of the focus having been concentrated on combining them with ferric oxides, aluminium based bimetal oxides, rare earth metal oxides and TiO_2 based binary NMOs[1,4]. Nevertheless, the leaching of metal ions in acidic environments and oxidation of metal oxides (manganese, aluminium, zinc, cadmium, copper and other heavy metal oxides fall into this category) raises concerns on the adsorbent longevity, potential health hazards and high costs. For example, aluminium-based sorbents for water defluoridation could be hazardous to humans as aluminium is neurotoxic and more attention should be given to metal oxides that are less of an environmental hazard (Mg, Fe, Ca, Ce, La, Ti, Zr oxides). In the application of these materials, it is important to study their regeneration, so that the recovery of the adsorbent for further use and safe disposal can be achieved [4,11,18]. The reported successes of some of the NMOs in mitigating water pollution have inspired the investigation on the synthesis and application of more novel nanostructured mixed oxides and nanocomposites for removal of fluoride and Cr(VI) ions from water. Furthermore, the use of iron based binary oxides as adsorbents enables ease of separation in solution due their magnetic properties [1,5,10,13,17]. As some NMOs studied are of high cost, this study aimed to produce adsorbents of low cost and develop more simple and practical methods of mixing a costly metal oxide and relatively cheap NMOs (like Ce, Mg or Fe oxides) while retaining high absorption capacities. Magnesium oxide (MgO) is relatively inexpensive owing to its abundance in nature [20]. Also, iron-based compounds are some of the most abundant materials on earth and they are easy to separate from solutions due to their magnetic properties. Cerium oxide (CeO_2) has desirable physical and chemical properties hence it has been widely used in catalysis and adsorption [22,23]. Furthermore, ceria has the lowest solubility among rare earth metal oxides, does not elute in aqueous solutions during the removal of ions and is the most abundant rare earth metal [22].

UNIVERSITY OF JOHANNESBURG

NMOs have great potential in adsorbing anionic pollutants, hence more studies on their application are imperative. NMOs are typically present in a very fine form which leads to problems of loss of activity due to agglomeration, poor selectivity and difficulty of separation from aqueous media [4]. These problems can be mitigated by fabrication of hybrid absorbents through coating NMOs particles onto porous supports. Several porous supports have been explored for this cause including chitosan [14], natural materials, metallic supports, zeolites and activated carbon and carbon nanotubes (CNTs) [4]. These studies have produced encouraging results albeit the materials have low adsorption capacities and selectivities, high expense and secondary pollution. Presently, studies on the regeneration of pollutant-loaded NMOs seem to be inadequate in comparison to the adsorption studies. Additionally, how to efficiently and economically separate the exhausted NMOs from water/wastewater still remains a challenge. Moreover, there is limited large scale exploitation of some of the materials attributed to environmental concerns and side effects [24,25,26]. Other issues including the interaction between support and supported NMOs, sustainability of the composite, practical application, effect of co-existing ions and chemical stability are critical and challenging, hence these call for investigation. Consequently, more studies on new novel porous supports have thus become imperative to derive the best benefits from NMOs and their nanocomposites. Some of the most exciting porous support materials are intrinsic conducting polymers (ICPs) including polyaniline (PANI) and polypyrrole (PPy). PANI and PPy are easy to synthesise using relatively cheap materials. Additionally, these polymers possess outstanding properties like chemical stability, large surface area, high affinity for anions and selectivity [27]. They contain amino groups which promote interaction with pollutants like Cr(VI) ions owing to strong binding ability. Their combination with magnetic and non-magnetic NMOs is beneficial in producing alternative hybrid materials. ICPs anchor NMOs moieties, producing nanocomposites with even more active sites for fluoride and Cr(VI) ions binding. Furthermore, there is improved separation of ions from aqueous solution, applicability and stability over wider pH ranges without compromising the nano-metal oxide properties. On the other hand, like most nanoscale materials, PANI and PPy tend to agglomerate due to van der Waals forces between layers reducing their adsorption ability. They have low mechanical and thermal strength and can be oxidatively degenerated at high Cr(VI) ions concentrations [5,13,17,24]. Nanocomposites of PANI fibers/PANI/PPy and NMOs produce hybrid inorganic/organic adsorbents with improved properties, applicability as well as ease of separation after adsorption [28]. More recently PANI-NMOs for removal of fluoride and Cr(VI) ions removal have been studied, but a majority of the studies have been limited to the use of homopolymer composites.

UNIVERSITY OF JOHANNESBURG

Currently different structures like nanotubes, nanowires and nanofibers [28] composites are an exciting group of materials hence the encouragement to fabricate metal oxides on polyaniline fibers in this study.

Some materials are reported to be efficient in laboratory bench scale experiments, but the materials, on application for real water treatment show poor capabilities inspiring the continuation of exploration for alternative competent materials. The use of pH values in the laboratory experiments which are close to natural water sources is very important and more such materials which are effective over a wide pH range are desirable. The preparation cost of nano-metal oxides may dominate the overall cost of the treatment process. Simple methods that use metal salts precursors rather than materials like metal alkoxides reactants and solvents which use expensive methods like micro emulsion, sol gel, microwave assisted, calcinations and also produce toxic organic waste that may not be worthwhile are needed.

1.4 Aim & objectives

The study aimed to synthesise and characterize hydrous cerium, magnesium and magnetic iron nano-metal oxides and their conducting polymer-based nanocomposites for the removal of fluoride and Cr(VI) ions from aqueous solution.

UNIVERSITY OF JOHANNESBURG

Specific Objectives

- To synthesize hydrous MgO-CeO_2 and CeO_2-Fe_3O_4 binary oxides from their precursor salts.

- To fabricate PANI/PPy based nanocomposites using as-synthesized hydrous CeO_2, Fe_3O_4 through precipitation and *in-situ* polymerisation.

- To characterize the as-synthesized materials by using various techniques including Fourier transform infrared spectroscopy (FTIR), X-ray diffraction (XRD) analysis, field emission scanning electron microscopy/energy dispersive X-ray spectroscopy (FE-SEM/EDS), high resolution transmission electron microscope (HR-TEM), Brunauer-Emmett-Teller (BET) surface area analysis,vibrating sample magnetometer

(VSM), thermogravimetric analysis (TGA), X-ray photoelectron spectroscopy (XPS) and dynamic mechanical anaysis (DMA).

- To evaluate the potential of mixed nano-metal oxides and their polymer modified nanocomposites for the removal of fluoride and Cr(VI) ions from water.

- To investigate the optimum conditions for the sorption of fluoride and Cr(VI) ions from aqueous solution using the as-synthesized adsorbents.

- To study the effect of co-existing ions on fluoride and Cr(VI) removal from aqueous solution by the as-synthesized adsorbents.

- To evaluate the regenerability of the as-synthesized nanocomposite adsorbents.

- To test the as-synthesized nanocomposite adsorbents for the removal of fluoride and Cr(VI) from real polluted water.

- To compare the adsorption capacities of the as-synthesized nanocomposite adsorbents with those reported in literature for the sorption of fluoride and Cr(VI) ions from aqueous solution and their efficacy.

UNIVERSITY OF JOHANNESBURG

1.5 Outline of thesis

The following outline provides a brief summary of what has been covered in the succeeding chapters of the thesis.

Chapter 2: Literature review

The literature review chapter gives a detailed discussion on fluoride and Cr(VI) ions in terms of their global occurrence, sources, exposure pathways, toxicity and conventional removal techniques for their removal from water. Emphasis was placed on adsorption, the various types of adsorbents used for removal of fluoride ions and Cr(VI) ions from water, nano-metal oxides and their polymer-based nanocomposites as emerging adsorbents and their potential application in removal of fluoride and Cr(VI) ions from water.

Chapter 3: Instrumentation

This chapter gives details of the various instruments used and the characterization techniques applied in this study.

Chapter 4: Rapid high adsorption performance of hydrous cerium-magnesium oxides for removal of fluoride from water.

This chapter describes the synthesis and characterization HCeMgO1:1 as a rapid high capacity adsorbent for removal of fluoride ions from water.

Chapter 5: High efficient removal of fluoride ions using hydrous CeO_2-Fe_3O_4 (HCeFe NFs-2) nanocomposite decorated polyaniline fibers nanocomposite.

This chapter describes the synthesis and characterization of HCeFe NFs-2 nanocomposite for efficient removal of fluoride ions from aqueous solution.

Chapter 6: Magnetic arginine-functionalized polypyrrole with improved and selective Cr(VI) ions removal from water.

This chapter describes the synthesis and characterization of Fe_3O_4@Arg-PPy for efficient removal of Cr(VI) ions from water.

Chapter 7: Conclusions and recommendations

All findings and evaluations obtained in this research are discussed in detail in this chapter as well as recommendations for further studies.

1.6 References

[1] V. Tomar, D. Kumar, A critical study on efficiency of different materials for fluoride removal from aqueous media, Chem. Cent. J. 7 (2013) 51.

[2] V. Khatibikamal, A. Torabian, F. Janpoor, G. Hoshyaripour, Fluoride removal from industrial wastewater using electrocoagulation and its adsorption kinetics, J. Hazard. Mater. 179 (2010) 276–280.

UNIVERSITY of JOHANNESBURG

[3] K.Y. Kumar, H.B. Muralidhara, Y.A. Nayaka, J. Balasubramanyam, H. Hanumanthappa, Low-cost synthesis of metal oxide nanoparticles and their application in adsorption of commercial dye and heavy metal ion in aqueous solution, Powder Technol. 246 (2013) 125–136.

[4] M. Hua, S. Zhang. B. Pan, W. Zhang, L. Lv, Q. Lu Zhang, Heavy metal removal from water/wastewater by nanosized metal oxides: a review, J. Hazard. Mater. 211 (2012) 317–331.

[5] E.J. Ncube, The distribution of fluoride in South African groundwater and the impact of on dental health, Doctoral dissertation, University of Pretoria, (2002).

[6] D. Dayananda, V.R. Sarva, S.V. Prasad, J. Arunachalam, N.N. Ghosh, Preparation of CaO loaded mesoporous Al_2O_3: Efficient adsorbent for fluoride removal from water, Chem. Eng. J. 248 (2014) 430–439.

[7] L. Valdez-Jiménez, C.S. Fregozo, M.M. Beltrán, O.G. Coronado, M.P. Vega, Effects of the fluoride on the central nervous system, Neurología 26 (2011) 297–300.

[8] J. Hu, J.H. Shipley, Evaluation of desorption of Pb(II), Cu (II) and Zn (II) from titanium dioxide nanoparticles, Sci. Total Environ. 43 (2012) 209–220.

[9] V.K. Bhart, A. Giri, K. Kumar, Fluorides Sources, toxicity and amelioration: review, Peertechz, J. Scie. Toxico. 2 (2016) 21–32.

[10] S. Ali, S.K. Thakur, A. Sarkar, S. Sheka, Worldwide contamination by fluoride ions, Environ. Chem. Lett. 14 (2016) 291–315

[11] Fluorides-Environmental Health Criteria 227, World Health Organization (WHO): Geneva, Switzerland, 2002.

[12] L. Chai, Y. Wang, N. Zhao, W. Yang, X. You, Sulphate-doped Fe_3O_4/Al_2O_3 nanoparticles as a novel adsorbent for fluoride removal from drinking water, Water Res. 47 (2013) 4040–4049.

[13] A.S. Adeleye, J.R. Conway, K. Garner, Y. Huang, Y. Su, A.A. Keller, Engineered nanomaterials for water treatment and remediation: Costs, benefits and applicability, Chem. Eng. J. 286 (2016) 640–662.

[14] S. Jagtap, M.K. Yenkie, N. Labhsetwar, S. Rayalu, Fluoride in drinking water and defluoridation of water, Chem. Rev. 112 (2012) 2454–2466.

[15] Y.Y. Chang, J.W. Lim, J.K. Yang, Removal of As (V) and Cr(VI) in aqueous solution by sand media simultaneously coated with Fe and Mn oxides, J. Ind. Eng. Chem. 18 (2012) 188–192.

[16] A.D. Venter, J.P. Beukes, P.G. Van Zyl, M. Josipovic, K. Jaars, V. Vakkari, Regional atmospheric Cr(VI) pollution from the bushveld complex, South Africa, Atmos. Pollut. Res. 7 (2016) 762–767.

[17] A.E. Chavez-Guajardo, J.C. Medina-Llanas, L. Maqueira, C.A. Andrade, K.G. Alves, C.P. de Melo, Efficient removal of Cr(VI) and Cu(II) ions from aqueous media by use of

UNIVERSITY OF JOHANNESBURG

polypyrrole and polyaniline magnetic nanocomposites, Chem. Eng. J. 281 (2015) 826–836.

[18] J. Wang, D. Kang, X. Yu, M. Ge, Y. Chen, Synthesis and characterization of Mg-Fe-La tri-metal composite as an adsorbent for fluoride removal, Chem. Eng. J. 264 (2015) 506–513.

[19] S. Ayoob, A.K. Gupta, V.T. Bhat, A conceptual overview on sustainable technologies for the defluoridation of drinking water, Critical. Review Environ. Sci. Technol. 38 (2008) 401–470.

[20] H. Zhou, W. Chen, X. Zhang, D. Shi, Preparation of nanometer magnesia and its properties for fluoride removal, Front Environ. Sci. 3 (2014) 97–108.

[21] I. Saha, I. Ghosh, D. Nandi, K. Gupta, D. Chatterjee, U.C. Ghosh, β-Cyclodextrin modified hydrous zirconium oxide: synthesis, characterization and defluoridation performance from aqueous solution, Chem. Eng. J. 263 (2015) 220–230.

[22] S. Deng, H. Liu, W. Zhou J. Huang, G. Yu, Mn-Ce oxide as a high-capacity adsorbent for fluoride removal from water, J. Hazard. Mater. 186 (2011) 1360–1366.

[23] D. Tang, G. Zhang, Efficient removal of F^- by hierarchical Ce-Fe bimetal adsorbent: thermodynamics, kinetics and mechanism, Chem. Eng. J. 283 (2016) 721–729.

[24] A. Olad, R. Nabavi, Application of polyaniline for the reduction of toxic Cr(VI) in water, J. Hazard. Mater. 147 (2007) 845–851.

[25] I. Mohmood, C.B. Lopes, I. Lopes, I. Ahmad, A.C. Duarte, E. Pereira, Nanoscale materials and their use in water contaminants removal-a review, Environ. Sci. Pollut. Res. 20 (2013) 1239–1260.

[26] Z. Li, T. Hulderman, R. Salmen, R. Chapman, S.S Leonard, S.H. Young, A. Shvedova, M.I. Luster, P.P. Simeonova, Cardiovascular effects of pulmonary exposure to single-wall carbon nanotubes, Environ. Health Perspect. 115 (2006) 377–382

[27] S. Sakar, E. Guibal, F. Quignard, A.K. SenGupta, Polymer-supported metals and metal oxide nanoparticles: synthesis, characterization and applications, J. Nanopart Res. 14 (2012) 715.

[28] X. Guo, G.T. Fei, H. Su, L. De Zhang, High-Performance and reproducible polyaniline Nanowire/tubes for removal of Cr(VI) in aqueous solution, Physi. Chem. 115 (2011) 1608–1613.

UNIVERSITY OF JOHANNESBURG

CHAPTER TWO

LITERATURE REVIEW

2.1 Introduction

This chapter is a review of the current global scenario of fluoride and Cr(VI) ions with attention being paid to their occurrence, sources and toxicity. The various techniques available for the removal of these ions are highlighted with much attention and prominence being given to adsorption technology because of its simplicity in design and implementation. Various adsorbents have been discussed and thoroughly scrutinised. Lastly the benefits of nanotechnology and nanomaterials have been discussed, particularly the nano-metals oxides and their conducting polymer composites which have been presented as feasible materials for future adsorption technology.

2.2 Fluoride in water

Water is an essential resource that drives and sustains life. Consequently, the inevitable upsurge in demand for water to produce food, supply industries and sustain urban and rural populaces culminated in an escalating scarcity of freshwater in numerous parts of the world [1]. Nearly 4 billion people in the world are affected by water scarcity [2]. To make matters worse, only 0.014% of the water in the world is fresh and accessible otherwise the remaining 97% is saline and less than 3% is difficult to access [3]. One of the measures that have been developed to mitigate water shortage is the use of underground water. It is the main source of water supplies in most developing countries [4]. Although underground water exploitation has been growing exponentially, it is often met with challenges of naturally occurring chemicals which have adverse health effects. Some naturally occurring toxic chemicals in ground water are fluoride ions. Fluoride is a halide ion of great importance due to its small size and high electronegativity. It is the 13th largest abundant element and is widely distributed in air, water, soil and food [5]. Fluorine forms fluoride ions after reaction and because of its high reactivity, it can combine with almost anything and this makes fluoride ions too abundant everywhere and can affect the biochemical functions of living organisms [6]. Generally, there are many compounds and minerals containing fluoride ions including fluorite (CaF_2), cryolite (Na_3AlF_6), topaz [($Al_2SiO_4(FOH_2)$], sellaite (MgF_2), bastnaesite [$(CeLa)(CO_3)F$] and fluorapatite [$Ca_5(PO_4)_3F$]

of which weathering of these compounds produce a lot of free fluoride ions [7]. Besides the dissolution of these minerals which leads to the contamination of ground water, vulcanicity, marine and anthropogenic activities also contribute to fluoride pollution [4,5,6]. WHO regulates fluoride ions in water to be below 1.5 mg/L [5].

2.2.1 Fluoride state of affairs worldwide

Fig. 2.1 and **Table 2.1** show a pathetic worldwide scenario of fluorides in water with millions of people affected by fluoride pollution. For example, 23 million people in India are severely affected and 40 million are exposed to the risk of fluoride contamination. Furthermore, almost every state in India is affected. In Africa underground water is the main source of drinking water. High fluoride levels have been reported in Morocco, Ethiopia, Algeria, South Africa with East Africa rift valley having the highest levels. China is the most affected in East Asia with 43 million cases having reported in east China alone. In South America, Argentina is the

UNIVERSITY OF JOHANNESBURG

most affected, whilst up north in USA, Mexico and Canada there are moderate effects. In Europe, fluoride contamination is generally within permissible levels [7].

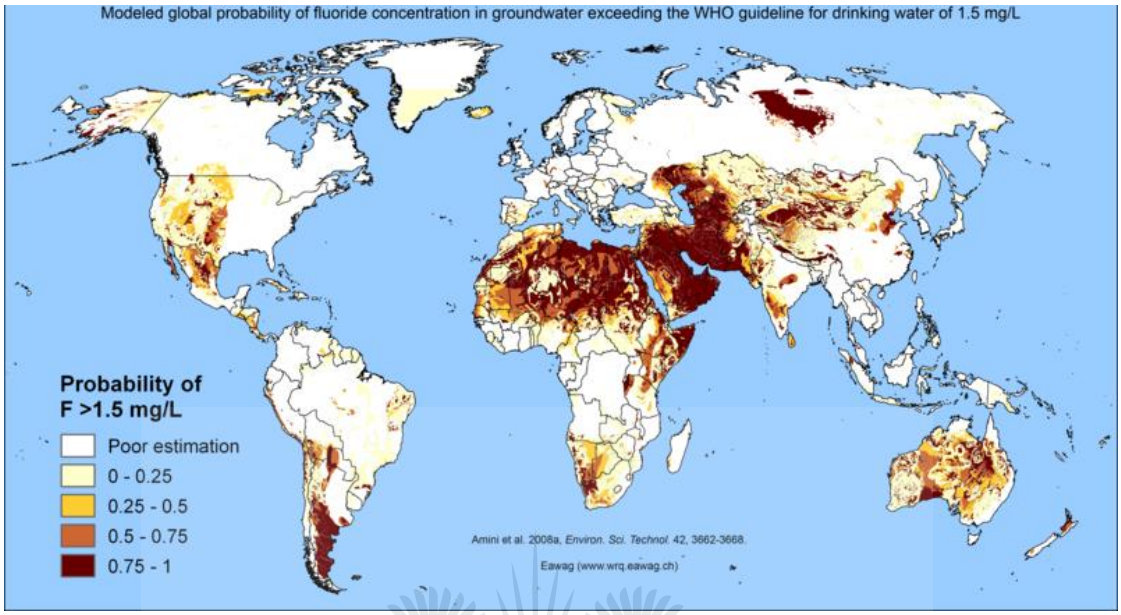

Fig. 2.1: Global fluoride situation [8]

There are twenty three countries globally that fall within the critical category of fluoride contamination as shown in **Table 2.1**:

Table 2.1: Global scenario of fluoride pollution [6].

UNIVERSITY OF JOHANNESBURG

Country	Fluoride level (mg/L) reported
South Africa	30.0
Ghana	0.11-4.6
Kenya	2-20
Nigeria	4.7-6.6
Senegal	4.6-7.4
Tanzania	8.0-12.7
Uganda	0.5-2.5
Sudan	0.6-3.2
Saudi Arabia	2.8
Turkey	13.7
Canada	4.3
Argentina	0.9-18.2
Brazil	2-3
Ethiopia	1.5-177
Mexico	1.5-2.8
USA	1.06-4.07
Germany	8.8
Korea	<5
Norway	0.02-9.46
Poland	>3
Spain	2.5-5.9
China	21.5
Finland	>3
India	0.5-69.7
Sri Lanka	10
Pakistan	8-13.52

UNIVERSITY OF JOHANNESBURG

In South Africa, there is a high prevalence of fluoride contaminated water and the highest concentrations were recorded in areas in the North West (Elandsfontein: 42.05 mg/L, Zoutpan: 40.77 mg/L, Ganyesa: 8.00 mg/L), Northern Cape (Marlborough: 34.64 mg/L), Eastern Cape (Dornkloof: 39.13 mg/L, The Apex: 3.92 mg/L and Grasrand: 19.52 mg/L), Kwazulu Natal (Kwazulu: 7.14 mg/L and Golokodo: 15.72 mg/L) and Limpopo (Kasteel 40.49 mg/L, Siloam 7.2 mg/L) provinces [9]. Furthermore, **Fig. 2.2** generally confirms this distribution. As a result

of this, fluoride removal from water has attracted much attention by researchers and its clean up from the environment, especially in water, is a top priority in South Africa.

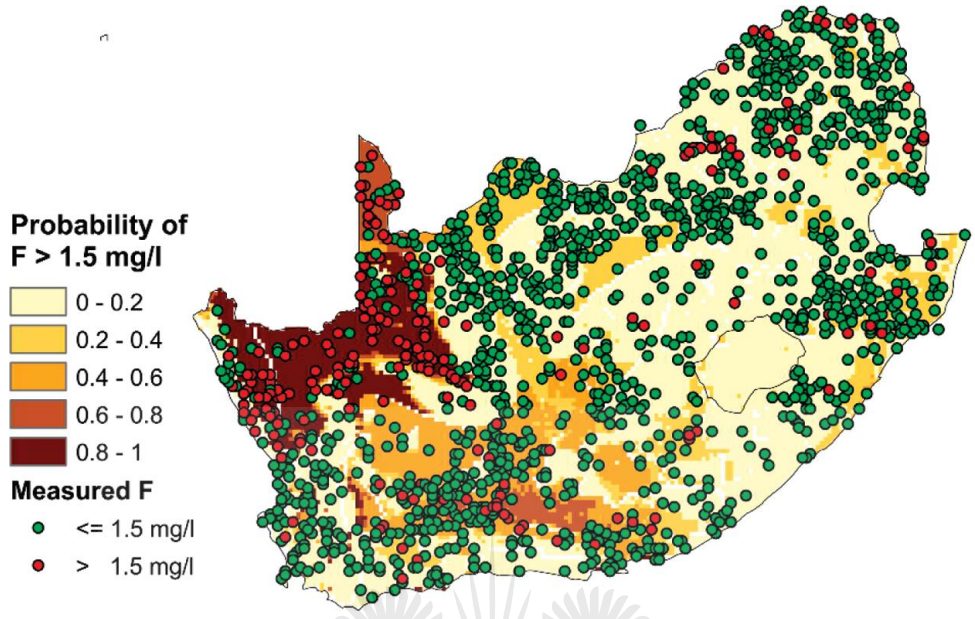

Fig. 2.2: South Africa fluoride situation [8]

2.2.2 Sources of fluoride and human exposure

The major sources of fluoride are from geogenic and anthropogenic activities [6]. Geogenic sources include ground water, marine and volcanic activities. The presence of fluoride in underground water, as mentioned earlier, results from the dissolution of fluoride bearing rocks such as fluorite, apatite, biotite, fluorspar, amphiboles, micas etc. For example, fluorspar (CaF_2) reacts as shown in **Equation (2.1)**:

$$CaF_2 + 2NaHCO_3 \rightarrow CaCO_3 + 2Na^+ + F^- + H_2O + CO_2 \quad (2.1)$$

The dissolution of fluoride containing rocks favour arid and semi-arid regions which explains the prevalence of fluoride in these areas like Ethiopia and locally, South Africa's North West province and semi-arid regions of other countries. Volcanic ash has a high level of fluoride since fluoride ions are released into the air in the form of hydrogen fluoride during volcanic eruptions [7]. Anthropogenic sources result from human industrial activities, food items, including dairy products and polluted industrial wastewater discharges. These are superphosphate fertilizer, glass and ceramic manufacturing industries, aluminium and zinc

smelting, production of steel, uranium enrichment, coal fire power stations, oil refineries, photovoltaic solar cells, silicon-based high tech-semiconductor production and municipal waste [6,7,8,10,11]

2.2.3 Trails of human exposure

The major pathways of human exposure to fluoride are food, water and medication.

2.2.3 Water

Water is the major pathway of human exposure to fluorides. This is predominantly because humans use a lot of water on a daily basis for drinking, washing, bathing and many other daily domestic and industrial activities. The exposure will depend on the level of fluoride in the water under use. As mentioned earlier, most of the water used in developing countries is ground water which really exposes human beings to the greatest geogenic source of fluorides [12].

2.2.3.2 Food

Several foods that are eaten contain traces of fluoride or have fluoride containing chemicals such as tea which comes from plant leaves and accumulates aluminium-fluoride complexes, wine, vegetables, fish, meat and fruits. Normally the level of fluoride in food stuffs is very low but there is a problem with bioaccumulation [5].

UNIVERSITY OF JOHANNESBURG

2.2.3.3 Medicines and cosmetics

Some cosmetics and medicines contain compounds with fluoride ions. Ironically, tooth paste is useful in preventing dental cavities but the protracted use of toothpaste will result in accumulation of calcium fluoride. Food add-ons like lozenges, drops and tablets mouthwash sold over the counter are some of the sources of fluoride [12].

2.2.3.4 Air

Volcanic activity and burning of fluoride containing compounds like coal introduce hydrogen fluoride in the air. This would be absorbed in the air during fog, rain and snow forming aerosol hydrogen fluoride. This may fall and become deposited on the land and is eventually washed into water bodies thus also quickening water fluoride exposure [5].

2.2.4 Fluoride toxicity

The initial steps in fluoride toxicity are a reduction in food intake and body weight [4] and dental fluorosis, where there is browning of teeth and blotching [5,13] as shown in **Fig. 2.3**.

UNIVERSITY
JOHANNESBURG

Fig. 2.3: Fluoride toxicity showing dental fluorosis [14]

Prolonged exposure to fluoride may result in skeletal fluorosis which usually happens after exposure to concentration between 4 to 10 mg/L [6]. Skeletal fluorosis is the weakening of bones and the malfunction of the skeleton system as shown in **Fig. 2.4**, which may culminate in reduced mobility [13].

Fig. 2.4: Fluoride toxicity showing skeletal fluorosis [15]

The chemistry behind beneficial and side effects of fluoride is as follows:

When fluoride is taken in low quantities, there is exchange between hydroxide ions and fluoride ions in calcium hydroxy-phosphate ($Ca_5(PO_4)_3OH$), the building block of skeletal material to fluorophosphate ($Ca_5(PO_4)_3F$) which is more acid resistant, hence no dental cavities occur [4] as shown **in Equation (2.2)**:

UNIVERSITY OF JOHANNESBURG

$$Ca_5(PO_4)_3\,OH + F^- \rightarrow Ca_5(PO_4)_3F + OH^- \quad (2.2)$$

If excessive fluoride is taken, the reaction above may go beyond replacement of hydroxide groups as shown in **Equation (2.3)**:

$$Ca_5(PO_4)_3F + 9F^- \rightarrow Ca_5F_{10} + 3PO_4^{3-} \quad (2.3)$$

The material formed, calcium decafluoride (Ca_5F_{10}) is hard, brittle and unsuitable as skeletal structure and functions, hence bone structures may be deformed or bent as shown in **Fig. 2.4** [6,9]. Other effects of fluoride toxicity are muscle degeneration, low haemoglobin content, skin rashes, depression, abdominal pains, urinary tract malfunction, reduced immunity, oxidative stress of kidney lungs and liver tissues, cancer, disruption of various oxidative processes like

glycolysis, oxidative phosphorylation, coagulation, decreased metabolic rate and neurodegeneration [4,6,9,13,16,17].

2.3 Chromium

2.3.1 Historical background

Chromium, a transition element, is the 21st abundant element in the earth‘s crust. It was discovered in 1797 by the French chemist Louis Nicholas Vauquelin. The major chromium compound is ferric chromite ($FeCrO_4$) mainly found in South Africa, Russia, Kazakhstan, India and the Philippines [18].

2.3.2 Chromium occurrence and production

The pie chart in **Fig. 2.5** shows the global chromium production in 2014. South Africa accounts for the largest amount of the world chromite production. Globally, there are large deposits of chromium which are possibly exploited and there is a great potential for chromium water pollution related problems.

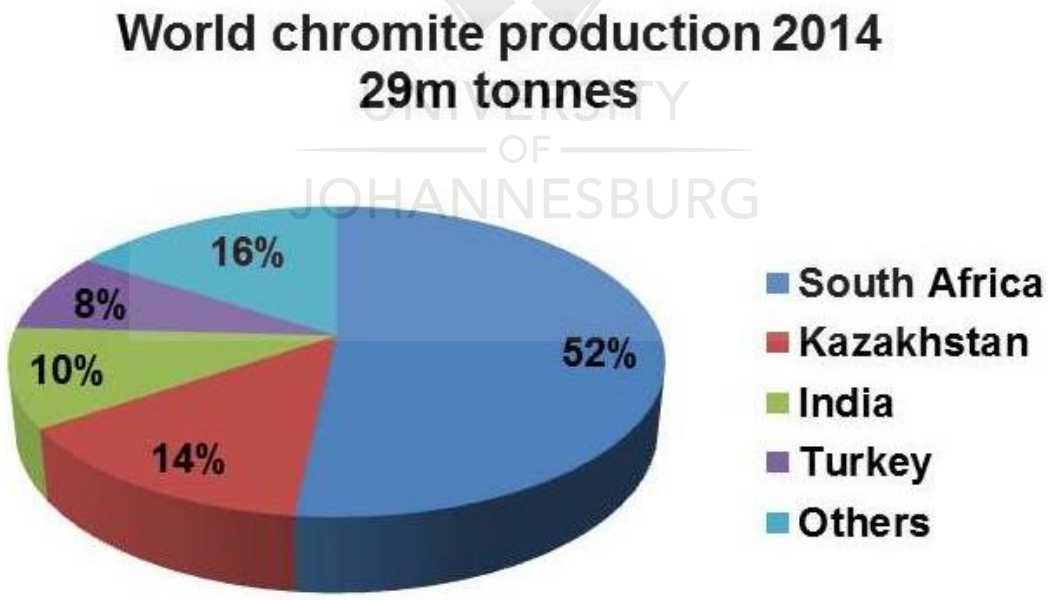

Fig. 2.5: World chromite production in 2014 [19]

2.3.3 Chromium in water

Chromium occurs in three main oxidation states (II), (III) and (VI), with (II) being unstable. It exhibits biologically significance in the more predominant (III) trivalent and hexavalent (VI) forms in aqueous solution [20]. Nevertheless, there is a great difference between the two states in terms of toxicity, with Cr(VI) being 500 times more toxic than Cr(III). Cr(III) is basically insoluble and is a micronutrient of biological relevancy. Cr(VI) is highly soluble (1680 g/L) over a wide pH range [22] and mobile, it exists in several forms including H_2CrO_4, $HCrO_4^-$, CrO_4^{2-} and $Cr_2O_7^{2-}$ depending on the pH. **Fig. 2.6** shows the relative distribution of different species of Cr(VI) in aqueous solution. As illustrated, at pH greater than 6 the CrO_4^{2-} is dominant whilst at below pH 6 Cr(VI) exists as H_2CrO_4, $HCrO_4^-$, with $HCrO_4^-$ being predominant. At very high concentrations of Cr(VI), $HCrO_4^-$ exists as the dimer form, $Cr_2O_7^{2-}$ [21,22]. Consequently, in aqueous environments, compounds that are in the form of Cr(VI) have high solubility and mobility hence may lead to possible Cr(VI) pollution.

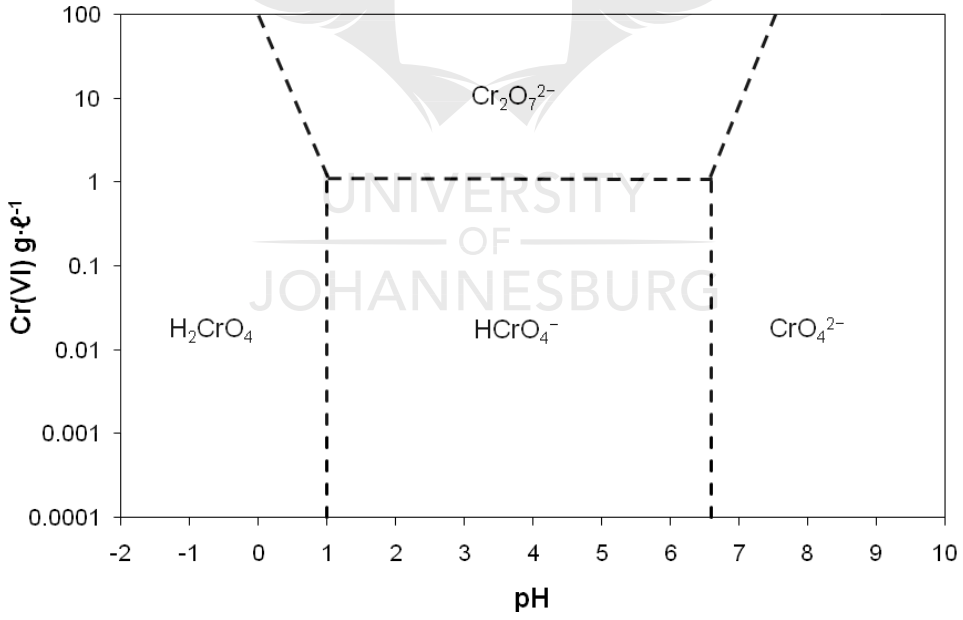

Fig 2.6: The relative distribution of different species of Cr(VI) in aqueous solution as function of pH [21]

Consequently, Cr(VI) has demonstrated too many adverse effects that it is of interest in water pollution than Cr(III).

2.3.4 Sources of Cr(VI) ions

The major sources of Cr(VI) are anthropogenic, besides some natural sources with the former contributing to 70% of the Cr(VI) in water [22]. These anthropogenic activities are in the ferrochrome industries where there is production of high speed steel alloys, cast irons and nonferrous alloys. Chromite ore ($FeCr_2O_4$), the main source of chromium is mostly mined in South Africa, Kazakhstan, India and Turkey globally, as mentioned before [19]. In electrical systems there is electroplating and electronic equipment manufacture [23]. In automobile making processes, stainless steel parts, catalytic converters, chrome trimming and other decorative purposes dominate [24]. Other sources are dye and pigment making, leather tanning, wood preservation, paint manufacture, chemical manufacture of brass, mining, nuclear power stations, pulp and paper making mills, production of fungicides, making of magnetic tapes and activated carbon and domestic effluent which account for 32% of the world total chromium [25,26,27]. **Table 2.2** shows chromium-containing industrial products and the type of chromium compounds which they contain.

Table 2.2: Products that contain hexavalent chromium [28]

Product	Types of Hexavalent chromium chemicals
Pigments in paints, inks and plastics	lead chromate (chrome yellow), chrome green, molybdenum orange, zinc chromate, calcium chromate, potassium dichromate, sodium chromate
Anti-corrosion coatings (spray plating and spray coating)	chromic trioxide (chromic acid), zinc chromate, barium chromate, calcium chromate, sodium chromate, strontium chromate
Stainless steel and other high chromium alloys	hexavalent chromium (when cast, or torch cut)
Textile dyes	ammonium dichromate, potassium chromate, potassium dichromate, sodium chromate
Wood preservation	chromium trioxide
Leather tanning	ammonium dichromate

In aqueous environments, the Cr(VI)-containing compounds have high solubility and mobility hence these myriad of processes and products may eventually produce effluent which can accumulate in water bodies and aquifers. Natural sources of Cr(VI) ions include weathering of rocks, especially serpentine bed rock, saline brines in evaporate basins and chromite ore bodies [29].

South Africa contains three quarters of the globally viable ferrochrome industry. There are 14 ferrochrome smelters and metallurgical industries dotted around the country. These are mostly located in or near the Bushveld Complex geological structure where the South African chromite

deposits are found. This region has globally some of the most important chromium and platinum group metals (PGMs) deposits. Little quantities of Cr(VI) are accidentally produced by several processing stages utilised in the ferrochrome industry. Furthermore, South Africa is also one of the major producers of PGMs whose mining and metallurgical refining industries expend noteworthy amounts of chromite ore, hence chromium water pollution is potentially a major threat in the country [30].

2.3.5 Cr(VI) exposure and toxicity

Human beings are exposed to Cr(VI) through three major pathways:

2.3.5.1 Dermal exposure

This exposure to chromium occurs through bathing, showering, swimming and contact with soil, though this is far less probable compared to occupational exposure. Due to its high solubility over a small range of pH, Cr(VI) is absorbed by the skin much faster than Cr(III). The corrosive nature of some chromium containing compounds leads to the burning of skin and irritation, dermatitis and allergies [22].

2.3.5.2 Inhalation

UNIVERSITY OF JOHANNESBURG

The exposure to dust, fumes and aerosol containing Cr(VI) can occur. This can lead to stomach ulcers [19], respiratory problems like wheezing, shortness of breath and nasal itching and weakened immune system [25].

2.3.5.3 Ingestion

This may involve eating food, drinking water and consuming Cr(VI) contaminated soil. Cr(VI) is absorbed through the gut but at low concentrations it can easily be reduced to Cr(III). Nevertheless, at high concentrations it can cause kidney and liver damage, lung cancer and gastrointestinal problems, among other problems [25,26].

Tap water tests in 31 out of 35 cites in USA showed the presence of Cr(VI) ions and in 25 of these cities the level was high enough to have cancer side effects. Furthermore, it is reported that at least 74 million Americans in 24 states drank Cr(VI) polluted tap water [31]. In India,

one of the most polluted areas is Sukinda in the Jajpur and Orisha state which has 70% of surface water and 60% of the drinking water containing Cr(VI) at levels more than twice the international standards. The number of people affected was 2.6 million with the major source of the Cr(VI) being the chromite mines and processing around these mines [32]. A good example is the case of chromite mine workers in Sikunda India. It was reported that infertility, birth defects and still births are prevalent. Statistics showed that 84.75% deaths have been reported in the mine and 86.42% in the villages around as well as gastrointestinal problems, tuberculosis and asthma as common ailments as a result of water contaminated with Cr(VI) ions [32]. In the South Africa south of Durban, there was a potentially fatal Cr(VI) pollution due to contaminated ground water under houses in the Merebank residential area and in ground water outside the Bayer factory in Tomango road [19,33].

2.3.6 Guideline limits for Cr(VI) in water

Due to potential Cr(VI) toxicity to human beings and other living organisms, its levels in drinking water, surface water, industrial wastewater and water used for other purposes are regulated. The acceptable standards of Cr(VI) in water in various parts of the world by different agencies like Bureau of Indian Standards (BIS-2012), World Health Organisation (WHO), USA Environmental Protection Agency (EPA) and South Africa are 0.05 mg/L for drinking water and 0.1 mg/L for surface water [22,31,33].

UNIVERSITY OF JOHANNESBURG

2.4 Techniques for removal of fluoride and Cr(VI) ions from water

As alluded to in the above sections, fluoride and Cr(VI) ions pose a great threat for human life especially through drinking and surface waters. This highlights the importance of implementing removal systems if water is to be regarded as safe and clean. It is also mandatory for water sources to meet regulatory permissible levels. Several conventional techniques have been developed to deal with these pollutants and are discussed here.

2.4.1 Precipitation-coagulation

This is principally the use of chemicals to transform substances into insoluble materials which become dense and settle down and are removed from a system. This is achieved either by converting the substance into a separable form or changing the solvent into some form which

removes the solubility of the pollutant [6]. The precipitation removal of fluoride can be accomplished by a simple Nalgonda technique (**Fig. 2.7**) where aluminium sulphate and lime are continuously added together with co-precipitators to remove fluoride ions [6,34,35]. What happens in the process is illustrated by **Equations (2.4)** to **(2.7)**:

$$Al_2(SO_4)_3 + 6H_2O \rightarrow 2Al(OH)_3 + 3SO_4^{2-} + 6H^+ \quad (2.4)$$

$$Al(OH)_3 + F^- \rightarrow A\text{-}F_{\ complex} + \text{undefined precipitate} \quad (2.5)$$

$$Ca(OH)_2 + 6H^+ \rightarrow 3Ca^{2+} + 6H_2O \quad (2.6)$$

$$Ca^{2+} + F^- \rightarrow CaF_2 \quad (2.7)$$

In the presence of phosphate ions

$$10Ca^{2+}{}_{(aq)}{}^{+} + 6P\ O_4{}^{2-}{}_{(aq)} + F^-{}_{(aq)} \rightarrow Ca_{10}(PO_4)F_{2(s)} \quad (2.8)$$

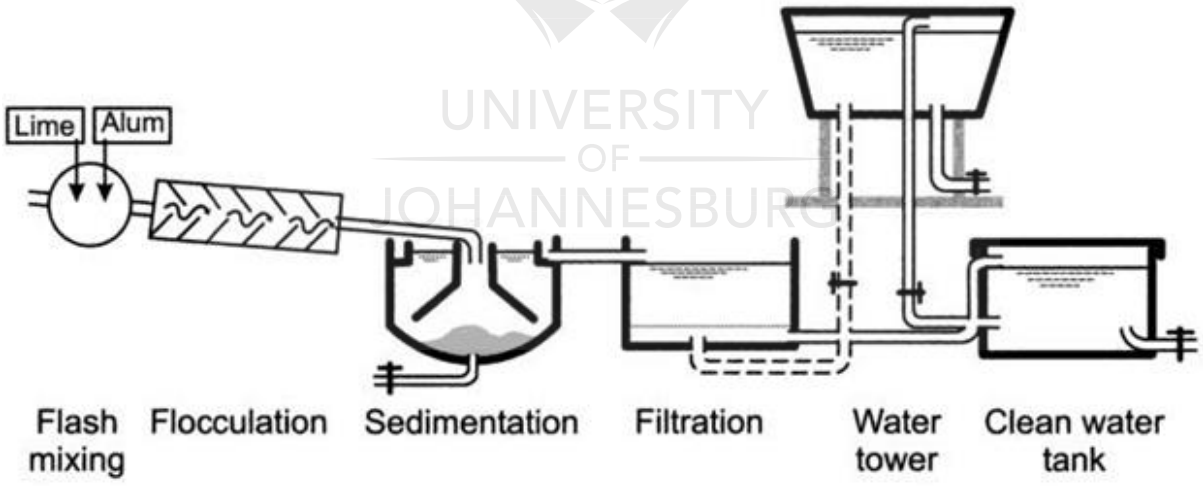

Fig. 2.7: Schematic diagram of Nalgonda technique [35]

This technique is simply adaptable to local communities and has low energy costs. However, desalination may be required, as dissolved solids increase, water hardness is also a challenge together with accumulation of much sludge [34,35].

For Cr(VI) ions, the precipitation-coagulation process can be conducted by the addition of chemicals like ferrous sulphate and lime. This most commonly used method in the South African ferrochrome (FeCr) industry for treating Cr(VI) wastewater, entails reducing Cr(VI) in solution to Cr(III) with ferrous iron. The Cr(III) is subsequently precipitated and disposed in landfills sites [19]. The ferrous ions reduce Cr(VI) to Cr(III) as shown in **Equations (2.9)** and **(2.10)**:

$$6Fe^{2+}_{(aq)} + Cr_2O_7^{2-}{}_{(aq)} + 14H^{+}_{(aq)} \rightarrow 6Fe^{3+}_{(aq)} + 2Cr^{3+}_{(aq)} + 7H_2O \quad (2.9)$$

The resulting state can be precipitated as hydroxides by lime and are removed [36].

$$Cr^{3+}_{(aq)} + 3OH^{-}_{(aq)} \rightarrow Cr(OH)_{3(s)} \quad (2.10)$$

This process also produces a lot of sludge which has to be disposed of every now and then from one land fill site to another, requires large volumes of costly chemicals, its efficiency is pH dependent, there is presence of salts and it cannot remove trace amounts of pollutants [37].

2.4.2 Membrane separation-based techniques

As new technologies emerged more sophisticated and comprehensive techniques based on membranes have been developed. These techniques operate on basis of a membrane, which is a diaphragm or partitioning layer between two phases that controls the movement of material between the two phases. These techniques are reverse osmosis (RO), nanofiltration (NF) and electrodialysis (ED) [6]. These technologies are being applied for the removal of fluoride and Cr(VI) ions from water.

In RO (**Fig. 2.8**), pressure forces a solution through the membrane but with the retention of solute on one side, permitting the pure solvent to pass through to the other side. It is a reversal of the normal osmosis process and pressure is applied against a concentration gradient [34,36]. RO can be used for the removal of Cr(VI) from electroplating effluent very well. In fluoride removal it produces high quality water [6]. However, it is an energy intensive process, has expensive equipment, needs monitoring and generates a lot of sludge [36].

UNIVERSITY OF JOHANNESBURG

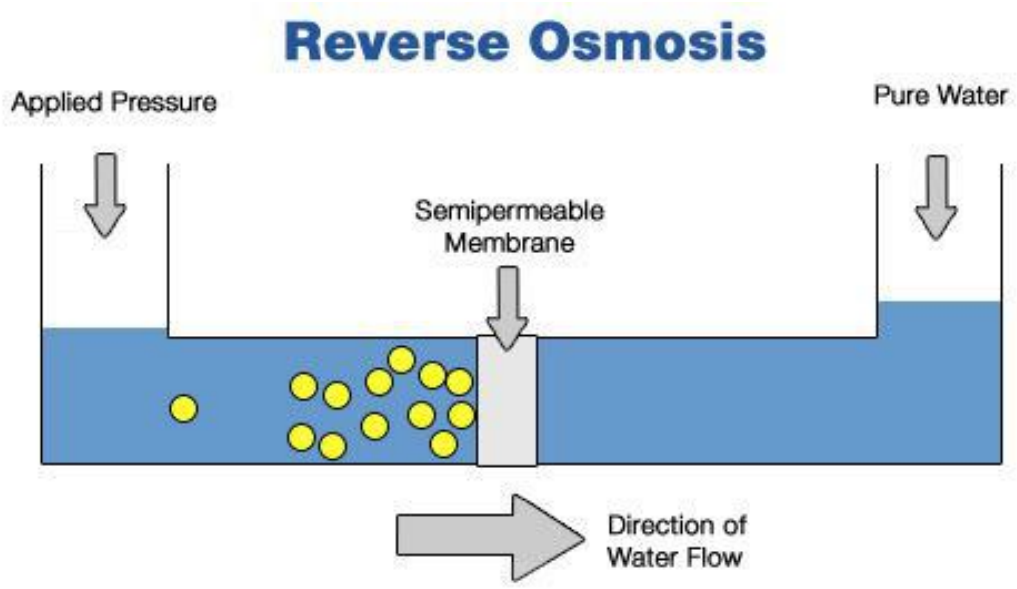

Fig. 2.8: Schematic diagram of reverse osmosis process [34]

Fig. 2.9 shows ED, which involves the use of a potential gradient to transport ions through an ion permeable membrane between solutions. Ions are driven because of the electric charge which they possess and they are driven through polymer fabricated membranes [10]. The potential field is produced by the application of a voltage between two electrodes which results in the movement of cations toward the negatively charged side of the membrane and the anions toward the positively charged side of the membrane. Studies have been conducted on fluoride ions removal from water using this technique. Amor et al. [37] studied the removal of fluoride ions from brackish water with total dissolved solids of 3000 ppm and fluoride concentration of 3 mg/L. It was reported that the water quality targets were achieved after electrodialysis. Recently, Sharma et al. [38] studied the removal of fluoride ions from brackish water using indigenous exchange resins with the salt and fluoride concentrations of 2050 mg/L and 5-20 mg/L, respectively. The study revealed that the optimum applied voltage was 2V/cell pair and the process was 87% efficient. On the other hand, Sadyrbaeva [39] studied the removal of Cr(VI) using tri-octylamine mixed with di(2-ethylhexyl) phosphoric acid in 1.2 dichloromethane as a liquid membrane in electrodialysis. The study revealed that 90% stripping degree was achieved in 1-4 h. However, electrodialysis has high capital and operation costs, needs expertise training and is subject to fouling of the membrane.

UNIVERSITY OF JOHANNESBURG

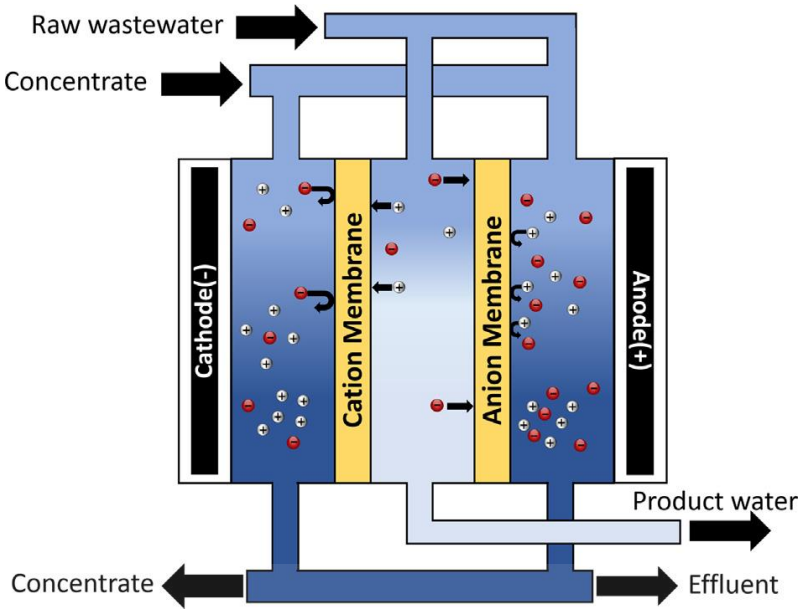

Fig. 2.9: Schematic diagram of electrodialysis process [40]

Recently NF, a relatively newer technology compared to RO, has become a well-accepted membrane process for water treatment. NF is a low-pressure technique which selectively eliminates larger dissolved solids in the order of nanometers and is commonly used to separate multivalent ions from monovalent species. NF membranes have relatively larger pores than RO and therefore offer less resistance to the passage of both solute and solvent. Hu et al. [41] applied the NF technique for removal of fluoride ions from water. The results of the study indicated that the rejection of NaF increased as the applied pressure and solution flux increased but the feed concetration was reduced. On the other hand, Barikhan et al. [42] studied the removal of Cr(VI) from sulphate containing water. The findings showed 96% rejection of Cr(VI) at 4 bars in 0.1 mg/L, pH above 7 and no significant rejection above this pressure. The simultaneous rejections of Cr(VI) and sulphate were 90 and 100% respectively. The membrane based techniques offer highly effective methods of removing pollutants, they can ensure constant water supplies with little or no chemical additions compared to precipitaion-coagulation, work over a wide pH range and eliminate interference by other ions, hence a global shift towards them [34]. However, compared to other methods this is a very expensive technology hence it cannot be availed to poor communities like those in the third world where the problem of water scarcity is severe. Furthermore, the treated water becomes acidic and would need pH correction, large volumes of water are wasted as brine, the disposal of the brine is also a problem and also, this process requires skilled operation [34,43].

UNIVERSITY OF JOHANNESBURG

2.4.3 Ion-exchange

This is a technique based on the exchange of ions between the effluent and a resin which has properties of regeneration after elution of the ions. The resin has acidic or basic functional groups for ion exchange. **Fig. 2.10** shows a schematic diagram of an anion exchange process where raw water enters from the top of a column with beads and leaves at the bottom after ion exchange between the water and the resin in the column [34,36].

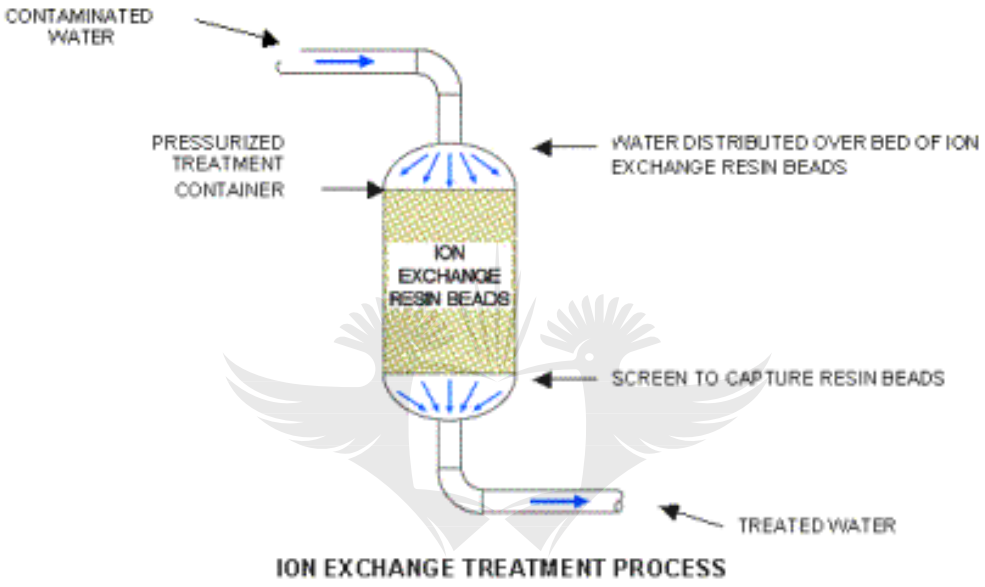

Fig. 2.10: Schematic diagram of an ion exchange process [34]

UNIVERSITY OF JOHANNESBURG

Fluoride ions can be removed from water by ion-exchange with a strongly acidic ion exchanger resin. In a study by Paudya et al. [44], an acidic ion exchanger was used to remove fluoride in trace amounts from the plating industry. The ion exchanger was made up of spent resin loaded with Zr(VI) ions. The process took place in six cycles before the material was exhausted and the trace amounts of fluoride ions were completely removed. Cr(VI) ions removal is also possible wih the ion-exchange process. A study by Gode and Pehlivan [45] used tertiary amines containing resins to remove Cr(VI) at various concentrations. Cr(VI) ions of concentration 100 mg/L were removed within 15 minutes and the process was pH dependent, exothermic, thus showing that ion exchange can be successful as a rapid removal method for Cr(VI) ions. The ion-exchange process can remove almost all the pollutant ions (above 90%) with the taste and colour of water unaffected. Less sludge is generated compared to other processes and it is highly selective. However, interference by sulphate, carbonate and phosphate ions in the case

of fluoride is a problem. Aditionally, regeneration of the resins usually produces pollutant rich waste which might defeat the whole purpose anyway. Resins are expensive for poor communities and other processes like pre-and post-treatment proceesses are required [34,36].

2.4.4 Adsorption

From the above discussion on the various traditional techniques for ions removal from water, several inherent drawbacks have been deduced. These range from high operational costs and sophistication, energy intensive, generation of large volumes of secondary pollutants e.g. sludge, fouling, low efficiency for the removal of trace levels of pollutants, requirement of large amounts of chemicals, sensitivity to pH, pre- and post-treatment. Consequently, a shift towards alternative techniques like adsorption is desirable. The adsorption technique involves the accumulation of material (adsorbate) liquid or gas on the surface of a solid phase material (adsorbent**)** as shown in **Fig. 2.11.** The process of adsorption can be a physical process where van der Waal's forces dominate or a chemical process where there are chemical reactions or a combination of both**.** The adsorbent material can interact with adsorbate ligands through electrostatic interaction or ion exchange.

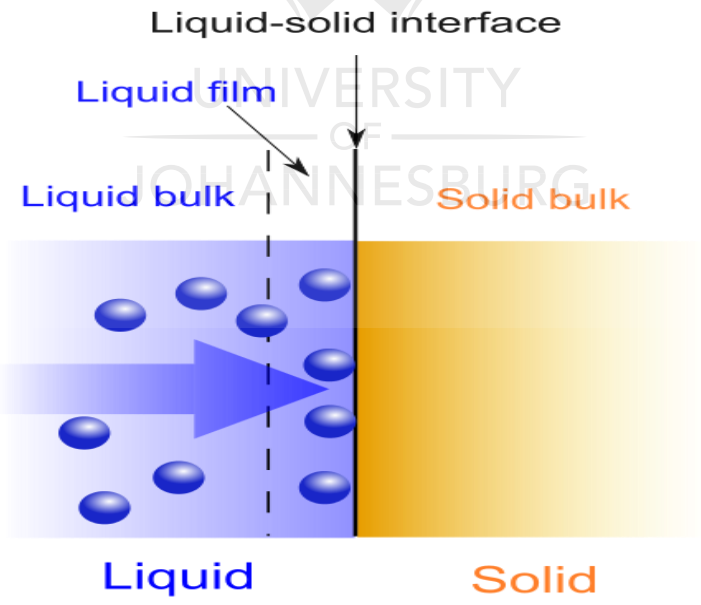

Fig. 2.11: Schematic diagram of adsorption process [46]

The adsorption technique has been the most preferable technique when compared to other techniques. It has exhibited several advantages compared to other methods for pollutants

removal from water, fluoride and Cr(VI) ions included. It is simple, robust, efficient, accessible and effective. This process is easy to design and operate, hence it can be utilised by developing country communities. The economic viability and environmental friendliness of the process cannot be overemphasised in the global scenario where the implementation of other techniques has been met with challenges [25,37,43].

2.5 Adsorbents utilised for removal of fluoride and Cr(VI) ions from water

There are numerous adsorbents available, nonetheless their choice is influenced by a number of dynamics which include pH, contact time, adsorption capacity, percentage removal of ions, effect of co-existing ions, regenerability of adsorbent and stability, mechanism of adsorption, temperature, dosage, surface area, cost, availability, selectivity, environmental effects, effectiveness and rate of diffusion and adsorption.

2.5.1 Conventional adsorbents

These are mainly activated carbon, silica, alumina, and calcium-based adsorbents and natural materials.

2.5.1.1 Carbon-based adsorbents

UNIVERSITY OF JOHANNESBURG

Carbonaceous materials, especially activated carbon (AC), traditionally have been effectively utilised for water pollution mitigation. This is because AC has a high surface area averaging 500 m^2/g upwards. However, commercial AC is very expensive and this limits its utilisation. Consequently, most studies recently have shifted towards fabrication of activated carbon from low cost materials and in some cases modifying commercial AC to further enhance its adsorption capacity and reduce the cost. Several studies have been reported over the last decade. Alagumuthu et al. [47] studied the utilisation of zirconium permeated activated carbon for the removal of fluoride ions. Several parameters were studied and the Langmuir isotherm best modelled the adsorption data as well as the pseudo-second-order kinetics. The regeneration of the adsorbent took place in three cycles and the adsorbent was also applied for the removal of fluoride ions from natural water. However, the adsorption capacity was very low (1.88 mg/g). Over the years, there has been a shift from commercial AC composites to utilisation of activated carbon from natural biomaterials in composites. Mariapan et al. [48] produced

chemically activated cotton nut shell carbon for fluoride ions removal. It was reported that the adsorption capacity was 1.38 mg/g at 303 K at a pH range of 2-7 with 85% removal. Several adsorption parameters were studied. The adsorption process, which was through chemisorption and physisorption processes, was best described by the Freundlich isotherm model. However, regeneration studies and effect of co-existing ions were not reported.

Recently Singh et al. [49] studied the removal of fluoride using activated carbon from bael (*aegle marmelos*) shells. The results of the study showed adsorption of 4 mg/L fluoride solution in 60 minutes with 52% removal. The maximum adsorption capacity was very low (1.07 mg/g) over a pH range of 2-10 at 2g/L adsorbent dose. In another study by Alverez et al. [49] lanthanum loaded commercial AC was utilised for the same pollutant and the adsorption capacity of the composite was much higher (91.99 mg/g) than that of unmodified (9.96 mg/g) AC at a pH of 7. On the other hand, AC has also been exploited for the removal of Cr(VI) ions from synthetic water. As early as 2009, Babu and Gupta [50] studied the removal of Cr(VI) from water using AC from Tamarind seeds where several adsorption parameters were investigated in the pH range 1-3. The Langmuir model adsorption capacity was 29.08 mg/g and the adsorption kinetics were pseudo-second-order modelled. However, the equilibrium time was too long (50 h) and the adsorbent regeneration as well as the effect of co-existing ions studies were not reported. More recently in 2015, studies were conducted on the utilisation of AC derived from biomaterials. El Nemr et al. [51] used activated carbon derived from red marine macro algae for the removal of Cr(VI) from synthetic and sea water. The adsorption capacity was 66.00 mg/g at a pH of 1. Zhang et al. [52] used humic acid modified bamboo buck-based AC to remove Cr(VI) and it was reported that the adsorption took place over a wide range of pH 2-9. With no humic acid, the adsorption capacity was 18.90 mg/g but with humic acid it increased to 19.53 mg/g suggesting synergistic behaviour between humic acid and AC for Cr(VI) removal.

Commercially produced AC has a high surface area but its global utilisation may be limited by economic viability [53]. This explains why most of the studies have focussed on its production of from cheap materials or modification of commercially produced AC to reduce costs. It also poses a problem of narrow pH range, poor regenerability and inability to remove trace amounts of pollutants. Moreover, treatment to enhance the chemical characteristics of AC may present

UNIVERSITY OF JOHANNESBURG

a problem of undesirably affecting its physical characteristics or vice versa. Hence more research must be focussed on better adsorbents.

2.5.1.2 Alumina-based adsorbents

Alumina is a porous form of Al_2O_3 and is commercially available. It has a surface area around 200 m^2/g, making it conventionally useful for water remediation. Nevertheless, its major problem has been its low adsorption capacity and slow adsorption rate. As a result, studies on the utilization of alumina have focused on its modification for removal of water pollutants [54]. Maliyekkal et al. [55] utilised magnesia modified activated alumina for the removal of fluoride ions. The study involved investigation of several parameters and detailed characterization. The Sips model best described the adsorption process with a maximum adsorption capacity of 10.12 mg/g. Co-existing ions had little effect on the adsorption and 95% of the fluoride was removed within 3 h of contact time. Moreover, several other studies were conducted over the past decade also focussing on the modification of alumina. These include one by Kumar et al. [56] who applied nano-alumina to remove fluoride ions from water through batch studies. It was reported that the Langmuir model best described the adsorption process with a maximum adsorption capacity of 14.00 mg/g at a pH of 6. The kinetics was pseudo-second-order modelled. However, regeneration studies and tests on fluoride containing groundwater samples were not reported. Camacho et al. [57] successfully applied sol-gel activated, CaO and MnO_2 modified alumina to remove fluoride ions. The sol-gel modified material's adsorption process was Freundlich modelled whilst the other two were best described by the Langmuir model. The CaO modified alumina displayed the highest adsorption capacity of 96.23 mg/g. In all cases, the adsorption kinetics was pseudo-second-order modelled and the materials were well evaluated for treatment of groundwater samples, but no regeneration studies were reported. More recently Ekka et al. [58] studied the application of ionic liquid modified alumina for the removal of fluoride ions. It was reported that the material was an encouraging adsorbent for fluoride ions with a maximum adsorption capacity of 25.00 mg/g. The process followed pseudo-first-order kinetics and Langmuir model of adsorption. The percentage removal of modified alumina was much higher than that of pristine alumina over a pH range of 2-8 in a time of 60 minutes. The increased adsorption capacity was ascribed to the increased number hydroxyl groups from the ionic liquid compound and increased surface area. Kundu et al. [59] studied the removal of fluoride ions using malic acid, citric acid and tartaric acid modified alumina and investigated various parameters. It was established that the maximum adsorption capacities were higher

UNIVERSITY OF JOHANNESBURG

than that of pristine alumina with citric acid modified adsorbent giving the highest adsorption capacity of 62.50 mg/g at pH 2-5. The effect of competing ions like sulphate, chloride and phosphate was negligible. The adsorption process was very fast with 50% removal of fluoride in 5 minutes and it was pseudo-first-order modelled. Similarly, more efforts were made by Yang et al. [60] who studied the application of fungus hyphae modified alumina for the same purpose. The study showed that the new adsorbent had superior properties than fungus hyphae and alumina separately, with a maximum adsorption of 105.00 mg/g and 90% fluoride removal in 40 minutes over a wide pH range of 3-10. The mechanism of adsorption was electrostatic interactions between fluoride ions and the hydroxyl groups of the alumina and hydrogen bonding between protonated amine groups of hyphae and fluoride ions. The increased adsorption capacity was attributed to increased surface area of adsorbent and increased number active functional groups.

For Cr(VI) removal, Bhattacharya et al. [61] studied the utilisation of clarified sludge, activated alumina and other adsorbents like rice husk ash, activated alumina, fuller's earth, fly ash, saw dust for removal of the ions from water. The investigated batch adsorption parameters included effect of pH which was found to be 2 and 3. The adsorption processes were well modelled by the Langmuir isotherms with clarified sludge modified alumina being the most effective amongst the other adsorbents, exhibiting an adsorption capacity of 25.57 mg/g in 2 h, much more effective than pristine alumina. The process of Cr(VI) adsorption was complex in nature. Studies on effect of co-existing ions and regeneration were not reported.

UNIVERSITY OF JOHANNESBURG

Almost a decade latter more studies were conducted with better modifiers for the alumina. Sankararamakrishnan et al. [62] studied the removal of the removal of Cr(VI) ions using carbon nanotubes and activated alumina composite. The adsorption capacity was very high (229.00 mg/g), at a pH of 2 and the composite demonstrated great potential from removal of Cr(VI) ions from water. The high adsorption capacity was attributed to high surface area of the composite and the presence of several functional groups. Gopalakannan et al. [63] utilised alumina-alginate composite for the removal of Cr(VI) ions from water. Various parameters were investigated. The maximum adsorption capacity of the composite was 17.45 mg/g compared to 9.45 mg/g for pristine alginate. The adsorption process was spontaneous, selective and endothermic. Sun et al. [64] used Fe^0 nanorods modified with chitosan in porous alumina to remove Cr(VI) ions from water. The reported maximum adsorption capacity was 118.76 mg/g and the adsorption of Cr(VI) took place by reduction of Cr(VI) to Cr(III). A Langmuir

modelled chemisorption adsorption process which was best described by pseudo-first-order kinetics was reported.

Alumina and its composites have been reported to demonstrate ample adsorption capabilities but the issues of expense, narrow pH range and the dissolution of aluminium ions which have health side effects (Alzheimer disease) remain debatable [65]. Furthermore, its performance is affected by the occurrence co-existing ions in water and it is easily soluble under high pH environments.

2.5.1.3 Calcium-based adsorbents

Calcium-based adsorbents are mainly lime, quick lime, calcium carbonate and calcite. Numerous studies on the removal of fluoride ions from water using calcium-based adsorbents have been reported over a decade ago, including Turner et al. [66] who utilised calcite to remove fluoride ions. The material was characterized using the atomic force microscopy (AFM) and X-ray photoelectron spectroscopy (XPS) techniques. The results indicated that both adsorption and precipitation were responsible for the removal of fluoride ions from water. Other variables which affect adsorption like effect of co-existing ions, regeneration, kinetics and thermodynamic isotherms were not reported. Islam and Patel [67] studied the utilisation of activated quicklime to remove fluoride ions. It was reported that 60.6% of the fluoride ions were removed. The adsorption process was very fast and Langmuir modelled, but the process was not appropriate for drinking water since it did not reduce the fluoride to below permissible levels. In another study Nie et al. [68] used aluminium modified calcium hydroxyapatite for the removal of fluoride ions. The process was spontaneous and endothermic with a maximum adsorption capacity of 32.57 mg/g. The Langmuir model best described the adsorption process which was pseudo-second-order modelled. The ions sulphate, chloride and nitrate had no effect on the adsorption process, but phosphate and carbonate ions interfered with the adsorption. Tchomgui-Kamga et al. [69] studied the utilisation of calcium rich charcoal produced from high temperature impregnation of $CaCl_2$ on wood for fluoride adsorption. The adsorbent was well characterized and revealed the presence of CaO and $CaCO_3$. The Langmuir model best described the adsorption processs with a maximum adsorption capacity of 19.05 mg/g achieved in 24 h. The material was selective as co-existing ions had very little effect on the fluoride adsorption. On the other hand, Correa et al. [70] utilised calcium phosphate synthesized by a simple process for removal of Cr(VI) from water.

UNIVERSITY OF JOHANNESBURG

The maximum adsorption capacity was very low though there was a highly selective adsorption process involving electrostatic interactions in acidic conditions. Moreover, Elyahyoui [71] studied the use of calcium carbonate for the removal of cobalt and Cr(VI) ions. The adsorption process was Langmuir modelled, endothermic and spontaneous taking place in 3 h. The pseudo-second-order model best described the kinetics.

Calcium-based adsorbents are studied for defluoridation and Cr(VI) ions removal because of calcium biocompatibility with the human body, low cost and being readily available. Nevertheless, calcium ions have a high affinity for fluoride ions making it difficult for regenerability of the adsorbent hence its stability and recyclability is compromised. Furthermore, they have a very low adsorption capacity for Cr(VI) ions, hence the need for fabrication of better adsorbents.

2.5.1.4 Natural materials as adsorbents

Traditionally, natural materials such as bentonite, montmorillonite, kaolinite, attapulgite, zeolites, halloysite and other clays were extensively studied for the removal of fluoride and Cr(VI) ions. These materials are naturally abundant and very cheap, hence there is a desire to utilise them. However, there was little success even in their modified form as their adsorption capacities were low. For example, Cengeloglu et al. [72] applied original and activated red mud to remove fluoride from water and investigated the effect of pH, contact time and adsorbent dose among other factors. The maximum adsorption capacities were 0.33 and 0.10 mg/g for activated red mud and original red mud, respectively at a pH of 5.5. The Langmuir model best described the adsorption process which took place in 2 h. Thakre et al. [73] studied the removal of fluoride ions using magnesium modified bentonite and various parameters for adsorption were studied. The process of adsorption was spontaneous and endothermic with a maximum adsorption capacity of 2.20 mg/g for an initial fluoride concentration of 5 mg/L. The removal efficiency of bentonite was enhanced by the magnesium dopant. The fluoride adsorption process was through ion exchange and electrostatic attractions mechanisms. The adsorbent could not effectively remove fluoride ions from ground water. Sequeira et al. [74] studied the removal of fluoride using aluminium modified haematite, zeolite tuff and calcite. Several parameters were explored, and the adsorption kinetics were pseudo-first-order and Elovich modelled. The maximum adsorption capacities on aqueous and drinking water obtained using zeolite tuff were 10.50 and 9.00 mg/g, respectively. The level of the fluoride was reduced to

UNIVERSITY OF JOHANNESBURG

1.16 and 0.08 mg/L on aqueous and drinking water, respectively. The adsorption process was Langmuir and Freundlich modelled, pH dependent and took place *via* a chemisorption mechanism. More recently, Biswas et al. [75] applied natural organic shale and heat activated shale from coal mines to remove fluoride ions from water. The effect of various adsorption parameters was explored over a pH range of 2.8 to 6.8. The maximum adsorption capacity of natural carbon shale was 0.33 mg/g with 88.3% removal whilst that of heat activated shale was 2.15 mg/g with 88.5% removal. The effect of co-existing ions showed that carbonate ions interfered with the adsorption most followed by nitrate, chloride and lastly phosphate ions.

On the other hand, Yua et al. [76] reported Cr(VI) removal from water using magnetite modified diatomite. The adsorbent was well characterized and adsorption studies indicated a pH dependent process. The maximum adsorption capacity was 12.31 mg/g with the process being Langmuir and pseudo-second-order modelled. The Cr(VI) adsorption took place through electrostatic attractions and reduction. Other earlier studies were conducted by Brum et al. [77] who utilised surfactant modified montmorillonite for the removal of Cr(VI) ions and natural peat by Torres et al. [78] with success, but there were low adsorption capacities among other challenges. Recently, Lv et al. [79] utilised iron modified and unmodified zeolite in both batch and column studies for the same ion. The adsorption process took place in 25 minutes. The kinetics was pseudo-second-order modelled and the Langmuir isotherm best described the adsorption process. Furthermore, Barkat et al. [80] applied Algerian bentonite to study the removal of Cd (II) and Cr(VI) from water. The adsorption capacity for Cr(VI) was 12.62 mg/g for initial concentrations of 50-100 mg/L at a pH of 6 and this took place in 120 minutes. The Langmuir isotherm best described the adsorption process and the kinetics were pseudo-second-order modelled. The adsorption process was spontaneous, favourable and exothermic. In a recent communication, Betchikou [81] reported the application of natural red mud to remove Cr(VI) for water where 90% removal of the ion was achieved. The adsorption capacity of the mud was 32.78 mg/g at an initial Cr(VI) ions concentration of 50 mg/L at a pH of 5. The Freundlich model best described the adsorption process which was pseudo-second-order modelled.

While use of these natural materials for fluoride and Cr(VI) removal has been successful, some drawbacks have emerged, including low adsorption capacities, narrow pH range of application, inability to remove trace amounts of pollutant and poor regeneration, hence a search for more viable adsorbents is indispensable.

UNIVERSITY OF JOHANNESBURG

2.5.1.5 Agricultural materials as adsorbents

Traditionally, agricultural materials have been the most over-utilised adsorbents for removal of pollutants. This is essentially because these materials are inexpensive, readily available in large quantities and renewable. The major constituents of these materials are lignin, hemicellulose, simple sugars, starch and lipids, encompassing various functional groups. Such materials include rice husks, maize stalks and cobs, groundnut husks, orange peels, coconut shell, banana peels and tea waste among others.

Countless studies have been conducted using the pristine materials or their modified forms for the removal of pollutants. Yadav et al. [82] utilised wheat straw, saw dust and sugarcane baggase carbon for fluoride removal. There was 40.2%, 49.8% and 56.4% removal and adsorption capacities of 1.73, 1.95 and 1.15 mg/g, respectively from 4 mg/L initial fluoride concentrations solutions. The isotherm data was well described by the Freundlich model. Cai et al. [83] used zirconium oxide loaded tea waste to remove fluoride from drinking water. The study revealed a maximum adsorption capacity of 12.43 mg/g over a wide pH range of 3-10 and the adsorption process followed Langmuir and pseudo-second-order models. Chloride, nitrate and hydrogen carbonate ions did not show interference with the adsorption apart from sulphate and phosphate ions. The adsorption mechanism was reported to be both ion exchange and electrostatic attractions between fluoride, hydroxyl ions and secondary amine groups from tea waste. The combination of the biomaterial and the ZrO_2 resulted in improved ion selectivity, pH range and adsorption capacities of a low-cost adsorbent material. In another study, Mondal [84] reported the use of banana peels (*musa acuminate*) on the removal of fluoride ions from water. The optimum pH for the removal was 4 and the maximum adsorption capacity was 1.20 mg/g over a period of 60 minutes. The Dubinin-Radushkevitch adsorption isotherm best described the adsorption process which was exothermic in nature. The order of effect of co-existing ions on the fluoride adsorption was carbonate > phosphate > sulphate > nitrate > chloride and effective removal of fluoride from real water samples was reported. More recently, Bibi et al. [85] utilised a mixture of potato peel powder and rise husks to remove fluoride from aqueous solution. The maximum adsorption capacity was 2.91 mg/g and there was 80% removal of fluoride at 30 mg/L initial fluoride concentration. The Langmuir isotherm best described the adsorption process at a pH of 7 and it had a pseudo-second-order modelled

kinetics. The adsorbent was applied to fluoride containing ground water samples where 90% removal was reported.

As for Cr(VI) ions, Hasan et al. [86] utilised maize bran, a waste from flour milling for its removal. Several adsorption parameters were investigated. There was a remarkable removal of Cr (VI) ions with a maximum adsorption capacity of 312.54 mg/g at a pH of 2 in 110 minutes. The adsorption process was Langmuir and pseudo-second-order modelled. Additionally, Bansal et al. [87] applied boiled and formaldehyde treated rice husks for the same ion. Various adsorption parameters were investigated. There was 71.0% and 76.5% removal of Cr(VI) ions with adsorption capacities of 8.50 and 10.40 mg/g, respectively. These were low adsorption capacities, suitable for low amount of pollutant only, hence this limits the applicability of the adsorbent. Malkoc et al. [88] used tea factory waste to remove Cr(VI) from water. The adsorption capacity was 54.65 mg/g at optimum of 2 and initial Cr(VI) ions concentration of 400 mg/L. The percentage removal increased from 37% to 99% with decrease in pH from 5-2. The Langmuir model bests described the adsorption processs which was endothermic and spontaneous. The kinetics was best described by the pseudo-second-order model. Mishra et al. [89] used waste plant materials such as *Portulaca Oleracea* to remove Cr(VI) ions. It was reported that the adsorption was very fast at pH 2-5 with a maximum adsorption capacity of 54.94 mg/g. The kinetics was pseudo-second-order-modelled with spontaneous and endothermic adsorption. Recently, Pakade et al. [90] reported on the utilisation of macadamia nuts shells to remove the same ion from water after acid and base treatment. It was reported that the working pH for the biosorption was 2, with contact time of 10 h at an initial Cr(VI) concentration of 100 mg/L. The maximum adsorption capacities for pristine macadamia nut shell, acid treated and base treated were 45.23, 44.83 and 42.44 mg/g, respectively. The Langmuir, Freundlich, Redlick-Peterson and Sips models were able to describe the adsorption process fully and the kinetics was best described by the pseudo-second-order model.

Agricultural waste material has generated much interest in adsorption technology nevertheless, a number of drawbacks are inherent. These materials have low adsorption capacity, generates a lot of sludge due too much dosage amounts which become secondary pollutant, have low selectivity and poor regeneration. Modification of these materials can improve their adsorption efficiency.

UNIVERSITY OF JOHANNESBURG

2.5.1.6 Biopolymer materials as adsorbents

Biopolymers are basically derived from plant, animal and microorganisms. These materials are polysaccharides, lipopolysaccharides, glycolipids, proteins and so on. Examples of these are chitosan, alginate, chitin, starch, collagen with chitosan and cellulose being the most abundant on earth. Biopolymers have excellent properties which make them applicable to removal of pollutants [91]. For example, cellulose contains hydroxyl groups and is composed of ß-(1,4) D-glucose linkages which can be functionalised with other chemical groups to enhance adsorption. Chitosan is an amino-based polysaccharide which can be used as an adsorbent due to the many −NH and OH groups. In acidic conditions, chitosan becomes protonated and attracts anionic pollutants [91,92]. Over the years, the use of biopolymers and their modified forms in the removal of fluoride and Cr(VI) ions has generated much interest and the most studied material is chitosan.

Kaygusuz et al. [93] used aluminium modified alginate beads to remove fluoride ions from water. The adsorption capacity was 75.20 mg/g, achieved in 4 h at a pH of 2. The adsorption process was Langmuir modelled and spontaneous with a physical adsorption mechanism. Chitosan has a very low adsorption capacity for fluoride ions unless it is modified. In a bid to increase chitosan adsorption capacity, Viswathan et al. [94] investigated the removal of fluoride ions using Fe(III) loaded carboxylated chitosan beads. The maximum adsorption capacity was 15.39 mg/g at 303 K and over 3-11 pH range. In another study, Jagtap et al. [95] synthesized Ti-modified chitosan and utilised the material for fluoride adsorption in both synthetic and groundwater. The effect of several parameters was studied and a maximum adsorption capacity of 7.21 mg/g at a pH of 7 was obtained. The isotherms and kinetics were Langmuir together with Freundlich and pseudo-second-order modelled, respectively. Co-existing ions negatively affected the fluoride ions removal hence, the material was not very selective. Furthermore, the adsorption of fluoride ions from synthetic water was better than from groundwater samples but the adsorption capacity was low. To further improve the versatility of chitosan, Pandi et al. [96] reported the removal of fluoride ions using magnetic hydrotalcite/chitosan composite and compared this with the pristine materials of the composite. It was reported that the composite had the highest adsorption capacity of 5.03 mg/g at a wide pH range of 3-11. Several adsorption parameters were investigated, the process was spontaneous and endothermic. The Langmuir model best described the adsorption process where the mechanism involved ion-exchange and complexation. As observed, the adsorption

capacity was low despite the modification. More recently, lanthanum loaded cellulose was utilised to remove fluoride from aqueous solution by Nagarag et al. [97]. The maximum adsorption was very low at 1.18 mg/g over a pH range of 2-7. The adsorption process was Freundlich modelled, spontaneous and involved ion exchange chemisorption. The adsorbent showed excellent removal of fluoride from real water samples.

On the other hand, Qui et al. [98] used polyaniline coated ethyl cellulose with a percentage of polyaniline ranging from 4-20% for Cr(VI) removal. The removal efficiency increased with an increase in the amount of polyaniline and the composite had a better adsorption capacity compared to pristine ethyl cellulose with a removal rate of 2 mg/L of Cr(VI) ions in 2 minutes. The adsorption process was Langmuir modelled with a maximum adsorption of 12.3 mg/g at of pH 2. The adsorption was enhanced by the amine groups of polyaniline including those present on ethyl cellulose. The kinetics was pseudo-second-order modelled. Karthik et al. [99] produced well characterized PPy functionalised chitin for Cr(VI) removal. The maximum adsorption capacities were 28.92-35.22 mg/g over temperatures of 303-323 K. The adsorption process was spontaneous, endothermic and pseudo-second-order modelled. Co-existing ions had much influence on the adsorption of Cr(VI) in the order was nitrate > chloride > sulphate > hydrogen carbonate hence, the material was not very selective.

Dima et al. [100] exploited chitin from sea food waste to make chitosan which was subsequently cross linked with tripolyphosphate to improve the stability of chitosan for Cr(VI) removal from water. The material was well characterized and batch studies were conducted on various adsorption parameters. The Langmuir isotherm best described the adsorption process and the kinetics were pseudo-second-order modelled. It was established that the adsorption process involved reduction of Cr(VI) to Cr(III) and the maximum adsorption capacity at a pH of 2 was 124.00 mg/g. More recently, Liang et al. [101] utilised a quartenised chitin/branched polyethyleimine composite for Cr(VI) removal. The adsorption process took place in 40 minutes with an adsorption capacity 387.70 mg/g at a pH range of 1-5. The mechanism of adsorption was reported to involve electrostatic attractions between quaternary ammonium and protonated amino groups and Cr(VI) ions. The adsorbent was reported to be highly selective, very stable and could be regenerated in 7 cycles. These were encouraging results which were enhanced by the presence of a conducting polymer. The use of biopolymers for removal of fluoride and Cr(VI) ions have been very encouraging over the years. However, they still have many drawbacks which limit their application. For example, chitosan is not very soluble in

many solvents due to crystallinity, it agglomerates or becomes gelatinous. Thus, the active binding sites are not readily available for sorption. Furthermore, it is in the form of chips or fine particles which have restricted its practicality mostly for column applications due to swelling, low mechanical strength and disintegration. Additionally, the material requires a high dose for adsorption, have low adsorption capacity, usually have very long contact times, may discharge organic constituents leading to high chemical and biological oxygen demand and have low selectivity [90,91,92].

2.5.2 Nanomaterial-based adsorbents

Nanomaterials are atoms/molecules in the size of 1-100 nanometres in at least one dimension. These materials have revolutionised the whole area of engineered materials. They have been established to have better application for various functions because their unique attributes including small size, high surface area, active atomicity, reactivity, tunability, catalysis and electrostatic properties [102,103].

As a result, recently there has been rapid attention globally among researchers on the application of nano-engineered materials for water remediation. Although conventional adsorbents have been used extensively, they possess inherent weaknesses of slow kinetics, low adsorption capacity, generation of large volumes of secondary pollutants, low selectivity, among others. Nano-engineered materials offer an alternative and reliable system for adsorption due to the shorter diffusion routes, high adsorption capacities, high selectivity, high regeneration capacities, stability and high surface area for adsorption. Thus, the benefits of nanotechnology in water treatment are measured as a great achievement and of boundless importance [102,103].

Generally, nanomaterials for water remediation fall into three major classes, namely carbon-based nanomaterials, metal-based and polymer-based nanomaterials.

2.5.2.1 Carbon-based nanomaterials

UNIVERSITY OF JOHANNESBURG

These are carbon nanotubes (CNTs), single walled carbon nanotubes (SWCNTs) and multi-walled nanotubes (MWCNTs), fullerenes, carbon dots, carbon nanorods, nanospheres and graphene/graphene oxide [102,103]. These materials are called tubes because they consist of carbon atoms in cylindrical form. A single rolled graphene sheet is called a SWCNT whilst multi-layer rolled together are called MWCNTs. The CNTs have unique properties that make them applicable to environmental water remediation. They have low density, high mechanical and thermal strength as well as good electrical properties. A lot of interest has been stimulated on the application for these materials and their modified composites for removal of fluoride and Cr(VI) ions over the past decade. Pristine CNTs material exhibit low adsorption capacities for these anions, as a result they are usually applied in their modified form [102]. Ruan et al. [104] synthesized hydroxyapatite/MWCNTs and applied the composite on the removal of fluoride ions from water. The resulting material had a surface area of 180 m^2/g and an adsorption capacity of 36.20 mg/g more than pristine hydroxyapatite whose surface area was 172 m^2/g and adsorption capacity of 17.80 mg/g. The adsorption process was endothermic, spontaneous and involved ion exchange and electrostatic attractions. The adsorbents were further applied for nuclear waste fluoride contaminated effluent. The level of fluoride was reduced from 8.79 mg/L to 0.25 mg/L showing applicability of the composite. Nevertheless, the application of CNTs for fluoride remediation is still in its infancy due to the limitations associated with large scale exploitation of these materials attributed to environmental concerns and side effects [105].

UNIVERSITY OF JOHANNESBURG

Then again, a substantial number of studies have been conducted on the removal of Cr(VI) ions from water using carbonaceous material. These include; Lv et al. [106] (MWCNTs+ Fe^0), Luo et al. [107] (MnO_2 /Fe_3O_4/oxidised MWCNTs), Dehghani et al. [108] (SWCNTs and MWCNTs) and Beheshti et al. [109] (chitosan/ MWCNTs/Fe_3O_4). High adsorption capacities and encouraging results were reported. More recently, Taghizadeh and Hassanpour [110] synthesized imprinted polymers on magnetic CNTs surface and applied the material on Cr(VI) ions removal from aqueous solution. Several parameters were investigated, with a maximum adsorption capacity of 56.10 mg/g at a pH of 3 within 30 minutes. The adsorption process was best described by the Langmuir model whilst the kinetics was described by the pseudo-second-order model. The presence of co-existing ions did not affect the Cr(VI) ions adsorption process and the adsorbent regeneration took place in 5 cycles. Nonetheless, more studies are necessary to exploit the potential of CNTs for removal of pollutants in drinking and environmental waters. However, their tangible application may be slowed down by their high cost [105], except where

cheaper materials have been used to produce the CNTs. Moreover, CNTs have low solubility leading to a challenge of collecting them from solution if they are not magnetic functionalised. Additionally, the aftermaths of their improper disposal need more attention [103]. The human health side effects are another challenge where on prolonged exposure, their toxicity leads to inflammation and oxidative related stress [105,111,112].

Graphene, the latest allotrope of carbon is considered to be an exciting material these days. Graphene and its composites can be utilized in several applications due to their outstanding two-dimensional nature and associated band structures [113]. It has a larger surface area and surface functional groups which make singles sheets of carbon hence its composites are an attractive adsorbent material for water pollutants. Graphene oxide (GO) is the material produced when graphene is oxidized. It has excellent properties with hydroxyl and carbonyl groups which increase its adsorption ability alongside prospective functionalization. Recently, there has been considerable research on application of GO in removal of water pollutants. Kanra et al. [113] synthesized an iron-aluminium oxides graphene composite for fluoride removal. It was reported that the maximum adsorption capacity was 27.80 mg/g at a pH of 7. The adsorption was endothermic, Langmuir modelled and the kinetics followed pseudo-second-order. Lv et al. [114] synthesized zero valent iron nanoparticles inside reduced graphene alginate beads of less than 100 nm size. These were utilized on Cr(VI) ions removal from aqueous solution and the reported maximum adsorption capacity was 33.90 mg/g at a pH of 3. Both the Langmuir and Freundlich isotherms described the adsorption very well and the adsorption process was pseudo-second-order modelled and endothermic. However, the synthesis of graphene in the laboratory still remains a challenge. Moreover, commercially made graphene is expensive. Furthermore, due to the characteristic hydrophilic nature of GO, it cannot be collected readily from its aqueous solution, which limits its utilisation as an adsorbent. Economic and environmental evaluations on the use of GO-based adsorbents need to be better understood fully in order to determine the potential benefits of these materials in water pollution remediation.

UNIVERSITY OF JOHANNESBURG

2.5.2.2 Nano-metal oxides (NMOs) as adsorbents

The term metal oxide is usually applied to solid ionic compounds that contain the anion O^{2-} and one, two or more metal cations [115]. Recently mixed nanosized metal oxides have emerged as promising adsorbents for water pollutants. They have outstanding physical and chemical properties owing to their small size and high charge density of edge surface sites namely particle size, electronic properties and the presence of coordinated atoms or O vacancies in oxide nanoparticles. Furthermore, they have occupied electronic states located above the valence band and as a result they have a rock salt crystal structure which increases their chemical activity [116,117,118]. As adsorbents, NMOs offer many advantages including, large surface areas, high adsorption capacities, regenerability, good acidic and basic properties, fast kinetics, amenability to doping and the ability to mimic natural soil systems [116,117,118,119,120]. Typical metal oxides are alkaline, alkaline earth, rare earth and transition metal oxides like nanosized ferric, manganese, aluminium, titanium, magnesium, zinc, zirconium, lanthanum and cerium oxides [115,118,121].

Over the last ten years there has been much interest in the application of NMOs especially in their mixed forms for removal of pollutants from water [118]. The binary Fe-Ti, Mn-Ce, Ce-Fe, Ce-Al, Al-Mg, Fe-Zr, Al-Fe and Mn-Al oxides [17,105,115,118,122] have been utilised for fluoride removal and more publications are still being released on their application for this cause. Tang and Zhang [17] synthesized Ce-Fe binary nano-metal oxides by a simple co-precipitation for the removal of fluoride ions by the batch process. The NMOs were reported to have a surface area of 165 m^2/g and the adsorption capacity was 60.97 mg/g over a wide pH range of 2.9-11 in 40 minutes. The adsorption process was well described by the Langmuir isotherm and the kinetics was pseudo-second-order modelled. For the effect of co-existing ions on fluoride adsorption, carbonate and hydrogen carbonate ions showed more interference, than sulphate, chloride and nitrate ions. The mechanism of adsorption was ion exchange between hydroxyl groups on the surface of the adsorbent and fluoride ions. In an effort to achieve a high surface area adsorbent, Wang et al. [122] prepared hollow Fe-Ce oxy hydrous metal micro cubes for fluoride removal by tuning the surface to afford a BET surface area of 242 m^2/g. A maximum adsorption capacity 146.59 mg/g at a pH of 5 within 20 minutes was achieved. The process was both Freundlich and Langmuir modelled and the pseudo-second-order model best described the kinetics where co-existing ions had very little effect on fluoride adsorption. More recently, Dilhon et al. [123] synthesized Ce-Zn binary nano-metal oxides by a simple precipitation method followed by their application for the removal of fluoride ions from solution. The adsorbent showed a high adsorption capacity of 194.00 mg/g at a pH of 7. The

UNIVERSITY OF JOHANNESBURG

adsorption process was Langmuir modelled and the pseudo-second-order model best describes the kinetics. The effect of co-existing ions was negligible with a mechanism of adsorption involving both ion exchange and electrostatic attractions between the surface hydroxyl groups of the NMOs and fluoride ions. On the other hand, Cao et al. [124] synthesized flowerlike α-Fe_2O_3 nanostructures in a template-free microwave assisted method. These were well characterized using XRD, XPS and synchrotron-based X-ray absorption near edge structure analysis. The material showed good adsorption properties for As(V) and Cr (VI) ions. The maximum adsorption capacities were 51 and 30.00 mg/g, respectively, showing that these low-cost nanostructures were attractive adsorbents for removal of the heavy metal anions. Although these results were relatively comparable to what was achieved with other adsorbents, the adsorption capacity was below that of electro spun α-Fe_2O_3 (90.90 mg/g) for the same Cr(VI) ion prepared by Nalbandian et al. [125]. These materials outperformed commercial materials. Weilong et al. [126] studied the removal of Cr(VI) using Fe/Mn binary nano-metal oxides. These were characterized by TEM, XRD, XPS and BET techniques. The adsorption capacity for a Mn-Fe 1:10 oxide was 24.56 mg/g and the Langmuir isotherm best described the adsorption process. The mechanism of adsorption was both electrostatic attractions and ion exchange. The binary oxides showed better adsorption capacities than the individual metal oxides.

The encouraging results obtained from these studies demonstrate the potential of NMOs for the efficient removal of fluoride and Cr(VI) from water and waste water. Thus, more investigations are imperative to produce more novel and cheap mixed metal oxides adsorbents. The fabrication of new NMOs and NMOs-based composite adsorbents is still in the developing stage. More investigations on various aspects need to be addressed, particularly the development of more facile processes to acquire the composite adsorbents. Their long-term performance and stability as well as their practical application in ground water and effluents containing fluoride and Cr(VI) ions have to be evaluated.

2.5.2.3 Polymer-based nanocomposites

Polymer-based nanocomposites have also generated much interest in recent years. These exhibit vast and tunable surface areas, increased pore size, can be regenerated and are selective. Moreover, they contain easily functionalised amine, hydroxyl and carbonyl groups which are important for adsorption [118]. As a result of their encouraging unique properties, there has

been an advent of a class of nanocomposites which involve nano-metal oxides and polymers. These inorganic/organic hybrid structures exhibit superior properties including stability, ease of separation in solution, large surface area, selectivity, increased adsorption capacity, environmentally friendliness, wide pH range of application and reproducibility [118,127]. While metal oxides have shown great potential in the removal of fluoride and Cr(VI) ions from water, problems of agglomeration leading to loss of activity, difficulty of separation in aqueous solution and weak mechanical strength have manifested, hence the need to fabricate them on porous supports.

Additionally, biopolymers like chitosan, chitin and cellulose are also a class of polymers that have been applied to remove water pollutants with great success due to the hydroxyl, amine and carbonyl functional groups which they possess. Their inherent drawbacks as discussed earlier, have led to their modification by incorporation of metal oxides. The shift has been towards the fabrication of biopolymer hybrid materials for the removal of fluoride and Cr(VI) ions. Some of the most exciting materials supports used for water remediation nanocomposites are intrinsic conducting polymers (ICPs). ICPs have been extensively studied recently compared to other host materials. They are an attractive option partly because they are porous, have controllable pore size, are easily functionalized and have good surface chemistry [117,118,128,129]. The charged functional groups bound to their matrices enhance infusion of inorganic pollutants of counter charges hence their application in adsorption of pollutants [12,128]. Examples of such materials are polypyrrole (PPy) and polyaniline (PANI). PANI and PPy are simple to synthesize using relatively cheap materials and they possess outstanding properties including chemical stability, large surface area, high affinity for pollutants and selectivity [129,130,131]. PANI exists in three delocalized oxidation states leucoemeraldine (reduced form), emeraldine (doped form) and pernigraniline (oxidized form) as shown in **Fig. 2.12**: PANI contains plentiful amine and imine functional groups which can adsorb anions through chelation and electrostatic attractions [133]. Moreover, the leucoemeraldine and emeraldine base forms can be reversibly oxidised to the pernigraniline base form, allowing PANI to acts as an electron donor for the reduction of Cr(VI) to Cr(III). Moreover, when doped, PANI acquires positive charges hence it adsorbs counter anions like fluoride and Cr(VI) through electrostatic attractions [133,134].

UNIVERSITY OF JOHANNESBURG

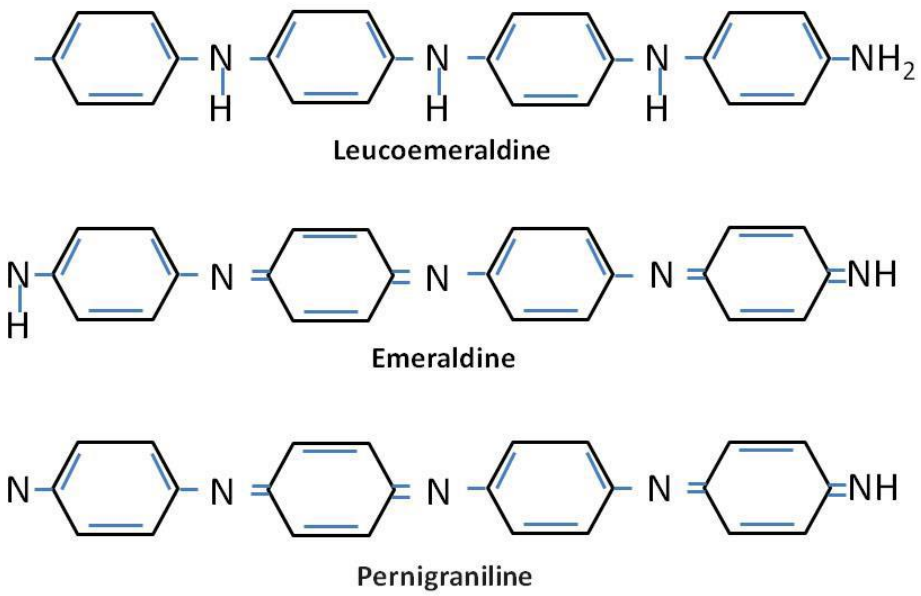

Fig. 2.12: Oxidation states leucoemeraldine (reduced form), emeraldine (doped form) and pernigraniline (oxidized form) [132]

PPy exists in the neutral or undoped form which has a benzenoid structure and the oxidised or doped form which has a quinoid structure, as shown in **Fig. 2.13** [135]. In the oxidised/doped form, PPy exhibits anion-exchange behaviour attributed to dopant ions in its structure. Furthermore, it displays anion-exchange behaviour when more dopants are incorporated into the polymer during polymerization [133,136]. Like PANI, PPy has the ability to reduce Cr(VI) to Cr(III) due to the electron donor rich amino groups [136].

UNIVERSITY OF JOHANNESBURG

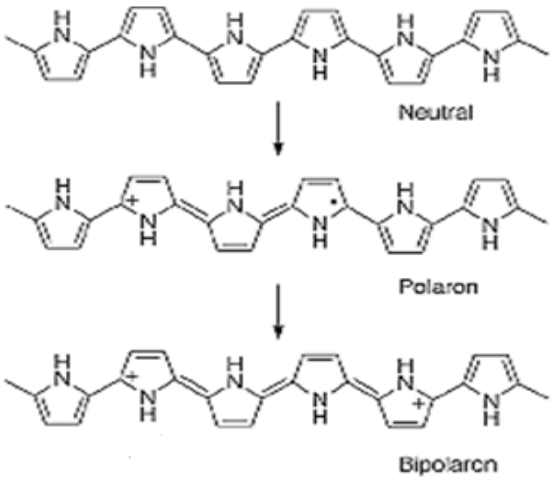

Figure 2.13: Structures of neutral PPy, partially oxidised/doped PPy containing the polaron and fully oxidised/doped PPy containing the bipolaron [135]

A review of literature over the years has revealed that not much has been reported on the application of pristine PANI and PPy on the removal of fluoride ions probably due to poor adsorption of the fluoride ions by these materials. A study by Karthiyeyan et al. [137], produced PPy and PANI for defluoridation of water and obtained adsorption capacities as low as 6.30 and 0.78 mg/g, respectively. The major problem of PANI and PPy has been the tendency of agglomerating via π-π interactions between chains reducing surface area and adsorption capacity [127,131]. To overcome these challenges researchers began to modify the polymer chain by incorporating other materials, for example alumina where the fluoride adsorption capacities were 6.60 and 8.00 mg/g, respectively [16]. The PPy/alumina and PANI/alumina composites were better than the pristine PANI and PPy but still the adsorption capacities were low. Later on, Bhaumik et al. [138] prepared PPy-Fe_3O_4 for the removal of fluoride ions from aqueous solution through batch studies. The maximum adsorption capacity was 17.60 to 23.30 mg/g at a pH of 6.5 over 20 minutes contact time. The adsorption process was best described by the Langmuir model and the kinetics was pseudo-first-order modelled. The presence of phosphate and sulphate ions reduced the adsorption of fluoride ions slightly whilst chloride and nitrate ions had no effect. An endothermic and spontaneous adsorption process through an ion exchange mechanism was reported. This demonstrated one feature of nano-metal oxides where ease of separation is enhanced by the magnetic property and the results were encouraging. Nevertheless, other issues like application on real underground water samples and the long-term applicability were still to be explored. Parashar et al. [9] synthesized a hydrous titanium oxide PPy nanocomposite for the removal of fluoride aqueous solution by batch studies. The maximum adsorption capacity was 31.93 mg/g at a pH of 6.5 within 30 minutes contact time. The adsorption process was Langmuir modelled and the kinetics followed the pseudo-second-order modelled with an endothermic and spontaneous adsorption. The fluoride removal was not affected by co-existing ions hence, the adsorbent had high selectivity. The adsorption mechanism was reported to be an ion exchange between hydroxyl groups of the metal oxide and between chlorides doped PPy with fluoride. Electrostatic interactions between protonated metal oxide surface and positive amine groups of the PPy moiety with fluoride ions also manifested. The reusability of the nanocomposite adsorbent in three cycles demonstrated its stability. The same authors reported a maximum adsorption capacity of 26.16 mg/g using PPy-hydrous tin oxide composite [139]. Furthermore, Rahman et al. [140] utilised Zr (IV)-doped

UNIVERSITY OF JOHANNESBURG

polypyrrole/zirconium (IV) iodate and obtained a maximum adsorption capacity of 183.50 mg/g whilst Nagaraj et al. [141] obtained an adsorption capacity of 4.70 mg/g with MgO-PPy for the same ion. On the other hand, more recently, Parashar et al. [142] fabricated hydrous zirconium oxide on PANI nanofibers ($HZrO_2$@PANI NFs) also for fluoride ions removal. The nanocomposite was well characterized and various adsorption parameters were investigated. The adsorption was Langmuir modelled with maximum adsorption capacities of 83.23 and 28.77 mg/at pH values of 3 and 6.5, respectively. The kinetics was pseudo-first-order modelled and the adsorption was spontaneous and exothermic. There was successful defluoridation of underground fluoride containing samples revealing a great potential for the nanocomposite.

As mentioned earlier, PANI and PPy, contain amino groups which have a reducing ability, thus they have found much applications for the removal of Cr(VI) ions from water. PANI is able to remove Cr(VI) from water as reported a decade ago by Olad and Nabavi [143] where the PANI in film and powder forms was produced in its various oxidation states for the removal of Cr(VI) ions. Various parameters were studied for the process and PANI was able to reduce Cr(VI) to Cr(III) ions with 98% of the pollutant having been removed. However, there was over oxidation and degeneration of the PANI material at high concentration of Cr(VI) ions in water causing leaching of adsorbent. This makes the application of pristine PANI for the removal of Cr(VI) ions to be restricted to low Cr(VI) ions concentration. Consequently, over the years research has shifted towards incorporation of dopants, metal oxides, co-polymerization and functional nanomaterials on PANI followed by application on high Cr(VI) concentrations removal. Several materials have been applied to modify PANI as shown in **Table. 2.3** producing very encouraging results for Cr(VI) ions uptake.

UNIVERSITY OF JOHANNESBURG

Table. 2.3: Adsorption capacities of different PANI composite adsorbents studied for the removal of Cr(VI) from aqueous solution.

Adsorbent	Adsorption capacity (mg/g)	Optimised pH	Temp (°C)	Ref.
PANI- coated ethyl Cellulose	38.80	1	Not specified	[98]
PANI coated chitin	24.60	4.2	30	[99]
PANI/PEG	69.00	5	Room temperature	[144]
PANI/jute fibre	62.90	3	20	[145]
PANI/Kapok fibre	44.10	4.5	30	[146]
PANI/sodium alginate nanofibers	73.30	4.2	30	[147]

Furtheremore, Mandal et al. [148] synthesized CeO_2-PANI composite for the removal of Cr(VI) ion using response surface methodology to predict the adsorption. The maximum adsorption capacity was 357.00 mg/g at a pH of 6. The Langmuir model best described the adsorption where the kinetics was pseudo-first-order modelled. In the presence of co-existing ions 96.4% of the Cr(VI) ions were removed and the order of interference of the ions was nitrate > bicarbonate > sulphate > carbonate > fluoride > chloride.

The tendency of PPy to agglomerate via π-π interactions between chains leads to reduced surface area and Cr(VI) ions adsorption capacity. Consequently, modification had to be performed. A number of PPy-composite adsorbents have been fabricated and applied for Cr(VI) ions removal as shown in **Table 2.4.**

UNIVERSITY OF JOHANNESBURG

Table 2.4: Adsorption capacities of different PPy composite adsorbents studied for the removal of Cr(VI) from aqueous solution.

Adsorbent	Adsorption capacity (mg/g)	Optimised pH	Temp (°C)	Ref.
Aspartic acid doped PPy	176.67	2	30	[27]
PPy/Fe_3O_4	169.40	2	25	[138]
Fe_3O_4 glycine doped PPy	238.00	2	25	[149]
Glycine doped PPy	217.39	2	25	[150]
PPy-PANI fibers	227.00	2	25	[151]
PPy coated hallocyte nanotubes	149.25	2	25	[152]
PPy-rGO/Fe_3O_4	226.80	3	30	[153]
PPy-PANI/Fe_3O_4	303.00	2	25	[154]
PPy/Fe_3O_4/AgCl	111.10	2	30	[155]
Fe_3O_4/PPy	208.77	2	33	[156]
GO/MnO_2/Fe_3O_4/PPy	374.53	2	35	[157]

In all the studies, there was considerable removal of Cr(VI) ions through adsorption and reduction to Cr(III) ions. Elsewhere, Guajardo et al. [133] produced polypyrrole (PPy)/maghemite and polyaniline (PANI) maghemite nanocomposites for the removal of

Cr(VI) by batch processes. The adsorption capacities for Cr(VI) adsorption was 171.00 mg/g with PPy/maghemite and 196.00 mg/g with PANI/maghemite. The optimum adsorption pH was 2 and the absorption time was 15 minutes for a concentration range of 50-100 mg/L. However, the effect of co-existing ions which is also necessary to approximate real waste water situations was not reported.

The synthesis and application of nano-metal oxides, amino doped conducting polymers and conducting polymer-based nanocomposites for fluoride and Cr(VI) ions water and waste water remediation is therefore a new and exciting area which needs further exploration on a variety of materials. Their long-term applicability, stability, mechanical properties and improvement of separation from solution is a milestone to realize the full potential provided by these inorganic/organic hybrid nanocomposites.

2.6 Conclusion

From the above discussion, the occurrence, sources and effects of fluoride and Cr(VI) ions have been highlighted. It is evident that these two ions pose a great threat to humankind and other living organisms. A variety of remediation technologies have been developed for fluoride and Cr(VI) removal from water including coagulation, precipitation, membrane process, electrochemical treatment, ion exchange and adsorption have been discussed. However, these methods have been found to have inherent weaknesses. The adsorption technique as a preferable process has been explained for the removal fluoride and Cr(VI) ions.

Various types of adsorbents for the removal fluoride and Cr(VI) ions been discussed. Commercially produced AC and alumina has a high surface area but have economics related limitations. Narrow pH range, poor regenerability and inability to remove trace amounts of pollutants, difficulty isolation and recovery of mesoporous carbons from aqueous media especially in powdered form and the dissolution of aluminium ions in solution which have health side effects (Alzheimer disease) remain questionable. The application of natural and agricultural waste materials for fluoride and Cr(VI) removal has been studied and applied extensively. The major drawbacks have been the low adsorption capacities, narrow pH range of application, low selectivity, inability to remove trace amounts, secondary pollutant generation and poor regeneration. The use of biopolymers like chitosan for adsorption has been very encouraging over the years. However, chitosan is not very soluble in many solvents due

to crystallinity, agglomeration or formation of a gel in aqueous media. Furthermore, it is in the form of chips or fine particles with low mechanical strength which have restricted its practicality mostly for column applications due to swelling and disintegration among other problems. CNTs for fluoride and Cr(VI) ions remediation have been reported but there are limitations associated with large scale exploitation of these materials attributed to the environmental concerns and side effects. Additionally, tangible application is restricted by their high cost except where they can be produced cheaply. The synthesis of large amounts of graphene in the laboratory still remains a challenge; moreover, commercially made graphene is expensive. Furthermore, the hydrophilic nature GO makes it difficult to be readily collected from aqueous solution, which limits its utilisation as an adsorbent.

Finally, nanomaterials in the form of NMOS including rare earth metal oxide-based materials have been found to show high anionic water pollutants removal efficiency in batch mode. Nevertheless, they are reported to be expensive and have optimum pH range adsorption in the more acidic range which might cause their dissolution, thus limiting their application in water treatment. Due to the large amounts of water to be treated, the process demands correspondingly high availability of nanosized-metal oxides quantities that are enough for that application. To reduce the cost, some cheaper components can be doped or mixed with these expensive metal oxides to enhance adsorption capacity of the cheaper metal oxides. For example, cerium oxide has the least expensive and solubility among rare earth metal oxides which does not leach during the removal of ions in aqueous solutions and has high adsorption potential for pollutants [118]. On the other hand, simply prepared MgO is a cheap adsorbent due to its compounds/raw materials abundancy. It has limited solubility in water, but show low adsorption capacity [115]. Its adsorption ability could be improved by doping with CeO_2 and soon which has shown encouraging results with other metal oxides. Iron-based nanoparticles have many desirable properties including separation in solution and are highly abundant metals on earth. Thus, the application of these NMOs in binary form is considered as a viable approach.

NMOs are effective and specific in adsorbing water pollutants, they are usually in very fine form leading to problems of loss of activity due agglomeration and difficulty of separation in aqueous media. These operational complications can be mitigated by synthesis of hybrid absorbents through impregnating or coating the NMOs particles onto/into porous supports. There is however still more opportunity for research on new simple novel composite materials

UNIVERSITY OF JOHANNESBURG

to support NMOs in the nanocomposite. Thus, the use of conducting polymers like PANI and PPy coated with nanosized-metal oxides is an exciting area where more and more composites with either single nanosized metal oxides or binary metal oxides can be explored.

Various critical aspects of adsorption have not been addressed fully in the reported studies such as desorption studies, effect of co-existing ions, equilibrium kinetics and modelling of results, practical application of adsorbents and mechanical properties. It is important that these aspects be studied if significant information is to be obtained from adsorption studies and where possible the use pH values approximating real polluted water values must be used in adsorption.

2.7 References

[1] C.J. Vörösmarty, P.B. McIntyre, M.O. Gessner, D. Dudgeon, A. Prusevich, P. Green, S. Glidden, S.E. Bunn, C.A. Sullivan, C.R. Liermann, P.M. Davies, Global threats to human water security and river biodiversity, Nature 467 (2010) 555.

[2] M.M. Mekonnen, A.Y. Hoekstra, Four billion people facing severe water scarcity, Sci. Adv. 2 (2016) e1500323.

[3] P. Steduto, J. Hoogeveen, J. Winpenny, J. Burke, Coping with water scarcity: an action framework for agriculture and food security, Food and Agriculture Organization of the United Nations Rome, Italy, (2017).

[4] B. Thole, Ground water contamination with fluoride and potential fluoride removal technologies for East and Southern Africa, Invetech (2013) 64–95.

[5] Fluorides-Environmental Health Criteria 227, World Health Organization (WHO): Geneva, Switzerland, (2002).

[6] V.K. Bhart, A. Giri, K. Kumar, Fluorides sources, toxicity and amelioration: review, Peertechz, J. Scie. Toxico. 2 (2016) 21–32.

[7] S. Ali, S.K. Thakur, A. Sarkar, S. Sheka, Worldwide contamination by fluoride ions, Environ. Chem. Lett. 14 (2016) 291–315.

[8] M. Amini, K. Mueller, K.C. Abbaspour, T. Rosenberg, M. Afyuni, K.N. Møller, M. Sarr, C.A. Johnson, Statistical modeling of global geogenic fluoride contamination in groundwaters, Environ. Sci. Technol. 42 (2008) 3662–3668.

[9] E.J. Ncube, The distribution of fluoride in South African groundwater and the impact of on dental health, Doctoral dissertation, University of Pretoria, (2002).

UNIVERSITY OF JOHANNESBURG

[10] H. Jemenez, E. Vences-Alvarez, J.L. Flores-Arciniega, H. Flores-Zuñiga, J.R Rangel-Mendez, Water defluoridation with special emphasis on adsorbents-containing metal oxides and/or hydroxides: a review, Sep. Purif. Technol. 150 (2015) 292–307.

[11] L. Tang, Y. Fang, Y. Pang, G. Zeng, J. Wang, Y. Zhou, Y. Deng, G. Yang, Y. Cai, J. Chen, Synergistic adsorption and reduction of hexavalent chromium using highly uniform polyaniline-magnetic mesoporous silica, Chem. Eng. J. 254 (2014) 302–312.

[12] L. Liu, Z. Cui, Q. Ma. W. Cui, X. Zhang, One-step synthesis of magnetic iron-aluminum oxide/graphene oxide nanoparticles as a selective adsorbent for fluoride removal from aqueous solution, RSC Adv. 6 (2016) 10783–10791.

[13] Scientific Committee on Health and Environmental Risks, Critical Review of any new evidence on the hazard profile, health effects and human exposure to fluoride and the Fluoridating Agents of Drinking Water, 2010. https://ec.europa.eu/health/scientific_committees/environmental_risks/.../scher_o_122 (date accessed May, 28 2018).

[14] C. Biggerstaff, How Much Fluoride is Too Much Fluoride: Who really benefits, Real Food Houston, 2011, (date accessed May 22, 2018).

[15] B. Bonez, Skeletal fluorosis, Dark art, disease, bones and more, (2016) (date accessed May 28, 2018).

[16] M. Karthikeyan, K.S. Kumar, K.P. Elango, Conducting polymer/alumina composites as viable adsorbents of fluoride ions from aqueous solution, J. Fluorine Chem. 130 (2009) 894–901.

[17] D. Tang, G. Zhang, Efficient removal of F^- by hierarchical Ce-Fe bimetal adsorbent: thermodynamics, kinetics and mechanism, Chem. Eng. J. 283 (2016) 721–729.

[18] N. Naseh, L. Taghavi, B. Barikbin, A.R. Harifi-Mood, The removal of Cr(VI) from aqueous solution by almond green hull waste material: kinetic studies, J. Reuse Desa. 7 (2017) 449–460.

[19] M.M. Loock, J.P. Beukes, P.G. Van Zyl, A survey of Cr(VI) contamination of surface water in the proximity of ferrochromium smelters in South Africa, Water SA. 40 (2014) 709–716.

[20] S. Shariati, M. Khabazipour, F. Safa, Synthesis and application of amine functionalized silica mesoporous magnetite nanoparticles for removal of Cr(VI) from aqueous solutions, J. Porous Mater. 24 (2017) 129–139.

[21] Cr(VI) compounds, IARC Monographs-100C, (1990) 148–165.

[22] Chromium in Drinking water, Document for public consultation, Prepared by Federal-Provincial-Territorial Committee on drinking water, 2015.

[23] K. Simeonidis, S. Mourdikourdis, E. Kaprara, M. Mitrakas, L. Polavarapu, Inorganic engineered nanoparticles in drinking water treatment: a critical review, Environ. Sci. Water Res. Technol. 2 (2016) 43–70.

UNIVERSITY OF JOHANNESBURG

[24] S.S. Liu, Y.Z. Chen, L. De Zhang, G.M. Hua, W. Xu, N. Li, Y. Zhang, Enhanced removal of trace Cr(VI) ions from aqueous solution by titanium oxide-Ag composite adsorbents, J. Hazard. Mater. 190 (2011) 723–728.

[25] S. Fan, Y. Wang, Y. Li, J. Tang, Z. Wang, J. Tang, X. Li, K. Hu, Facile synthesis of tea waste/Fe_3O_4 nanoparticle composite for hexavalent chromium removal from aqueous solution, RSC Adv. 7 (2017) 7576–7590.

[26] X. Sun, L. Yang, H. Zing, J. Zhao, X. Li, Y. Huang, H. Liu, High capacity adsorption of Cr (VI) from aqueous solution using polyethylenimine-functionalized poly (glycidyl methacrylate) microspheres, Colloids Surf. A Physicochem. Eng. Asp. 457 (2014) 160–168.

[27] A. Amalraj, M.K. Selvi, A. Rageswari, A. Pius, Preparation and characterization of aspartic acid doped polypyrrole for the efficient removal of Cr(VI) from aqueous solution, J. Water Process Eng. 11 (2016) 162–173.

[28] T. Perry, Hexavalent chromium, Safety at work, https://slideplayer.com/slide/4731467/, (date accessed May, 28 2018).

[29] M.G. Steinpress, Naturally occurring Cr(VI) in groundwater, Cr(VI) Handbook, CRC Press LLC. (2004) 90–93.

[30] A.D. Venter, J.P. Beukes, P.G. Van Zyl, M. Josipovic, K. Jaars, V. Vakkari, Regional atmospheric Cr(VI) pollution from the bushveld complex, South Africa, Atmos. Pollut. Res. 7 (2016) 762–767.

[31] R. Sutton, Chromium-6 in US tap water, Washington, DC: Environmental Working Group, 2010.

[32] B. Walsh, The world's most polluted places, A project of Blacksmith Institute, Time Magazine, (2007) 16–17.

[33] T. Carnie, Fatal chemical found in Durban groundwater, IOL. 2004 (date accessed May, 28 2018).

[34] S. Ayoob, A.K. Gupta, V.T. Bhat, A conceptual overview on sustainable technologies for the defluoridation of drinking water, Critical Review Environ. Sci. Technol. 38 (2008) 401–470.

[35] Fluoride treatment methods, https://www.bibliocapleyades.net/salud-fluor23.htm, (date accessed May, 28 2018).

[36] A. Gupta, Methods of removing chromium from water, https://www.slideshare.net/ArvindGupta9/methods-for-removal-of-chromium (date accessed May, 28 2018).

[37] Z. Amor, B. Bariou, N. Mameri, M. Taky, S. Nicolas, A. Elmidaoui, Fluoride removal from brackish water by electrodialysis, Desalination 133 (2000) 215–223.

[38] P.P. Sharma, V. Ydav, P.D. Maru, B.S. Makwana, S. Sharma, V. Kulsherestha, Mitigation of fluoride from brackish water via Electrodialysis: An Environmental

UNIVERSITY OF JOHANNESBURG

friendly process, Chemistry Select. 3 (2018) 799–784.

[39] T.Z. Sadyrbaeva, Removal of Cr(VI) from aqueous solutions using novel liquid membrane-electrodialysis process, Chem. Eng. Process. 99 (2016) 183–191.

[40] T.D. Oyoh, Desalination in water treatment and sustainability, Bachelors Thesis, Construction Engineering, Hame University of Applied Sciences, (2017) 36–37.

[41] K. Hu, J.M. Dickson, Nanofiltration membrane performance on fluoride removal form water, J. Membr. Sci. 279 (2006) 529–538.

[42] B. Barikhan, S. Bagher Mortazavi, G. Moussavi, Simultaneous removal of Cr(VI) from water containing sulphate using nanofiltration, Desalin. Water Treat. 53 (2015) 1885–1901.

[43] R.C. Maheshwari, Fluoride in drinking water and its removal, J. Hazard. Mater. 137 (2006) 456–463.

[44] H. Paudya, K. Inouue, H. Kawakita, K. Ohto, H. Kamata, S. Alam, Removal of fluoride by effectively using spent cation exchange resin, J. Mater. Cycles Waste Manage. (2017) 795–984.

[45] F. Gode, E. Pehlivan, Removal of Cr(VI) using two Lewatit-anion exchange resins, J Hazard. Mater. 119 (2005) 175–182.

[46] Absorption versus Adsorption, Diffen, Science, Chemistry, (date accessed 27/05/18).

[47] G. Alagumuthu, M. Rajan. Equilibrium and kinetics of adsorption of fluoride onto zirconium impregnated cashew nut shell carbon, Chem. Eng. J. 158 (2010) 451−457.

[48] R. Mariappan, R. Vairamuthu, A. Ganapaty, Use of chemically activated cotton nut shell carbon for the removal of fluoride contaminated drinking water: Kinetics evaluation, Chin. J. Chem. Eng. 23 (2015) 710–721.

[49] K. Sigh, D.H. Lataye, K. Wasewar, Removal of fluoride from aqueous using bael (Aegle marmelos) shell activated carbon: kinetic, equilibrium and thermodynamic study, J. Fluorine Chem. 194 (2017) 23–32.

[50] S. Gupta, B.V. Babu, Utilization of waste product (tamarind seeds) for the removal of Cr(VI) from aqueous solutions: equilibrium, kinetics, and regeneration studies, J. Environ. Manage. 90 (2009) 3013–3022.

[51] A. El Nemr, A. El-Sikaily, A. Khaled, O. Abdelwahab, Removal of toxic chromium from aqueous solution, wastewater and saline water by marine red alga Pterocladia capillacea and its activated carbon, Arab. J. Chem. 481 (2015) 105–117.

UNIVERSITY OF JOHANNESBURG

[52] Y.J. Zhang, J.L. Oua, Z.K. Duan, Z.J. Xing, Y. Wang, Adsorption of Cr(VI) on bamboo bark-based activated carbon in the absence and presence of humic acid, Colloids Surf. A Physicochem. Eng. Asp. 481 (2015) 108–115.

[53] C.Y. Yin, M.K. Aroua, W.M. Daud, Review of modifications of activated carbon for enhancing contaminant uptakes from aqueous solutions, Sep. Purif. Technol. 52 (2007) 403–415.

[54] A. Bhatnagar, E. Kumara, M. Sillanpää, Fluoride removal from water by adsorption-A review, Chem. Eng. J. 171 (2011) 811–840.

[55] S.M. Maliyekkal, S. Shukla, L. Philip, I.M. Nambi, Enhanced fluoride removal from drinking water by magnesia-amended activated alumina granules, Chem. Eng. J. 140 (2008) 183–192.

[56] E. Kumar, A. Bhatnagar, U. Kumar, M. Sillanpää, Defluoridation from aqueous solutions by nano-alumina: characterization and sorption studies, J. Hazard Mater. 186 (2011) 1042–1049.

[57] L.M. Camacho, A. Torres, D. Saha, S. Deng, Adsorption equilibrium and kinetics of fluoride on sol-gel-derived activated alumina adsorbents, J. Colloid Interface Sci. 349 (2010) 307–313.

[58] B. Ekka, R.S. Dhaka, R.K. Patel, P. Dash, Fluoride removal in waters using ionic liquid-functionalised alumina as a novel adsorbent, J. Clean. Prod. 151 (2017) 303–318.

[59] S. Kundu, I.H. Chowdhury, P.K. Sinha, M.K. Naskar, Effect of organic acid-modified mesoporous Alumina toward fluoride Ions removal form water, J. Chem. Eng. Data. 62 (2017) 2067–2974.

[60] J. Yang, M. Yu, W. Chen, Adsorption of chromium form aqueous solution by activated carbon prepared from longan seed: Kinetics, equilibrium and thermodynamics, J. Ind. Eng. 21 (2015) 414–422.

[61] A.K. Bhattacharya, T.K. Naiya, S.N. Mandal, S.K. Das, Adsorption, kinetics and equilibrium studies on removal of Cr(VI) from aqueous solutions using different low-cost adsorbents, Chem. Eng. J. 137 (2008) 529–541.

[62] N. Sankararamakrishnan, M. Jaiswal, N. Verma, Composite nanofloral clusters of carbon nanotubes and activated alumina: an efficient sorbent for heavy metal removal, Chem. Eng. J. 235(2014) 1–9.

[63] V. Gopalakannan, S. Periyasmy, N. Viswanathan, One pot eco-friendly synthesis of highly dispersed alumina supported alginate biocomposite for efficient Cr(VI) removal, J. Water Process Eng. 10 (2016) 113–119.

[64] L. Sun, Z. Yuan, W. Gong, L. Zhang, Z. Xu, G. Su, D. Han, The mechanism study of trace Cr(VI) removal form water using Fe^0 nanorods modified with chitosan in porous anodic alumina, Appl. Surf. Sci. 328 (2015) 606–613.

[65] M. Mahopatra, S. Anand, B.K. Mishra, D.E. Giles, P. Sigh, Review of fluoride removal form drinking water, J. Environ. Manage. 91 (2009) 66–67.

UNIVERSITY OF JOHANNESBURG

[66] B.D. Turner, P. Binning, S.L.S. Stipp, Fluoride removal by calcite: evidence for fluorite precipitation and surface adsorption, Environ Sci. Technol. 39 (2005) 9561–9568.

[67] M. Islam, R.K. Patel, Evaluation of removal efficiency of fluoride from aqueous solution using quicklime, J. Hazard. Mater. 143 (2007) 303−310.

[68] Y. Nie, C. Hu, C. Kong, Enhanced fluoride adsorption using Al(III) modified calcium hydroxyapatite, J. Hazard. Mater. 233 (2012) 194–197.

[69] E. Tchomgui-Kamga, E. Ngameni, A. Darchen, Evaluation of removal efficiency of fluoride from aqueous solution using new charcoals that contain calcium compounds, J. Colloid Interface Sci. 346 (2010) 494–499.

[70] F.G. Correa, J.J. Becerril, E.G. Alcantara, Study of Co(II) and Cr(VI) adsorption from aqueous solution by $CaCO_3$/sub 3, J. Chem. Soc. Pakistan. 35 (2013)1088–1095.

[71] A. Eleyahaoui, K. Ellouzi, H. Al Zabadi, B. Razzouki, S. Bouhlassa, K. Azzaoui, E. M. Meldoubi, O. Hamed, S. Jodeh, A. Lamhamdi, Adsorption of Cr(VI) on calcium phosphate: Mechanisms and stability constants of surface complexes, Appl. Sci. 7 (2017) 2–14.

[72] Y. Çengeloğlu, E. Kir, M. Ersöz, Removal of fluoride from aqueous solution using red mud, Sep. Purif. Technol. 28 (2002) 81–86.

[73] D. Thakre, S. Rayalu, R. Kawade S. Meshram J. Subrt, N. Labhsetwar, Magnesium incorporated bentonite clay for defluoridation of drinking water, J. Hazard. Mater. 180 (2010) 122–130.

[74] A. Teutli-Sequeira M. Solache-Río, V. Martínez-Miranda, I. Linares-Hernández, Comparison of aluminium modified natural materials in the removal of fluoride ion, J. Colloid Interface Sci. 418 (2014) 254–260.

[75] G. Biswas, M. Dutta, S. Dutta, K. Adhikari, A comparative removal of fluoride from contaminated water using shale collected from different coal mines in India, Environ. Sci. Pollut. Res. Int. Res. 23 (2016) 9418–9431.

[76] P. Yuan, D. Liu, M. Fan, D. Yang, R. Zhu, F. Ge. H. He, Removal of hexavalent Cr(VI) ions from aqueous solutions by the diatomite-supported/unsupported magnetite nanoparticles, J. Hazard. Mater. 17 (2010) 614–621.

[77] M.C. Brum, J.L. Capitaneo, J.F. Oliveira, Removal of hexavalent chromium from water by adsorption onto surfactant modified montmorillonite, Miner. Eng. 23 (2010) 270–272.

[78] A. León-Torres, E.M. Cuerda-Correa, C. Fernández-González, M.F. Franco, V. Gómez Serrano, On the use of a natural peat for the removal of Cr(VI) from aqueous solutions, J. Colloid Interface Sci. 386 (2012) 325–332.

[79] G. Lv. Z. Li, W.T. Jian, C. Ackley, N. Fenske, N. Demarco, Removal of Cr(VI) from water using Fe-modified natural zeolite, Chem. Eng. Res. Des. 92 (2014) 384–390.

UNIVERSITY OF JOHANNESBURG

[80] M. Barkat, S. Chegrouche, A. Mellah, B. Bensmain, D. Nibou, M. Boufatit, Application of Algerian bentonite in the removal of Cd (II) and Cr(VI) from aqueous Solutions, J. Surf. Eng. Mater Advanced Technol. 4 (2014) 210–226.

[81] L. Bentchikou, F.Z. Mechelouf, F. Neggaz, A. Mellah, Removal of hexavalent chromium from water using natural brown clay, J. of Turkish Chem. Soc. 1 (2017) 43–52.

[82] A.K. Yadav, R. Abbassi, A. Gupta, M. Dadashzadeh, Removal of fluoride from aqueous solution and groundwater by wheat straw, sawdust and activated bagasse carbon of sugarcane, Ecol. Eng. 52 (2013) 211–218.

[83] H. Cai, L. Xu, G. Chen, C. Peng, F. Ke, Z. Liu, D. Li, Z. Zhang, X. Wan, Removal of fluoride from drinking water using ultrafine tea processed using a ball mill, Appl. Surf. Sci. 375 (2016) 74–84.

[84] N.K. Mondal, Natural banana (*musa acuminate*) Peel: An unconventional adsorbent for removal of fluoride from aqueous solution through batch Study, Water Conserv. Sci. Eng. 1 (2017) 223–232.

[85] S. Bibi, A. Farooqi, A. Yasmin, M.A. Kamran, N.K. Niazi, Arsenic and fluoride removal by potato peel and rice husk (PPRH) ash in aqueous environments, Int. J. Phytoremediation. 19 (2017) 1029–1036.

[86] S.H. Hasan, K.K. Singh, O. Prakash, M. Talat, Y.S. Ho, Removal of Cr(VI) from aqueous solutions using agricultural waste 'maize bran, J. Hazard Mater. 152 (2008) 356–365.

[87] M. Bansal, U. Garg, D. Singh, V.K. Garg, Removal of Cr(VI) from aqueous solutions using pre-consumer processing agricultural waste: A case study of rice husk, J. Hazard. Mater. 162 (2009) 312–320.

[88] E. Malkoc, Y. Nuhoglu, Potential of tea factory waste for Cr(VI) removal from aqueous solutions: Thermodynamic and kinetic studies, Sep. Purif. Technol. 54 (2007) 291–298.

[89] A. Mishra, A. Dubey, S. Shingal, Biosorption of Cr(VI) from aqueous solution using waste plant biomass, Int. J. Environ. Sci. 12 (2015) 1415–1426.

[90] V.E. Pakade, T.D. Ntuli, A.E. Ofamaja, Biosorption of hexavalent chromium from aqueous solution by Macadamia nutshell powder, Appl. Water Sci. 7 (2017) 3015–3030.

[91] P. Kanmani, J. Aravand, M. Kamarag, P. Sureshbabu, S. Karthikeyan, Environmental applications of chitosan and cellulosic biopolymers: A comprehensive outlook, Bioresour. Technol. 242 (2017) 295–303.

[92] S.K. Shukla, A.K. Mishra, O.A. Arotiba, B.B. Mamba, Chitosan-based nanomaterials: A state-of-the-art review, Int. J. Biol. Macromol. 59 (2013) 46–58.

[93] H. Kuygusuz, S. Uzaşçı, F.B. Erim, Removal of fluoride from water using aluminium alginate beads, Clean-Soil Air Water. 43 (2013) 724–730.

[94] N. Viswanathan, S. Meenakshi, Selective sorption of fluoride using Fe (III) loaded carboxylated chitosan beads, J. Fluor. Chem. 129 (2008) 503–509.

UNIVERSITY OF JOHANNESBURG

[95] S. Jagtap. D. Thakre S. Wanjari, S. Kamble, N. Labhsetwar, S. Rayalu, New modified chitosan-based adsorbent for defluoridation of water, J. Colloid Interface Sci. 332 (2009) 280–290.

[96] K. Pandi, S. Periyasamy, N. Viswanathan, Remediation of fluoride from drinking water using magnetic iron oxide coated hydrotalcite/chitosan composite, Int. J. Biol. Macromol. 104 (2017) 1569–1577.

[97] A. Nagaraj, K.K. Sadasivuni, M. Rajan, Investigation of lanthanum impregnated cellulose, derived from biomass, as an adsorbent for the removal of fluoride from drinking water, Carbohydr. Polym. 176 (2017) 402–410.

[98] B. Qiu, C. Xu, D. Sun, H. Yi, J. Guo, X. Zhang, H. Qu, M. Guerrero, X. Wang, N. Noel, Z. Luo, Polyaniline coated ethyl cellulose with improved hexavalent chromium removal, ACS Sustainable Chem. Eng. 2 (2014) 2070–2080.

[99] R. Karthik, S. Meenakshi, Synthesis, characterization and uptake of Cr(VI) using polypyrrole functionalised chitin, Synth. Met. 198 (2014) 181−187.

[100] J.B. Dima, C. Sequeiros, N.E. Zaritzky, Hexavalent chromium removal in contaminated water using reticulated chitosan micro/nanoparticles from seafood processing wastes, Chemosphere 141 (2015) 100−111.

[101] X. Liang, X. Fan, R. Li, S. Li, S. Shen, D. Hu, Efficient removal of Cr(VI) from water by quartenized chitin/branched polyethylenimine biosorbent with hierarchical pore structure, Bioresour. Technol. 250 (2018) 178–184.

[102] A.S. Adeleye J.R. Conway, K. Garner, Y. Huang, Y. Su, A.A. Keller, Engineered nanomaterials for water treatment and remediation: Costs, benefits and applicability, Chem. Eng. J. 286 (2016) 640–662.

[103] G. Ghasemzadeh, M. Momenpour, F. Omidi, M.R. Hosseini, M. Ahani, A. Barzegari, Applications of nanomaterials in water treatment and environmental remediation, Front. Environ. Sci. Eng. 8 (2014) 471–482.

[104] Z. Ruan, Y. Tiana, J. Ruan, G. Cui, K. Iqbal, A. Iqbal, H. Ye, Z. Yang, S. Yan, Synthesis of hydroxyapatite/multi-walled carbon nanotubes for the removal of fluoride ions from solution, Appl. Surf. Sci. 412 (2017) 578–590.

[105] A. Dhillon, S. Prasad, D. Kumar, Recent advances and spectroscopic perspectives in fluoride removal, Appl. Spectrosc. Rev. 4928 (2016) 1–56.

[106] X. Lv, J. Xu, G. Jiang, X. Xu, Removal of Cr(VI) from wastewater by nanoscale zero-valent iron particles supported on multiwalled carbon nanotubes, Chemosphere 85 (2011) 1204–1209.

[107] C. Luo, Z. Tian, B. Yang, L. Zhang, S. Yan, Manganese dioxide/iron oxide/acid oxidized multi-walled carbon nanotube magnetic nanocomposite for enhanced hexavalent chromium removal, Chem. Eng. J. 234 (2013) 256–265.

UNIVERSITY OF JOHANNESBURG

[108] M.H. Dehghani, M.M. Taher, A.K. Bajpai, B. Heibati, I. Tyagi, M. Asif, S. Agarwal, V.K. Gupta, Removal of noxious Cr(VI) ions using single-walled carbon nanotubes and multi-walled carbon nanotubes, Chem. Eng. J. 279 (2015) 344–352.

[109] H. Beheshti M. Irani, L. Hosseini A. Rahimi M. Aliabadi, Removal of Cr(VI) from aqueous solutions using chitosan/MWCNT/Fe_3O_4 composite nanofibers-batch and column studies, Chem. Eng. J. 284 (2016) 557–564.

[110] M. Taghizadeh, S. Hassnpour, Selective adsorption of Cr(VI) ions from aqueous solutions using a Cr(VI)-imprinted polymer supported by magnetic multiwall carbon nanotubes, Polymer 132 (2017) 1–11.

[111] I. Mohmood C.B. Lopes I. Lopes, I. Ahmad A.C. Duarte, E. Pereira, Nanoscale materials and their use in water contaminants removal-a review, Environ. Sci. Pollut. Res. 20 (2013) 1239–1260.

[112] Z. Li, T. Hulderman, R. Salmen, R. Chapman, S.S Leonard, S.H. Young, A. Shvedova, M.I. Luster, P.P. Simeonova, Cardiovascular effects of pulmonary exposure to single-wall carbon nanotubes, Environ. Health Perspect. 115 (2007) 377.

[113] S. Kanra, S. Debnath, P. De, K. Parashar, K. Kriveshni, P. Sasikumar, U.C. Ghosh, Preparation, characterization and evaluation of fluoride adsorption efficiency from water of iron-aluminium oxide-graphene oxide composite material, Chem. Eng. J. 306 (2016) 269–270.

[114] X. Lv, Y. Zhang, W. Fu, J. Cao, J. Zhang, H. Ma, G. Jiang, Zero valent iron nanoparticles embedded into reduced graphene oxide alginate beads for efficient Cr(VI) removal, J. Colloid Interface Sci. 506 (2017) 633–643.

[115] J. Jeevanadam, K.J. Klabunde, Synthesis, properties and applications of oxide nanoparticles adsorbents in J.A. Rodríguez, M Fernández-García, N.J. Whiley: (2007) chapter 14.

[116] J. Lu, D. Liu, J. Hao, G. Zhang, B. Lu, Phosphate removal from aqueous solutions by a nano-structured Fe-Ti bimetal oxide adsorbent, Chem. Eng. Res. Des. 93 (2015) 652–661.

[117] T. Basu, U.C. Gosh, Nano-structured iron (III)-cerium (IV) mixed oxide: synthesis, characterization and arsenic sorption kinetics in the presence of co-existing ions aiming to apply for high arsenic ground water treatment, Appl. Surf. Sci. 283 (2013) 471–481.

[118] M. Hua, S. Zhang, B. Pan, W. Zhang, L. Lv, Q. Zhang, Heavy metal removal from water/wastewater by nanosized metal oxides: a review, J. Hazard. Mater. 211 (2012) 317–331.

[119] A.A. Ismail, A.A. El-Midany, A.I. Ibrahim, H. Matsunaga, Heavy metal removal using SiO_2-TiO_2 binary oxide: experimental design approach, Adsorption 14 (2008) 21–29.

[120] R.G. Gohari, W.J. Lau, T. Matsuura, A.F. Ismail, Fabrication and characterization of novel PES/Fe-Mn binary oxide UF mixed matrix membrane for adsorptive removal of As(III) from contaminated water solution, Sep. Purif. Technol. 118 (2013) 64–72.

UNIVERSITY OF JOHANNESBURG

[121] K. Biswas, K. Gupta, A. Goswami, U.C. Ghosh, Fluoride removal efficiency from aqueous solution by synthetic iron(III)-aluminum(III)-chromium (III) ternary mixed oxide, Desalination 255 (2010) 44–51.

[122] X. Wang, G. Zhang, H. Lan, R. Liu, H. Liu, J. Qu, Preparation of hollow Fe-Al binary oxyhydroxide for efficient removal of fluoride ions, Colloids Surf. Physicochem. Eng. Asp. 520 (2017) 580–589.

[123] A. Dilhon, S.K. Soni, D. Kumar, Enhanced fluoride removal performance by Ce-Zn binary metal oxide: Adsorption characteristics and mechanism, J. Fluorine Chem. 199 (2017) 67–76.

[124] C.Y. Cao, J. Qu, W.S Yan, J.F. Zhu, Z.Y. Wu, W.G. Song, Low-cost synthesis of flowerlike α-Fe_2O_3 nanostructures for heavy metal ion removal: Adsorption property and mechanism, Langmuir 28 (2012) 4573−4579.

[125] M.J. Nalbandian, M. Zhang, J. Sanchez, Y.H. Choa, J. Nam, D.M. Cwiertny, N.V. Myung, Synthesis and optimization of Fe_2O_3 nanofibers for chromate adsorption from contaminated water sources, Chemosphere 144 (2016) 975–981.

[126] W. Weilong, F. Xiaobo, Efficient removal of Cr(VI) with Fe/Mn mixed metal oxide nanocomposites synthesized by a grinding, J. Nanomater. 2013 (2013) 1–8.

[127] S. Sakar, E. Guibal, F. Quignard, A.K. SenGupta, Polymer-supported metals and metal oxide nanoparticles: synthesis, characterization and applications, J. Nanopart Res. 14 (2012) 1–24.

[128] E.N. Zare, A. Motahari, M. Sillanpää, Nano adsorbents on conducting polymer nanocomposite with main focus on polyaniline and its derivatives for the removal of metal ions/dye: A review, Environ. Res. 162 (2018) 173–195.

[129] N. Ghaemi, A new approach to copper ion removal from water by polymeric nanocomposite membrane embedded with alumina nanoparticles, Appl. Surf. Sci. 364 (2016) 221–228.

[130] M.L. Paul, J. Samuel, N. Chandrasekaran, A. Mukherjee, Preparation and characterization of layer-by-layer coated nano metal oxides-polymer composite film using Taguchi design method for Cr(VI) removal, J Environ. Chem. Eng. 2 (2014) 1937–1946.

[131] N.H. Kera, M. Bhaumik, N. Ballav, K. Pillay, S.S. Ray, A. Maity, Selective removal of Cr(VI) from aqueous solution by polypyrrole/2.5-diaminobenzene sulfonic acid composite, J. Colloid Interface Sci. 476 (2016) 144–157.

[132] S. Kalluri, A.M. Asha, S. Parvathy, T.N. Kim, N. Sivakumar, K.R.V. Subramanian, S.V. Nair, A. Balakrishnan, Electrospun nanofibers of polyaniline-carbon black composite for conductive electrode applications,Trends in Polyaniline Research, Nova Science Publishers, New York, (2013) 181–202.

[133] A.E. Chavez-Guajardo, J.C. Medina-Llanas, L. Maqueira, C.A. Andrade, K.G. Alves, C.P. de Melo, Efficient removal of Cr(VI) and Cu(II) ions from aqueous media by use

of polypyrrole and polyaniline magnetic nanocomposites, Chem. Eng. J. 281 (2015) 826–836.

[134] C.O. Baker, X. Huang, W. Nelson, R.B. Kaner, Polyaniline nanofibers: broadening applications for conducting polymers, Chem. Soc. Rev. 46 (2017) 1510–1525.

[135] M.S. Freund, B.A. Deore, Self-Doped Conducting Polymers, John Wiley & Sons, Ltd, Chichester, England, (2007).

[136] M. Omastová, M. Mičušík, Polypyrrole coating of inorganic and organic materials by chemical oxidative polymerisation, Chem. Pap. 66 (2012) 392–414.

[137] M. Karthikeyan, K.K. Satheeshkumar, K.P. Elango, Defluoridation of water via doping of polyanilines, J. Hazard. Mater. 163 (2009) 1026–1032.

[138] M. Bhaumik, T.Y. Leswifa, A. Maity, V.V. Srinivasu, M.S. Onyango, Removal of F^- from aqueous solution by polypyrrole/Fe_3O_4 magnetic Nanocomposite, J. Hazard. Mater. 186 (2011) 150–159.

[139] K. Parashar, N. Ballav, S. Debnath, K. Pillay, A. Maity, Rapid and efficient removal of F^- from aqueous solution using polypyrrole coated hydrous tin oxide composite, J. Colloid Interface Sci. 476 (2016) 103–118.

[140] N. Rahman, M. Nasir, Development of Zr(IV)-doped polypyrrole/zirconium(IV) iodate composite for efficient removal of fluoride from water environment, J. Water Process Eng. 19 (2017) 172–184.

[141] A. Nagaraj, D. Govindaraj, M. Rajan, Magnesium oxide entrapped polypyrrole hybrid nanocomposite as an efficient selective scavenger for fluoride ion in drinking water, Emergent Materials (2018) 1–9.

[142] K. Parashar, N. Ballav, S. Debnath, K. Pillay, A. Maity, Hydrous ZrO_2 decorated polyaniline nanofibres: Synthesis, characterization and application as an efficient adsorbent for water defluoridation surface, J. Colloid Interface Sci. 50 (2017) 342–358.

[143] A. Olad, R. Nabavi, Application of polyaniline for the reduction of toxic Cr(VI) in water, J. Hazard. Mater. 147 (2007) 845–851.

[144] M.R. Samani, S.M. Borghei, A. Olad, M.J. Chaichi, Removal of chromium from aqueous solution using polyaniline-poly ethylene glycol composite, J. Hazard. Mater. 184 (2010) 248–254.

[145] P.A. Kumar, S. Chakraborty, M. Ray, Removal and recovery of chromium from wastewater using short chain polyaniline synthesized on jute fiber, Chem. Eng. J. 141 (2008) 130–140.

[146] Y. Zheng, W. Wang, D. Huang, A. Wang, Kapok fiber oriented-polyaniline nanofibers for efficient Cr(VI) removal, Chem. Eng. J. 191 (2012) 154–161.

[147] R. Karthik, S. Meenakshi, Removal of Cr(VI) ions by adsorption onto sodium alginate-polyaniline nanofibers, Int. J. Biol. Macromol. 72 (2015) 711–717.

[148] S. Mandal, S.S. Mahapatra, R.K. Pat, Enhanced removal of Cr(VI) by cerium oxide polyaniline composite: optimisation and modelling using response surface methodology and artificial neural networks, J. Environ. Chem. Eng. 3 (2015) 870–885.

[149] N. Ballav, H.J. Choi, S.B. Mishra, A. Maity, Synthesis, characterization of Fe_3O_4@ glycine doped polypyrrole magnetic nanocomposites and their potential performance to remove toxic Cr(VI), J. Ind. Eng. Chem. 20 (2014) 4085–4093.

[150] N. Ballav, H.J. Choi, A. Maity, S.B. Mishra, High efficient removal of Cr(VI) using glycine doped polypyrrole adsorbent from aqueous solution, Chem. Eng. J. 198 (2012) 536–546.

[151] M. Bhaumik, A. Maity, V.V. Srinivasu, M.M. Onyango, Removal of hexavalent chromium from aqueous solution using polypyrrole-polyaniline nanofibers, Chem. Eng. J. 181–182 (2012) 323–333.

[152] N. Ballav, H.J. Choi, S.B. Mishra, A. Maity, Polypyrrole-coated halloysite nanotube clay nanocomposite: synthesis, characterization and Cr(VI) adsorption behaviour, Appl. Clay Sci. 102 (2014) 60–70.

[153] H. Wang, X. Yuan, Y. Wu, X. Chen, L. Leng, H. Wang, H. Li, G. Zeng, Facile synthesis of polypyrrole decorated reduced graphene oxide-Fe_3O_4 magnetic composites and its application for the Cr(VI) removal, Chem. Eng. J. 262 (2015) 597–606.

[154] N. Kera, B. Bhaumik, K. Kriveshini, S.S. Ray, A. Maity, Selective removal of toxic Cr(VI) from aqueous solution by adsorption combined with reduction at a magnetic nanocomposite surface, J. Colloid Interface Sci. 503 (2017) 214–228.

[155] W. Sun, Y. Zhou, Q. Su, L. Chen, Y. Wang, J. Liu, Y. Sun, H. Ma, Removal of Cr(VI) from aqueous solutions using polypyrrole-based magnetic composites, Polym. Bull.74 (2017) 1157–1174.

[156] U.O. Aigbe, R. Das, W.H. Huo, V. Srinivasu, A. Maity, A novel method for removal of Cr(VI) using polypyrrole magnetic nanocomposite in the presence of unsteady magnetic fields, Sep. Purif. Technol. 194 (2018) 377–387.

[157] W. Liu, L.Yang, S. Xu, Y. Chen, B. Liu, Z. Li, C. Jiang, Efficient removal of hexavalent chromium from water by an adsorption-reduction mechanism with sandwiched nanocomposites, RSC Adv. 8 (2018) 15087–15093.

CHAPTER THREE

INSTRUMENTAL ANALYSIS

3.1 Introduction

This chapter describes the instrumentation and techniques used for the various characterizations of different materials in this research study and for the analysis of fluoride and chromium in solutions. The operational principle of each instrument is briefly discussed together with the details for the analyses carried out.

3.2 Fourier transform infrared spectroscopy (FTIR)

The principle behind the FTIR technique is that infrared radiation (IR) passes through a material where it is absorbed and transmitted depending on the nature of the material. The aim of this technique is to measure how well a sample absorbs light at each wavelength. The (IR) region within the electromagnetic spectrum wavelengths ranges from 0.78 to 1000 μm or wavenumbers from 13,000 to 10 cm^{-1} comprising the near IR region (13000-4000 cm^{-1}), mid IR region (4000-200 cm^{-1}) and the far IR region (200-100 cm^{-1}). Most light to medium weight organic compounds and elements have chemical bonds vibrations falling into the 4000-200 cm^{-1} region. When IR is shown on the sample molecules, they selectively absorb the characteristic frequencies (specific wavelengths) of IR radiation, leading to changes in the dipole moment of sample molecules [1]. This results in the vibrational energy levels of sample molecules transmitting from ground state to higher energy excited state. The difference between the vibrational energies of ground and the excited state defines the frequency of the absorption peak whilst its intensity is controlled by the changes in the dipole moment of the sample molecule. Each material has a unique combination of atoms leading to a possible identification of different kinds of materials as the different groups of atoms have different vibration wavelengths. Thus, FTIR is a fingerprinting technique. A typical FTIR instrument schematic diagram is presented in **Fig. 3.1**[2]:

UNIVERSITY OF JOHANNESBURG

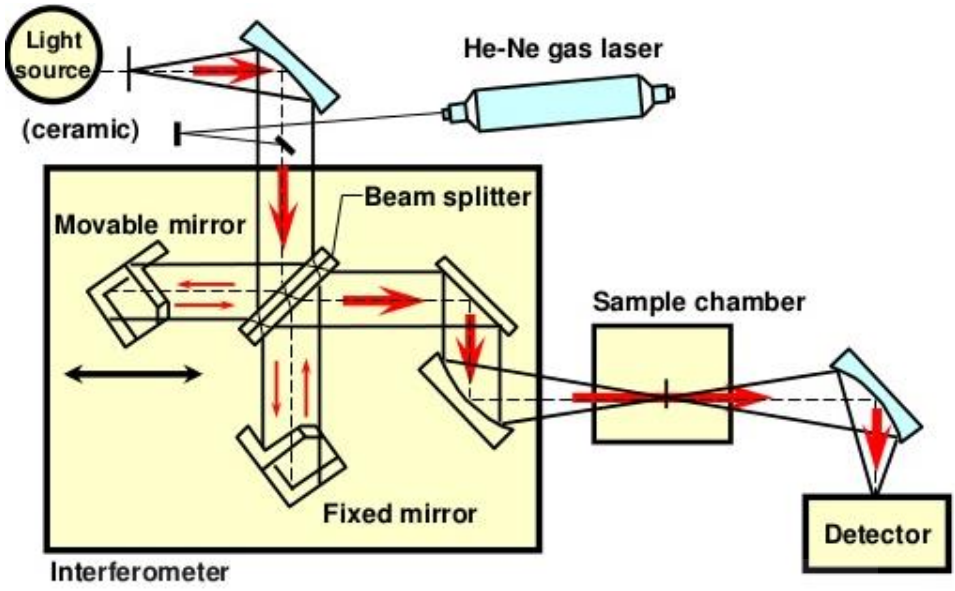

Fig. 3.1: Schematic representation of a simple FTIR spectrometer layout [2]

During sample analysis, light from the source goes through an opening which regulates the quantity of light going to the sample, then into an interferometer for special encoding. The light beam then shines on the sample where there is transmission and reflection of frequency energy specific for the sample. From there, the beam is directed to a detector for the final measurement, then to a computer for signal digitalisation and Fourier transformation into a spectrum. The FTIR spectra of materials in this study were obtained using a Perkin Elmer Spectrum 100 Spectrometer (Perkin Elmer, USA) with an ATR accessory that employs a germanium crystal. The spectra were obtained in the range of 500-4000 cm^{-1} with 4 cm^{-1} resolution and 32 scans [3].

3.3 X-ray diffraction analysis (XRD)

XRD is a non-destructive technique used to determine the atomic and molecular structure of crystals when a beam of incident ray shines on crystalline material. The material then diffracts the incident ray in a variety of specific directions [4]. It is used to measure crystal size, calculate lattice strain, chemical configuration, state the order and determine phase diagrams. An outline of the XRD instrument is shown in **Fig. 3.2** [5].

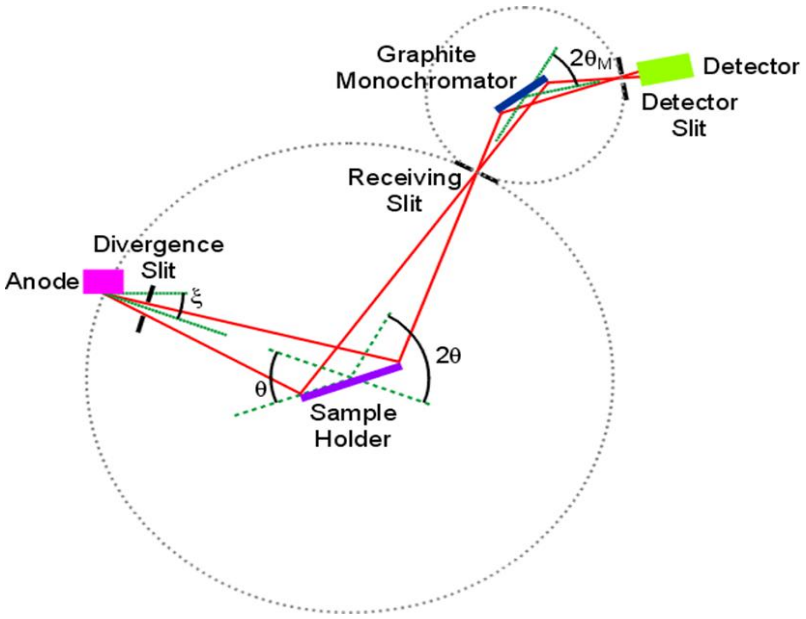

Fig. 3.2: Schematic representation of an X-ray diffractometer set up [5]

The X-rays are produced in a tube called the cathode ray through heating an element and they are then focused onto a target sample. The X-rays bombard the material with incident electrons and may have sufficient energy to remove electrons producing an electron spectra. The interaction between the incident rays and the sample produced intense X-rays positive intereference when it satisfies Bragg's law **Equation (3.1)**:

$$n\lambda = 2d\sin\theta \quad (3.1)$$

where λ, θ, d *and* n are the wavelength of the X-rays, angle of diffraction, interplanar spacing and order of diffraction, respectively. The X-ray instrument is designed in such a way that the sample rotates in the path of the accurately paralled X-ray beam at an angle. At the same time, a detector is mounted on an arm which collects the diffracted X-rays and rotates at an angle 2θ [6]. The detector records and processes this signal into 2θ versus count rate output using a computer or printer. A PANalytical X'Pert PRO-X-ray diffractometer (PANalytical, The Netherlands) using CuKα radiation with a wavelength of 1.5505 Å was used for the XRD characterization of the adsorbents in this study. The X-ray spectra were recorded for 2θ values ranging from 5 to 90 with tube current and generator voltage of 30 mA and 45 kV, respectively.

UNIVERSITY OF JOHANNESBURG

3.4 Brunauer-Emmett-Teller surface area analysis (BET)

The BET technique, with an instrumental layout is shown above in **Fig. 3.3** [7] allows the determination of surface area and porosity of a material. To determine the efficacy, stability and utility of a material, these two properties are critical [8].

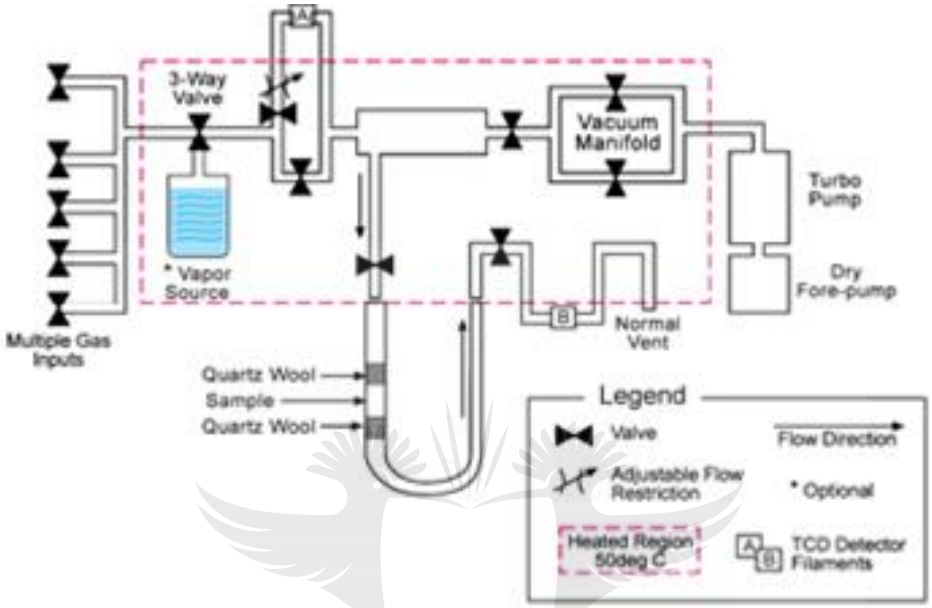

Fig. 3.3: Schematic representation of the BET instrument [7].

UNIVERSITY OF JOHANNESBURG

A gas, usually nitrogen is used to cool the surface of the material to obtain detectable amounts of adsorption. Known quantities of nitrogen gas are let out stepwise into a sample and a relative pressure below atmospheric pressure is attained through the creation of partial vacuum conditions. After saturation, the material will not adsorb any more gas and when the adsorption layers are formed, the sample is removed from nitrogen exposure. The sample is then heated to release nitrogen with the heat being quantified. The data collected is displayed in the form of BET isotherms and a plot of adsorbed gas versus relative pressure. Analysis of this data will provide information on porosity, pore volume and surface area of a sample. The number of gas molecules required to form a monolayer onto the surface of the material is calculated based on the amount of N_2 gas adsorbed at a given pressure by applying the BET theory. The N_2 gas adsorption and desorption curves are obtained and the acquired information is then used to calculate BET specific surface area using the following BET **Equations (3.2)** and **(3.3)**:

$$\frac{1}{v\left[\left(\frac{p_o}{p}\right)-1\right]} = \frac{c-1}{v_m c}\left(\frac{p}{p_o}\right) \tag{3.2}$$

$$S_{BET} = 0.269 v_m \sigma_m \tag{3.3}$$

The variables p and p_o are the equilibrium and saturation pressures at the temperature of the adsorbate and V is the volume of gas, respectively. Additionally, v_m, c, σ_m and S_{BET} are the monolayer adsorbed gas quantity, BET constant, area occupied by one adsorbed molecule in a monolayer and specific surface area of the material, respectively [9]. In this study, a Micromeritics ASAP 2020 gas adsorption apparatus (Micromeritics, USA) using low temperature (-198.50 °C) N_2 adsorption-desorption technique was used for BET surface area, pore size and pore volume measurements.

3.5 Scanning electron microscopy (SEM)

The SEM technique has a high magnification electron microscope which utilises a focused beam to produce images of a material by scanning its surface. The low energy beam of electrons interacts with the atoms of a material, producing many signals that contain topological and composition information about the surface of a material [10]. **Fig. 3.4** below shows a schematic layout of the SEM microscope [11].

UNIVERSITY OF JOHANNESBURG

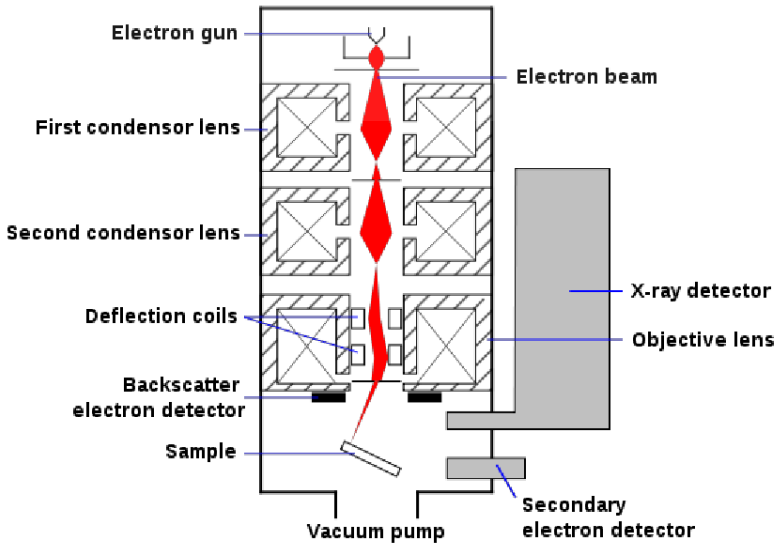

Fig. 3.4: Schematic representation of a typical SEM [11].

The electron beam scans the material in a rectangular pattern for image capture and reconstruction. The interactions of the electron beam and atoms of the material produce signals which enable the image to be produced. These signals can be secondary, backscattered electrons, X-rays, adsorbed and transmitted current. The secondary electrons produce the image of the sample when incident electrons are directed on the sample. Back-scattered electrons produce the crystal structure and orientation while X-rays are used to produce energy dispersive X-rays (EDX). In EDX, an incident electron beam strikes a sample and a certain amount of energy is transferred to electrons higher than their binding energies resulting in the ejection of inner orbital electrons from an atom. The electrons from deeper orbitals replace the ejected ones and occupy the empty orbitals together with the emission of X-rays from the atom. Each element has a characteristic electronic structure and distinctive set of X-rays associated with it [10,12]. Thus, EDX spectra are analysed to determine the elements present in a sample and quantitative analysis is also possible since the intensities of the X-rays are proportional to the amount of atoms emitting X-rays. Mapping analyses on the distribution of elements on particles and their surfaces can also be obtained.

The surface morphology of materials in this study was analysed using a Zeiss Auriga Cobra FIB microscope from Germany coupled with an Energy Dispersive X-ray analyser (EDX). The samples were stuck with double sided carbon tape to an Al stub and carbon-coated before analysis.

UNIVERSITY OF JOHANNESBURG

3.6 Transmission electron microscopy (TEM)

The TEM is an instrument which focusses a beam of electrons through a specimen in order to produce its image. For this to happen, the specimen must be very thin or in the form of a suspension on a grid. The image is made from the interaction of the material with the penetrating electron beam, followed by magnification and focussing of the beam onto a screen. Because of the smaller deBrogile wavelengths, the TEM technique can produce high resolution images than light microscopes [13,14]. As a result, the instrument can capture finer details as small as atomic thickness. In this case, it produces a high-resolution transmission electron (HR-TEM) image. For example, it can give the fringe lattice spacing a nano-metal oxide characteristic of that oxide. A general outline of the TEM is shown in **Fig. 3.5**. The TEM contains an electron source, thermionic gun, electron beam, electromagnetic lenses, sample stage, fluorescent screen and a computer. TEM produces a high resolution black and white

image from the interaction between specimen and energetic electrons. Air has to be removed out of the vacuum chamber to create space for electrons. The beam then passes through various electromagnet lenses to a column and makes an image. A good image in obtained by a manipulative skill of varying the voltage of the gun, accelerating or decelerating the speed of electrons and changing wavelength of the electromagnetic waves. The scanning transmission electron microscope (STEM) is also used alongside the TEM [15]. It focusses a beam across a fine spot which is then scanned in a raster manner. This beam goes across the sample specimen and makes STEM able to do elemental mapping of the specimen by energy dispersive X-ray spectroscopy (EDS). It has the same instrument layout as the TEM. TEM is similar to SEM somehow but they are different in that (i) SEM utilises backscattered electrons to produce an image of a specimen but TEM uses transmitted electrons and (ii) the TEM magnification and resolution (about 50 million) are very high compared to SEM (2 million).

A high-resolution transmission electron microscope (JEOL-JEM 2100, Japan) with LaB6 filament operated at 200 kV was used in this study to characterize the samples. The samples were prepared by the dispersion of the specimen in water or alcohol through ultrasonication and then dropping the mixtures onto a copper grid.

UNIVERSITY OF JOHANNESBURG

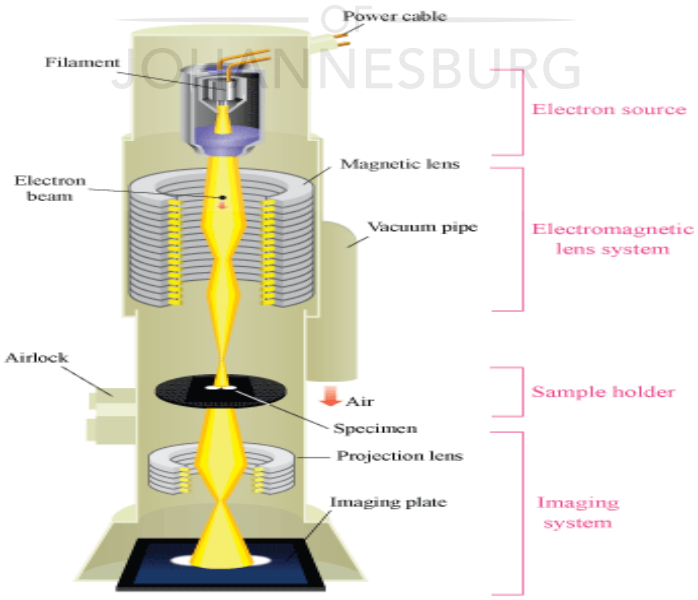

Fig. 3.5: A diagrammatic representation of TEM [14].

3.7 Thermogravimetric analysis (TGA)

This is a procedure which measures the mass of a sample as temperature, time and atmosphere pressure changes. It provides information about phase transitions, adsorption-desorption, thermal stability, composition, estimated life time, oxidative stability, decomposition kinetics, moisture and volatile content of materials [16,17]. A diagram of the TGA instrument is shown below in **Fig. 3.6**. It consists of a precision balance and a simple pan inside a furnace with a programmable temperate control. The furnace temperature is increased at a constant rate of 5 or 10 °C every minute. During this process, the change in mass of the material is monitored in an inert environment purged by nitrogen gas. The thermogravimetric data is recorded and processed by a computer. The interpretation of the data is conducted by plotting a change in mass versus temperature curve which gives a thermogram of the material [18].

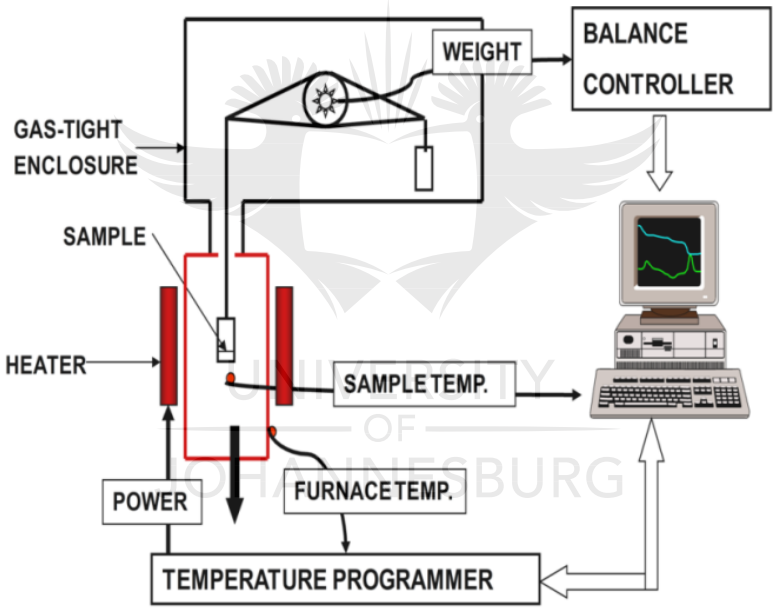

Fig. 3.6: Schematic representation of a thermogravimetric analyzer [17].

In this study, TGA and DTA experiments were performed on a TG Q500 (TA Instruments, USA).The air flow rate was 50 mL/min with a heating rate of 10 °C/min from ambient temperature to 800 °C.

3.8 X-ray photoelectron spectroscopy (XPS)

This is one of the most proficient surface techniques which measures elemental composition at 1-10 nm depth, empirical formulae, chemical shift, surface uniformity and electronic states of each element. This is achieved by shining Al-Kα or Mg-Kα monochromatic X-rays on the surface of a sample placed in a high vacuum chamber (10^{-8} millibars). This causes photoelectrons to be emitted by the core levels atoms of the materiel [19]. The energy of the emitted core-level electrons depends on the binding energy characteristic of each element and given by **Equation (3.4)**:

Binding energy, $E_{binding} = E_{photon} - E_{kinetic\ energy\ of removed\ electron}$ + *work function of the spectrophotometer* (3.4)

An illustration of the XPS instrument is shown in **Fig. 3.7** [20]. The instrument is comprised of an X-ray source which produces the monochromatic light, sample chamber and the electronic analyser. The kinetic energy of the emitted photoelectrons can be measured using an electron energy analyser recorder through counting the number of photoelectrons and a spectrum is produced. This gives the intensity of a peak (counts per second) against binding energy hence, elemental identity, chemical state and quantity can be obtained [21].

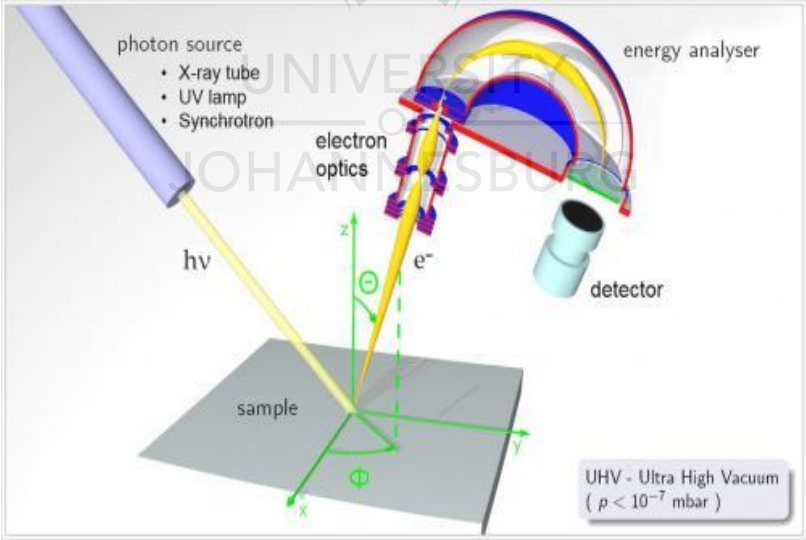

Fig. 3.7: Basic instrumental layout of an XPS [20].

For this study, the XPS of the materials was analysed using Kratos Axis Ultra device and Cryogen-free ARPES and high-resolution XPS Apparatus (SPECS Surface Nano Analysis GmbH) with Al monochromatic X-ray sources (1486.6 and 1486.71 eV, respectively.

3.9 Vibrating sample magnetometry (VSM)

This is a technique which measures the magnetic strength of a material. A diagram of the VSM is shown in **Fig. 3.8** [22]. Magnetism in a sample is induced when it is placed into a constant magnetic field and this causes it to vibrate [23]. Consequently, an alternative electromotive force is produced in the coils arranged around the sample and which is proportional to the magnetisation of the specimen. The set of coils arranged around the sample will pick up the induced current which is then amplified and relayed to a computer. The output is a characteristic hysteresis loop hence, it shows the magnetic property and strength of the sample [24].

The magnetisation curve of the Fe_3O_4@Arg-PPy nanocomposite before and after Cr(VI) adsorption were acquired at room temperature using a vibrating sample magnetometer (VSM, Quantum design, USA) with a maximum applied magnetic field of 10 kOe.

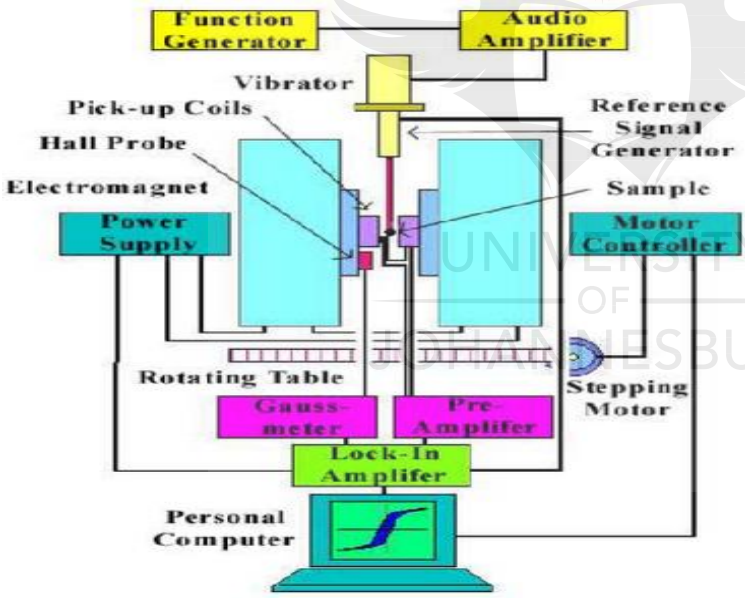

Fig 3.8: Schematic diagram of VSM [22].

3.10 Dynamic mechanical analysis (DMA)

The dynamic mechanical analysis (DMA) technique works by application of a sinusoidal deformation to a specimen whose dimensions are known through subjecting it to a controlled

stress or strain. The deformation is related to stiffness hence, DMA can measure the mechanical strength of a material. The sinusoidal strain wave is generated by a force motor which is then transmitted to the sample through a drive shaft. **Fig. 3.9** shows a schematic layout of DMA instrument [25]. A temperature dependent behaviour of the sample is studied by observing the variation in the force and phase angle at stable oscillation amplitude. The storage modulus and tan δ, which signifies the ratio of the loss modulus to the storage modulus data are thus obtained [26].

For this study, the mechanical assay was executed using a DMA 8000 dynamic mechanical analyser (Perkin Elmer), operated at the frequency of 1 Hz and amplitude of oscillation 0.05 mm. The temperature ranged from 0 to 150 °C, with a heating rate of 2 °C/min.

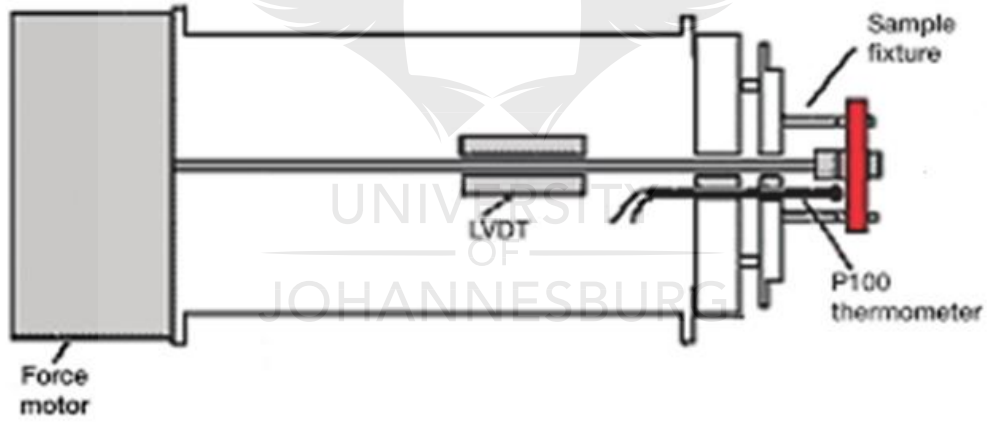

Fig. 3.9: Schematic layout of DMA [25]

3.11 Determination of pH at point-of-zero charge

This is the measurement of the surface charge of material in colloidal form. It uses the influence of an electric field on charged particles so that they possess electrophoretic, electroosmotic, streaming and sedimentation potential [27]. **Fig. 3.10** [28] shows a schematic exposition on point-of-zero charge (pH_{pzc}) measurement principle:

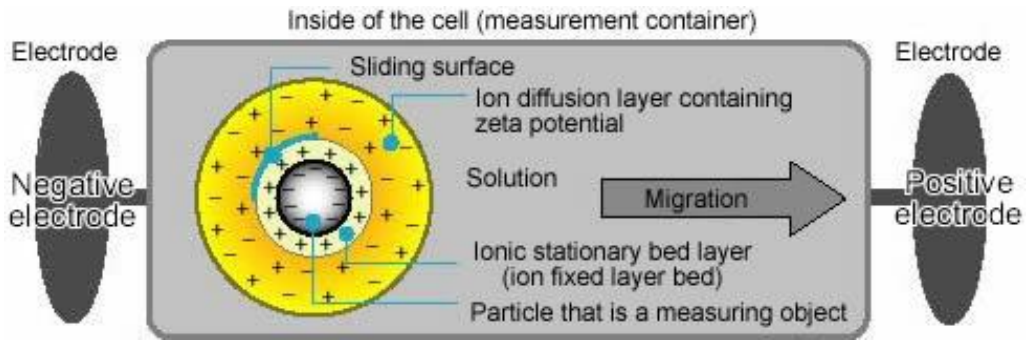

Fig. 3.10: A schematic explanation of point-of-zero charge measurement [28].

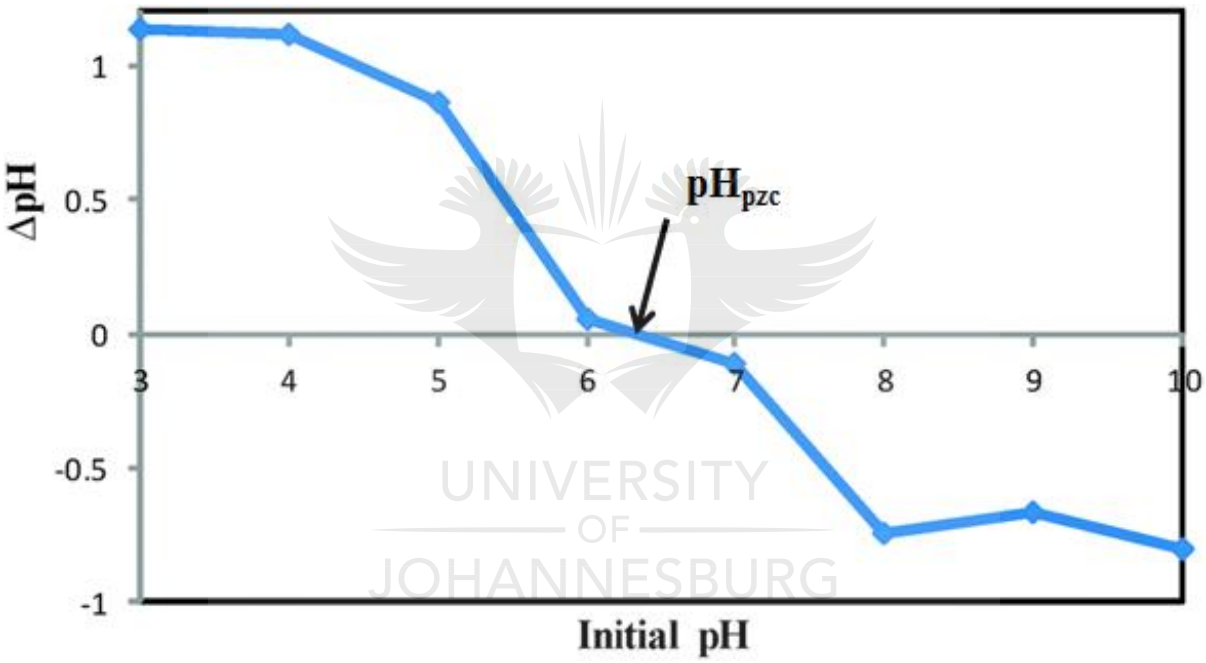

Fig. 3.11: Determination of pH at point-of-zero charge plot [29]

A relatively simple method to determine pH_{pzc} involves finding the change in pH on a pollutant solution before adsorbent and after addition of adsorbent material for a period of 12 h contact time. The difference in pH, is given by **Equation (3.5)**:

$$\Delta pH = pH_{final} - pH_{initial} \quad (3.5)$$

The value of ΔpH will be positive or negative, depending on the net surface charge of the adsorbent. A positive value means the adsorbent surface is positively charged and a negative value means it is negatively charged at that pH. A plot of initial *pH* versus change in ΔpH will produce a curve and the pH_{pzc} is the pH at which the curve crosses the initial *pH* axis line as shown in **Fig. 3.11** [29].

The pH at point-of-zero charge was determined using a change in pH method with a Thermo Scientific pH meter in this study.

3.12 Determination of the concentrations of fluoride and chromium in solutions

The analytical techniques employed for the determination of the concentration fluoride and chromium are described below:

3.12.1 Fluoride ion selective electrode

A fluoride ion selective electrode selectively responses to the concentration of fluoride ions in solution. A diagram of this instrument is shown in **Fig. 3.12** [30]. It consists of built in reference electrode and a sensitive membrane bonded to an epoxy material. During measurement, a potential will develop across the membrane and the analyte solution. This potential is proportional to the activity of fluoride ions in solution which is governed by the Nernst equation, **Equation (3.6)**:

UNIVERSITY OF JOHANNESBURG

$$E = E_0 + S * logA \quad (3.6)$$

Where *E* is the potential measured, E_o, *A* and *S* are the constant reference potential, activity of fluoride ions and the slope of the calibration curve (usually 0.05916), respectively [31]. The activity of fluoride, *A* is given by **Equation (3.7)**:

$$A = Y_i * C_f \quad (3.7)$$

where Y_i is the activity coefficient and C_f is the concentration of the fluoride ions. To produce a constant ionic strength in solution, a total strength adjustor buffer (TISAB) is added; this reduces the interference of aluminium and iron in the measurement and decomplexes fluoride

ions. For the Thermo Scientific Orion fluoride ion selective electrode, the TISAB is prepared by dissolving 58 g of NaCl and 57 mL of 99.99% glacial acetic acid in 500 mL of deionised water, adjusting the pH to 5.5 using 5 M NaOH followed by addition of deionised water to 1 L [30]. This was used for this study and the calibration of the fluoride electrode was performed using 10, 1 and 0.1 mg/L fluoride solutions which were mixed with equal volumes of TISAB before measurement.

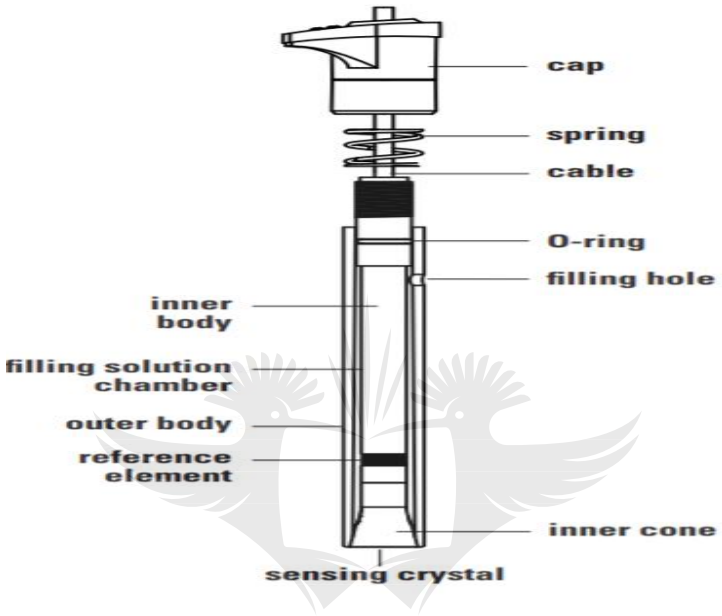

Fig. 3.12: Basic structure of a fluoride ion selective electrode [30].

UNIVERSITY OF JOHANNESBURG

3.12.2 UV-vis spectrophotometer

The UV-vis spectrophotometry is used in the quantitative and qualitative analysis of organic and inorganic compounds in water. The principle behind this technique is that when matter interacts with light, there is an increase in energy of its atoms and molecules. This light must be in the visible or ultraviolet region of the electromagnetic spectrum. The spectrophotometric behaviour of matter is underpinned by the Beer-Lambert' law in **Equation (3.8)**:

$$A = ebc \tag{3.8}$$

Where *A* is the absorbance, *e*, *c* and *b* are the molar absorptivity, concentration of an analyte in solution and cell length, respectively. A great number of molecules obey this law where their absorbance or reflectance depends on the colour of the solution. By measuring the absorbance of a solution against a blank, it is possible to determine the concentration of a substance using this law. The general layout of the UV-Vis spectrophotometer is shown in **Fig. 3.13** [32]. It consists of a light source, for example a tungsten filament which produces light in the UV-Vis region, a sample holder and a detector [33]. A sample is placed in a cuvette cell and its absorbance measured against a blank in another cuvette at a certain wavelength.

In this study the spectrophotometric determination of Cr(VI) ions was performed using the diphenylcarbazide method which involved the use 0.05, 0.25, 0.5, 0.1 and 1 mg/L Cr(VI) standard solutions and a blank. This involved complexing Cr(VI) ion sample solutions with diphenylcarbazide in acid to produce a red-violet coloured complex with an intensity proportional to the concentration of Cr(VI) ions [34]. The Cr(VI) concentrations in treated samples in this study were determined using a Lambda 750S UV-Visible spectrophotometer (Perkin Elmer, USA) at 540 nm wavelength.

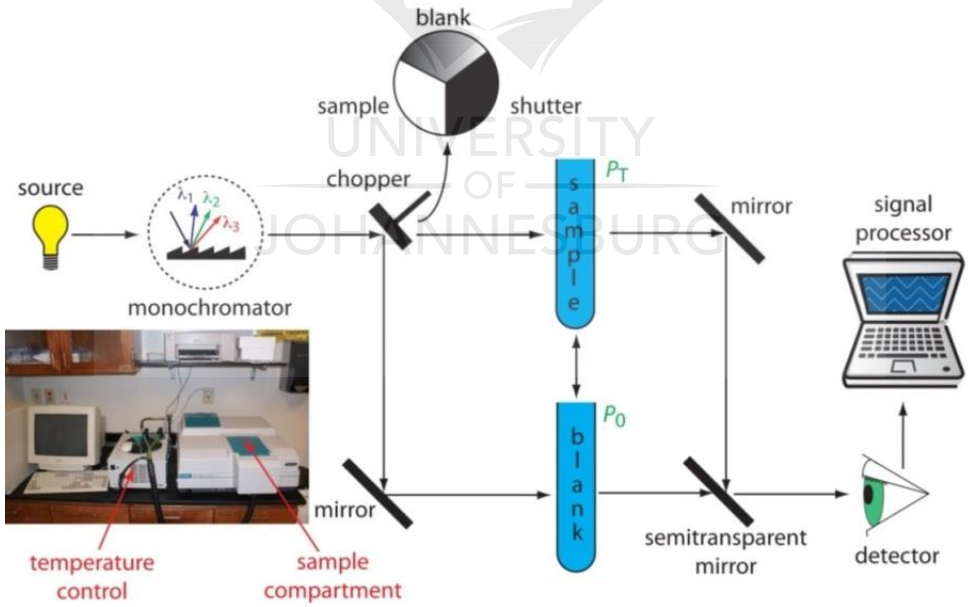

Fig. 3.13: Schematic diagram of UV-Vis spectrophotometer [32]

3.12.3 Ion chromatography-inductively coupled plasma mass spectrometry (IC-ICP-MAS)

IC-ICP-MS is one of the most powerful hyphenated instruments for the analysis of samples. It is suitable for the analysis of different forms of an element in water, food and pharmaceuticals through speciation and quantification [35]. The ion chromatography (IC) separates ions according to charge [36,37] and the then ICP-MS determines and detects ions in a separate form [38,39]. A schematic lay out of the IC-ICP-MS is shown in **Fig. 3.13** [38]. In IC, charged species in solution compete with the eluent ions (mobile phase) for sites on the stationary phase (ion-exchange resin) which are oppositely charged to that of the charged species. The mobile phase is delivered to the column by a pump. The sample is introduced either manually or through an auto-sampler into a fixed loop which makes sure that there is reproducibility of sample volume injected. The mobile phase transfers the sample from the loop into the separator column where the analyte ions of interest are retained on the stationary phase by replacing eluent ions. A guard column is often included to improve the lifespan of the separator column. The retention time for the ions in the column is affected by their affinity for the stationary phase. The retained ions are removed from the stationary phase by a suitable eluent and are typically detected by conductivity measurements. Cations can be eluted by using a strongly acidic solution such as HCl or HNO_3 while anions are eluted by employing a strong base such as NaOH, $NaHCO_3$ or Na_2CO_3 or a mixture of bases. A suppressor serves to lower the contribution of the eluent ions to the conductivity signal to improve the sensitivity of the method. The output from the detector is processed to obtain a chromatogram.

UNIVERSITY OF JOHANNESBURG

Inductively coupled plasma mass spectrometry **(**ICP-MS) consists of element gas module, an automated sampler system, gradient pump and ICP-MS detector where ions are subjected to high temperature decomposition, atomisation and detection. It involves the ionization of a sample with inductively coupled plasma at a very high temperature and the separation and quantification of the ions generated by mass spectrometry [38,39]. Typically, argon gas (Ar) is used for the plasma owing to its sufficiently high ionization potential and capability to ionize most elements, except fluorine (F), helium (He) and neon (Ne). The inductively coupled plasma is produced in the ICP source through a high frequency generator surrounding a quartz tube into which the Ar gas flows. The liquid form of the sample is introduced through a nebulizer into the plasma, there it is evaporated, vaporized, atomized and partly ionized into a mixture of excited atoms, ions and electrons. From the plasma, the sample goes into the mass spectrometer where the ions are accelerated into the mass analyser, by an applied electric or magnetic field and separated according to their mass to charge ratios (*m/z*). The ions then go

into the detector, usually a channel electron multiplier, where ions of varying *m/z* values are collected and the signal is then processed to obtain a mass spectrum.

The chromium speciation to determine the Cr(III) and Cr(VI) concentrations in sample solutions was conducted using ion chromatography with inductively coupled plasma-mass spectrometer (IC-ICP-MS) (Thermo Scientific, USA) for this study.

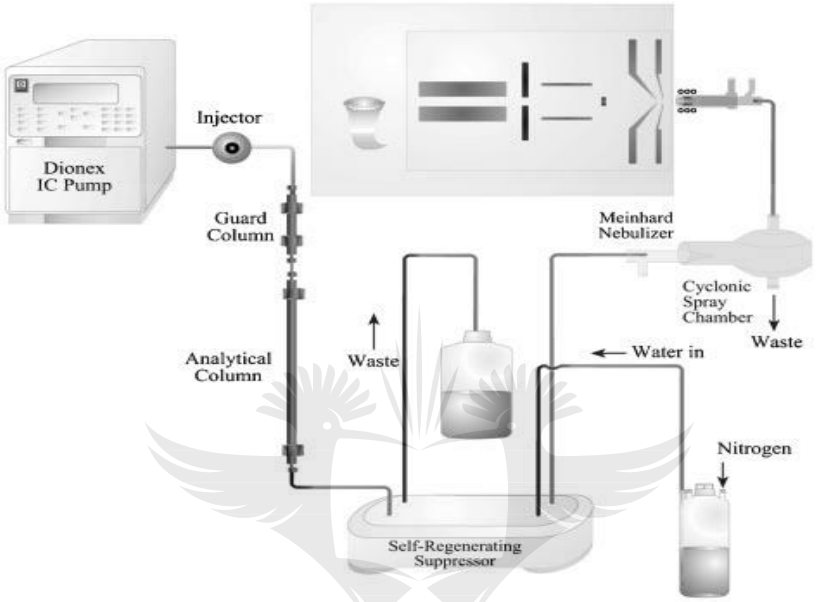

Fig. 3.14: Schematic diagram of IC-ICP-MS spectrometer [38]

UNIVERSITY OF JOHANNESBURG

3.13 References

[1] B. Stuart, Infrared spectroscopy: Fundamentals and applications, John Wiley 1–1.2.

[2] A.T. Aiswarya, FTIR, (date accessed May 28, 2018).

[3] W.M. Doyle, Principles and applications of Fourier transform infrared (FTIR) process analysis, Process Control and Qual. 2 (1992) 11–4.

[4] A. Chauhan, P. Chauhan, Powder XRD technique in science and technology, J Anal. Bioanal. Tech. 5 (2014) 1−5.

[5] Instrument X-ray Optics, School of Crystallography, Birkbeck College, University of London, Chapter 2 (2006), (date accessed May 28, 2018).

[6] U.P. Agarwal, S.A. Ralph, C. Baez, R.S. Reiner, S.P. Verrill, Effect of sample moisture content on XRD-estimated cellulose crystallinity index and crystallite size, Cellulose 24 (2017) 1971–1984.

[7] N. Verma, BET Surface area and pore volume analyzer, Research and development, Indian Institute of Technology, Kanpur, (2012).

[8] U. Kuila, M. Prasad, Specific surface area and pore size distribution in clays and shales, Geophys. Prospect. 61 (2013) 341–362.

[9] D.P. Lappham, J.L. Lapham, Gas adsorption on commercial magnesium stearate: effects of degassing on nitrogen BET surface area and isotherm characteristics, Int. J. Pharm. 530 (2017) 364–376.

[10] J. Österreicher, F. Grabner, A. Schilffl, S. Scharz, G.R. Bourret, Information depth in a backscattered electron microscopy of nanoparticles within a solid matrix material, Characterization Mater. Charact. 138 (2018) 145–153.

[11] H.A. Abudayyeh, Synthesis and Analysis of ZnO Nanowires, BSc. Thesis, Hebrew, University of Jerusalem, Israel, (2012) 63–64.

[12] K. Vos, N. Vandnberghe, J. Elsen, Surface textural analysis of quartz grains by scanning electron microscopy (SEM): From sample preparation to environmental interpretation, Earth-Sci. Rev. 128 (2014) 93–104.

[13] K. Park, D.B. Kittelson, P.H. McMurry, Structural properties of exhaust particle measured by transmission electron microscopy (TEM): Relationships to particle mass and mobility, Aerosol Sci. Technol. 38 (2004) 881–889.

[14] Transmission electron microscope (TEM), Principle of TEM, Department of Physics, The Chinese University of Hong Kong, (2018) (date accessed May 28, 2018).

[15] K.C. Kim, S.H. Park, M.Y. Na, H.J. Chang, W.T. Kim, D.H. Kim, Preparation of nanoporous GeO_x by de-alloying $Al_{60}Ge_{30}Mn_{10}$ amorphous alloy, Microscopy 64 (2015) i117–i117.

[16] S. Loganathan, R.B. Valapa, R.K. Mishra, G. Pugazhethi, S. Thomas, Thermogravimetric analysis of Nanomaterial, Micro and Nanotechnologies, Chapter 4, (2017) 67–108.

[17] M. Price, D.J. Hourston, F. Dumont, Thermogravimetry of Polymers, Encyclopedia of Analytical Chemistry, John Wiley and Sons Ltd, Chichester, (2000) 8094–8105.

[18] L.B. Fitaroni, J.A. deLima, S.A. Cruz, W.R. Waldman, Thermal stability of polypyrrole-montmorillonite clay nanocomposite: limitation of the thermogravimetric analysis, Polym. Degrad. Stab. 111 (2015) 102–108.

[19] M.H. Engelhard, T.C. Droubay, Y. Du, X-Ray Photoelectron Spectroscopy, Encyclopaedia of spectroscopy, 3rd edition, (2017) 716–724.

[20] M. Kreier, Photoemission spectroscopy, Commons (2014) 21–41.

[21] D. Briggs, J.T. Grant, Surface analysis of Auger and X-ray photoelectron spectroscopy, Im Publications, Chichester, UK, 2003.

[22] D. Sander, Advanced Magnetometry, Max Plank Institut for Microstrukturphysik, Halle, German, (2005) (date accessed July 7, 2018).

[23] N.H. Kera, B. Bhaumik, K. Kriveshini, S.S. Ray, A. Maity, Selective removal of toxic Cr(VI) from aqueous solution by adsorption combined with reduction at a magnetic nanocomposite surface, J. Colloid Interface Sci. 503 (2017) 214–228.

[24] M.I. Khali, Co-precipitation in aqueous solution of magnetite nanoparticles using iron(III) salts as precursors, Arab. J. Chem, 8 (2015)279–284.

[25] Dynamic Mechanical Analysis, A Beginner's Guide, Perkin Elmer, (2013) 1–10.

[26] B.C. Anderson, P.D. Bloom, K.G. Baikerikar, V.V. Sheares, S.K. Mallapragada, Al-Cu-Fe quasicrystal/ultra-high molecular weight polyethylene composites as biomaterials for acetabular cup prosthetics, Biomaterials 23 (2002) 1761–1768.

[27] A. Sze, D. Erickson, L. Ren, D. Li, Zeta potential measurement using Smoluchowski equation and slope of the current-time relationship in electroosmotic flow, J. Colloid Interface Sci. 261 (2003) 402–410.

[28] Microtec Co Ltd, What is zeta potential, (date accessed February 13, 2018).

[29] M. Ahmadi, T. Madrakian, A. Afkhami. Solid phase extraction of doxorubicin using molecularly imprinted polymer coated magnetite nanospheres prior to its spectrofluorometric determination, New J. of Chem. 39 (2015) 163–171.

[30] Thermoscientific, Thermo Scientific Orion, Fluoride ion selective electrode Revision B (2016) 1–2.

[31] S. Levin, S. Krishnan, S. Rajkumar, N. Halery, P. Balkunde, Monitoring fluoride in water using a smartphone, Sci. Total Environ. 551–555 (2016) 101–107.

[32] D. Harvey, UV/vis and IR Spectroscopy, Chemistry, LibreTexts, Chapter 10.3 (2017) (date accessed February 13, 2018).

[33] G. Duffy, I. Maguire, B. Heery, P. Gers, J. Ducrée, F. Regan, ChromiSense: A colourimetric lab-on-a-disc sensor for chromium speciation in water, Talanta 178 (2018) 392–399.

[34] K.A. Stancheva, B.I. Bognadav, D.P. Geogiev, Y.H. Hristov, I.G. Markovstaka, Spectrophotometric determination of hexavalent content of cement-an assessment of the optimal conditions for the analysis of Cr(VI), Eurasian J. Anal. Chem. 8 (2013) 10–16.

[35] K.M. Kubachka, N.V. Shockey, T.A. Hanley, S.D. Conklin, D.T. Heitkemper, Arsenic in rice and rice products using high performance liquid chromatography-inductively coupled plasma mass spectrometry determination, (2017) version 1.1.

[36] H. Günzler, A. Williams, eds., Handbook of Analytical Techniques, WILEY-VCH Verlag GmbH, Weinheim, (2001).

[37] F.A. Settle, Handbook of Instrumental Techniques for Analytical Chemistry, Prentice Hall PTR, Upper Saddle River, New Jersey, (1997).

UNIVERSITY OF JOHANNESBURG

[38] H. Gürleyük, D. Wallschläger, Determination of Cr(III) and Cr(VI) using supressed ion chromatography inductively coupled plasma mass spectrum, J. Anal. At. Spectrom. 16 (2001) 926–930.

[39] Chromedia Analytical Sciences, Inductively Coupled Plasma (ICP)–MS, http://www.chromedia.org/chromediawaxtrappthcseDsHiemBpdmBlIEcCE&subNavrggpgpDsHiemBpdmBlIEcCEZ (date accessed May 23, 2018).

UNIVERSITY OF JOHANNESBURG

CHAPTER FOUR

RAPID HIGH ADSORPTION PERFORMANCE OF HYDROUS CERIUM-MAGNESIUM OXIDES FOR REMOVAL OF FLUORIDE FROM WATER

4.1 Introduction

The literature survey discussion in chapter 2 highlighted critical issues on nano-metal oxides and their composites for the removal of naturally and anthropogenically abundant fluoride [1-8]. The detrimental effects of fluoride ions (F^-) have culminated in the setting of strict limits [3-8]. A variety of methods for defluoridation have been highlighted in the literature survey, including adsorption which employs a variety of adsorbents which have inherent draw backs, of which this study tried to address [9-16]. Nanosized-metal oxides have been reported to be significantly encouraging as future materials in water contaminants remediation. Their success [8,10,11,16,17] encouraged us to explore the synthesis and application of more novel nanostructured bimetal metal oxides. The nano-sized metal oxides reported in the literature for defluoridation include Fe, Mn, Al, Ti, Ca, Mg and Zr oxides and rare earth metal oxides like CeO_2. The latter have high sorption capacities for F^- ions removal [18,20,21]. However, their optimum adsorption pH range is more acidic and this, is likely to induce their dissolution and are costly [22-24].

UNIVERSITY OF JOHANNESBURG

This chapter presents the details of the study on the doping of CeO_2 with MgO. CeO_2 has a high sorption capacity for F^- ions but it is expensive for use on its own as sole oxide adsorbent. It was hypothesized that its cost would be reduced by mixing it with cheaper MgO. A simple preparation method to combine a rare earth metal with cheaper nontoxic MgO which has equally been reported as a highly efficient adsorbent in defluoridation and afford a wide pH application range was thus envisaged [18,22-28].

This study thus reports the synthesis of a series of Ce-Mg bimetal oxides by a simple co-precipitation method and their application in F^- remediation. The optimised adsorbent was characterized using various physico-chemical techniques. The effect of adsorbent dose, contact time, solution pH, initial concentration, temperature and competing ions on the adsorption was

The work presented here has been published in the Journal of Molecular Liquids, 265 (2018) 496-509. https://doi.org/10.1016/j.molliq.2018.06.015

studied. The kinetics and thermodynamics of the adsorption process were also investigated. Regeneration studies as well as real groundwater samples tests were performed using the synthesized ideal adsorbent.

4.2 Materials and methods

4.2.1 Synthesis of hydrous cerium-magnesium oxides composite

A facile co-precipitation method was employed for the synthesis of hydrous Ce-Mg bimetal oxides (HCeMgO). In a typical synthetic procedure, 0.04 moles of $Ce(NO_3)_3 \cdot 6H_2O$ and 0.04 moles of $Mg(NO_3)_3 \cdot 6H_2O$ (analytical grade, Sigma-Aldrich, USA) were dissolved in 400 mL of deionized water. Then, 64 mL of 2M NaOH (analytical grade, Sigma-Aldrich, USA) aqueous solution was added dropwise under magnetic stirring to adjust the pH to 10 at ambient temperature. The resulting precipitate was vigorously stirred for 1 h, aged for 24 h, centrifuged, washed three times with deionised water, dried for an additional 24 h in an oven set at 100 °C, and finally ground into a fine powder to afford HCeMgO1:1. Likewise, stirred mixtures of $Ce(NO_3)_3 \cdot 6H_2O$ and $Mg(NO_3)_3 \cdot 6H_2O$ with Ce:Mg molar ratios of 2:1, 1:2 and 1:3 with 80, 56, 40 mL of 2M NaOH were treated separately as described above to achieve HCeMgO 2:1, HCeMgO 1:2, and HCeMgO 1:3, respectively. To determine the composite with the optimum ratio, these adsorbents as well as pure hydrous cerium oxide ($HCeO_2$) and hydrous magnesium oxide (HMgO) were examined in the adsorption of 10 mg/L of F^- ions solution at pH = 5.5 and adsorbent dose of 0.03 g in 50 mL. The experimental results suggested that HCeMgO1:1 composite, obtained with less cerium salt, was the optimum adsorbent.

UNIVERSITY OF JOHANNESBURG

4.2.2 Characterization of HCeMgO1:1

The HCeMgO1:1 composite was characterized by several techniques. The FTIR spectra of the optimised HCeMgO1:1 composite and F^- ions loaded binary metal oxide (HCeMgO1:1+F) were obtained using a Perkin Elmer Spectrum 100 Spectrometer (Perkin Elmer, USA) in the range of 500-4000 cm^{-1} with 4 cm^{-1} resolution and 32 scans. The surface morphology and microstructure of HCeMgO1:1 composite were studied by FE-SEM and HR-TEM using Zeiss Auriga Cobra FIB microscope and a high resolution transmission electron microscope (JEOL–JEM 2100, Japan) with LaB6 filament operated at 200 kV, respectively. TGA and DTA experiments were performed in air at a flow rate of 50 mL/min and a heating rate of 10 °C/min

on TG Q500 (TA Instruments, USA). A Micrometrics ASAP 2020 gas adsorption apparatus (Micrometics, USA) using low temperature (-198.50 °C) N_2 adsorption-desorption technique was used for BET surface area measurements. A PANalytical X'Pert PRO-diffractometer (PANalytical, The Netherlands) using CuKα radiation with a wavelength of 1.5505 Å with slits at 45 kV/30 mA and 2θ values ranging from 5 to 90 was used for the XRD characterization of the adsorbent. XPS studies were carried out on Kratos Axis Ultra device with Al monochromatic X-ray source (1486.6 eV) to establish the elemental composition of HCeMgO1:1 before and after F^- adsorption. The point-of-zero charge was determined using a change in pH method with a Thermo Scientific pH meter.

4.2.3 Batch adsorption experiments

A 1000 mg/L stock solution of F^- ions was prepared by dissolving 0.221 g of oven dried NaF (analytical grade, Sigma-Aldrich, USA) in 100 mL of deionised water. Solutions of NaF required for the F^- ions adsorption experiments were prepared by appropriate dilutions from the 1000 mg/L stock solution. Adsorption studies were conducted in batch mode using polypropylene plastic bottles containing 50 mL of 10 mg/L F^- solution which was contacted with 0.03 g adsorbent. The experiments were conducted in triplicate. The F^-/adsorbent suspensions were agitated in a temperature controlled water bath shaker at 200 rpm for 24 h at 25 °C. The effect of pH on F^- adsorption was studied by adjusting the pH (from 2-11) of F^- solution using 0.1M HCl (analytical grade, Sigma-Aldrich, USA) and 0.1M NaOH solutions. Real field water samples containing 5 mg/L F^- ions concentration were also tested for the removal of F^- ions.

Determination of F^- ions in the filtered samples was conducted using a fluoride ion-selective electrode (ThermoORION) in the form of conductance, as described elsewhere [22,25,32]. Calibration of this electrode was performed using 10.0, 1.0 and 0.1 mg/L of F^- ions solutions with Total Ionic Strength Adjustment Buffer (TISAB II) reagent. The buffer was made by dissolving 58 g of NaCl and 57 mL of 99.99% glacial acetic acid in 500 mL of deionised water, adjusting the pH to 5.5 using 5 M NaOH followed by addition of deionised water to 1 L. The adsorption efficiency for F^- ions removal was calculated using **Equation (4.1)**:

$$\%\, removal = \left(\frac{C_o - C_e}{Co}\right) \times 100 \qquad (4.1)$$

where C_o and C_e are the initial and equilibrium F^- ions concentrations, respectively.

For the adsorbent dosage study effect, the amounts of optimised HCeMgO1:1 adsorbent were varied from 0.05 to 0.1 g with the same procedure followed as for the pH effect investigation. The experiment were conducted in triplicate. The adsorption capacity of the adsorbent at equilibrium was determined from **Equation (4.2)**:

$$q_e = \left(\frac{C_o - C_e}{m}\right) V \quad (4.2)$$

where q_e (mg/g) is the amount of F^- ions at equilibrium per unit mass of adsorbent. C_o, C_e, m and V are the initial F^- ions concentration, equilibrium F^- ions concentration, adsorbent mass and volume of the sample in L, respectively.

The adsorption performance was further studied by investigating adsorption isotherms at 15, 25, 35 and 45 °C using a Sep. Sci MRC Refrigerated Shaker Bath, South Africa and varying the initial F^- ions concentration from 5-100 mg/L. The data obtained from the adsorption isotherm studies were used to calculate the thermodynamic parameters of the adsorption process such as Gibbs free energy ($\Delta G°$), enthalpy ($\Delta H°$) and entropy ($\Delta S°$) change. The kinetics of adsorption was also studied to predict the adsorption rate and modelling of adsorption based water treatment. These were conducted at concentrations of 10, 15, 25 and 40 mg/L for 0 to 160 minutes shaking time at optimised pH 5.5 and adsorbent dose 0.03 g in 50 mL. The samples were filtered and analysed for residual F^- ions after treatment. The adsorption capacity of the adsorbent (q_t) at time t was obtained using **Equation (4.3)**:

$$q_t = \left(\frac{C_o - C_t}{m}\right) V \quad (4.3)$$

where q_t (mg/g) is the amount of F^- adsorbed per unit mass of the adsorbent at time t and C_t (mg/L) is the concentration of the F^- ions at time t.

UNIVERSITY OF JOHANNESBURG

4.2.3.1 Effect of competing ions

The possible interference presented by competing ions is a fundamental study because no single ion is found in isolation in natural water bodies. A mixture of ions such as Cl^-, SO_4^{2-}, NO_3^-, HCO^-_3 and PO_4^{3-} are usually encountered in polluted water. This study was achieved by dissolving the precursor salts of the above-mentioned ions together with F^- ions at 10, 20 and 40 mg/L concentrations in deionised water. The resultant solutions were each treated with the optimised adsorbent dose at the optimised pH for 24 h, followed by analysis of the residual F^- ions.

4.2.3.2 Desorption and regeneration studies

Successive adsorption and desorption studies were conducted to establish the reusability of the spent adsorbent. This was conducted by keeping 50 mL of 10 mg/L F^- ions-containing solution in contact with 0.03 g dose of adsorbent at pH 5.5. The F^- ions loaded adsorbent was then treated with 0.05, 0.025, 0.05 and 0.1M NaOH solutions. It was found that 0.1M NaOH produced the highest desorption ability. Hence, the latter NaOH concentration was used for four adsorption-desorption consecutive cycles.

4.3 Results and discussion

UNIVERSITY OF JOHANNESBURG

4.3.1 Adsorbent optimisation

To achieve the best performing composition of HCeMgO for F^- ions removal, adsorbent optimisation experiments were conducted. **Fig. 4.1** shows that the Ce-Mg ratio had a significant influence on adsorption efficiency. The highest sorption efficiency (76.8%) for the bimetal oxide obtained with less rare metal, was achieved at Ce/Mg salt molar ratio of 1:1, denoted as HCeMgO1:1. This ideal nanocomposite was adopted for all studies as it was expected to produce high adsorption. Moreover, F^- ions adsorption removal efficiency of the binary HCeMgO1:1 differs from that of $HCeO_2$ (96.8%) by a small margin. Thus cost effectiveness could be achieved with HCeMgO1:1 for all adsorption studies.

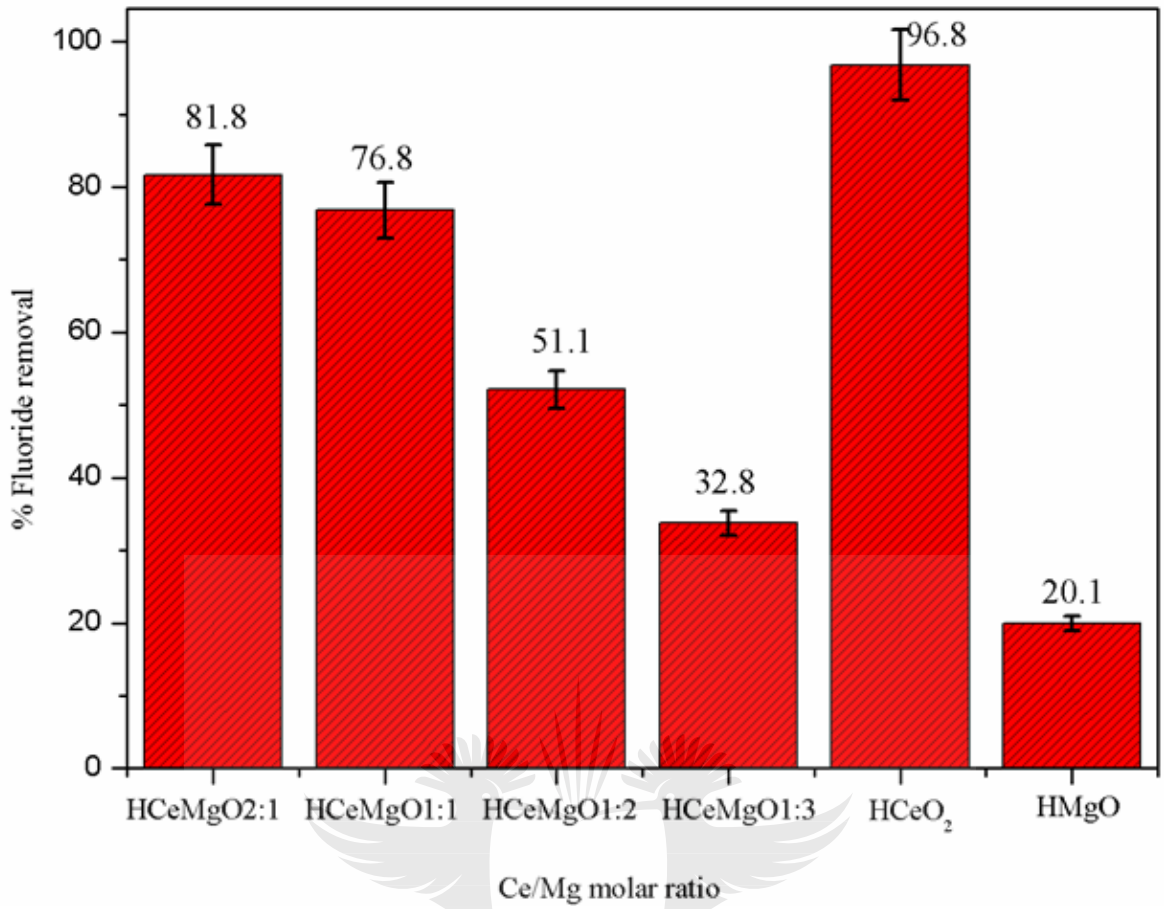

Fig.4.1: Comparison of percentage adsorption of F^- ions on hybrid adsorbent prepared at different Ce/Mg molar ratio. Sorption conditions: 0.03 g of adsorbent in 50 mL of 10 mg/L F^- ions solution at pH 5.5 and 25 °C for 24 h.

UNIVERSITY OF JOHANNESBURG

4.3.2 Physico-chemical characterization

4.3.2.1 FTIR spectral analysis

Fig. 4.2(A) shows the FTIR spectra of HCeMgO1:1 (a) before and (b) after F^- ions adsorption. Observed bands at 657, 1358, 1635 and 3369 cm^{-1} are signature bands of hydrous metal oxides present in HCeMgO1:1 [18,22]. The bands at 3369 and 1635 cm^{-1} are assigned to the stretching vibration of adsorbed water and bending vibration of hydroxyl groups, respectively [23]. The bands at 1512, 1412 and 1358 cm^{-1} correspond to the lattice vibration of Ce-Mg mixed metals, while the band at 657 cm^{-1} is attributed to metal-oxygen stretching [13]. After adsorption, bands at 3369 and 1635 cm^{-1} shifted to 3410 cm^{-1} and 1643 cm^{-1}, owing to the combined interaction of Ce-F and Mg-F bonds formation [21–23]. The disappearance of the band at 1358

cm^{-1} after adsorption as well as the formation of a new band at 1309 cm^{-1} affirms replacement of HCeMgO1:1 surface hydroxyl groups after F^- ions adsorption process [2,28].

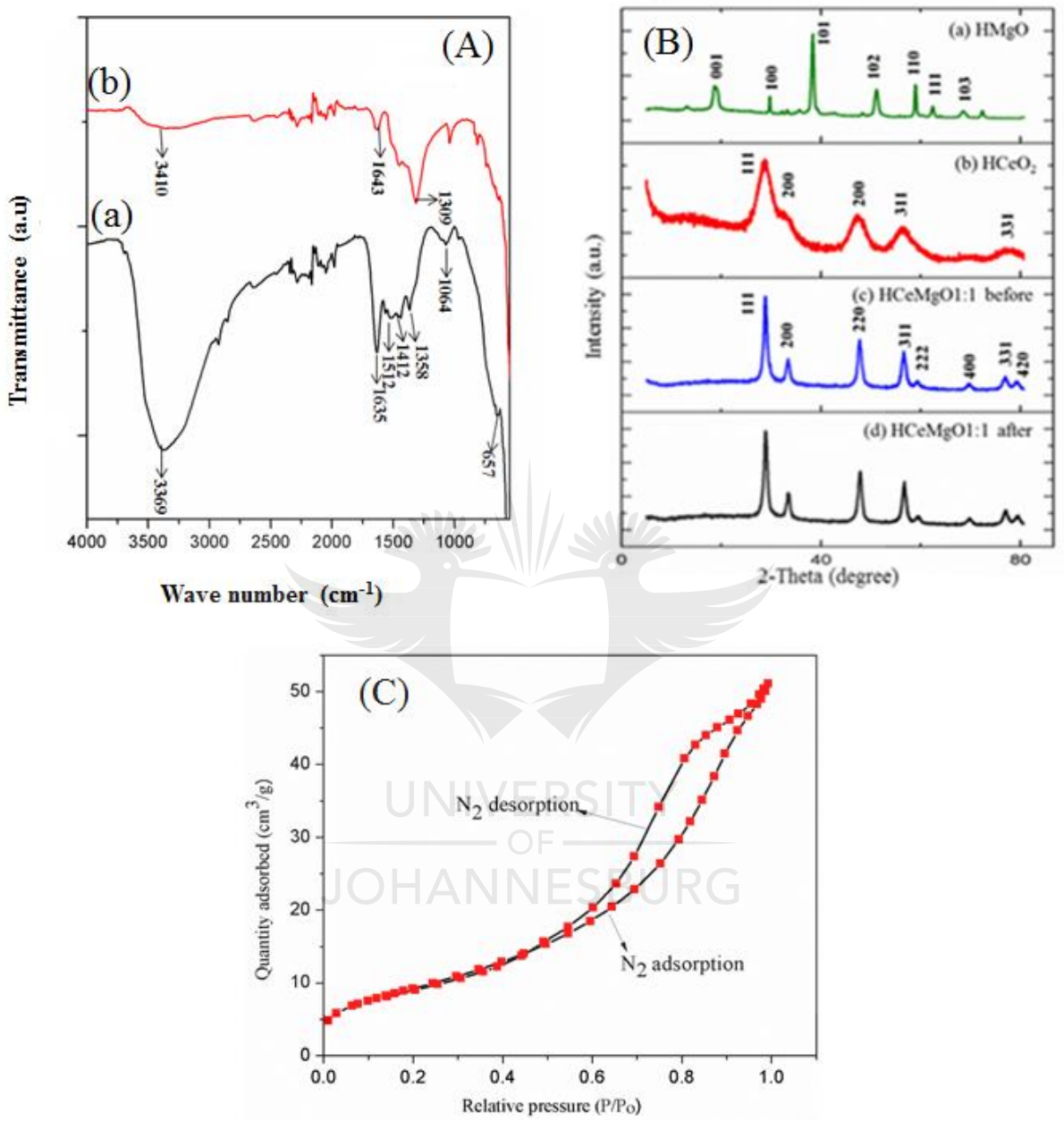

Fig. 4.2: FTIR spectra of (A) HCeMgO1:1 adsorbent before (a) and after (b) sorption (B) XRD patterns of (a) HMgO (b) $HCeO_2$ (c) and (d) HCeMgO1:1 before and after F^- ions adsorption (C) N_2 adsorption-desorption isotherms of HCeMgO1:1.

4.3.2.2 XRD analysis

XRD patterns of (a) HMgO (b) $HCeO_2$, (c) and (d) HCeMgO1:1 before and after F^- ions adsorption are shown in **Fig. 4.2(B)**. The diffraction peaks at 28.7, 33.1, 47.6 and 56.6° are characteristic of CeO_2 [20, 23, 24] and those at 20, 38, 50, 62.5 and 70° are typical peaks for HMgO [26–31]. The diffraction peaks of HCeMgO1:1 show a slight shift of patterns to wide angles (28.70, 33.70, 47.94, 56.78 and 76.89°), and high intensity relative to those of pristine $HCeO_2$, indicating the incorporation of Mg^{2+} in the lattice structure of CeO_2 [23,24]. The HMgO peaks are hardly detected in the HCeMgO1:1 XRD pattern, probably as a result of the contraction of the MgO unit cell after entering the CeO_2 structure to form a Ce-Mg solid solution and this can be attributed to the smaller ionic radius of Mg^{2+} (0.072 nm) relative to that of Ce^{4+} (0.097 nm) [20,23,28]. An amorphous phase of MgO may also have resulted in the HCeMgO1:1 adsorbent [23]. This analysis indicates that both HMgO and $HCeO_2$ are incorporated in the new structure. On the other hand, the XRD patterns of HCeMgO1:1 before [**Fig 4.2(B)(c)**] and after [**Fig. 4.2(B)(d)**] adsorption did not display significant change.

4.3.2.3 BET surface area analysis

The specific surface area plays a crucial role for the evaluation of the textural properties of an adsorbent. **Fig. 4.2(C)** shows the N_2 adsorption-desorption isotherm of HCeMgO1:1. The BET surface area of the adsorbent was 34.07 m^2/g, a value slightly higher than that of pristine HMgO (33.7 m^2/g). The N_2 adsorption-desorption isotherm of HCeMgO1:1 is type IV with a H2 hysteresis loop, according to IUPAC classification [22]. The average pore diameter, estimated around 8.42 nm is larger than that of F^- ions (0.133 nm), indicating that the latter are able to enter easily into the optimised adsorbent pores.

4.3.2.4 TEM and SEM

The FE-SEM and HR-TEM images are shown in **Figs. 4.3(A)** and **(B)**. The FE-SEM image in **Fig. 4.3(A)** shows large clusters of semi-spherical nanoparticles. The HR-TEM images in **Figs. 4.3(B)** and **(C)**, on the other hand, disclose agglomerated nanoparticles with 0.311 nm spacing of the crystallography plane, value close to 0.32 nm for (111) facet of CeO_2 [24], but significantly smaller. This is probably due to displacement of large Ce^{4+} by small Mg^{2+} in the CeO_2 lattice structure and formation of solid solution. A Ce-Mg solid solution structure

contributes to the formation of partly amorphous particles. These HR-TEM results are in good agreement with XRD analysis, where the Ce^{4+} dominated the crystal structure. The presence of crystals with relatively large size is due to the preparation method of hydrous oxides. Co-precipitation enhances the degree of aggregation, owing to the difference in solubility of $Mg(OH)_2$ and $Ce(OH)_4$. Ce^{4+} has higher reactivity and can also form stronger bond with hydroxide ions (K_{sp} = 2.0 x10^{-20}) than Mg^{2+} ion (K_{sp} = 5.6 x 10^{-12}). Consequently Mg^{2+} may form more aggregation during the reaction [22,23] and this may explain its low XRD peaks in the bimetal oxide spectra.

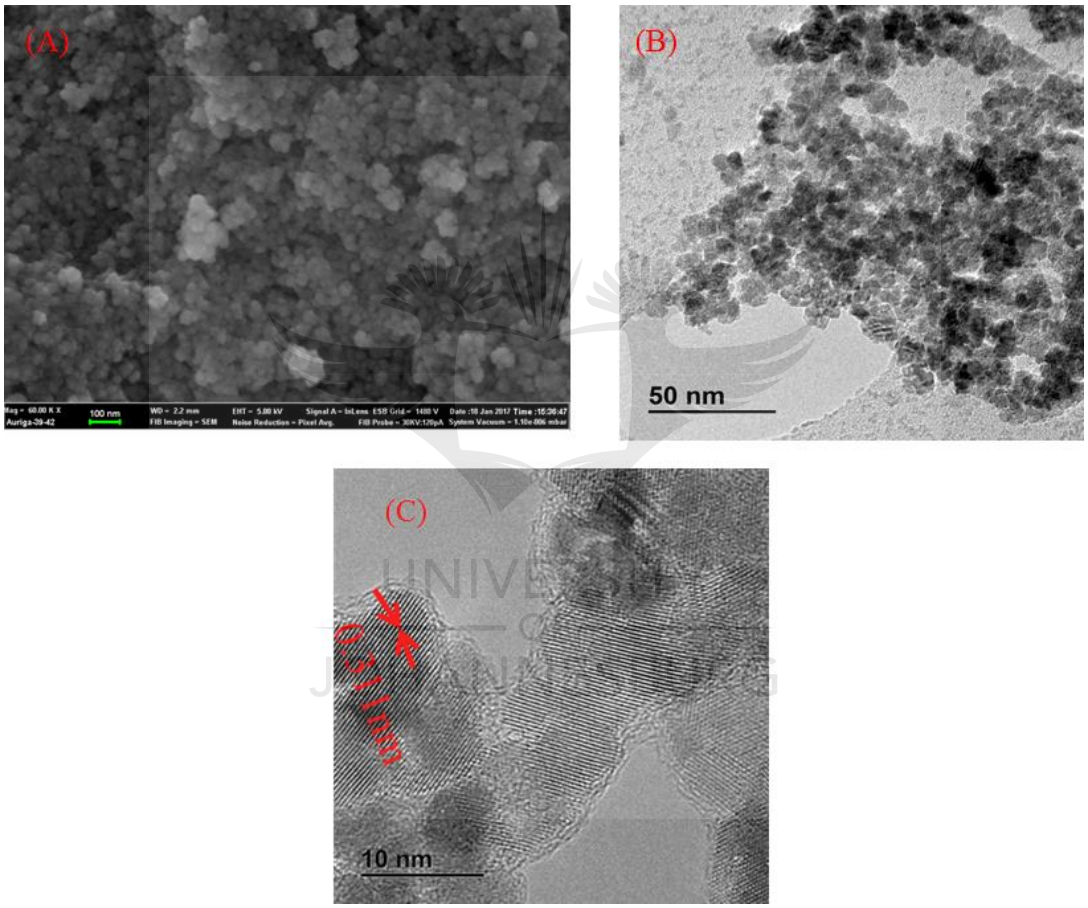

Fig. 4.3: (A) FE-SEM (B) TEM and (C) HR-TEM images of HCeMgO1:1 composite.

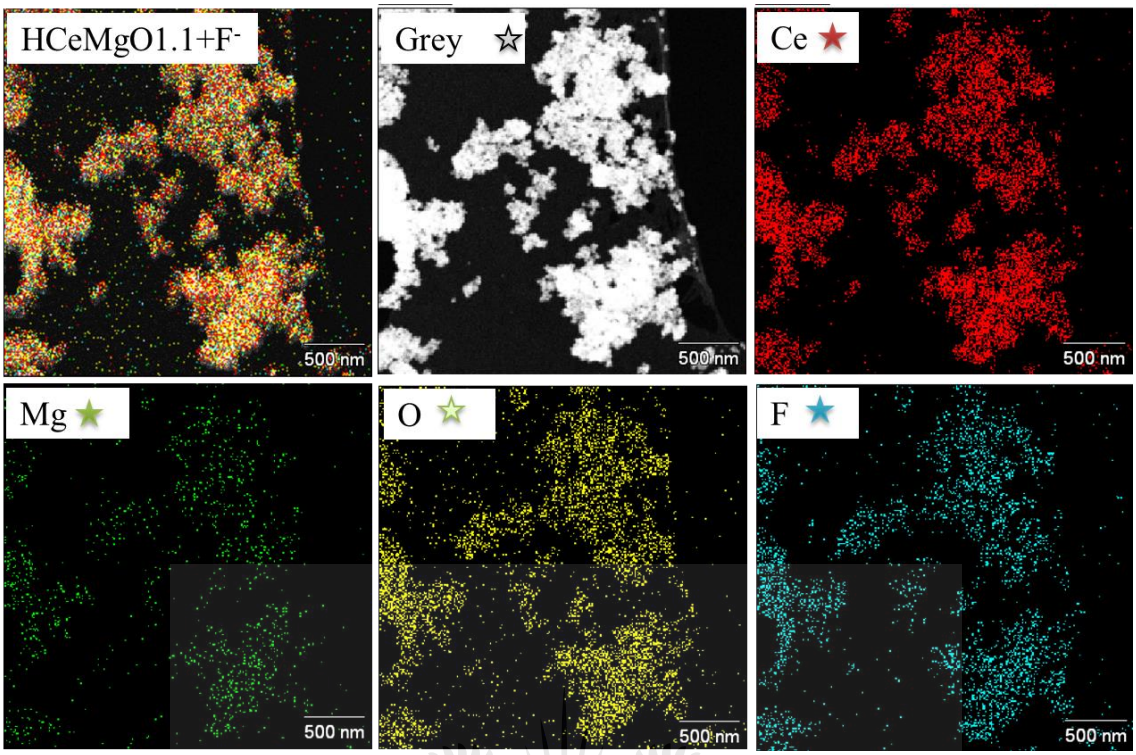

Fig. 4.4: STEM images of HCEMgO1:1 adsorbent after F^- ions adsorption and mapping of O, Ce, Mg and F.

4.3.2.5 Energy dispersive X-ray spectra

The EDS spectrum before adsorption in **Fig. 4.5(A)** clearly shows the presence of Ce, Mg and O elements within the structure of HCeMgO1:1 composite. **Fig. 4.4**, on the other hand, displays the HCeMgO1:1 STEM images elemental mapping of O, Ce, Mg, and F after adsorption and the corresponding EDS spectrum is presented in **Fig. 4.5(B).** It can be clearly observed from the mapping images that all the elements are well-distributed on the surface of the adsorbent. It is also evident that F^- ions were incorporated in the HCeMgO1:1 adsorbent, since a fluoride peak is detected in the EDS after adsorption. Furthermore, analysis of the atomic percentage of Ce and Mg revealed a ratio 1:1, which confirms the co-precipitation proportion of the precursor salts during synthesis of HCeMgO1:1. Interestingly, the F^- ions laden adsorbent reveals a reduced atomic ratio of O (69.98%) in **Fig. 4.5(B)**, relative to 97.71% before adsorption **(Fig. 4.5(A))**. This observation, in conjunction with FTIR analysis, reaffirms that oxygen atoms are replaced during the adsorption process. An anion exchange adsorption mechanism by replacement of surface OH groups with F^- ions is therefore supported.

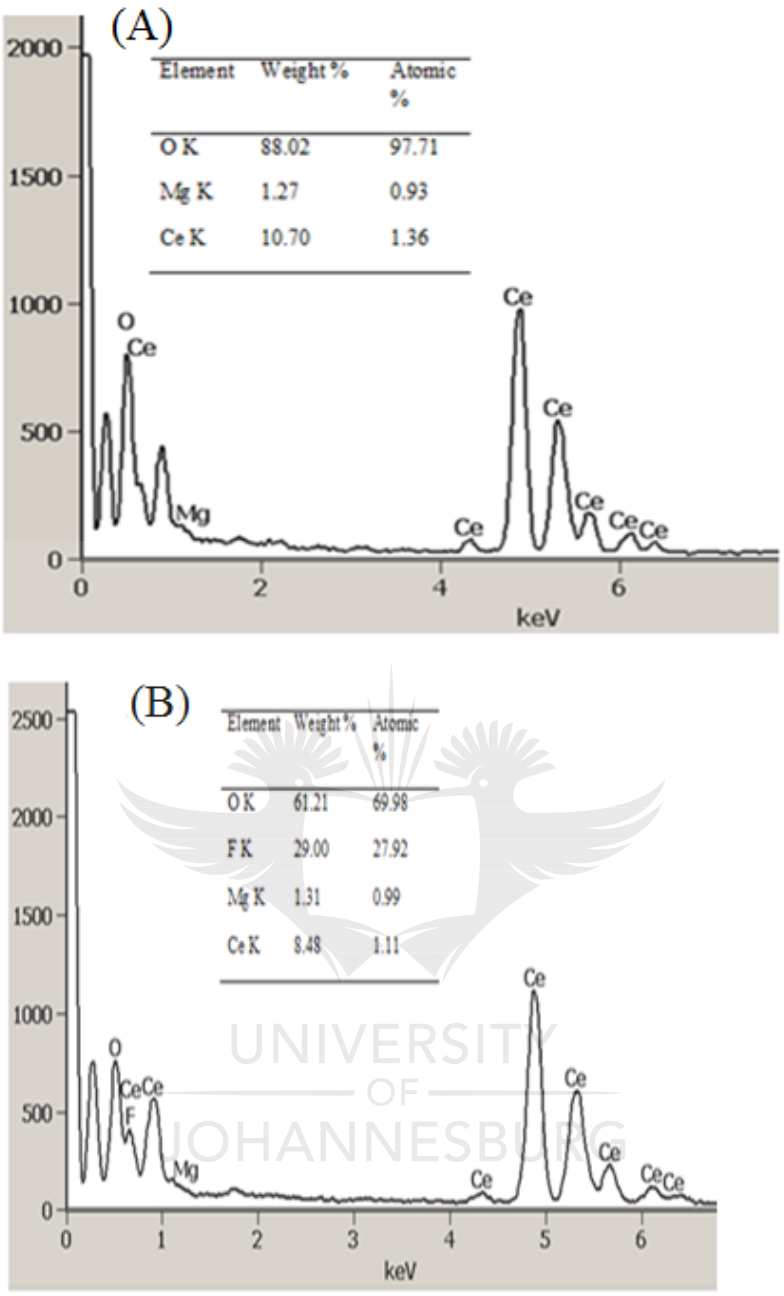

Fig. 4.5: EDS spectra of HCeMgO1:1 (A) before and (B) after F^- ions adsorption.

4.3.2.6 XPS analysis

The wide-scan XPS spectra of HCeMgO1:1 before and after adsorption were obtained to investigate changes in the elemental compositions of the adsorbent. **Fig. 4.6(A)** and **Table 4.1** show the XPS survey spectra and elementary composition of virgin and F^- ions loaded adsorbent. The spectrum on HCeMgO1:1 before adsorption contains energy bands for O 1s

(531 eV), Ce 3d (898.46-910 eV) and Mg 1s (1304.58 eV). The adsorption of F^- ions on HCeMgO1:1 was confirmed by the appearance of a new F 1s core level peak in the XPS wide scan spectra after adsorption, at 684.3 eV binding energy as exposed in **Fig. 4.6(B)** [10,24, 30].

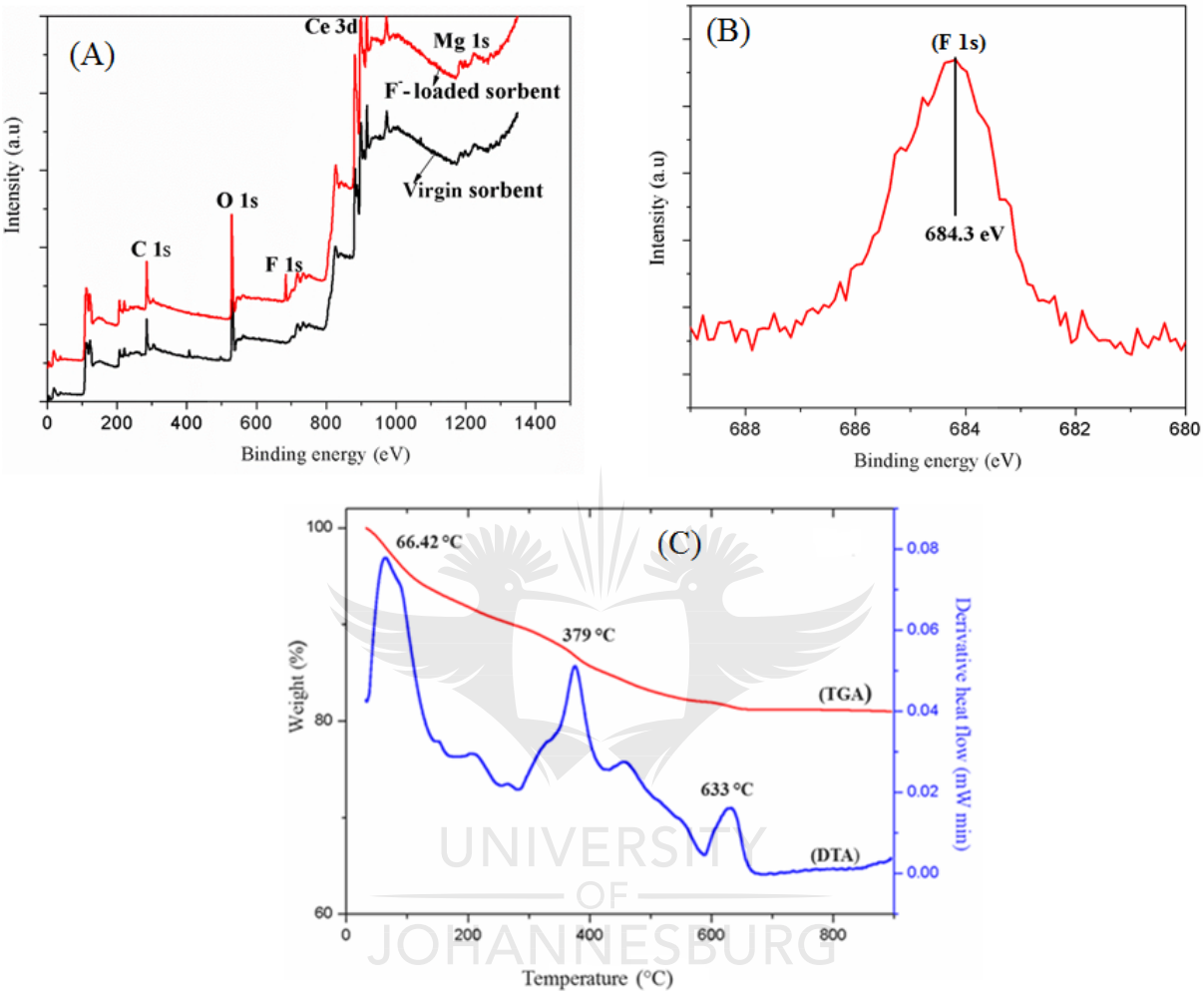

Fig. 4.6: (A) Wide-scan XPS spectra for HCeMgO1:1 before and after sorption (B) core-level XPS spectrum of F 1s (C) TGA and DTA plots for HCeMgO1:1 adsorbent.

Table 4.1: Summary of atomic ratio of HCeMgO1:1 before and after adsorption from XPS study.

Atomic ratio,%	Ce	Mg	O	F
Virgin sorbent	0.71	1.03	98.26	0
F^- loaded sorbent	0.56	0.87	88.61	9.96

UNIVERSITY OF JOHANNESBURG

4.3.2.7 Thermogravimetric-Differential thermal analysis

TG-DTA was performed to determine the thermal stability of the HCeMgO1:1 adsorbent **[Fig. 4.6(C)]**. The weight loss occurred in three stages with the initial of about 10.04% being the loss of surface water in the temperature range of 30-250 °C followed by the second weight loss (7.62%) associated with the exothermic effect around 379 °C in the DTA spectrum due to lattice water molecules [32]. Further reduction in weight (1.22%) at 633 °C is probably ascribed to phase transition from hydroxides to oxides [27]. This shows that HCeMgO1:1 is applicable for water treatment up to 250 °C.

4.3.2.8 Point of Zero charge

The point-of-zero charge is a parameter which characterizes the surface charge of an adsorbent, hence it was determined. The pH_{pzc} of HCeMgO1:1 was found to be 5.8 as shown in **Fig. 4.7(A)**. This information indicates that below pH 5.8, HCeMgO1:1 surface is positively charged and can therefore accommodate anions.

UNIVERSITY OF JOHANNESBURG

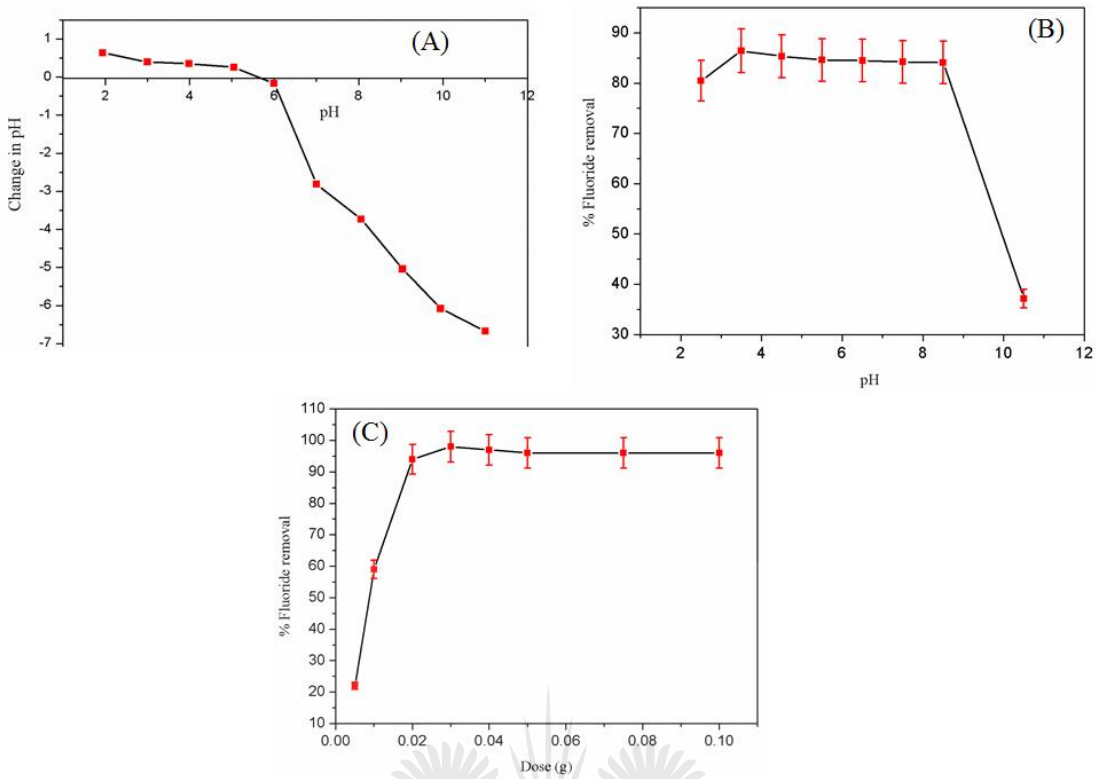

Fig. 4.7: (A) Determination of point-of-zero charge of HCeMgO1:1 (B) effect of pH using 10 mg/L F^- ions solution (adsorbent dose: 0.03 g/50 mL of F^- ions solution, contact time: 24 h and temperature: 25 °C) and (C) effect of adsorbent dose on adsorption of F^- ions on HCeMgO1:1 using 10 mg/L F^- ions solution at pH 5.5 and 25 °C.

UNIVERSITY OF JOHANNESBURG

4.3.3 Batch adsorption study

4.3.3.1 Effect of pH on the removal of F^- ions

Solution pH is a key parameter affecting the adsorption process. Its effect on F^- ions removal was studied from pH 2 to 10.5 using 0.03 g of adsorbent mass in 50 mL of 10 mg/L F^- ions solution. As shown in **Fig. 4.7(B)**, the sorption occurred over a range of pH 2-8.5 from which percentage removal was between 80 and 88%, with optimum pH found at 3.5. Afterwards, the percentage removal decreased to 38% as the pH increased. At pH above the pH_{pzc} the adsorbent surface is negatively charged and induces coulombic repulsion to F^- ions. Moreover, at relatively higher pH 9-11, the solution contains more hydroxyl ions than hydrogen ions, leading

to competitive adsorption between hydroxyl and F^- ions on the active sites. Hence, the decrease in absorption efficiency observed at relatively high pH [22,32-34].

4.3.3.2 Effect of adsorbent dose

The effect of HCeMgO1:1 dose on the removal of F^- ions at pH 5.5 was investigated. **Fig. 4.7(C)** shows that the percentage removal increased from 22% to 98% when the adsorbent dose increased from 0.005 to 0.03 g. This is due to an increase in available active adsorption sites for F^- ions uptake [31]. Thereafter no further increase in removal efficiency was observed as the adsorbent dose increased to 0.1 g. This could be attributed to the fact that at high dosage, active sites overlap, resulting in less available binding sites for adsorption [31]. Thus for the current study, 0.03 g dose was identified to serve as optimum adsorbent dosage for further experiments.

4.3.3.3 Adsorption isotherms

In order to design and operate an efficient adsorption system, the interactions between adsorbent and adsorbate need to be understood. This is often achieved by studying the adsorption isotherms. The temperature effect on the adsorption of F^- ions onto HCeMgO1:1 was therefore studied at 15, 25, 35 and 45 °C and **Figs. 4.8(A)**, **(B)** and **(C)** show the isotherm experiments results.

UNIVERSITY OF JOHANNESBURG

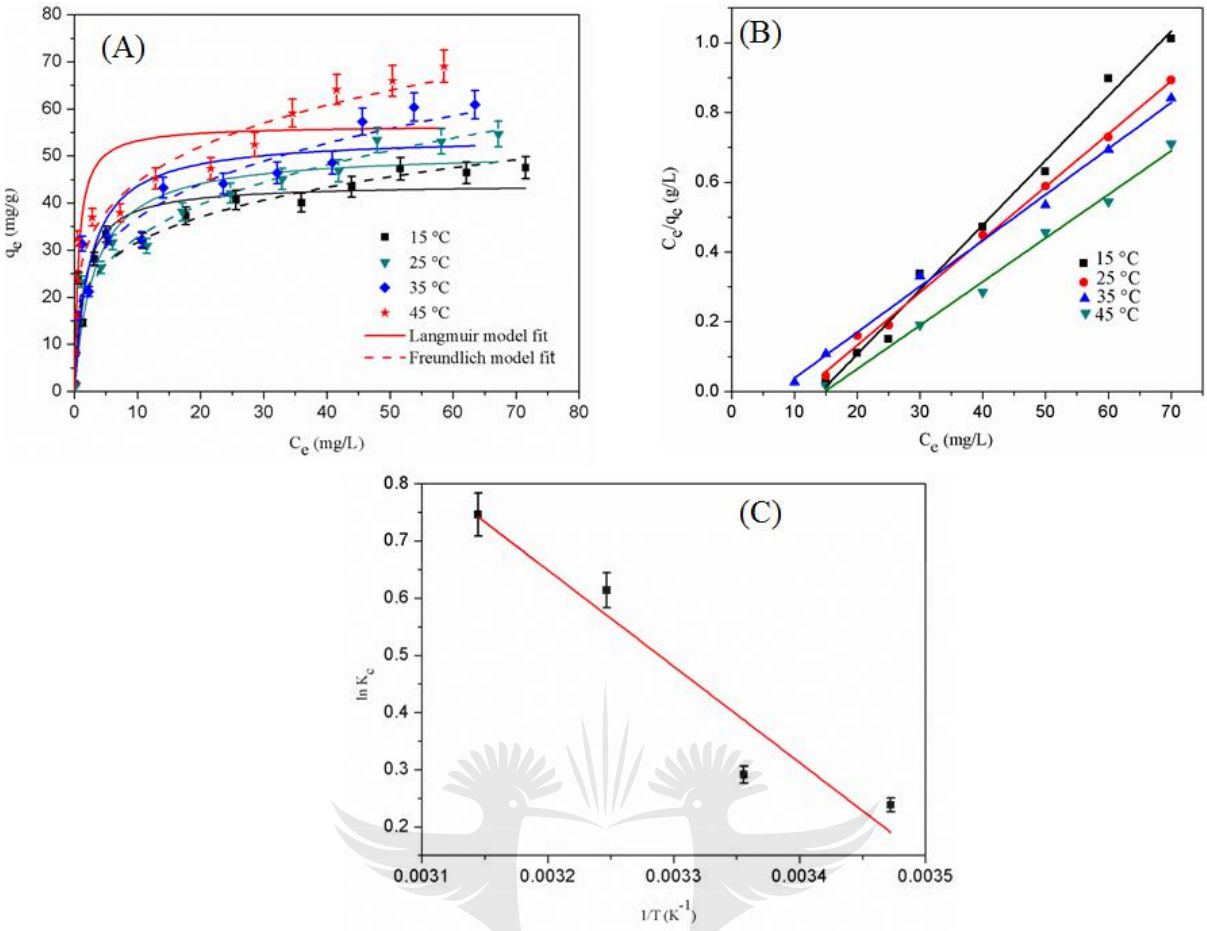

Fig. 4.8: (A) Adsorption equilibrium isotherms for F^- ions removal by HCeMgO1:1 and the data fit to nonlinear Langmuir and Freundlich isotherm models; (B) Fit of data to linearized Langmuir model (C) Van't Hoff's plot for the determination of thermodynamic parameters.

UNIVERSITY OF JOHANNESBURG

These results indicate that adsorption of F^- ions increases with an increase in temperature, suggesting an endothermic process. The increase in temperature results in an increase in the binding ability of F^- ions onto the adsorbent surface, thereby enhancing the extent of adsorption [31]. Two common analytical isotherm equations, namely, the Langmuir and the Freundlich isotherms were applied to model the data. The Langmuir model assumes monolayer coverage and the adsorbate can be equally adsorbed on all sorption sites. There is also no lateral interaction between ions [31,32]. The Langmuir linear and nonlinear forms are represented by **Equations (4.4)** and **(4.5)**, respectively:

$$\frac{C_e}{q_e} = \frac{1}{q_m b} + \frac{C_e}{q_m} \qquad (4.4)$$

$$q_e = \frac{bq_m\ C_e}{1+bC_e} \quad (4.5)$$

where C_e (mg/L) is the equilibrium concentration of F^- ions in solution. q_e and q_m (mg/g) are the amount of F^- ions adsorbed per unit mass of adsorbent at equilibrium and maximum adsorption capacity, respectively. b (L/mg) is the Langmuir constant related to the affinity of the binding sites for F^- ions [32]. Both the nonlinear and linear fits of Langmuir model are shown in **Figs. 4.8(A)** and **(B)** and the calculated isotherm parameters are summarized in **Table 4.2**. These include q_m and b at different temperatures for linear and nonlinear Langmuir fits. The increase in q_m with temperature confirms that the adsorption process was endothermic in nature and the general increase in Langmuir constant (b) with temperature indicates greater binding energies at higher temperatures. The dimensionless constant R_L is another important parameter of the Langmuir isotherm which reveals favourability or non-favourability of adsorption. This factor is expressed using **Equation (4.6)**:

$$R_L = \frac{1}{1+bCo} \quad (4.6)$$

where C_o (mg/L) is the initial F^- ions concentration. If R_L is such that $0 < R_L < 1$ the adsorption process is favourable. $R_L > 1$, on the other hand, indicates unfavourable adsorption. Linear adsorption is articulated when $R_L = 1$ and irreversible adsorption when $R_L = 0$. In the present adsorption process, R_L values were between 0 and 1 thus suggesting favourable adsorption [20,31].

UNIVERSITY OF JOHANNESBURG

The nonlinear [22] and linear [35] forms of Freundlich isotherm represented by **Equations (4.7)** and **(4.8),** were also evaluated for isotherm data:

$$q_e = K_f\ C_e^{\,1/n} \quad (4.7)$$

$$ln\ q_e = lnK_f + \frac{1}{n}\ lnC_e \quad (4.8)$$

where K_f (mg/g) and $1/n$ are the Freundlich constants related to adsorption capacity and intensity of adsorption, respectively [36]. Values of $1/n$ range from 0 to 1 and if close to zero denote more surface homogeneity. On the other hand, n values between 1 and 10 signify favourable adsorption [37]. K_f and 1/n values were determined and are summarized in Table

4.2. The values of *n* ranged between 0 and 10 for linear Freundlich isotherm, also indicate favourable adsorption.

Fig. 4.8(A) shows the nonlinear of equilibrium data for Freundlich model. When comparing the two adsorption isotherm models, the R^2 values for Langmuir (R^2_{linear} = 0.9909-0.9976) were higher than those for the Freundlich (R^2_{linear} = 0.9498-0.9727) for all temperatures. This specifies that F^- ions adsorption onto HCeMgO1:1 surface was homogeneous and took place through monolayer coverage, as Langmuir isotherm best described the process [32,38,39]. The q_m values evaluated from the data ranged from 54.05 to 80.00 mg/g for the linear isotherm. The performance of HCeMgO1:1 for F^- ions adsorption was also assessed by comparison with other available materials in the literature (**Table 4.3**). Relative to the listed adsorbents, HCeMgO1:1 exhibited higher adsorption efficiency. As a result, this adsorbent has good prospect for treatment of groundwater with a high F^- ions content.

Table 4.2: Langmuir and Freundlich isotherms parameters for the sorption of F^- ions onto HCeMgO1:1.

Isotherm models	Temperature			
	15 °C	25 °C	35 °C	45 °C
Langmuir				
Linear				
q_{max} (mg/g)	54.05	66.23	75.76	80.00
b (L/mg)	0.073	0.0894	0.1417	0.0675
R_L	0.1227	0.1227	0.0882	0.1563
R^2	0.9909	9976	0.9959	0.9931
Non-linear model				
Best-fit values				
q_m	44.08	51.03	54.09	56.47
b	0.6687	0.3189	0.4151	1.643
Std. Error				
q_m	2.103	3.501	3.796	3.202
b	0.2016	0.1233	0.1661	0.6209
95% Confidence Intervals				
q_m	39.49 to 48.66	43.40 to 58.66	45.82 to 62.36	49.49 to 63.44
b	0.2295 to 1.108	0.05030 to 0.5875	0.05329 to 0.7769	0.2895 to 2.995
Goodness of Fit				
Degrees of Freedom	12	12	12	12
R^2	0.8978	0.8671	0.8481	0.8603
Absolute Sum of Squares	292.7	503.2	709.5	845.2
Sy.x	4.939	6.475	7.689	8.393
Number of points Analyzed	14	14	14	14
Freundlich				
Linear				
K_f (mg/g)	2.155	1.888	2.167	2.118
n	1.285	1.215	1.283	1.332
R^2	0.9498	0.956	0.9640	0.9727
Non-linear model				

UNIVERSITY OF JOHANNESBURG

Best-fit values				
K_f	1.883	1.729	2.031	2.650
n	4.424	3.606	3.868	4.441
Std. Error				
K_f	1.802	1.551	1.865	1.864
n	0.5361	0.3321	0.3990	0.4134
95% Confidence Intervals				
K_f	1.490 to 2.275	1.391 to 2.067	1.624 to 2.437	2.243 to 3.056
n	3.256 to 5.592	2.882 to 4.329	2.999 to 4.738	3.541 to 5.342
Goodness of Fit				
Degrees of Freedom	12	12	12	12
R^2	0.9154	0.9527	0.9510	0.9597
Absolute Sum of Squares	24.23	17.91	22.88	24.40
$Sy.x$	4.494	3.863	4.366	4.510
Number of points analyzed	14	14	14	14

Table 4.3: Comparative assessment of F^- ions adsorption capacity of HCeMgO1:1 with other reported materials.

Adsorbent	Adsorption capacity (mg/g)	Studied pH range	Ref.
Polypyrrole/Fe_3O_4 magnetic nanocomposite	17.6-22.3	6.5	[3]
CeO_2 and ZrO_2 mixed meta oxides	12.4	5.8	[20]
Fe-Ce bimetal oxides	60.97	na	[22]
Al-Ce mixed metal oxide	27.5	6.0	[23]
Mn-Ce bimetal oxides	45.5	6.0	[24]
CeO_2/MgO-Fe layered double hydroxides	42.6	na	[30]
Mg-Fe double hydroxides	50.91	7.0	[31]
Polypyrrole hydrous tin oxide nanocomposite	28.99	6.5	[32]
Fe_3O_4@$Al(OH)_3$ magnetic material	88.48	6.5	[36]
Ti –Fe oxide nano-adsorbent	47.0	na	[38]
MnO_2-Al_2O_3 composite material	18.6	7.0	[40]
Hydroxyapatite/MWCNTs	30.22	7.0	[41]
La oxide + activated carbon hybrid adsorbent	9.98	7.0	[42]
Fe-Sn bimetal oxide	10.50	6.4	[43]
Chitosan/montmorillonite/ZrO_2 composite	23.0	4.0	[44]
Fe doped TiO_2 nano-adsorbent	53.22	7.0	[45]
Hydrous CeO_2-MgO bimetal composite	66.23	5.5	This study

*na- not available

4.3.3.4 Thermodynamic parameters for F^- ions adsorption by HCeMgO1:1

Change in Gibbs free energy ($\Delta G°$), enthalpy ($\Delta H°$) and entropy ($\Delta S°$) were evaluated from adsorption isotherm data using **Equations (4.9)** and **(4.10)**:

$$\Delta G° = -RT\ lnK_c = -RT\ ln\ (m\frac{q_e}{C_e}) \quad (4.9)$$

$$ln\ (m\frac{q_e}{C_e}) = \frac{\Delta S°}{R} - \frac{\Delta H°}{RT} \quad (4.10)$$

where R (J/mol K) is the gas constant, m (g) is the adsorbent dose in a volume of 1 L, and K_c is the equilibrium constant. The ratio mq_e/C_e is the adsorption affinity. The values of $\Delta H°$ and $\Delta S°$ were determined from the slope and intercept of the plot of ln (mq_e/C_e) versus $1/T$, as shown in **Fig. 4.8(C)**. The values of $\Delta G°$ were calculated by using **Equation (4.9)**. These calculated parameters are shown in **Table 4.4**. The positive $\Delta H°$ value indicates endothermic process during F^- ions adsorption using HCeMgO1:1 composite [23,31,46]. The process also occurred with increasing entropy as indicated by the positive $\Delta S°$ values, suggesting an increase in randomness with an upsurge in number of F^- ions. In addition, this process was spontaneous under the experimental conditions, as evidenced from the negative $\Delta G°$ values [23,31,47].

Table 4.4: Thermodynamic parameters for F^- ions adsorption onto HCeMgO1:1.

Temperature (°C)	$\Delta G°$ (kJ/mol)	$\Delta H°$ (kJ/mol)	$\Delta S°$ (kJ/mol/K)
15	-0.571	+13.04	+0.0473
25	-0.721		
35	-1.570		
45	-1.972		

UNIVERSITY OF JOHANNESBURG

4.3.3.5 Adsorption kinetics

Adsorption kinetics is useful in predicting the adsorption rate that gives more insight into design and modelling for adsorption-based water treatment processes. An adsorbent must have rapid adsorption kinetics to be considered feasible for practical application. **Fig. 4.9(A)** shows the results from the effect of contact time experiments for the adsorption of F^- ions on HCeMgO1:1 adsorbent using four different initial F^- ions concentrations: 10, 15, 25 and 40 mg/L. Within 5 to 20 min of contact time, the adsorption capacity increased rapidly to 12, 21, 33 and 37 mg/g for solution of initial F^- ions concentrations 10, 15, 25 and 40 mg/L, respectively. The encountered contact time was much shorter than those reported for some adsorbents in the literature. This faster kinetics is attributed to the shorter diffusion routes associated with mixed metal oxides [8,23].

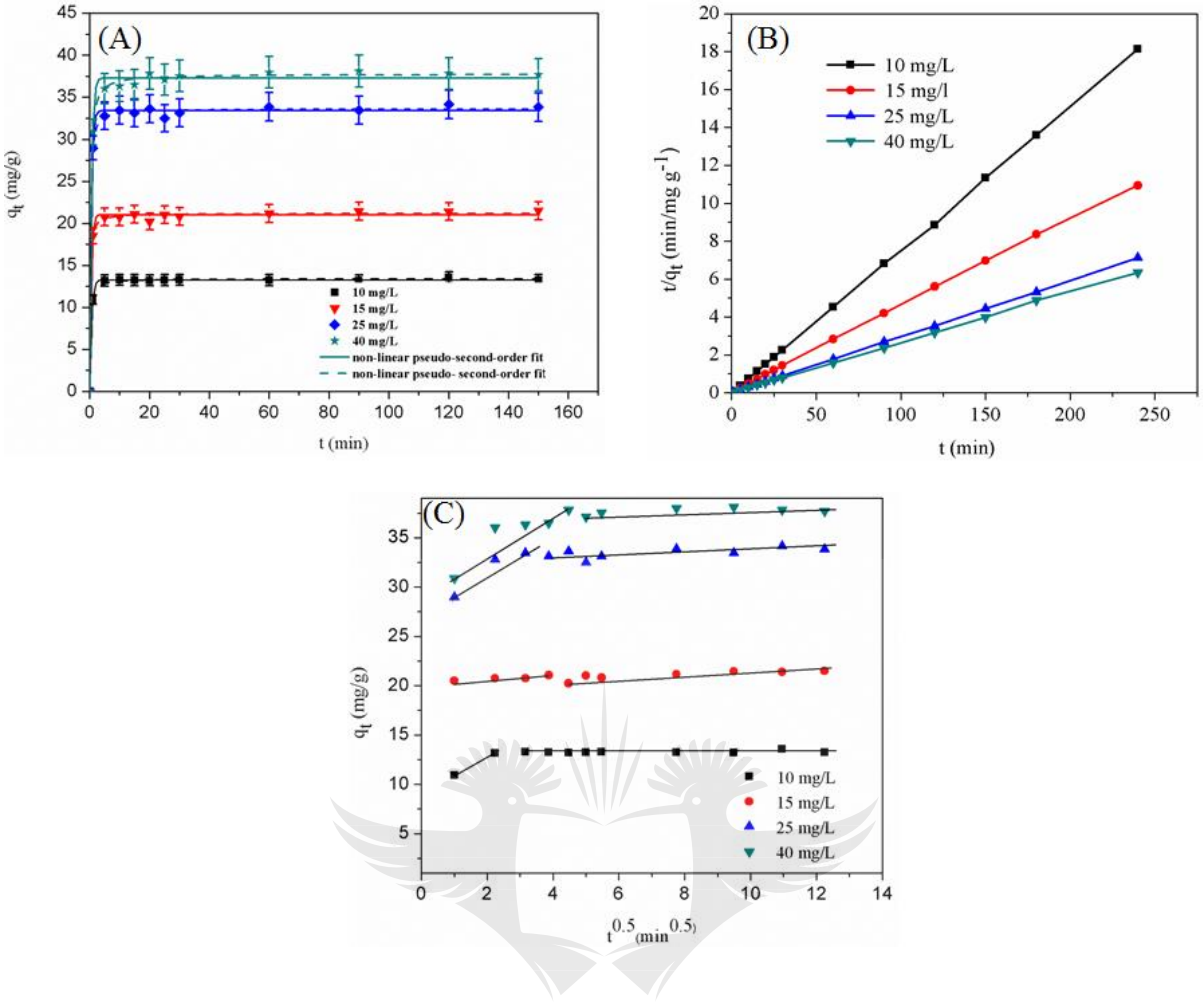

Fig. 4.9: Effect of contact time on the adsorption of F^- ions onto HCeMgO1:1 (A) pseudo-first-order and pseudo-second-order nonlinear fitting; (B) fit of data to linearized pseudo-second-order kinetic model at pH 5.5 (adsorbent dose: 0.03 g/50 mL of F^- ions solution, temperature: 25 °C) and (C) intra-particle diffusion model for adsorption of F^- ions by HCeMgO1:1.

Pseudo-first-order and pseudo-second-order kinetic models were employed to investigate the adsorption kinetics and understand the mechanism involved. These are represented by **Equations (4.11)** to **(4.14)**:

$$q_t = q_e(1 - exp(^{-k_1\, t}) \tag{4.11}$$

$$log(\, q_e \, - \, q_t\,) = log(q_e\,) - \frac{k_1}{2.303}\, t \tag{4.12}$$

$$q_t = \frac{k_2 q_e 2\ t}{1 + k_2\, q_e\, t} \tag{4.13}$$

$$\frac{t}{q_t} = \frac{1}{k_2 q_e 2} + \frac{t}{q_e} \quad (4.14)$$

where k_1 (1/min) and k_2 (g/mg.min) are pseudo-first-order and second-order-rate constants, respectively. q_e and q_t (mg/g) are adsorption capacities at equilibrium and time t (min), respectively. **Figs. 4.9(A)** and **(B)** show both the linear and non-linear kinetic modelling of pseudo-second-order model. Fit of kinetic data to nonlinear pseudo-first-order model is shown in **Figs. 4.9(A)**. The values of all kinetic parameters are reported in **Table 4.5**. The R^2 values obtained from the pseudo-second-order model (R^2_{linear} = 0.9998-1.000 and $R^2_{non\text{-}linear}$ = 0.9984-0.9988) are higher than those from pseudo-first-order model (R^2_{linear} = 0.1161-0.9853 and $R^2_{non\text{-}linear}$ = 0.9933-0.9977). Both the experimental and modelled q_e values obtained from pseudo-second-order model correlated well. F^- ions adsorption by HCeMgO1:1 therefore followed pseudo-second-order kinetics. There was also a general decrease in the values of k_2 with an increase in initial F^- ions concentration (from 3.856 to 0.4422 g/mg/min). This occurs because of faster adsorption from dilute solutions, as less F^- ions migrate to the adsorption sites in contrast to concentrated solutions [20,36,48,49]. In order to identify the rate determining step, the Webber-Morris intra-particle diffusion model was employed and is represented by **Equation (5.15)**:

$$q_t = k_{int}\, t^{0.5} + C_i \quad (4.15)$$

UNIVERSITY OF JOHANNESBURG

where k_{int} (mg/gmin$^{0.5}$) is the intra-particle diffusion rate constant and C_i (mg/g), the constant related to the magnitude of the boundary layer thickness. **Fig. 4.9(C)** represents a plot of $t^{0.5}$ against q_t for different F^- ions initial concentrations. There are two linear portions involved in the sorption of F^- ions on HCeMgO1:1 adsorbent. The initial portion may be governed by boundary layer diffusion and the second by intra-particle diffusion [50]. From the slopes of the initial linear portion of the curves, the values of k_{int} for the four different concentrations were obtained and presented in **Table 4.5**, together with the R^2 values. k_{int} values increased from 1.1350 to 2.1616 mg/g min$^{0.5}$ as the initial concentration increased from 10 mg/L to 40 mg/L. However, the linear plots did not pass through the origin, denoting a complex situation in which both film diffusion and intra-particle diffusion contribute to the rate limiting step [50, 51]. The magnitude of C_i increases with increasing initial concentration of F^- ions. This indicates an increase in boundary layer effects [32].

Table 4.5: Kinetics parameters for the sorption of F^- ions by HCeMgO1:1 at different concentrations.

Kinetic models	Initial concentration (mg/L)			
	10	15	25	40
Pseudo-first order				
Linear				
k_1(1/min)	0.0170	0.0237	0.0210	0.0180
q_e (mg/g	0.000762	0.9390	1.7500	1.9050
R^2	0.1161	0.9534	0.9390	0.9853
Nonlinear				
Best-fit values				
q_e	13.26	21.02	33.40	37.29
k_1	1.724	2.122	2.023	1.758
Std. Error				
q_e	0.03263	0.1181	0.1534	0.2265
k_1	0.04507	0.1540	0.1138	0.1152
95% Confidence Intervals				
q_e	13.19 to 13.33	20.75 to 21.28	33.05 to 33.74	36.79 to 37.79
k_1	1.623 to 1.824	1.779 to 2.465	1.769 to 2.277	1.502 to 2.015
Goodness of Fit				
Degrees of Freedom	10	10	10	10
R^2	0.9933	0.9965	0.9977	0.9960
Absolute Sum of Squares	0.1064	1.396	2.351	5.127
Sy.x	0.1031	0.3736	0.4849	0.7160
Number of points Analysed	12	12	12	12
Pseudo second order				
Linear				
k_2 (g/mg.min)	3.856	0.500	0.2086	0.4422
q_e (mg/g)	13.26	21.14	33.54	37.30
R^2	1.000	0.9998	0.9999	0.9998
Nonlinear				
Best-fit values				
k_2	0.3407	0.3229	0.1842	0.1161
q_e	13.40	21.18	33.68	37.75
Std. Error				
k_2	0.02959	0.04778	0.02032	0.008769
q_e	0.05481	0.1102	0.1406	0.1380
95% Confidence Intervals				
k_2	0.2748 to 0.4067	0.2164 to0.4294	0.1390 to 0.2295	0.09660 to 0.1357
q_e	13.28 to 13.53	20.94 to 21.43	33.36 to 33.99	37.44 to 38.06
Goodness of Fit				
Degrees of Freedom	10	10	10	10
R^2	0.9985	0.9975	0.9984	0.9988
Absolute Sum of Squares	0.2486	1.026	1.663	1.571
Sy.x	0.1577	0.3203	0.4077	0.3964
Number of points Analyzed	12	12	12	12
Intra-particle diffusion				
k_{int} (mg/g/min $^{0.5}$)	1.1350	1.1970	2.2193	2.16157
C_i (mg/g)	10.024	20.411	27.199	28.830
R^2	0.8424	0.8189	0.9139	0.8549

UNIVERSITY OF JOHANNESBURG

4.3.3.6 Effect of co-existing ions

In general, drinking water can have a complex matrix, it may contain several anions along with F^- ions like, SO_4^{2-}, Cl^-, HCO_3^-, PO_4^{3-} and NO_3^-, which might compete for binding sites with F^- ions, hence interfering with its adsorption [50,52]. The effect of various anions on the F^- ions removal efficiency by HCeMgO1:1 adsorbent was investigated. The initial concentration of F^- ions was kept constant at 10 mg/L whilst that of interfering ions was varied from 0 to 40 mg/L and the pH was adjusted to 5.5. The concentration range of the co-existing ions and pH were adjusted according to those known to exist under environmental conditions. The results which are presented **in Fig. 4.10(A)** indicate that Cl^- ions actually increases F^- ions uptake. This is probably attributed to increased coulombic repulsive forces that occur during the process and the fact that chloride is larger than fluoride so it is unlikely to displace fluoride from the adsorbent sites [32]. NO_3^- and HCO_3^- ions had very little effect on the F^- ions removal whilst SO_4^{2-} and PO_4^{3-} ions caused a decrease in the adsorption of F^- ions for all concentrations studied (10-40 mg/L). The PO_4^{3-} ions, however, had the greater effect with the F^- ions uptake decreasing from 90.70% to 62.29% when PO_4^{3-} ions concentration increased from 0 to 40 mg/L. Thus the order of interference was $PO_4^{3-} > SO_4^{2-} > HCO_3^- > NO_3^- > Cl^-$. This is related to the formation of inner and outer sphere complexes associated with the different ions. F^- ions are adsorbed through inner-sphere complexations which also happen to take place with PO_4^{3-} ions, hence competitive adsorption [32,46]. In addition, the order of interference relatively compares to the Z/R (charge/radius) values of competitive anions: PO_4^{3-} (3/3.40) > SO_4^{2-} (2/2.40) > Cl^- (1/1.18) > NO_3^- (1/2.81). The greater the charge/radius, the more likely the anion is attracted to the adsorbent surface and hence the more it interferes with F^- ions adsorption [36,46]. It is reported that the concentration of PO_4^{3-} in drinking water is normally low thus its effect on F^- ions removal may be minimal [20,32].

4.3.3.7 Desorption studies

The reusability of an adsorbent is an important factor which affects its feasibility for large scale water treatment applications, and a high quality adsorbent must satisfy this factor. Various concentrations of NaOH ranging from 0.05 to 0.1M were used for desorption in order to find the best desorbing concentration. It was found that maximum regeneration of 97.50% was achieved by a 0.1M NaOH solution. This concentration of NaOH was then used for further adsorption-desorption experiments. The F^- loaded HCeMgO1:1 adsorbent was subjected to

four adsorption-desorption successive cycles**. Fig. 4.10(B)** illustrates the variation of the percentage removal with the number of adsorption-desorption cycles. The adsorbent maintained its higher efficiency up to three cycles, followed by a reduction to 62.4% in the 4th cycle, probably due to desorption and regeneration operations. This study suggests that HCeMgO1:1 can be used for four regeneration cycles.

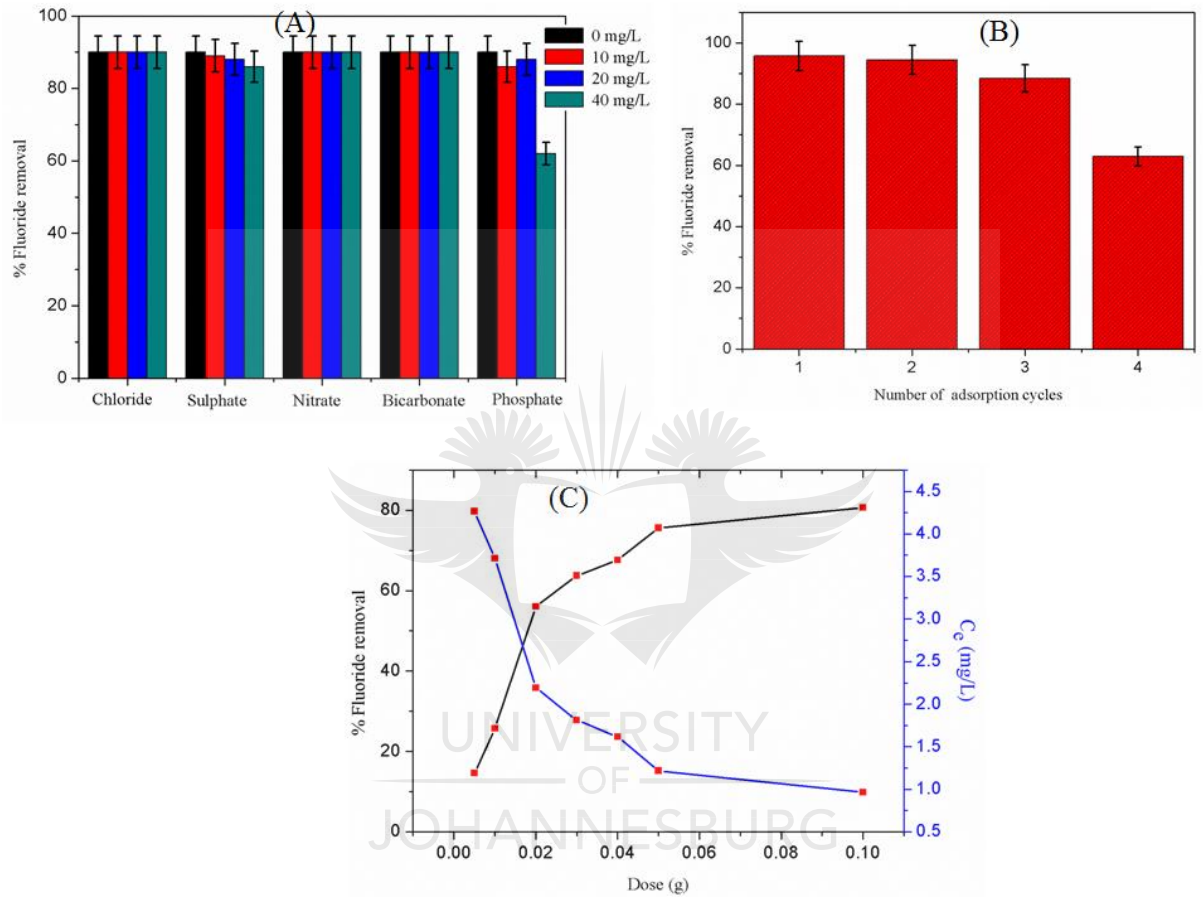

Fig. 4.10: (A) Effect of co-existing ions on F⁻ ions adsorption at pH 5.5 (adsorbent dose: 0.03 g/50 mL of F⁻ ions solution, contact time: 24 h and temperature: 25 °C) (B) F⁻ ions removal efficiency on the recycled HCeMgO1:1 (C) Effect of adsorbent dosage on % F⁻ ions removal and equilibrium F⁻ ions concentration using groundwater samples.

4.3.3.8 Performance on natural water samples

To evaluate the F⁻ ions removal efficiency of the HCeMgO1:1 adsorbent in natural water samples, fluoride-containing underground water from Moletjie village, Limpopo Province South Africa, was used. The water had a F⁻ ions concentration of 0.416 mg/L and a pH of 7.88.

The fluoride ions concentration was then increased to 5 mg/L by spiking, and its new pH was measured to be 8.3. Thereafter, the as-prepared natural water was contacted with doses of HCeMgO1:1 adsorbent ranging from 0.05 to 0.1 g in 50 mL of volume without adjusting the pH. An increase in HCeMgO1:1 dosage resulted in an increase of F^- ions removal and a decrease in equilibrium F^- ions concentration as shown in **Fig. 4.10(C)**. This adsorbent was able to reduce the F^- ions level to about 1.0 mg/L, value below the limit of 1.5 mg/L, as recommended by WHO.

4.3.4 Adsorption mechanism

XPS and FTIR techniques were used to study the interaction between F^- ions and the presence of functional groups on the adsorbent. **Fig. 4.6(A)** presents the XPS wide-scan spectra of the sorbent before and after adsorption. From the FTIR data **(Fig. 4.2(A)),** the HCeMgO1:1 surface hydroxyl groups were very proactive in the adsorption of F^- ions. As observed in **Fig. 4.11**, the O 1s spectra of the virgin sorbent exhibit two signature peaks, with binding energies 529.71 and 531.96 eV, which can be assigned to oxygen (O^{2-}) of metal (Ce/Mg) oxide and surface hydroxyl groups, respectively [10,22,36,51-53].

Further, the peak area ratio and peak intensity of O^{2-} after adsorption are higher, comparative to the same peak before adsorption. The peak area ratio assigned to O^{2-} of the adsorbent increases from 61.46% to 88.42%. However, the area of peaks assigned to OH groups decreased from 38.54% to 11.58% after adsorption **(Fig. 11A** and **(B))**, pointing out that this group was involved in the F^- ions adsorption [10,22,24]. This observation is consistent with the FTIR analysis in terms of involvement of OH groups in adsorption. The pH_{pzc} (pH = 5.8) is an important parameter as discussed earlier. From **Fig. 4.7(B)**, it can be observed that adsorption efficiency is high from pH 2 to 8.5, but decreases sharply as the pH increases further. When $pH < pH_{pzc}$, protonation leads to the formation of positively charged MOH_2^+ species (**Equation (4.6)**), and there may be adsorption of anionic F^- through electrostatic attractions and anionic exchange. With regard to $pH > pH_{pzc}$, the adsorbent surface of HCeMgO1:1 becomes negatively charged. Thus repulsion is set to take place with F^- ions. In this case, the adsorption process can only proceed through anionic exchange [23,32]. Both fluoride and hydroxyl ions are isoelectronic and the ability of the former to coordinate with Ce^{4+} and Mg^{2+} ions is relatively higher than that with OH^-, supporting the possibility of anion exchange at the surface of HCeMgO1:1 [52,54].

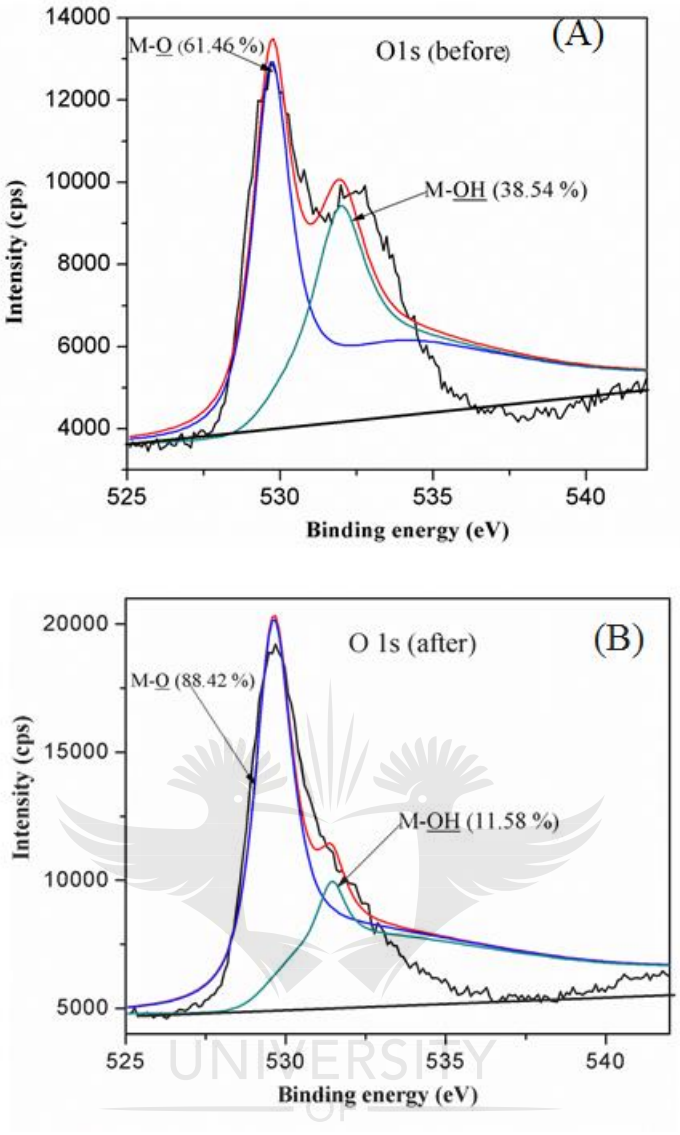

Fig.4.11: XPS O 1s spectra (A) before and (B) after adsorption.

Therefore, the F^- ions adsorption mechanism onto HCeMgO1:1 in aqueous matrix can be described as both electrostatic interactions and ion exchange. The following equations illustrate the possible adsorption mechanisms (**Equations (4.16** to **4.18**)):

(a) Electrostatic attraction

$$M\text{-}OH_{(s)} + H^+_{(aq)} \rightarrow M\text{-}OH_2{}^+_{(s)} \quad (4.16)$$

$$M\text{-}OH_2{}^+_{(s)} + F^-_{(aq)} \rightarrow M\text{-}OH_2{}^+\text{---}F^-_{(s)} \quad (4.17)$$

(b) Ion exchange

$$M\text{-}OH_{(s)} + F^-_{(aq)} \rightarrow M\text{-}F_{(s)} + OH^-_{(aq)} \quad (4.18)$$

4.4 Conclusion

Hydrous Ce-Mg binary metal oxides were synthesized by a co-precipitation method and applied as an adsorbent for F^- ions removal from water. HCeMgO adsorbent demonstrated rapid adsorption of F^- ions within 5–20 minutes. This fast kinetics was attributed to shorter diffusion path associated with nano-metal oxides. The successful adsorption of F^- ions on the fabricated hydrous binary nano-metal oxides was confirmed with the appearance of a fluoride peak on the EDS and XPS spectra. This adsorbent performed well over a wide pH range 2-8.5. Maximum adsorption capacity obtained from the best fitting Langmuir isotherm was 66.23 mg/g at 25 °C, and the process seemed to involve both electrostatic and anion exchange. Thermodynamic data ($\Delta G°$ = -0.721 kJ/mol at 25 °C and $\Delta H°$ = +13.04 kJ/mol) exposed a spontaneous and endothermic process. A pseudo-second-order model best described the adsorption kinetics and the process was hindered by phosphate and sulphate ions. The adsorbent maintained its relatively high adsorption efficiency over four cycles, comparable to those reported in literature. Additionally, treatment of 50 mL fluoride-spiked groundwater samples (5 mg/L F^- ions concentrations) with 0.1 g of HCeMgO1:1 reduced the F^- ions level to 1.00 mg/L. Hence, this material can serve as alternative adsorbent for removal of F^- ions from drinking water.

UNIVERSITY OF JOHANNESBURG

4.5 References

[1] S. Ali, S.K. Thakur, A. Sarkar, S. Sheka, Worldwide contamination by fluoride ions, Environ. Chem. Lett. 14 (2016) 291–315.

[2] Fluorides. Environmental Health Criteria 227, World Health Organization (WHO): Geneva, Switzerland 2002, 1–268.

[3] M. Bhaumik, T.Y. Leswifa, A. Maity, V.V. Srinivasu, M.S. Onyango, Removal of F^- from aqueous solution by polypyrrole/Fe_3O_4 magnetic nanocomposite, J. Hazard. Mater. 186 (2011) 150–159.

[4] D. Dayananda, V.R. Sarva, S.V. Prasad, J. Arunachalam, N.N. Ghosh, Preparation of CaO loaded mesoporous Al_2O_3: Efficient adsorbent for F^- removal from water, Chem. Eng. J. 248 (2014) 430–439.

[5] S. Blagojevic, M. Jakovljevic, M. Radulovic, Content of fluorine in soils in the vicinity of aluminium plant in Podgorica, J. Agric. Sci. 47 (2002) 1–8.

[6] K. Biswas, K. Gupta, A. Goswami, U.C. Ghosh, F^- removal efficiency from aqueous solution by synthetic iron(III)-aluminium(III)-chromium (III) ternary mixed oxide, Desalination 255 (2010) 44–51.

[7] N. Esmaeeli, H. Faghihian, S. Naeimi, Magnetization and modification of ETS-4 titanosilicate for removal of fluoride from aqueous solutions, J. Alloys Compd. 744 (2018) 271–280.

[8] J. Hu, J.H. Shipley, Evaluation of desorption of Pb (II), Cu (II) and Zn (II) from titanium dioxide nanoparticles, App. Clay Sci. 103 (2015) 20–27.

[9] M. Chiban, M. Zerbet, G. Carja, F. Sinami, Application of low-cost adsorbents for arsenic removal: A review, J. Environ. Chem. Ecotoxicol. 4 (2011) 91–102.

[10] J. Wang, D. Kang, X. Yu, M. Ge, Y. Chen, Synthesis and characterization of Mg-Fe-La tri-metal composite as an adsorbent for F^- removal, Chem. Eng. J. 26 (2015) 506–513.

[11] M.H. Stannic, M.E. Ravančić, A. Flanagan, Review on adsorption of F^- from aqueous solution, Materials 7 (2014) 6317–6366.

[12] A.E. Chávez-Guajardo, J.C. Medina-Llamas, L. Maqueira, C.A.S. Andrade, K.G.B. Alves, C.P. de Melo, Efficient removal of Cr(VI) and Cu(II) ions from aqueous media by use of polypyrrole/maghemite and polyaniline/maghemite magnetic nanocomposites, Chem. Eng. J. 281 (2015) 826–836.

[13] T. Mahmood, S.U. Din, A. Naeem, S. Mustafa, M. Waseem, M. Hamayun, Adsorption of arsenate from aqueous solution on binary mixed oxide of iron and silicon, Chem. Eng. J. 192 (2012) 90–98.

[14] Z. Jin, Y. Jia, K.S. Zhang, L.T. Kong, B. Sun, W. Meng, J. Liu, Effective removal of fluoride by porous MgO nanoplates and its adsorption mechanism, J. Alloys Compd. 675 (2016) 292–300.

[15] I. Saha, A. Ghosh, D. Nandi, K. Gupta, D. Chatterjee, U.C. Ghosh, Beta-cyclodextrin modified hydrous zirconium oxide: Synthesis, characterization and defluoridation performance from aqueous solution, Chem. Eng. J. 263 (2015) 220–230.

[16] M.G. Sujana, S. Anand, Iron and aluminium based hydroxides: A novels sorbent for the removal of F^- from water, Appl. Surf. Sci. 7 (2010) 6956–6962.

[17] T. Basu, U.C. Gosh, Nano-structured iron (III)-cerium (IV) mixed oxide: Synthesis, characterization and arsenic sorption kinetics in the presence of co-existing ions aiming to apply for high arsenic ground water treatment, Appl. Surf. Sci. 2 (2013) 471–481.

[18] R.R. Devi, I.M. Umlong, P.K. Raul, B. Das, S. Banerjee, L. Singh, Defluoridation of water using nanomagnesium oxide, J. Exp. Nanosci. 9 (2012) 512–524.

UNIVERSITY OF JOHANNESBURG

[19] A.A. Markeb, A. Alonso, A. Sánchez, X. Font, Adsorption process of fluoride from drinking water with magnetic core-shell Ce-Ti@ Fe3O4 and Ce-Ti oxide nanoparticles, Sci. Total Environ. 598 (2017) 949–958.

[20] A. Gosh, S. Chakrabarti, K. Biswas, U.C. Gosh, Agglomerated nanoparticles of hydrous Ce(IV) and Zr(IV) mixed oxide: Preparation, characterization and physicochemical aspects on F^- adsorption, Appl. Surf. Sci. 307 (2014) 665–676.

[21] A.M. Rauchir, M.J. Basu, Adsorption of F^- onto mixed rare earth metal oxides, Sep. Purif. Technol. 24 (2001) 121–127.

[22] D. Tang, G. Zhang, Efficient removal of F^- by hierarchical Ce-Fe bimetal adsorbent: Thermodynamics, kinetics and mechanism, Chem. Eng. J. 283 (2016) 721–729.

[23] H. Liu, S. Deng, Z. Li, J. Huang, Preparation of Al-Ce adsorbent and its application for deflouridation of drinking water, J. Hazard. Mater. 179 (2010) 424–430.

[24] S. Deng, H. Liu, J. Huang, G. Yu, Mn-Ce oxide as a high capacity adsorbent for F^- removal from water, J. Hazard. Mater. 186 (2011) 1360–1366.

[25] X. Wang, G. Zhang, H. Lan, R. Liu, J. Qu, Preparation of hollow Fe-Al binary oxyhydroxide for efficient removal of fluoride ions, Colloids Surf. A Physicochem. Eng. Asp. 520 (2017) 580–589.

[26] Z. Jin, Y. Jia, T. Luo, L.T. Kong, B. Sun, W. Shen, F.L. Meng, J.H. Liu, Efficient removal of F^- by hierarchical MgO microspheres: Performance and mechanism study, Appl. Surf. Sci. 357 (2015) 1050–1088.

[27] N. Chubar, New inorganic ion exchangers based on Mg-Al hydrous oxides: (Alkoxide-free) sol-gel synthesis and characterization, J. Colloid Interface Sci. 357 (2011) 198–209.

[28] J. Wang, W. Xu, L. Chen, Y. Jia, L. Wang, X.J. Huang, J. Lui, Excellent F^- removal performance by CeO_2 and ZrO_2 nanocages in water environment, Chem. Eng. J. 231 (2013) 195–205.

[29] S. Moriyana. K. Sasaki, T. Hirajima, Effect of temperature on Mg-Al bimetallic oxides as sorbents for removal of F^- from aqueous solution, Chemosphere 95 (2014) 597–603.

[30] T. Zhang, Q. Li, H. Xiao, Z. Mei, H. Lu, Y. Zhou, Enhanced F^- removal from water by non-thermal plasma CeO_2/Mg-Fe layered doubled hydroxides, Appl. Clay Sci. 72 (2013) 117–123.

[31] D. Kang, X. Yu, S. Tong, M. Ge, J. Zuo, C. Cao, C. Song, Performance and mechanism of double layered hydroxides for F^- and arsenate removal from aqueous solution, Chem. Eng. J. 228 (2013) 731–740.

[32] K. Parashar, N. Ballav, S. Debnath, K. Pillay, A. Maity, Rapid and efficient removal of F^- from aqueous solution using polypyrrole coated hydrous tin oxide composite, J. Colloid Interface Sci. 476 (2016) 103–118.

UNIVERSITY OF JOHANNESBURG

[33] K. Mukhopadhyay, A. Ghosh, S.K. Das, B. Show, P. Sasikumar, U.C. Ghosh, Synthesis and characterization of cerium (IV)-incorporated hydrous iron (III) oxide as an adsorbent for fluoride removal from water, RSC Adv. 7 (2017) 26037–26051.

[34] S.K. Swain, P. Patnaik, P.C. Patnaik, U. Jha, R.K. De, Development of new alginate entrapped Fe(III)-Zr(IV) binary mixed oxide for removal of fluoride from water bodies, Chem. Eng. J. 215–216 (2013) 763–771.

[35] K.Y. Foo, B.H. Hammed, Insights into modelling of isotherm adsorption systems, Chem. Eng. J. 156 (2010) 2–10.

[36] X. Zhao, J. Wang, F. Wu, T. Wang, Y. Cai, Y. Shi, G. Jiang, Removal of F^- from aqueous media by Fe_3O_4 @ $Al(OH)_3$ magnetic nanomaterials, J. Hazard. Mater. 173 (2010) 102–109.

[37] M. Mohapatra, D. Harisprasad, L. Mohapatra, S. Annand, B.K. Mishra, Mg-doped nanoferrydrite-A new adsorbent for F^- removal from aqueous solution, Appl. Surf. Sci. 258 (2012) 4228–4236.

[38] L. Chen, B.Y. He, S. He, T.J. Wang, C.L. Su, Y. Jin, Fe–Ti oxide nano-adsorbent synthesized by co-precipitation for F^- removal from drinking water and its adsorption mechanism, Powder Technol. 227 (2012) 3–8.

[39] X. Dou Y. Zhang, H. Wang, T. Wang, Y. Wang, Performance of granular zirconium-iron oxide in the removal of F^- from drinking water, Water Res. 45 (2011) 3571–3578.

[40] S. Alemu, S. Mulugeta, F. Zewge, B.S. Chandravanshi, Water defluoridation by aluminium oxide-manganese oxide composite material, Environ. Technol. 15 (2014) 1893–1903.

[41] Z. Ruan, Y. Tiana, J. Ruan, G. Cui, K. Iqbal, H. Ye, Z. Yang, S. Yana, Synthesis of hydroxyapatite/multi-walled carbon nanotubes for the removal of fluoride ions from solution, App. Surf. Sci. 412 (2017) 578–590.

[42] A. Alvarez, L.H. Velazquez-Jimenez, L.P. Chazaro-Ruiz, P.E. Diaz-Flores, J.R. Rangel-Mendez, F^- removal in water by a hybrid adsorbent lanthanum-carbon, J. Colloid Interface Sci. 455 (2015) 194–202.

[43] K. Biswas, K. Gupta, U.C. Ghosh, Adsorption of F^- by hydrous iron (III) tin (IV) bimetal mixed oxide from the aqueous solution, Chem. Eng. J. 149 (2009) 196–206.

[44] A. Teimouri, S.G. Nasab, S. Habibollahi, H.M. Fazel Najafabadi, A.N. Chermahini, Synthesis and characterization of a chitosan/montmorillonite/ZrO_2 nanocomposite and its application as an adsorbent for removal of F^-, RSC Adv. 5 (2015) 6771–6781.

[45] L. Chen, S. He, B.Y. He, T.J. Wang, C.L. Su, C. Zhang, Y. Jin, Synthesis of iron doped titanium oxide nanoadsorbent and its adsorption characteristics for F^- in drinking water, Ind. Chem. Res. 51 (2012) 13150–13156.

[46] L. Liu, Z. Cui, Q. Ma, W.C. Cui, X. Zhang, One-step synthesis of magnetic iron-aluminium oxide/graphene oxide nanoparticles as selective adsorbent for F^- removal form aqueous solution, RSC Adv. 8 (2016) 10783–10791.

UNIVERSITY OF JOHANNESBURG

[47] S. Kanra, S. Debnath, P. De, K. Parashar, K. Pillay, P. Sasikumar, U.C. Gosh, Preparation characterization, and evaluation of adsorption efficiency of Iron-Aluminium oxide-graphene oxide composite material, Chem. Eng. J. 306 (2016) 269–279.

[48] H.R. Mahmoud, S.A. El-Molla, M. Saif, Improvement of physicochemical properties of Fe_2O_3/MgO nanomaterials by hydrothermal treatment for dye removal from industrial wastewater, Powder Technol. 249 (2013) 225–233.

[49] Y. Zhang, X. Lin, Q. Zhou, X. Lou, Fluoride adsorption from aqueous solution by magnetic core-shell Fe_3O_4@alginate-La particles fabricated via electro-coextrution, Appl. Surf. Sci. 389 (2016) 34–45.

[50] S.D. Meenakshi, M. Rajaran, S. Rajendram, Z.R. Kennedy, G. Brindha, Synthesis and characterization of magnesium oxide nanoparticles, Elixier Nanotechnol. 50 (2012) 10618–10620.

[51] S. Debnath, M. Kitinyu, M. Onyango, Removal of Congo red from solution using two variant calcium and iron based mixed oxides nano-particle agglomerates, J. Ind. Chem. Eng. 20 (2014) 2119–2129.

[52] J. Zhu, X. Lin, P. Wu, Q. Zhou X. Luo, Fluoride removal from aqueous solution by Al(III)-Zr(VI) binary oxide adsorbent, App. Surf. Sci. 357 (2015) 91–100.

[53] Y. Yu, J.P. Chen, Key factors for optimum performance phosphate removal from contaminated water by Fe-Mg-La tri-metal composite sorbent, J. Colloid interface Sci. 445 (2015) 300–311.

[54] S.K. Swain, S. Mishra, T. Patnaik, R.K. Patel, U. Jha, R.K. Dey, Fluoride removal performance of a new hybrid sorbent of Zr(IV)-ethylenediamine, Chem. Eng. J. 184 (2012) 72–81.

UNIVERSITY OF JOHANNESBURG

CHAPTER FIVE
HYDROUS CEO_2-FE_3O_4 DECORATED POLYANILINE FIBERS NANOCOMPOSITE FOR EFFECTIVE DEFLUORIDATION OF DRINKING WATER

5.1 Introduction

As previously highlighted in chapter 4, groundwater, an economical source of drinking water in developing countries, is often affected by fluoride pollution owing to anthropogenic and natural activities [1,2,3]. Over 24 countries including South Africa, are harshly affected by high fluoride ions concentrations in drinking water hence its limit is set below 1.5 mg/L [4,5]. Amongst the assortment of technologies available for its removal, adsorption offers many advantages and various adsorbent materials have been tested including our previous study in chapter 4 [6-11]. However, drawbacks have been encountered in the application of some of many of the materials [6,9,12]. Nano-metal oxides including Ce-Mg [13], Mn-Ce [14], Ce-Fe [15,16], Ce-Al [17], Al-Mg [18], Fe-Zr [19], Al-Fe [20] and Mn-Al [21] oxides are also noteworthy materials in scavenging fluoride ions (F^-) from water. Several studies on their application and advantages have been reported [15,21-23] and these merits have also been realised in our study in chapter 4. Nevertheless, despite their merits and the success in our study in chapter 4, they still present major shortcomings, including loss of activity due to agglomeration and difficulty of isolation from aqueous medium [22,23]. These limitations led researchers to focus on embedding nano-metal oxide particles onto porous supports including conducting polymers [2,5,6,7,8]. Polyaniline (PANI) a conducting polymer, is such a suitable material because of its unique properties [12,24,25], but has low adsorption fluoride capacity in pristine form [12,24,26,27]. Furthermore, the oxides of iron are prevalent in nature and ceria is among the cheapest of the rare earth metal oxides with high fluoride adsorption ability.

This chapter focusses on a study in which optimised hydrous cerium-iron oxides (CeO_2-Fe_3O_4) deposited PANI nanofibers (HCeFe NF-2) nanocomposite was fabricated by a simple co-precipitation deposition of the NMOs onto polyaniline nanofibers (PANI NFs) network. It was envisaged that the yielded hybrid nanocomposite would produce synergistic fluoride adsorption qualities, prevent agglomeration and enable ease of separation from solution. HCeFe NF-2 was characterized using a combination of microscopic and spectrometric

The work presented in this chapter has been published in the Journal of Colloid and Interface Science, 532 (2018) 500–516. https://doi.org/10.1016/j.jcis.2018.07.134A

techniques together with a batch mode investigation on the influence of various adsorption parameters on fluoride ions removal from both aqueous and groundwater samples.

5.2 Materials and methods

5.2.1 Materials

Sodium fluoride (NaF > 99%), cerium nitrate (Ce $(NO_3)_3.6H_2O$) (> 99%), iron (III) chloride anhydrous ($FeCl_3$ > 97 %), iron (II) sulphate ($FeSO_4.7H_2O$), aniline (ANI, 99%) and all other chemicals of analytical grade were acquired from Sigma-Aldrich, USA. A 1000 mg/L stock solution of F^- ions was prepared by dissolving 0.221 g of NaF in 100 mL of deionised water. 0.1 M NaOH (> 99.9% grade) and 0.1 M HCl (Sigma-Aldrich, USA) aqueous solutions were used to adjust the pH.

5.2.2 Preparation of hydrous HCeFe NFs composite

5.2.2.1 Synthesis of polyaniline nanofibers

Polyaniline nanofibers were synthesized using a method reported elsewhere [25]. 6 g of $FeCl_3$ was dissolved into 80 mL of deionised water under vigorous stirring, followed by a rapid addition of 0.8 mL of aniline monomer. The mixture was stirred for 5 minutes, left unstirred for 48 h, filtered and washed with acetone and deionised water. The obtained nanofibers were dried at 60 ^oC for 12 h.

UNIVERSITY OF JOHANNESBURG

5.2.2.2 Synthesis of the nanofibers composites

Previous investigation on the defluoridation potential of hydrous Ce-Fe nano-metal oxides adsorbent revealed that Ce:Fe molar ratios 0.4:1, 0.5:1, 0.6:1 and 1:1 exhibited almost equivalent adsorption capacities [15]. In the current study a Ce: Fe ratio of 1:1 was adopted for the preparation of hydrous CeO_2-Fe_3O_4 bimetal oxides (HCeFe) and HCeFe NFs. 0.53 g of $FeCl_3$, 0.26 g of $FeSO_4.7H_2O$ and 2.17 g of $Ce(NO_3)_3.6H_2O$ were dissolved in 80 mL of deionised water. 2M NaOH was then added dropwise with magnetic stirring under ambient temperature until pH 8.0, and the resulting precipitate was vigorously stirred for 1 h, aged for 24 h, centrifuged, washed four times with deionised water, oven dried for extra 24 h at 60 °C and ground to afford HCeFe bimetal oxides. With regard to the preparation of the desired

HCeFe NFs, 0.53 g of $FeCl_3$, 0.26 g of $FeSO_4.7H_2O$ and 2.17 g of $Ce(NO_3)_3.6H_2O$ were dissolved in 80 mL of deionised water with stirring, followed by the addition of 0.1, 0.2 and 0.3 g of PANI NFs in three separate mixtures and sonication for 15 minutes. Next, in each reaction mixture, 2M NaOH was added dropwise with magnetic stirring under ambient temperature until pH 8. The resulting precipitates were treated as for the synthesis of HCeFe bimetal oxides. The products were denoted HCeFe NFs-1, HCeFe NFs-2 and HCeFe NFs-3, respectively. To determine the ideal adsorbent for F^- ions adsorption, optimisation study was carried out using the as-synthesized adsorbents under the following conditions; 50 mL aqueous solution of 20 mg/L F^- ions, pH 6.0 ± 0.2 and adsorbent dose of 0.03 g.

5.2.3 Characterization

The FTIR spectra of the prepared pristine PANI nanofibers, HCeFe NFs and F^- loaded HCeFe NFs were acquired using a Perkin Elmer Spectrum 100 Spectrometer (Perkin Elmer USA) in the range of 500-4000 cm^{-1}. The surface morphology and microstructure of the HCeFe NFs were studied by FE-SEM and HR-TEM using the microscopes, Zeiss Auriga Cobra FIB, Germany and a high resolution TEM (JEOL –JEM 2100, Japan) with LaB6 filament operated at 200 kV, respectively. TGA and DTA experiments were performed in air flowing at 50 mL/min and 10 °C/min heating rate on a TGA Q500 (TA Instruments, USA). A Micromeritrics ASAP 2020 gas adsorption instrument (Micromeritics, USA) using low-temperature (-198.50 °C) N_2 adsorption-desorption technique was used for BET surface area measurements. A PANalytical X'Pert PRO-X-ray diffractometer (PANalytical, The Netherlands) using CuKα radiation with a wavelength of 1.5505 Å with adjustable slits at 45 kV/30 mA for 2θ values ranging from 5 to 90 was used for XRD characterization. XPS studies were conducted on a Kratos Axis Ultra device with Al monochromatic X-ray source (1486.6 eV) to establish the elemental composition of the HCeFe NFs before and after F^- adsorption. The mechanical assay was executed using a DMA 8000 dynamic mechanical analyser (Perkin Elmer), operated at the frequency of 1 Hz and amplitude of oscillation 0.05 mm. The temperature ranged from 0 to 150 °C, with a heating rate of 2 °C/min. The mean dimensions of the samples plaques were 1.15 x 7.36 x 12.61, 0.96 x 7.36 x 12.29 and 0.96 x 7.36 x 12.27 mm^3 for PANI NFs, HCeFe NFs-2 and bimetal oxides HCeFe NPs, respectively. The temperature dependent behaviour was investigated by observing the variation in force and phase angle at steady amplitude of oscillation. The point-of-zero charge was measured using a change in pH approach with a Thermo Scientific pH meter as reported in other studies [15].

UNIVERSITY OF JOHANNESBURG

5.2.4 Batch adsorption experiments

Test solutions for F^- removal were prepared by suitable dilutions from the stock solution. Adsorption studies were conducted in triplicate in plastic containers using 50 mL of 20 mg/L F^- ions solution at pH 6.0 ± 0.2 and 0.03 g of adsorbent, followed by shaking in a thermostatic water bath shaker at 200 rpm for 24 h. The pH influence was established by varying the initial pH (2-12) using 20 mg/L of F^- ions solution. The pH adjustment was conducted using 0.1M HCl and 0.1M NaOH solution.

The determination of residual F^- ions in filtrate samples was conducted using an ion selective electrode (ThermoORION) in the form of conductance, as described elsewhere [28-30]. The fluoride electrode was calibrated using 10.0, 1.0 and 0.1 mg/L F^- ion solutions by mixing these with an equivalent volume of Total Ionic Strength Adjustment Buffer (TISAB II). The buffer was made by dissolving 58 g of NaCl and 57 mL of 99.99% glacial acetic acid in 500 mL of deionised water, adjusting the pH to 5.5 using 5M NaOH and subsequently adding deionised water to 1L [8,25]. The percentage removal of F^- ions was estimated using **Equation (5.1)**:

$$\%\, removal = \left(\frac{C_o - C_e}{Co}\right) \times 100 \tag{5.1}$$

where C_o and C_e are the initial and equilibrium F^- ions concentration, respectively.
The influence of the adsorbent dose was investigated by changing the amounts of the adsorbent from 0.05 to 0.1 g using 20 mg/L of F^- ions solution at the optimised pH 6.0 ± 0.2. The equilibrium adsorption capacity of the adsorbent is given by **Equation (5.2)**:

$$q_e \left(\frac{C_o - Ce}{m}\right) V \tag{5.2}$$

where q_e (mg/g) and V (L) denote the equilibrium amount of F^- ions per unit mass of adsorbent and the solution volume, respectively.

To understand the adsorption accomplishment and adsorption mechanism, adsorption isotherms were investigated at pH 6.0 ± 0.2 for different temperatures (15, 25, 35 and 45 °C) with initial F^- ions concentration ranging from 5-100 mg/L and 0.03 g adsorbent dose. The experiment was conducted in triplicate. The isotherm data associated with the adsorption process were used to determine the thermodynamic parameters such as Gibbs free energy

($\Delta G°$*),* enthalpy *(*$\Delta H°$*)* and entropy *(*$\Delta S°$*)* change. Adsorption kinetics is essential for the prediction of the rate and modelling of water treatment systems. This was studied using 50 mL solutions of different initial F^- ions concentrations (10, 20, 30 and 40 mg/L) at 25 °C, 0.03 g adsorbent dose and pH 6.0 ± 0.2 for 0 to 180 minutes shaking. The adsorption capacity of the adsorbent *(*q_t*)* at time *t* was obtained using **Equation (5.3)**:

$$q_t = (\frac{C_o - C_t}{m})V \tag{5.3}$$

where q_t (mg/g) and C_t (mg/L) represent the quantity of F^- taken per unit mass of adsorbent and the concentration of F^- ions at time *t*, respectively.

5.2.4.1 Effect of co-existing ions

The influence of co-existing ions is fundamental because no single ion is found sequestrated in natural water bodies. Hence this was performed by dissolving precursor salts of the selected ions (Cl^-, SO_4^{2-}, NO_3^-, HCO^-_3, PO_4^{3-}) together with F^- ions at 0, 10, 20 and 40 mg/L concentrations in deionised water. The resultant solutions were shaken using the optimised adsorbent dose at pH 6.0 ± 0.2 for 24 h followed by analysis for the residual F^- ions.

5.2.4.2 Regeneration studies

UNIVERSITY OF JOHANNESBURG

Typically, 0.03 g of adsorbent was added to 50 mL of 20 mg/L F^- ions solution at pH of 6.0 ± 0.2. The F^- loaded adsorbent was treated with 0.05, 0.025, 0.05, 0.075 and 0.1 M NaOH solutions and it was found that 0.1 M NaOH solution produced the highest desorption ability. This was then adopted for three consecutive desorption cycles. 2M HCl was employed for regeneration of the adsorbent.

5.3 Results and discussion

5.3.1 Optimisation study

The as-prepared three nanofiber composite adsorbents with different amounts of polyaniline fiber (HCeFe NFs-1, HCeFe NFs-2 and HCeFe NFs-3) along with PANI NFs and HCeFe were compared for their F^- adsorption at pH 6.0 ±0.2 using 0.03 g adsorbent dose in 50 mL of 20 mg/L F^- solution. The results are presented in **Fig. 5.1(a)**. The percentage F^- removal of HCeFe NFs-1(26.20% PANI NFs loading) and HCeFe NFs-3 (78.4% PANI NFs loading) were 70.3 and 59.5, values lower than that of 91.4 removal percentage by HCeFe NFs-2 (52.4% PANI NFs loading). A relatively high amount of PANI NFs loading as compared to metal oxides causes a decrease in F^- uptake. This observation could be ascribed to the optimal structure of hydrous cerium iron bimetal oxide deposited polyaniline with the maximum accessibility of binding sites of all components. Therefore, HCeFe NFs-2 with the highest adsorptive capacity (See **Fig. 5.1**) was adopted as the ideal adsorbent and further compared with pristine PANI NFs and hydrous CeO_2-Fe_3O_4. As illustrated in **Fig. 5.1**, HCeFe NFs-2 showed the highest percentage removal of F^- (91.4%), relative to PANI NFs (28.1%) and HCeFe (62.2%) counterparts.

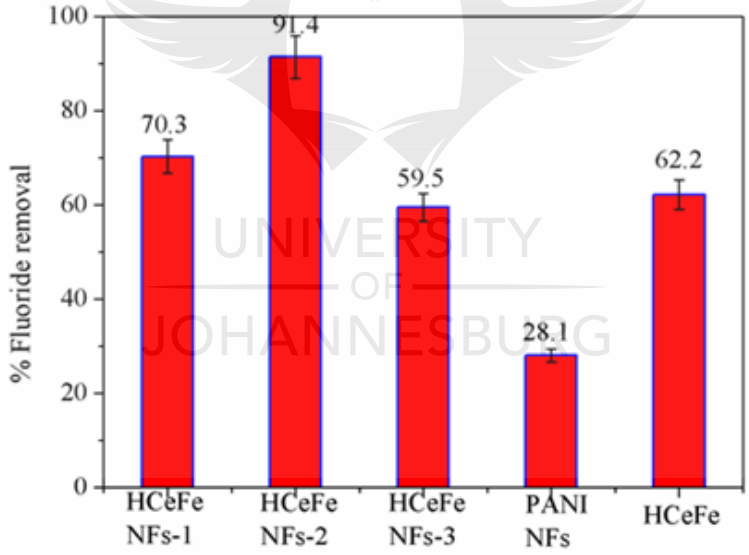

Fig. 5.1: Comparison of adsorption efficiency of nanocomposites at different loading amounts of PANI NFs and comparison of adsorption efficiency of nanocomposite, PANI NFs and hydrous CeO_2-Fe_3O_4 for fluoride ions adsorption using 0.03 g adsorbent, 50 mL of 20 mg/L F^- at pH 6.0 ± 0.2 and temperature of 25 °C.

5.3.2 Physico-chemical characterization

5.3.2.1 FTIR spectral analysis

The FTIR spectrum of pristine PANI NFs is shown in **Fig. 5.2(A)(a)**. The bands at 1554 and 1478 cm^{-1} are ascribed to the C=N and C=C vibration of benzenoid/quinonoid moieties of the polymer chain. Those at 1281 and 1220 cm^{-1} are attributed to the C–N and C–H stretching vibration of the aromatic amine [12,27]. **Fig. 5.2(A)(b)**, on the other hand, represents the spectrum of the HCeFe NFs-2 adsorbent. The bands at 3227 and 1644 cm^{-1} correspond to stretching and bending vibration of H_2O and surface-bonded OH groups. The bands at 1118 and 1076 cm^{-1} correspond to bending vibration of OH groups of the metal oxides [13,16,31]. Those at 778, 685 and 658 cm^{-1} can be attributed to the Fe-O/Ce-O bonds [15,27]. There is evidence of incorporation of hydrous metal oxide in HCeFe NFs-2 adsorbent, owing to the bands at 3227, 1644, 1076, 685 and 658 cm^{-1}, which are absent in the spectrum of pristine PANI NFs. In addition, the observed shift of the bands at 1554 and 1478 cm^{-1}, initially present in the FTIR spectrum of PANI NFs, to 1481 and 1309 cm^{-1} in HCeFe NFs-2 adsorbent spectrum suggests strong interaction between CeO_2/Fe_3O_4 nanoparticles and the PANI NFs [32]. In the spectrum of HCeFe NFs-2 after adsorption procedure **(Fig. 5.2(A)(c))**, the bands at 3227, 1118 and 1076 cm^{-1} shifted to 3204 cm^{-1}, 1090 cm^{-1} and 1067 cm^{-1}, respectively and the intensity of the band at 1644 cm^{-1} decreased. These observations are attributed to the adsorption of F^- ions onto the prepared adsorbent.

5.3.2.2 XRD analysis

UNIVERSITY OF JOHANNESBURG

Fig. 5.2(B) shows the XRD of the PANI NFs, $HCeO_2$-Fe_3O_4, HCeFe NFs-2. The pattern in **Fig. 5.2(B)(a)** reveals the characteristic peaks of PANI NFs at 2θ of 7.39, 15.51, 20.40 and 25.47° [12,27,33]. Characteristic peaks of CeO_2 at 28.90 (111), 33.70 (200), 47.94 (220), 56.80 (311) and 76.60° (331) are shown in **Fig. 5.2(B)(b)** [13,14,15,30]. The absence of the peaks corresponding to Fe_3O_4 may be attributed to the formation of Fe_3O_4-CeO_2 solid solution, in analogy with literature precedent [14,15]. Relative to XRD spectrum of pristine PANI NFs and HCeFe bimetal oxides, **Fig. 5.2(B)(c)** revealed the coexistence of both components in HCeFe NFs-2 with a PANI characteristic peak at 25.47°.

5.3.2.3 BET surface area analysis

The specific surface area is a significant parameter for the evaluation of textural properties of an adsorbent. This was calculated by means of the BET method. The BET surface area of HCeFe NFs-2 adsorbent was 66 m^2/g, much higher than that of previously reported pristine PANI NFs (39 m^2/g) [34]. This might be due to the prevention of π-π aggregation in PANI NFs and their decoration with nano-metal oxides. As shown in **Fig. 5.2(C)**, the N_2 adsorption-desorption isotherm is of type IV with hysteresis loop of nature H3, according to the IUPAC classification [16]. The estimated pore size and volume were 4.18 nm and 0.077 cm^3/g, respectively **(Fig. 5.2(D))**. Since this pore size was larger than that of F^- ions (0.133 nm), we envisaged that F^- ions will be able to access the mesoporous material easily.

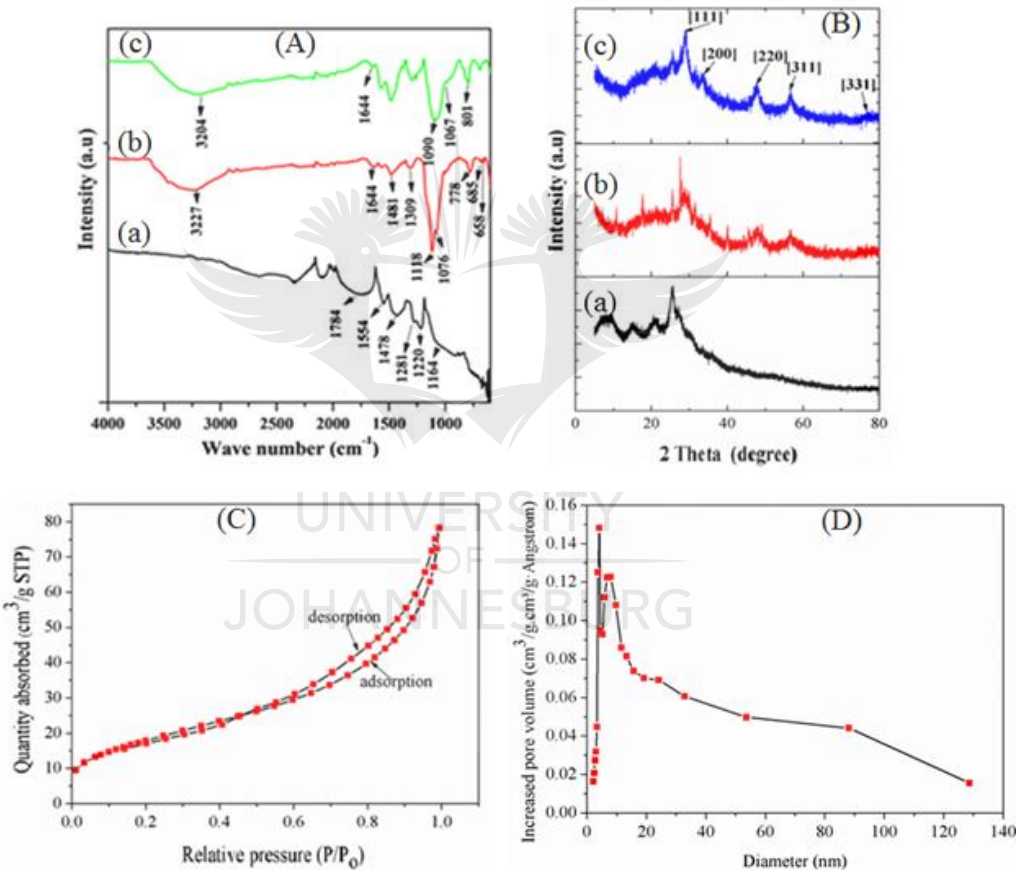

Fig. 5.2: (A) FTIR spectra of (a) pristine PANI NFs, (b) HCeFe NFs-2 adsorbent before and (c) after F^- ions uptake; (B) XRD patterns for (a) PANI NFs (b) hydrous CeO_2-Fe_3O_4 composite and (c) HCeFe NFs-2: (C) N_2 adsorption-desorption isotherm HCeFe NFs-2 composite; (D) pore size distribution curve.

5.3.2.4 XPS analysis

Figs. 5.3(A)(a) and **(b)** show the XPS wide scan spectra of HCeFe NFs-2 before and after F^- adsorption, repectively. Energy bands due to Cl 2p (198.04 eV), C1s (283.98 eV), N1s (398.64 eV), O1s (529.77 eV), Fe 2p (710.12 and 723.66 eV) and Ce 3d (883.37 and 901.11 eV) are noticed [16]. The N 1s and C 1s peaks are associtated with the quinonoid imine, benzenoid amine, doped imine electronic states and the C chain which characterize the backbone of PANI NFs in HCeFe NFs-2 [12,23].

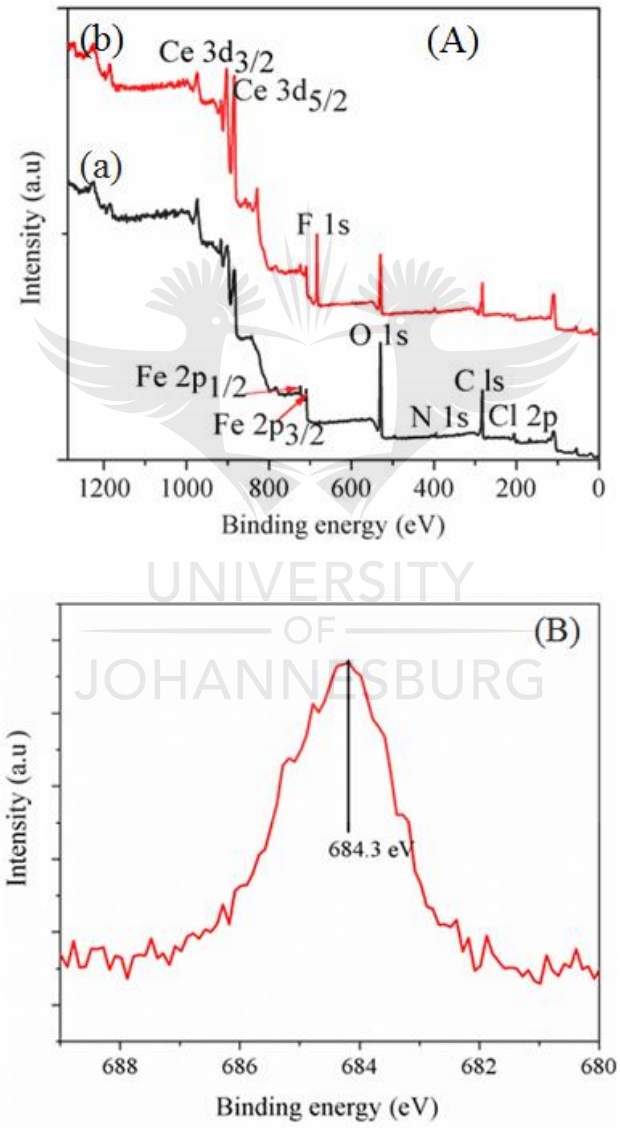

Fig. 5.3: (A) Wide scan XPS spectra of HCeFe NFs-2 (a) before and (b) after F^- ions adsorption; (B) core level XPS spectrum of F 1s.

In addition, the two peaks at binding energies 710.12 and 723.66 eV correspond to Fe $2p_{3/2}$ and Fe $2p_{1/2}$, as a result of Fe element arising from Fe_3O_4, in correlation with literature precedent [35]. A new F 1s core level peak in the XPS wide spectrum at 684.3 eV binding energy (also shown separately in **Fig. 5.3(B)**) is clearly observed in **Fig. 5.3(A)(b)** after adsorption, confirming the uptake of F^- ions onto the adsorbernt [16]. Furthermore, there is a reduction in the intensity of Cl 2p core level peak after F^- adsorption, indicating possible replacement of doped Cl^- ions from PANI NFs.

5.3.2.5 Thermogravimetric-Differential thermal analysis

The TG-DTA thermograms of HCeFe and HCeFe NFs-2 are shown in **Fig. 5.4(A)** and **(B)**. These two materials underwent different thermal decomposition patterns with different percentages of weight loss being observed. With regard to HCeFe, there was an initial weight loss of 10.43% in the range of 50-100 °C due to surface-attached water, followed by a weight loss of 4.66% associated with the exothermic effect around 222 °C as a result of the absorbed water molecules. Thereafter, a final weight loss step amounting to 7.11% up to 693 °C was noticed, most likely as a result of phase transition [15]. Likewise, HCeFe NFs-2 indicated an early weight loss of about 10.86% owing to the loss of surface water in the temperature range of 50-105 °C and subsequent 6.38% weight loss around 206 °C. The observed high weight loss of 30.52% around 350-435 °C is certainly attributed to the thermal decomposition of the PANI NFs skeleton in HCeFe NFs-2 [27,32]. The phase transition, on the other hand, occurred at around 700 °C. Thus HCeFe NFs-2 can be used as highly stable material for water remediation in the adsorption process.

UNIVERSITY JOHANNESBURG

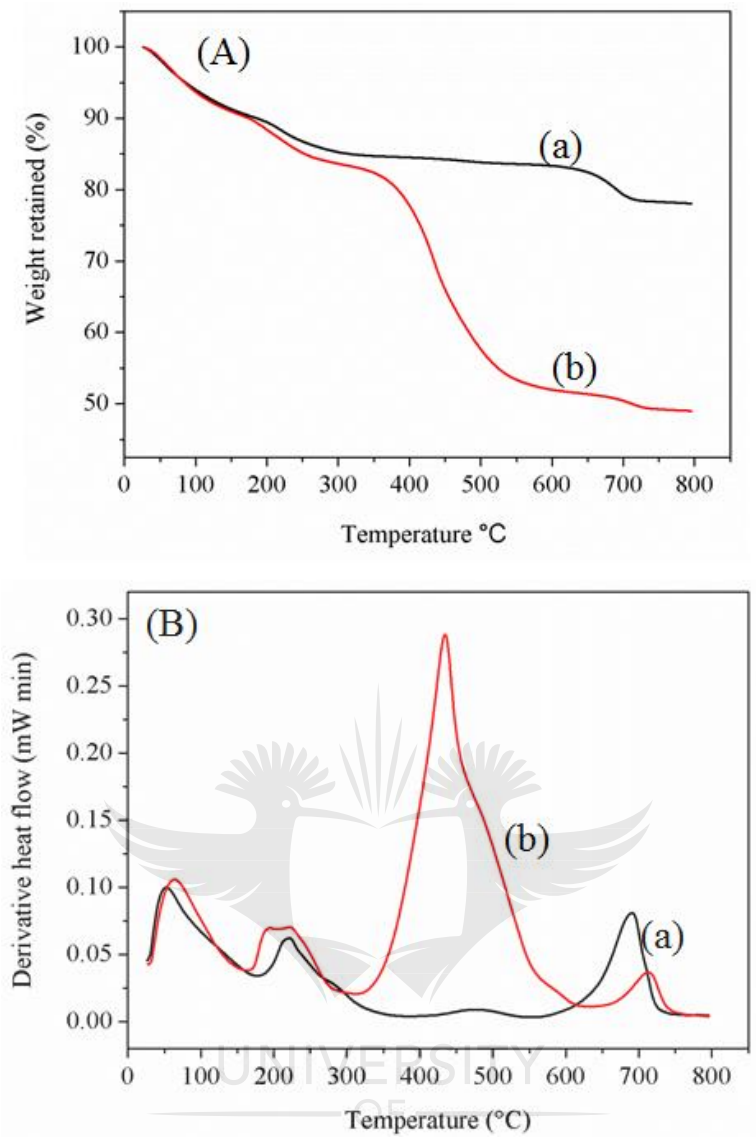

UNIVERSITY OF JOHANNESBURG

Fig. 5.4: (A) TGA and (B) DTA plots of (a) hydrous CeO_2-Fe_3O_4 and (b) HCeFe NFs-2 composite.

5.3.2.6 TEM and SEM

The SEM image of HCeFe NFs-2 is displayed in **Fig. 5.5(a)**. HCeFe NFs-2 morphology consists of nanofibers with agglomerated spherical particles of $HCeO_2$-Fe_3O_4. The HR-TEM image of HCeFe NFs-2 **(Fig. 5.5(b))** revealed that the material is made up of two different components with the black spots indicating the nano-metal oxides and the light-coloured layer indicating PANI NFs. This observation confirms that the agglomerated metal oxides are facilely deposited onto PANI NFs matrix. **Fig. 5.5(c)** shows the HR-TEM images of HCeFe NFs-2 composite at higher magnification. The metal oxides on the PANI NFs exhibited the

lattice fringe with 0.31-0.32 nm spacing corresponding to the (111) crystallography plane of CeO_2 [16,17]. Moreover, the amorphous nature of some of the particles could be attributed to the presence of solid solution of CeO_2 and Fe_3O_4 [15]. These TEM results are in good agreement with XRD analysis where the Fe_3O_4 peaks could hardly be observed due to their amorphous behaviour in this material [16].

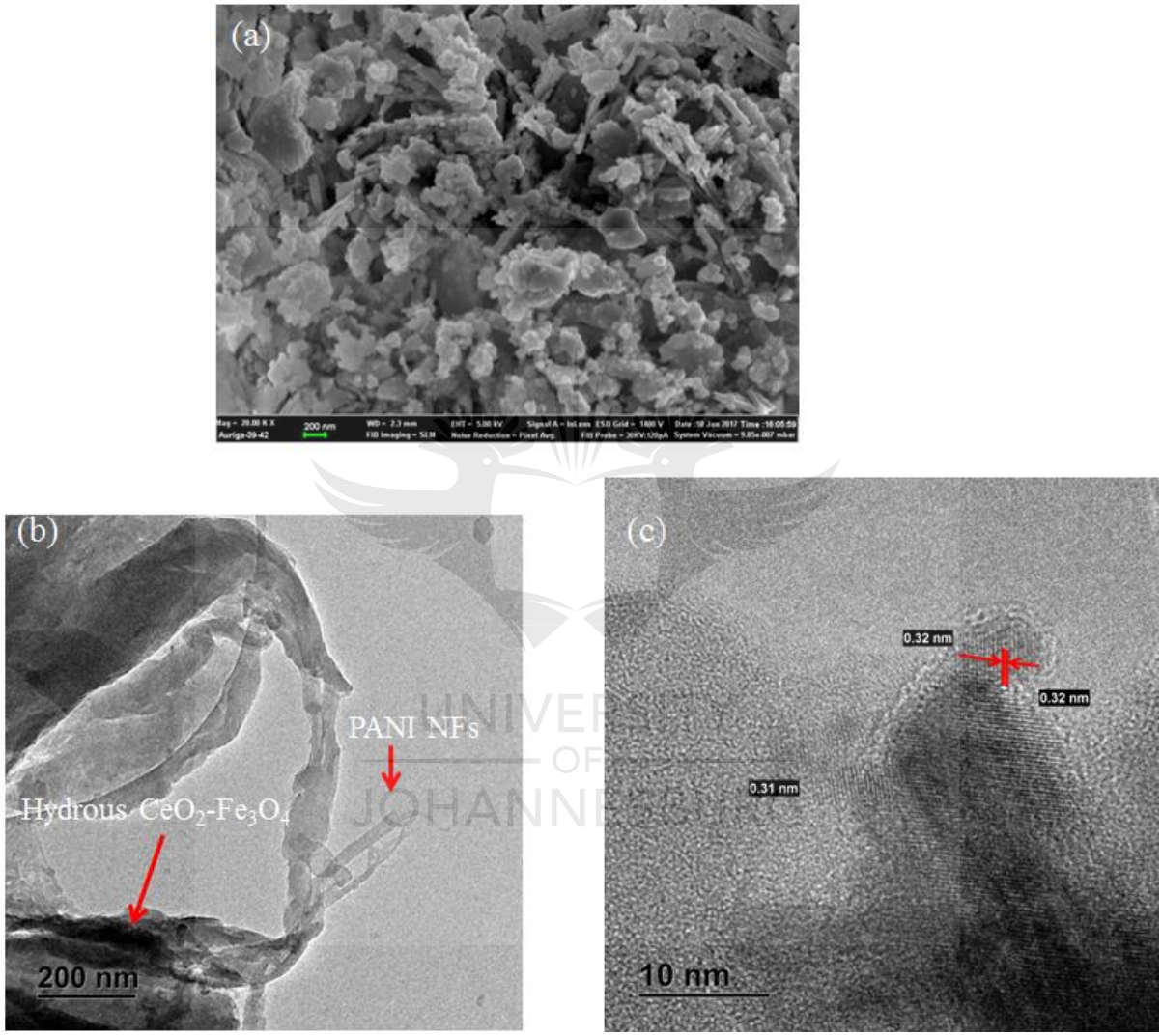

Fig. 5.5: (a) SEM, (b) TEM and (c) HR-TEM images of HCeFe NFs-2.

TEM mapping was accomplished to consolidate the presence of hydrous Ce and Fe oxides in the HCeFe NFs-2 structure as well as its F^- ions uptake ability. **Fig. 5.6** shows a uniform distribution of C, N, O, Ce , Fe and F elements at the surface of HCeFe NFs-2 after treatment.

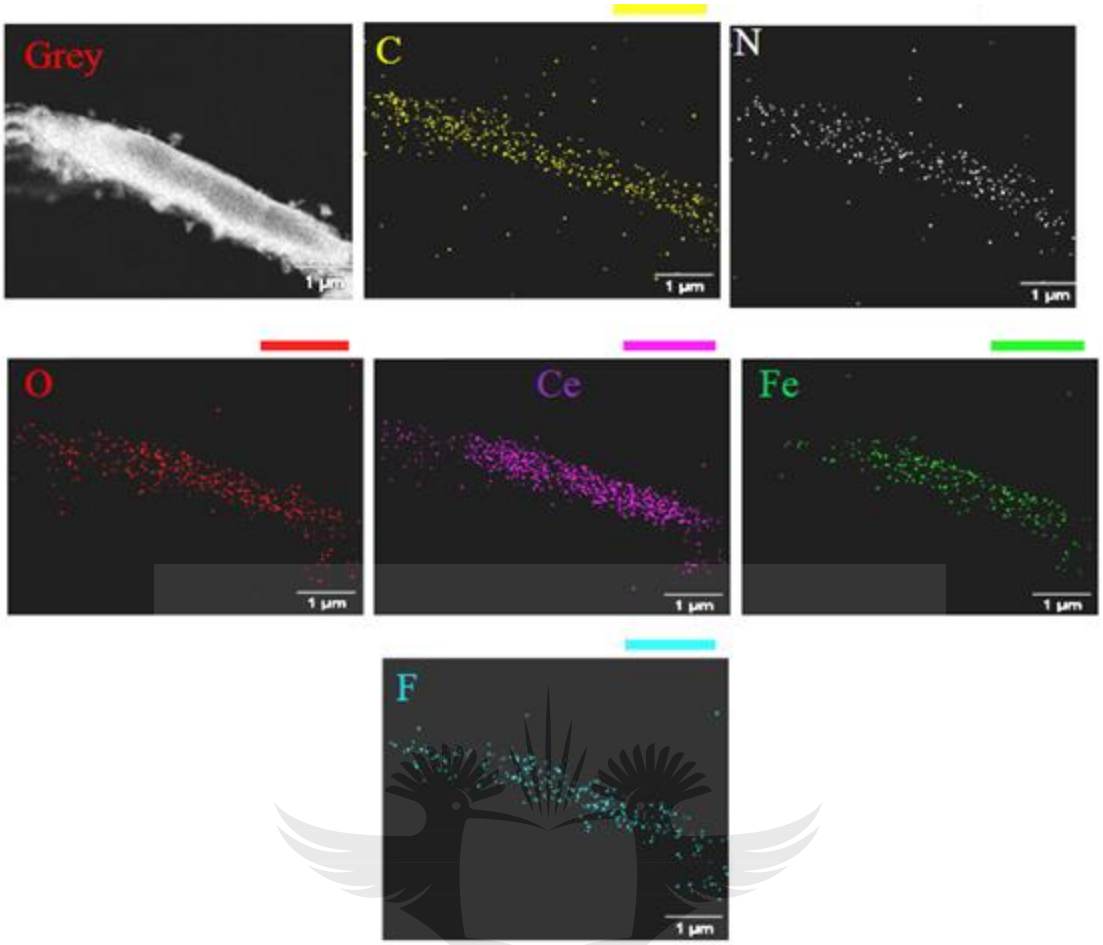

Fig. 5.6: STEM elemental mapping (C, N, O, Ce, Fe and F) for HCeFe NFs-2 composite after fluoride adsorption.

UNIVERSITY OF JOHANNESBURG

5.3.2.7 Energy dispersive X-ray spectra

The EDX analysis of SEM image of HCeFe NFs-2 adsorbent shown in **Fig. 5.7(b)** clearly revealed the existence of Ce and Fe besides C, N, Cl and O elements. Peaks corresponding to C, O, N, Cl, Ce and Fe elements were detected at energy values of 0.277, 0.525, 0.525, 2.667, 4.667 and 6.404 keV, respectively. This highlights the presence of Ce and Fe on the polyaniline nanofiber. Nevertheless, the EDX spectrum of pristine PANI NFs only revealed peaks for C, N and Cl as presented in **Fig. 5.7(a).** The specrtrum after adsorption of F^- ions is shown in **Fig. 5.7(c).** Comparing **Fig. 5.7(b)** with **5.7(c)**, a new peak corresponding to F element appears at energy value 0.667 keV, revealing F^- ions uptake onto the adsorbent.

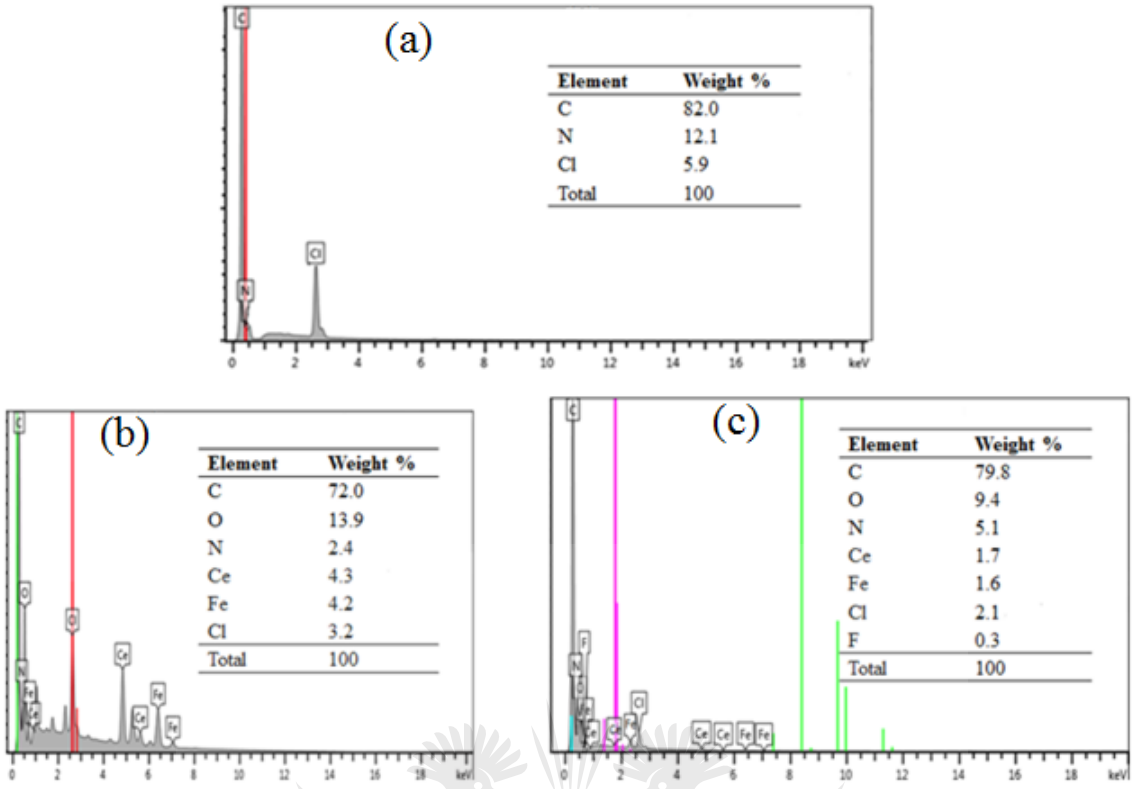

Fig. 5.7: EDX spectra of (a) PANI NFs (b) HCeFe NFs-2 composite before and (c) after F^- ions adsorption.

UNIVERSITY OF JOHANNESBURG

5.3.2.8 Point-of-zero charge analysis

The pH at the point-of-zero charge (pH_{pzc}) is a parameter which indicates the zero electrostatic potential of a surface at that particular pH, hence it was investigated. The pH_{pzc} of HCeFe NFs-2 was found to be around 6.6, as shown in **Fig. 5.8(a)**. Thus, at pH < 6.6 the surface of HCeFe NFs-2 is predominantly positive and above, it is expected to be predominantly negative. Therefore F^- ions can be attracted to the surface of the prepared adsorbent at pH < 6.6 through electrostatic interactions among other mechanisms.

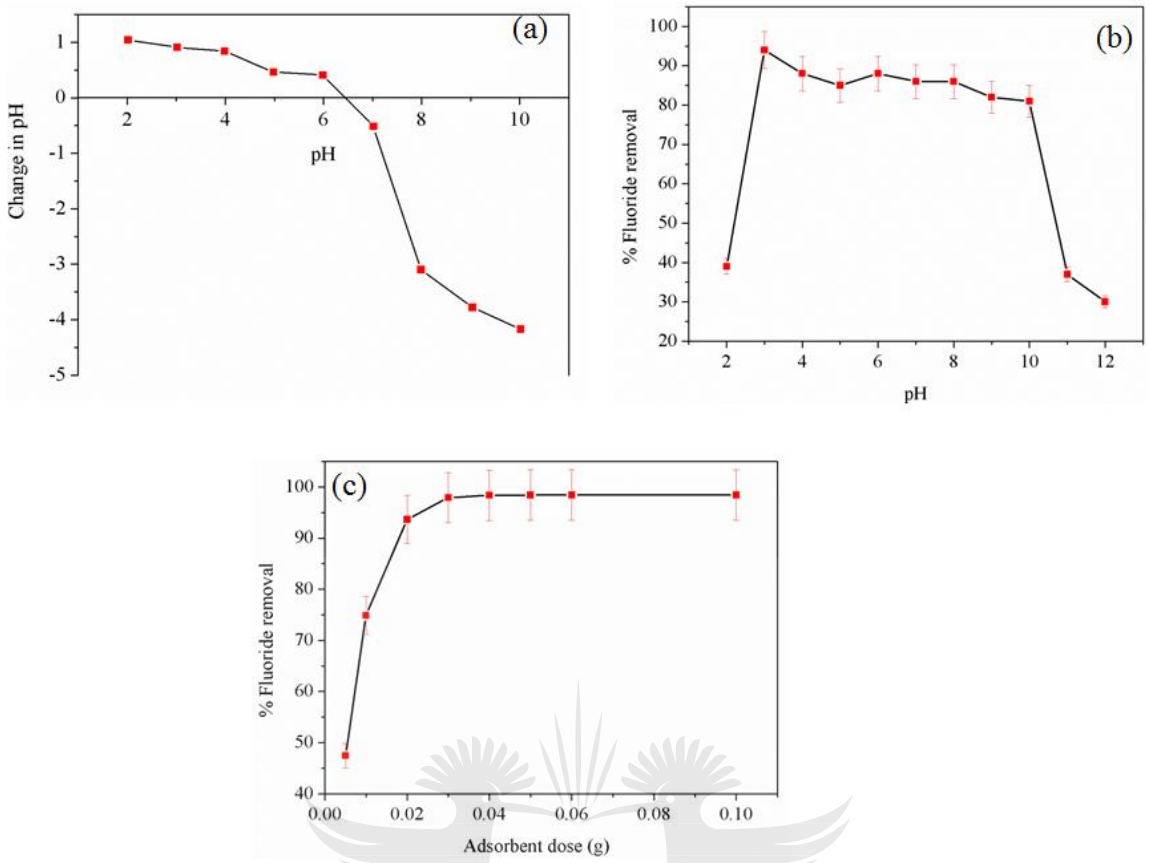

Fig. 5.8: (a) Determination of pH at the point-of-zero charge of HCeFe NFs-2 composite; Influence of (b) pH using 0.03 g dose and (c) HCeFe NFs-2 dose on F^- ions adsorption at pH 6.0 ± 0.2 for 24 h shaking time.

UNIVERSITY OF JOHANNESBURG

5.3.4 Batch adsorption study

5.3.4.1 Effect of pH on the removal of F^- ions

Solution pH is a principal factor that affects adsorption at the solute/solid interface. Its influence on F^- ions removal was studied from pH 2 to 12. As shown in **Fig. 5.8(b)** the sorption occurred over a pH range of 3-10 from which the percentage removal was almost constant between 94.00 and 80.61%. Maximum adsorption was observed at pH 3 (94.00%) and gradually decreased to 38% as the pH increased to 11. This could be attributed to the fact that at pH 2, most of F^- exists as neutral hydrogen fluoride which limits its adsorption. In addition, at very high pH 11-12 the solution has more hydroxyl than hydrogen ions, leading to competitive adsorption between hydroxyl and F^- ions on the active sites [15,29,30]. The effect of pH is regarded as related to point-of-zero charge (pH_{zc}) of an adsorbent. At pH < pH_{pzc}, there

is protonation of the nitrogen atoms on PANI NFs and hydrous metal oxides, giving rise to an overall positive charge of the adsorbent's surface, resulting in possible electrostatic interactions and thereby adsorption of F^- ions [6,15,19]. The adsorbent surface being negatively charged when pH was over 6.6, this may serve as another reason for the decrease in adsorption capacity with increasing pH. In that regard, electrostatic repulsion exists between F^- and hydroxyl groups on the adsorbent surface and only anionic exchange is expected to take place [20]. This demonstrates the applicability of HCeFe NFs-2 adsorbent for the removal of F^- over a wide pH range of 3-10.

5.3.4.2 Effect of adsorbent dose

The influence of HCeFe NFs-2 adsorbent amount on the adsorption of F^- was investigated at pH 6.0 ± 0.2 and at 25 °C and the results are presented in **Fig. 5.8(c)**. The percentage of F^- removal increased from 47.44% to 98.00% with increasing the dose from 0.005 to 0.03 g as more active sites for F^- adsorption became available [30]. The removal efficiency remained constant as adsorbent amount increased from 0.04 to 0.1 g. This could be because at high dosage, active sites overlap or agglomerate and this lead to less available sites for adsorption [36]. Consequently, 0.03 g dose was adopted for the entire adsorption investigations.

5.3.4.3 Adsorption isotherms

UNIVERSITY OF JOHANNESBURG

Adsorption isotherms are important in appreciating the interaction between adsorbent and pollutant for the planning and operation of a tangible adsorption system. The effect of temperature on the adsorption of F^- ions by HCeFe NFs-2 was therefore studied at 15, 25, 35 and 45 °C and the results are presented in **Fig. 5.9(a)**, **(b)** and **(c)**. The adsorption of F^- decreases with increase in temperature, suggesting an exothermic nature of the process. The increase in temperature has previously been reported to decrease the attachment tendency of F^- ions onto Ce-Fe bimetal oxides surface and thereby weakening the degree of adsorption [15,16]. The adsorption data were analysed using two common isotherm models, the Langmuir and the Freundlich. The Langmuir model simulates monolayer exposure and that all the active sites at the surface of the adsorbent have equivalent affinity for the adsorbates with no lateral interaction between molecules [37,38]. The Langmuir linear and nonlinear forms are represented by **Equations (5.4)** and **(5.5)** respectively.

$$\frac{C_e}{q_e} = \frac{1}{q_m b} + \frac{C_e}{q_m} \quad (5.4)$$

$$q_e = \frac{bq_m C_e}{1+bC_e} \quad (5.5)$$

where C_e (mg/L) and q_e (mg/g) are the equilibrium concentration of F^- ions in solution and the amount of F^- ions adsorbed per unit mass of adsorbent at equilibrium, respectively. q_m is the maximum adsorption capacity; b (L/mg) is the Langmuir constant related to the F^- ions affinity for the binding sites [9,36]. The fit of the isotherm data by nonlinear and linear form of the Langmuir model is presented in **Fig. 5.9(b)** and **(c)** and the calculated isotherm parameters are summarised in **Table 5.1**. The Langmuir parameters q_m and b at different temperatures were evaluated for linear and nonlinear Langmuir model fit and are also presented in **Table 5.1**. The q_m values evaluated from the data, ranged from 117.64 to 93.46 mg/g for linear and 110.20 to 89.17 mg/g for nonlinear fit. The decrease in q_m with temperature further validates the exothermic nature of the adsorption and the general decrease in b with temperature indicates lesser energy of binding at higher temperatures [7]. The dimensionless constant R_L is an essential parameter which indicates favourability or non-favourability of adsorption of Langmuir isotherm model. It is expressed by **Equation (5.6)**

$$R_L = \frac{1}{1+bCo} \quad (5.6)$$

UNIVERSITY OF JOHANNESBURG

R_L values within the range $0 < R_L < 1$ for each of the different initial concentrations indicate favourable adsorption. Whereas, $R_L = 1$, $R_L = 0$ and $R_L > 1$ suggest linear, irreversible and unfavourable adsorption process, respectively. For this study, the R_L values were established to be between 0 and 1, defining a favourable adsorption process (**Table 5.1**).

The nonlinear [7] and linear [39] forms of the Freundlich isotherm were also evaluated for the isotherm applicability of the data and these are represented in **Equation (5.7)** and **(5.8)**.

$$q_e = K_f C_e^{\,1/n} \quad (5.7)$$

$$lnq_e = lnK_f + \frac{1}{n} lnC_e \quad (5.8)$$

where K_f denotes the Freundlich isotherm constant related to adsorption capacity. The coefficient *1/n*, on the other hand, is associated with the heterogeneity of the adsorption site energies and adsorption intensity [29]. The higher the K_f value, the greater will be the adsorption efficiency. Moreover, *n* values within the range 0 and 10 indicate stronger adsorbate/adsorbent interaction and thereby better adsorption processes [28,40]. The K_f and *1/n* values were evaluated and are shown in **Table 5.1**. The values of *1/n*, obtained using the curve plotted ln q_e against ln C_e are as follows; 0.364, 0.512, 0.319 and 0.361 for the temperatures 15, 25, 35 and 45 °C, respectively. The smallest value of 1/*n*, that is, 0.32 and higher value of *n* (3.12) indicates active interaction between HCeFe NFs-2 and F^- ions [6,38].

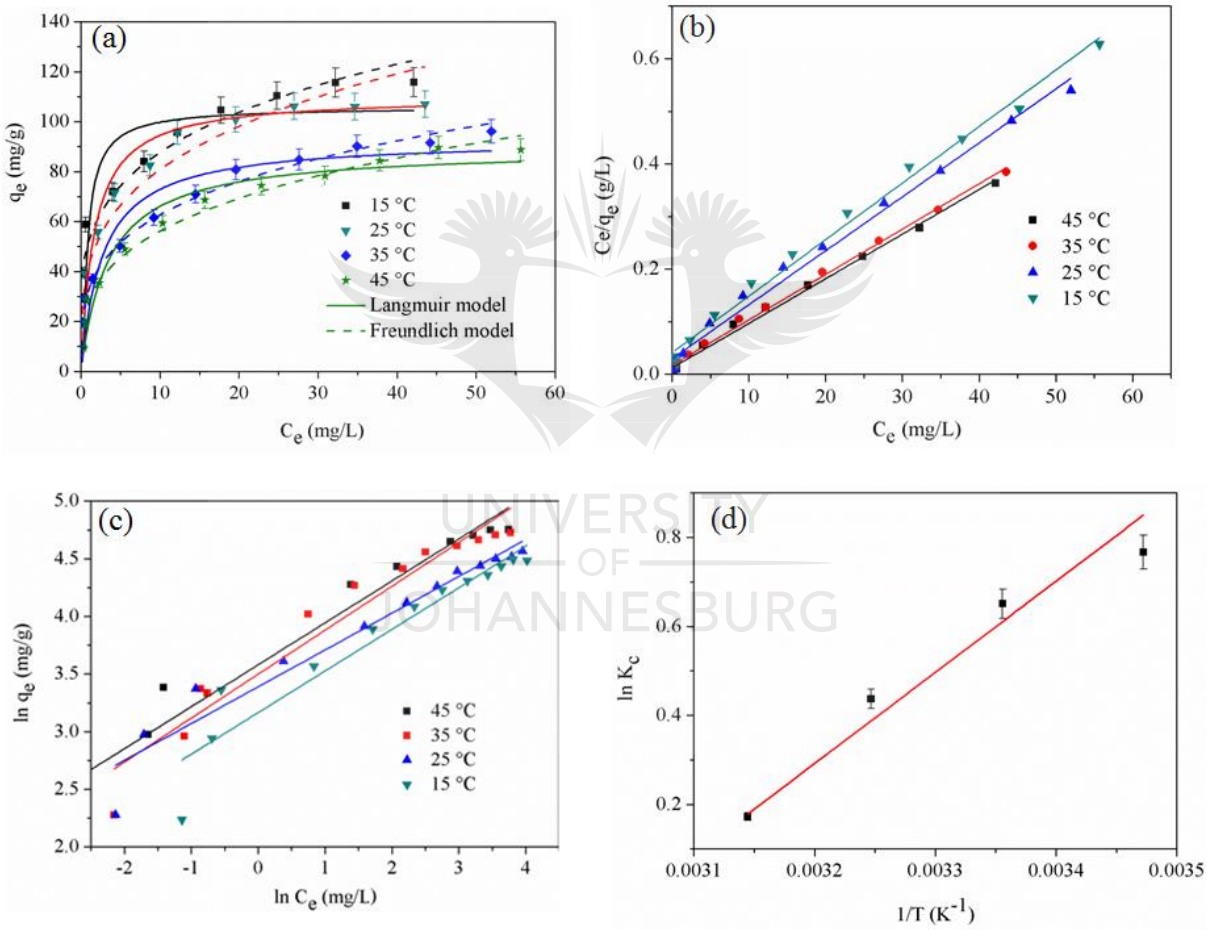

Fig. 5.9: (a) Adsorption equilibrium isotherms for F^- ions removal by HCeFe NFs-2 composite and the data fit to Langmuir and Freundlich nonlinear models; Fit of data to linearized (b) Langmuir and (c) Freundlich models; (d) Van't Hoff's plot for the determination of thermodynamic parameters.

Fig. 5.9(b) and **(c)** show the linear fit of the equilibrium data for the Langmuir and Freundlich models. Comparing both models, it is observed that the R^2 values for the Langmuir (R^2_{linear} = 0.9906-0.9970) were higher than those obtained from the Freundlich model (R^2_{linear} = 0.9136-0.9520) for all temperatures. Based on this comparison, the Langmuir isotherm best described the adsorption process and the evaluated q_m values ranged from 117.64−93.46 mg/g for 15 to 45 °C. These obtained q_m values were much higher than those for previously reported hydrous Ce-Fe binary metal oxides 24.80 mg/g [15] and pristine PANI 0.77 mg/g [12]. Furthermore, the performance of HCeFe NFs-2 for the adsorption of F^- ions was also assessed by comparison with other related adsorbents in the literature as shown in **Table 5.2**. It is evident that HCeFe NFs-2 has very high adsorption capacity and can therefore be seen as good material for application in water defluoridation.

Table 5.1: Langmuir and Freundlich parameters for the sorption of F^- ions onto HCeFe NFs-2 composite.

Isotherm models	Temperature /K			
	288	298	308	318
Langmuir				
Linear model				
q_m (mg/g)	117.64 ± 5.882	116.28 ± 5.814	97.08 ± 4.854	93.46 ± 4.673
b (L/mg)	0.692 ± 0.0346	0.494 ± 0.0247	0.335 ± 0.0167	0.258 ± 0.0129
R_L	0.0588 ± 0.0029	0.0787 ± 0.0039	0.109 ± 0.0054	0.123 ± 0.0062
R^2	0.9950	0.9970	0.9906	0.9922
Non-linear				
Best-fit values				
q_m	110.2	105.9	92.90	89.17
b	0.6039	1.683	0.3655	0.2866
Std. Error				
q_m	4.107	5.134	5.753	4.557
b	0.1174	0.4799	0.1255	0.07303
95% Confidence Intervals				
q_m	101.0 to 119.3	94.46 to 117.3	80.08 to 105.7	79.02 to 99.32
b	0.3423 - 0.8655	0.6135 -2.752	0.08592 -0.6451	0.1238 -0.4493
Goodness of Fit				
Degrees of Freedom	10	10	10	10
R^2	0.9648	0.9175	0.9117	0.9405
Absolute Sum of Squares	548.9	1376	892.3	520.5
Sy.x	7.408	11.73	9.446	7.214
Number of points Analyzed	12	12	12	12

UNIVERSITY OF JOHANNESBURG

Freundlich linear model				
K_f (mg/g)	35.90 ± 1.795	33.09 ± 1.655	29.67 ± 1.484	23.71 ± 1.186
1/n	0.364 ± 0.018	0.5123± 0.025	0.319 ± 0.0160	0.361 ± 0.0181
R^2	0.9520	0.9412	0.9455	0.9136
Non-linear model				
Best-fit values				
K_f	49.29	42.46	32.95	27.95
n	4.041	3.575	3.579	3.300
Std. Error				
K_f	3.784	3.274	1.629	1.981
n	0.4180	0.3240	0.1932	0.2307
95% Confidence Intervals				
K_f	40.86 to 57.72	35.17 to 49.75	29.32 to 36.58	23.54 to 32.36
n	3.109 to 4.972	2.853 to 4.296	3.148 to 4.009	2.786 to 3.814
Goodness of Fit				
Degrees of Freedom	10	10	10	10
R^2	0.9455	0.9569	0.9860	0.9749
Absolute Sum of Squares	909.9	671.6	142.0	219.8
Sy.x	9.539	8.195	3.768	4.688
Number of points Analyzed	12	12	12	12

Table 5.2: Comparative assessment of F^- ions adsorption capacity of HCeFe NFs-2 composite with other reported materials.

Adsorbent	Adsorption Capacity (mg/g)	Optimum pH	Ref.
Polypyrrole+ hydrous TiO_2	31.95	6.5	[2]
Fe_3O_4@Alg-La	45.23	4.0	[7]
Fe_3O_4 polypyrrole	17.6–22.3	6.5	[8]
PANI-Aluminium oxide	6.60	3.0	[12]
Hydrous cerium-iron(III) oxide	24.80	5.0–7.0	[15]
Fe_3O_4@$Al(OH)_3$ magnetic material	88.48	6.5	[20]
β-Cyclodextrin modified hydrous ZrO_2	17.73	6.9	[36]
Hydrous Zirconium oxide	124.00 and 68.00	4.0 and 7.0	[41]
CeO_2–ZrO_2 nanocages	175.00	4.0	[42]
HCeFe NFs-2 nanocomposite	116.28	6.0	Present work

5.3.4.4 Thermodynamic parameters for F^- adsorption by HCeFe NFs-2

The thermodynamic characteristic parameters, $\Delta G°$, $\Delta H°$ and $\Delta S°$ were evaluated from adsorption isotherm data using **Equation (5.9)** and **(5.10)**:

$$\Delta G° = -RT \ln K_c = -RT \ln \left(m \frac{q_e}{C_e}\right) \quad (5.9)$$

$$\ln \left(m \frac{q_e}{C_e}\right) = \frac{\Delta S°}{R} - \frac{\Delta H°}{RT} \quad (5.10)$$

where R (J/mol K), T (K) and K_c are the molar gas constant, temperature and the equilibrium constant, respectively. The ratio mq_e/C_e is the adsorption affinity. The values of $\Delta H°$ and $\Delta S°$ were computed from the slope and intercept of the plot of ln (mq_e/C_e) versus $1/T$, respectively as shown in **Fig. 5.9(d)**. The values of $\Delta G°$ were calculated by using **Equation (5.9)**. The thermodynamic parameters are presented in **Table 5.3**. The negative value of $\Delta H°$ confirms the feasibility of an exothermic adsorption process, as reported previously on the use of metal oxide-based nanoadsorbents [7,15,16]. The negative value of $\Delta S°$ indicates decrease in amount of species at the solid-liquid interface and hence randomness. The negative values of $\Delta G°$ (-1.835 to -0.455 kJ/mol) suggest a spontaneous F^- adsorption process through physical sorption under experimental conditions. Moreover, its decrease in magnitude with increase temperature indicates that the process was more favourable at low temperatures.

Table 5.3: Thermodynamic data from effect of temperature on adsorption

Temperature (°C)	$\Delta G°$ (kJ/mol)	$\Delta H°$ (kJ/mol)	$\Delta S°$ (kJ/mol/K)	R^2
15	-1.835 ± 0.09	-15.10	-0.0458	0.999
25	-1.612 ± 0.08			
35	-1.190 ± 0.06			
45	-0.455 ± 0.02			

5.3.4.5 Adsorption kinetics

Kinetics studies are useful in predicting the adsorption rate that gives insight into design and modelling for adsorption based water treatment processes [8]. An adsorbent must have rapid adsorption kinetics to be considered feasible for industrial application. The effect of contact time for F^- adsorption on HCeFe NFs-2 adsorbent was studied for four initial F^- ions

concentrations 10, 20, 30 and 40 mg/L at 25 °C as shown in **Fig. 5.10(a)**. F^- ions adsorption increased with contact time and was relatively rapid, with most of the adsorption taking place in the first 10, 45, 75 and 90 minutes, respectively. This time range is shorter as compared to some reported adsorbent contact times in literature [28,41,42]. To study the kinetic mechanism of the adsorption, the nonlinear and linear pseudo-first-order and pseudo-second-order kinetic models, were employed and these are represented by **Equations (5.11)** to **(5.14)**:

$$q_t = q_e(1 - \exp(^{-k_1\,t}) \tag{5.11}$$

$$\log(q_e\ -\ q_t\ ) = \log(q_e\ ) - \frac{k_1}{2.303}\ t \tag{5.12}$$

$$q_t = \frac{k_2 q_e 2\ t}{1 + k_2 q_e t} \tag{5.13}$$

$$\frac{t}{q_t} = \frac{1}{k_2 q_e 2} + \frac{t}{q_e} \tag{5.14}$$

where k_1 (min^{-1}) and k_2 (g/mg.min) are the pseudo-first-order and pseudo-second-order-rate constants respectively. q_e and q_t (mg/g) are the adsorption capacities at equilibrium and time t (min), respectively. The non-linear and linear plots of the pseudo-second-order and pseudo-first kinetics models are illustrated in **Fig. 5.10(a), (b)** and **(c)**. The values for the rate constants and other parameters computed from linear and non-linear regression plots are shown in **Table 5.4**. The R^2 values obtained from the pseudo-second-order model (R^2_{linear} = 0.9999-1.000 and $R^2_{nonlinear}$ = 0.8800-0.9685) are greater than those from the pseudo-first-order model (R^2_{linear} = 0. 0.9609-0.9998 and $R^2_{nonlinear}$ = 0.8377-0.9739). Furthermore, the q_e values acquired from the pseudo-second-order model were in close concurrence with the experimental values. Consequently, it can be deduced that the F^- ions adsorption onto HCeFe NFs-2 followed the pseudo-second-order kinetics model. The values of k_2 generally decreased from 0.2471 to 0.0302 (g/mg.min) with surge in initial F^- ions concentration, owing to the increase in the rate of adsorption with decrease in concentration. Moreover, to understand the nature of the rate controlling step in the adsorption of F^- ions, the Webber-Morris intra-particle diffusion model was employed and the equation is as follows:

$$q_t\ =\ k_{int}\, t^{0.5} + C_i \tag{5.15}$$

where k_{int} (mg/g $min^{0.5}$) and C_i (mg/g) are the intra-particle diffusion rate constant and constant linked to the magnitude of the boundary layer thickness, respectively. Plots of $t^{0.5}$ against q_t produced for different initial F^- ions concentrations are shown in **Fig. 5.10(c)**. The initial part may be governed by boundary layer diffusion and the second part by intra-particle diffusion. The values of k_{int} for the four different concentrations of F^- ions were acquired from the slopes of the initial linear part of the curves and displayed in **Table 5.4**, together with the R^2 values. The values of k_{int} increased from 7.7319 to 19.9730 mg/g.$min^{0.5}$ as the initial concentration increased from 10 mg/L to 40 mg/L. The deviation of the straight lines from the origin could be attributed to the variance between the rate of mass transfer in the initial and final stages which indicates a complex situation in which both film diffusion and intra-particle diffusion contribute to the rate determining step [2].

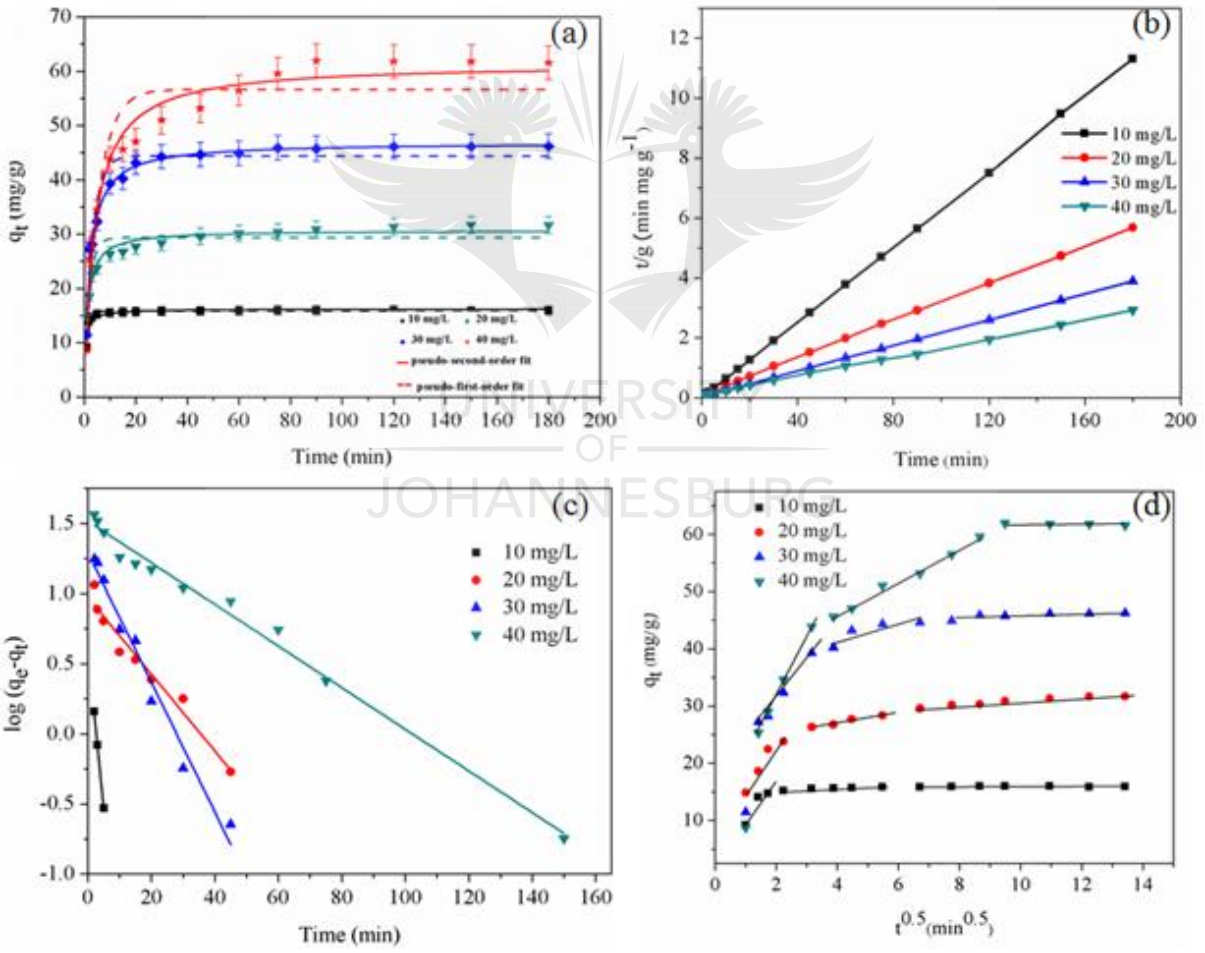

Fig. 5.10: (a) Effect of contact time on the adsorption of F^- ions on HCeFe NFs-2 composite and fit of kinetic data to (a) pseudo-first-order and second order nonlinear (b) pseudo-second-order linear (c) pseudo-first-order linear kinetic models: at pH 6.0 ± 0.2,

adsorbent dose 0.03 g, contact time 24 h and temperature 25 °C; (d) Intra-particle diffusion model.

Table 5.4: Summary of kinetics parameters for the sorption of F^- ions by HCeFe NFs-2 composite at different concentrations.

Kinetic models	Initial concentration (mg/L)			
	10	20	30	40
Pseudo- first-order				
Linear				
k_1 **(g**/mg min)	0.527 ± 0.0264	0.063 ± 0.00315	0.106 ± 0.00532	0.03408 ± 0.0017
q_e (mg/g)	4.095 ± 0.205	9.304 ± 0.465	19.56 ± 0.978	32.88 ± 1.644
R^2	0.9998	0.9609	0.9767	0.9877
Non-linear				
Best-fit values				
q_e	15.81	29.33	44.38	56.62
k_1 (1/min)	0.9376	0.5083	0.3328	0.1876
Std. Error				
q_e	0.08338	0.6314	0.8082	1.790
k_1	0.03711	0.06403	0.03263	0.02971
95% Confidence Intervals				
q_e	15.63 to 15.99	27.97 to 30.69	42.63 to 46.12	52.75 to 60.48
k_1	0.8574-1.018	0.3700 -0.6466	0.2624-0.4033	0.1234-0.2517
Goodness of Fit				
Degrees of Freedom	13	13	13	13
R^2	0.9739	0.8377	0.9374	0.8948
Absolute Sum of Squares	1.098	57.91	88.84	378.7
Sy.x	0.2906	2.111	2.614	5.397
Number of points Analyzed	15	15	15	15
Pseudo-second – order				
Linear				
k_2 (g/mg. min)	0.247 ± 0.0302	0.142 ± 0.00708	0.112 ± 0.00559	0.0302 ± 0.00151
q_e *(mg/g)*	15.94 ± 0.797	30.30 ± 1.515	44.82 ± 2.241	63.78 ± 3.189
R^2	1	1	1	0.999
Non-linear				
Best-fit values				
k_2	0.1215	0.02615	0.01047	0.004054
q_e	16.18	30.65	46.85	61.39
Std. Error				
k_2	0.01802	0.002436	0.0009763	0.0005160
q_e	0.2010	0.3478	0.6084	1.249
95% Confidence Intervals				
k_2	0.08260 to 0.1604	0.02089 to 0.03142	0.008361 to 0.01258	0.002940 to 0.005169
q_e	15.74 - 16.61	29.90 -31.40	45.53 -48.16	58.69 -64.08
Goodness of Fit				

UNIVERSITY OF JOHANNESBURG

Degrees of Freedom	13	13	13	13
R^2	0.8800	0.9635	0.9753	0.9685
Absolute Sum of Squares	5.053	13.04	35.06	113.5
Sy.x	0.6234	1.001	1.642	2.955
Number of points Analyzed	15	15	15	15
Intraparticle diffussion				
k_{int} (mg/g. min)$^{1/2}$	7.732 ± 0.387	7.442 ± 0.387	11.147 ± 0.557	19.973± 0.999
C_i (mg/g)	1.971 ± 0.0985	8.039 ± 0.401	6.461 ± 0.323	7.4874 ± 0.374
R^2	0.885	0.929	0.877	0.879

5.3.4.6 Desorption studies and mechanical stability of HCeFe NFs-2

Regeneration of the utilised adsorbent is very important to assess its potential and costs effectiveness [43]. The adsorbent regeneration efficiency of HCeFe NFs-2 was evaluated by employing desorption-adsorption experiments. The adsorbent maintained its original efficiency up to two cycles as illustrated in **Fig. 5.11(a)**. In the third cycle a reduction to 64.2% is observed. This suggests that HCeFe NFs-2 can be used for 3 consecutive adsorptions-desorption cycles.

The dynamic mechanical analysis of PANI NFs, HCeFe NFs-2 and bimetal oxides HCeFe NPs is shown in **Fig. 5.11(b)** and **(c)**. The results revealed that HCeFe NFs-2 displays better mechanical properties than PANI NFs. For the complete temperature array tested, the storage modulus of HCeFe NFs-2 was slightly higher relative to PANI NFs **(Fig. 5.11(b))**. This observation is attributed to the presence of nano-metal oxides, which restrict the mobility of PANI macromolecular chains in HCeFe NFs-2 [44,45]. An opposite trend to the variation in storage modulus was observed for the loss factor, tan δ as shown in **Fig. 5.11(c)**. The tan δ, represents the proportion of the loss modulus to the storage modulus and is strongly related to structural transformations. The tan δ data of HCeFe NFs-2 were found to be lower than those of PANI NFs, indication that the presence of metal oxides in HCeFe NFs-2 serves as reinforcement in the PANI matrix and decreases the damping behaviour [46].

UNIVERSITY OF JOHANNESBURG

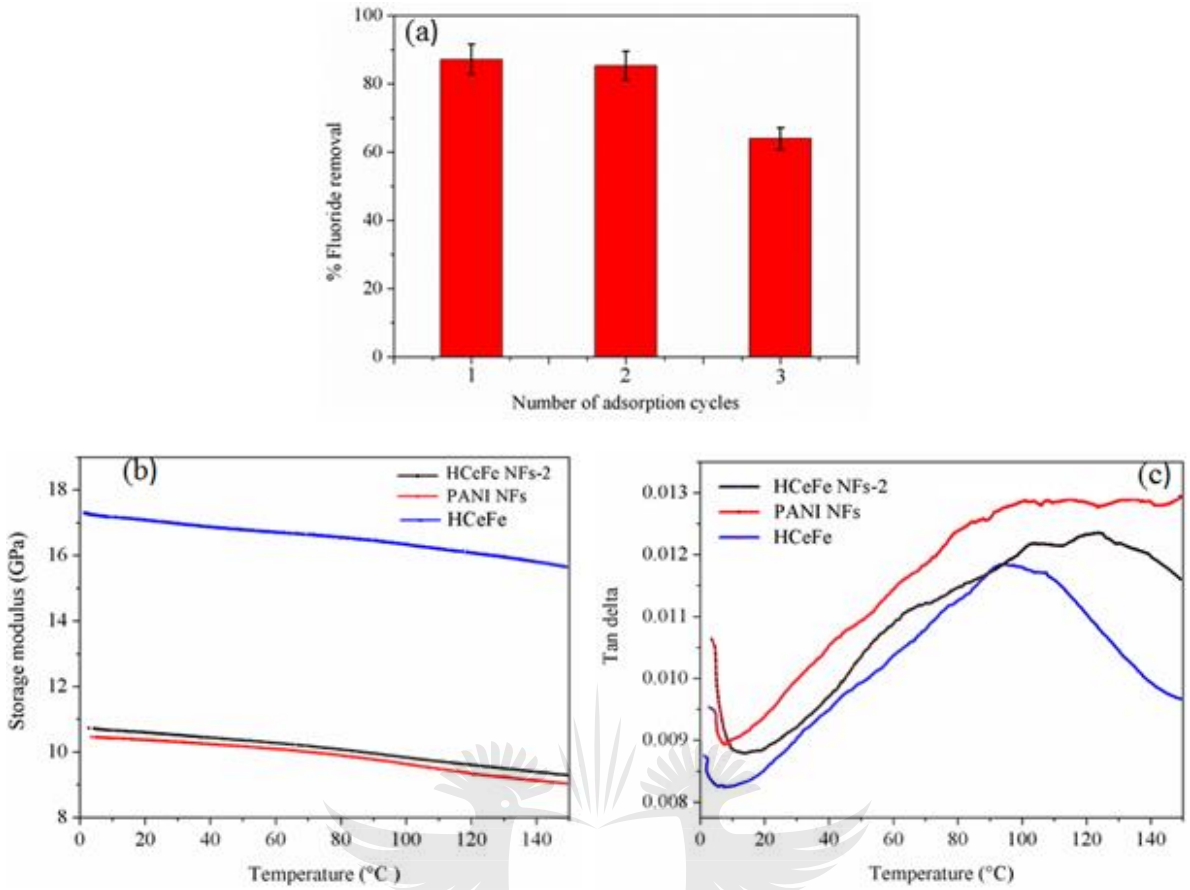

Fig. 5.11. (a) Adsorption and desorption cycles of HCeFe NFs-2 composite; Variation of (b) storage modulus and (c) tan δ against temperature for PANI NFs, HCeFe NFs-2 and hydrous CeO_2-Fe_3O_4 adsorbents.

UNIVERSITY OF JOHANNESBURG

5.3.4.7 Effect of co-existing ions

Numerous ions are simultaneously present in natural water and wastewater systems. The effect of several anions like sulphate (SO_4^{2-}), chloride (Cl^-), bicarbonate (HCO_3^-), phosphate (PO_4^{3-}) and nitrate (NO_3^-) on the F^- adsorption onto HCeFe NFs-2 is illustrated in **Fig. 5.12(a)**. The sorption of F^- ions is influenced by SO_4^{2-}, HCO_3^- and PO_4^{3-} ions, with PO_4^{3-} ions having the greatest effect. F^- uptake decreased from 84.47 to 35.80% when phosphate ions increased from 0 to 40 mg/L. The order of interference was $PO_4^{3-} > HCO_3^- > SO_4^{2-} > NO_3^- > Cl^-$. The Cl^- and NO_3^- ions had very little interference as they are well known as low affinity ligands, forming outer-sphere complexes with active sites on the surface of the adsorbent [2]. This order of interference is closely related to the Z/R (charge/radius) values of the anions PO_4^{3-} (3/3.40) > SO_4^{2-} (2/2.40) > Cl^- (1/1.18) > NO^-_3 (1/2.81). Fortunately, the concentration of PO_4^{3-} ions in

drinking water is ordinarily depressed hence its competitive impact on F^- ions removal may be minimal [43,47,48]

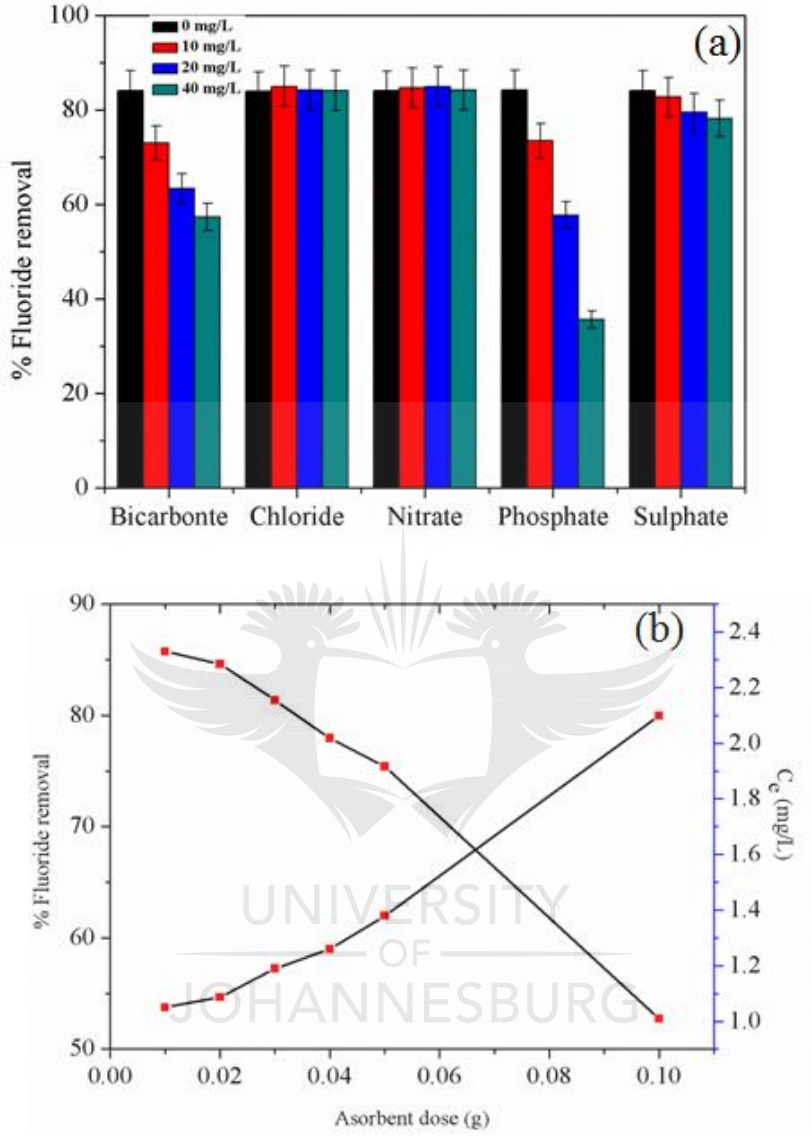

Fig. 5.12: (a) Effect of co-existing ion on the adsorption of F^- ions at pH = 6 ± 0.2, adsorbent dose of 0.03 g per 50 mL of solution at 25 °C and (b) Effect of adsorbent dose on % F^- ions removal and equilibrium F^- ions concentration using field collected fluoride-containing water sample.

5.3.4.8 Performance on natural water samples

The potential applicability of HCeFe NFs-2 composite for real F^- containing samples from a shallow well at Nemutenzi village (444785E/7828266N), in Nyanyadzi/Hot Spring area of

Manicaland Province of Zimbabwe was evaluated. This was done by spiking well water to increase its concentration of F^- ions from 2.96 mg/L to 5.0 mg/L. Other characteristics of this water were pH = 7.4, PO_4^{3-} 1.31 mg/L, SO_4^{2-} 12.67 mg/L, NO_3^- 1.70 mg/L and electrical conductivity 750 μS/cm. The adsorbent mass was varied from 0.01 to 0.1 g, using 50 mL F^- ions solution at pH 7.4 and 25 °C for 24 h in batch adsorption. **Fig. 5.12(b)** shows the influence of adsorbent dose on % F^- ions removal and equilibrium F^- ions concentration. It was found that 0.1 g of HCeFe NFs-2 achieved F^- ions removal up to a concentration of 1.00 mg/L, below the stipulated standard permissible limit of 1.5 mg/L [15,49].

5.3.4.9 Adsorption mechanism

The pH_{pzc}, FTIR and XPS results were employed to provide the plausible adsorption mechanism. From **Fig. 5.8(b)**, it was observed earlier that the percentage of F^- ions removal was high from pH 3 to10. However, a drastic decrease was experienced with further increase in pH. At pH < pH_{pzc}, protonation encourages the development of positively charged MOH_2^+ and NH^+ groups, hence F^- ions adsorption is probably occurring through coulombic attractions [15,25,50]. Solution pH measurements before and after adsorption showed an increase in pH, implying that hydroxyl groups were perhaps being released as a result of ionic exchange [51]. At high solution pH > pH_{pzc} the adsorbent surface is predominantly negatively charged and electric repulsion is set to take place. Thus, the only conceivable F^- removal arising is through ions exchange between F^- and surface-bonded OH groups [15,49,52], together with Cl^- counter ions doping the PANI NFs moiety [53]. These proposed mechanisms are in agreement with the FTIR spectrum and XPS data. FTIR spectrum of HCeFe NFs-2 after adsorption **(Fig. 5.2(A)(c))**, showed that the bands at 3227, 1118 and 1076 cm^{-1} shifted to 3204, 1090 and 1067 cm^{-1}, respectively. In addition, the weakening of these bands indicates reduction in the amount of surface hydroxyl groups after F^- ions adsorption, certainly as a result of substitution during the adsorption process.

The XPS spectra of Ce 3d in **Fig. 5.13(a)** and **(b)** show the presence of both Ce(VI) and Ce(III) in HCeFe NFs-2 adsorbent. Before adsorption, as shown in **Fig. 5.13(a)**, peaks at 882.5, 885.3, 898.5 and 903.8 eV are observed. The peaks at 882.5 and 898.5 eV are ascribed to Ce(IV) $3d_{5/2}$ and $3d_{3/2}$, respectively. The peaks at 885.3 and 903.8 eV are attributed to Ce(III) $3d_{5/2}$ and $3d_{3/2}$ [14,16,50]. After fluoride adsorption, the peaks at 882.5, 885.3 and 903.8 eV shifted to higher energy 883.1, 886.7 and 905.5 eV, respectively. This exposes a possibility of OH bonded to

Ce(III) and Ce(IV) contributing to the F^- ions adsorption [14,15,48,50]. The binding of electronegative fluoride onto Ce leads to a decrease in its electron density, hence a shift in the Ce(IV) $3d_{5/2}$ and Ce(III) $3d_{3/2}$ binding energies [48]. The Fe 2p core level spectrum for HCeFe NFs-2, on the other hand, exhibits contribution of $2p_{1/2}$ and $2p_{3/2}$ components with binding energies of 710.3, 713.7, 723.6 and 725.8 eV, corresponding to Fe^{2+} $2p_{3/2}$, Fe^{3+} $2p_{3/2}$, Fe^{2+} $2p_{1/2}$ and Fe^{3+} $2p_{1/2}$, respectively as shown in **Fig. 5.13(c)** [16,54]. Hence, this analysis reveals the stability of Fe_3O_4 chemical states in the HCeFe NFs-2 adsorbent. Although no significant change was observed on the Fe 2p core level spectrum after adsorption in **Fig. 5.13(d)**, this ferroferric oxide is set to form a solid solution with CeO_2. This effect leads to increased surface area as well as the number of binding sites for F^- ions adsorption.

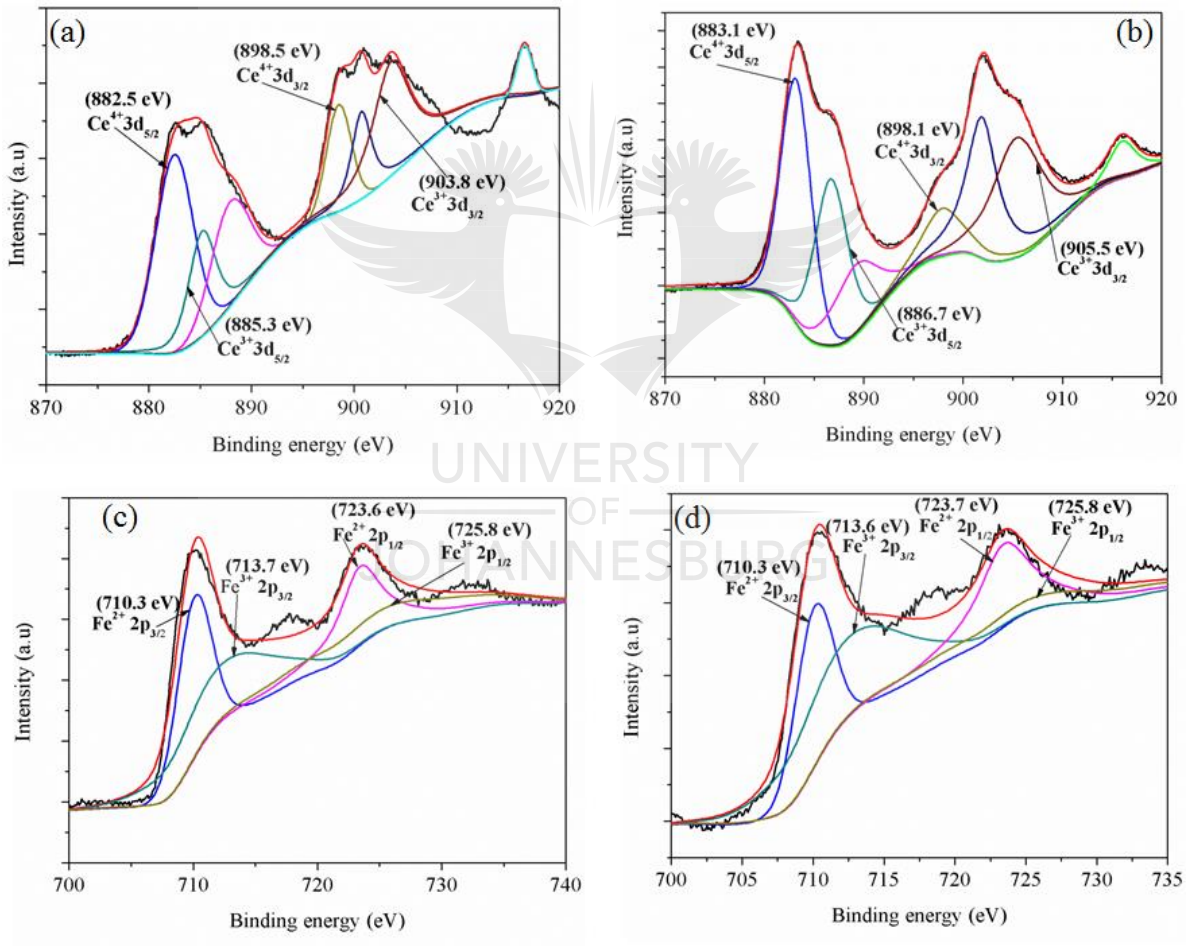

Fig. 5.13: XPS core level spectra of; Ce 3d (a) before and (b) after adsorption; Fe 2p (c) before and (d) after adsorption.

A step further, the N 1s core level spectra of HCeFe NFs-2 adsorbent before and after the adsorption procedure are presented in **Fig. 5.14(a)** and **(b)**. The spectrum before adsorption shows binding energies at 398.3, 399.1 and 400.0 eV, ascribed to the quinonoid imine (=N−), benzenoid amine (− NH−) and positively charged doped imine (−NH^{+}·), respectively. There is a noteworthy change in the positively charged doped imine binding energy from 400.0 to 400.3 eV. The latter exerts an attractive interaction to the counter ion Cl^- ions which are substituted by the extremely electronegative F^- ions during adsorption [25,55]. This statement is in good agreement with the reduction in Cl 2p peak intensity in the wide scan spectrum of HCeFe NFs-2, after F^- adsorption **(Fig. 5.3(A)(b))**. The deconvoluted spectra of O 1s before and after adsorption are shown in **Fig. 5.14(c)** and **(d)**. The peaks corresponding to oxygen of Ce/Fe oxides (M-O), adsorbent surface hydroxyl groups (M-OH) and H_2O are evidenced [14,16,49,50]. Moreover, the peak area of M-O increased from 23.35 to 31.12% whilst that of M-OH decreased from 58.77 to 41.90%. The decrease in M-OH peak area is certainly attributed to the participation of these hydroxyl groups in the adsorption of F^- ions. This reaffirms an ionic exchange mechanism [42,43,56].

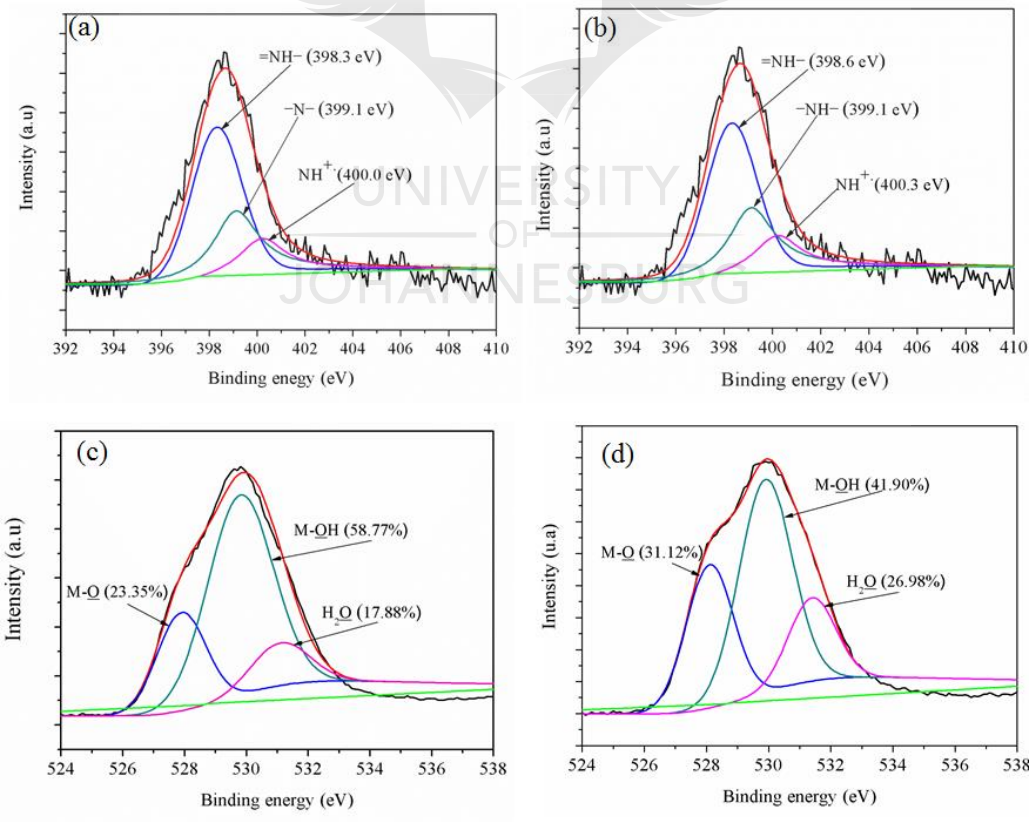

Fig. 5.14: XPS spectra of (a) N 1s before and (b) after adsorption; (c) O 1s before and (d) after adsorption.

Therefore, the plausible reaction mechanisms are as follows:

$$\begin{bmatrix} MOH_2^+ + F^- \longrightarrow MOH_2^+..F^- \\ NH^+ + F^- \longrightarrow NH^+..F^- \end{bmatrix}$$ **Electrostatic attraction**

$$\begin{bmatrix} MOH + F^- \longrightarrow MF + OH^- \\ NH^+Cl^- + F^- \longrightarrow NH^+F^- + Cl^- \end{bmatrix}$$ **Ion exchange**

5.4 Conclusion

In this study, a series of HCeFe NFs was prepared by fast polymerisation of aniline and subsequent co-precipitation deposition of CeO_2-Fe_3O_4 on the PANI NFs. The novel nanocomposites were tested for their potential to serve as adsorbents in water defluoridation process, as opposed to conventional PANI or well reported nano-metal oxides. The optimized adsorbent HCeFe NFs-2 with 66 m^2/g BET surface area exhibited good F^- ions removal over a broad pH range 3-10. The Langmuir isotherm described the adsorption well and implied monolayer adsorption with maximum capacity of 116.28 mg/g at pH 6.0 ± 0.2 and 25 °C. The thermodynamic parameters indicated an exothermic and spontaneous nature of the process. The relatively rapid kinetics of F^- ions adsorption onto HCeFe NFs-2 composite conformed to the pseudo-second-order model. According to FTIR and XPS spectra analysis, together with pH_{pzc} measurement, the mechanisms involved both electrostatic attractions and ion exchange. The regeneration study indicated that this material could be used in three consecutive cycles before being discarded. Batch treatment of 50 mL spiked groundwater samples with 0.1 g of HCeFe NFs-2 reduced the F^- ions level from 5.00 mg/L to 1.00 mg/L, below the WHO permissible level. Henceforth, this material can serve as suitable alternative for defluoridation of drinking water. Further investigation on the application of HCeFe NFs-2 for large scale water treatment could be assessed in fixed-bed column dynamic system.

5.5 References

[1] S. Ayoob, A.K. Gupta, V.T. Bhat, A conceptual overview on sustainable technologies for the defluoridation of drinking water, Crit. Rev. Environ. Sci. Technol. 38 (2008) 401−470.

[2] K. Parashar, N. Ballav, S. Debnath, K. Pillay, A. Maity, Hydrous titanium oxide@polypyrrole hybrid nanocomposite as an efficient selective scavenger for the defluoridation of drinking water, RSC Adv. 6 (2016) 99482–99495.

[3] G. Biswas, M. Kumari, K. Adhikari, S. Dutta, A Critical Review on Occurrence of Fluoride and Its Removal through Adsorption with an Emphasis on Natural Minerals, Curr. Pollution Rep. 3 (2017) 104−119.

[4] R.A. Fallahzadeh, M. Miri, M. Taghavi, A. Gholizadeh, R. Anbarani, A. Hosseini-Bandegharaei, M. Ferrante, G.O. Conti, Spatial variation and probabilistic risk assessment of exposure to fluoride in drinking water, Food Chem. Toxicol. 113 (2018) 314–321.

[5] S. Kumari, S. Khan, Defluoridation technology for drinking water and tea by green synthesized Fe_3O_4/Al_2O_3 nanoparticles coated polyurethane foams for rural communities, Sci. Rep. 7 (2017) 8070.

[6] K. Parashar, N. Ballav, S. Debnath, K. Pillay, A. Maity, Rapid and efficient removal of fluoride ions from aqueous solution using a polypyrrole coated hydrous tin oxide nanocomposite, J. Colloid Interface Sci. 476 (2016) 103−118.

[7] Y. Zhang, X. Lin, Q. Zhou, X. Lou, Fluoride adsorption from aqueous solution by magnetic core-shell Fe3O4@alginate-La particles fabricated via electro-coextrution, Appl. Surf. Sci. 389 (2016) 34–45.

[8] M. Bhaumik, T.Y. Leswifa, A. Maity, V.V. Srinivasu, M.S. Onyango, Removal of F^- from aqueous solution by polypyrrole/Fe_3O_4 magnetic nanocomposite, J. Hazard. Mater. 186 (2011) 150–159.

[9] A. Bhatnagar, E. Kumar, M. Sillanpää, Fluoride removal from water by adsorption-a review, Chem. Eng. J. 171 (2011) 811–840.

[10] L.H. Velazquez-Jimenez, E. Vences-Alvarez, J.L. Flores-Arciniega, H. Flores-Zuñiga, J.R. Rangel-Mendez, Water defluoridation with special emphasis on adsorbents-containing metal oxides and/or hydroxides: A review, Sep. Purif. Technol. 150 (2015) 292–307.

[11] A.M. Rauchir, M.J. Basu, Adsorption of fluoride onto mixed rare earth metal oxides, Sep. Purif. Technol. 24 (2001) 122–127.

[12] M. Karthekeyan, K.S. Kumar, K.P. Elango, Conducting polymer/alumina composites as viable adsorbents of fluoride ions from aqueous solution, J. Fluorine Chem. 130 (2009) 894–901.

[13] M. Chigondo, H.K. Paumo, M. Bhaumik, K. Pillay, A. Maity, Rapid high adsorption performance of hydrous cerium-magnesium oxides for removal of fluoride from water, J. Mol. Liq. 265 (2018) 496–509.

[14] S. Deng, H. Liu, W. Zhou, J. Huang, G. Yu, Mn-Ce oxide as a high-capacity adsorbent for fluoride removal from water, J. Hazard. Mater. 186 (2011) 1360–1366.

[15] K. Mukhopadhyay, A. Ghosh, S.K. Das, B. Show, P. Sasikumar, U.C. Ghosh, Synthesis and characterization of cerium(IV)-incorporated hydrous iron(III) oxide as an adsorbent for fluoride removal from water, RSC Adv. 7 (2017) 26037–26051.

[16] D. Tang, G. Zhang, Efficient removal of fluoride by hierarchical Ce-Fe bimetal adsorbent: thermodynamics, kinetics and mechanism, Chem. Eng. J. 283 (2016) 721–729.

[17] H. Liu, L. Deng, Z. Li, G. Yu, J. Huang, Preparation of Al-Ce hybrid adsorbent and its application for defluoridation of drinking water, J. Hazard. Mater. 179 (2010) 424–430.

[18] N. Chubar, New inorganic ion exchangers based on Mg-Al hydrous oxides: (Alkoxide-free) sol-gel synthesis and characterization, J. Colloid Interface Sci. 357 (2011) 198–209.

[19] X. Dou, Y. Zhang, H. Wang, T. Wang, Y. Wang, Performance of granular zirconium-iron oxide in the removal of fluoride from drinking water, Water Res. 45 (2011) 3571–3578.

[20] X. Zhao, J. Wang, F. Wu, T. Wang, Y. Cai, Y. Shi, G. Jiang, Removal of fluoride from aqueous media by Fe_3O_4@$Al(OH)_3$ magnetic nanomaterials, J. Hazard. Mater. 173 (2010) 102–109.

[21] S. Alemu, Mulugeta, F. Zewge, B.S. Chandravanshi, Water defluoridation by aluminium oxide-manganese oxide composite material, Environ. Technol. 35 (2014) 1893–1903.

[22] M. Hua, S. Zhang, B. Pan, W. Zhang, L. Lv, Q. Zhang, Heavy metal removal from water/wastewater by nanosized metal oxides: A review, J. Hazard. Mater. 211 (2012) 317–331.

[23] S. Sakar, E. Guibal, F. Quignard, A.K. SenGupta, Polymer-supported metals and metal oxide nanoparticles: synthesis, characterization and applications, J. Nanopart. Res. 14 (2012) 715.

[24] L. Tang, Y. Fang, Y. Pang, G. Zeng, J. Wang, Y. Zhou, Y. Deng, G. Yang, Y. Cai, J. Chen, Synergistic adsorption and reduction of hexavalent chromium using highly uniform polyaniline-magnetic mesoporous silica composite, Chem. Eng. J. 254 (2014) 302–312.

[25] K. Parashar, N. Ballav, S. Debnath, K. Pillay, A. Maity, Hydrous ZrO_2 decorated polyaniline nanofibres: Synthesis, characterization and application as an efficient adsorbent for water defluoridation, J. Colloid Interface Sci. 508 (2017) 342–358.

[26] M. Karthekeyan, K.S. Kumar, K.P. Elango, Batch sorption studies on the removal of fluoride ions from water using eco-friendly conducting polymer/bio-polymer composites, Desalination 267 (2011) 49–56.

[27] S. Mandal, S.S. Mahapatra, R.K. Patel, Enhanced removal of Cr(VI) by cerium oxide polyaniline composite: Optimization and modeling approach using response surface methodology and artificial neural networks, J. Environ. Chem Eng. 3 (2015) 870–885.

UNIVERSITY OF JOHANNESBURG

[28] H.M. Cai, G.J. Chen, C.Y. Peng, Z.Z. Zhang, Y.Y. Dong, G.Z. Shang, X.H. Zhu, H.J. Gao, X.C. Wan, Removal of fluoride from drinking water using tea waste loaded with Al/Fe oxides: A novel, safe and efficient biosorbent, Appl. Surf. Sci. 328 (2015) 34–44.

[29] S.K. Swain, T. Patnaik, P.C. Patnaik, U. Jha, R.K. Dey, Development of new alginate entrapped Fe(III)-Zr(IV) binary mixed oxide for removal of fluoride from water bodies, Chem. Eng. J. 215–216 (2013) 763–771.

[30] L. Liu, Z. Cui, Q. Ma. W. Cui, X. Zhang, One-step synthesis of magnetic iron-aluminium oxide/graphene oxide nanoparticles as selective adsorbent for fluoride removal form aqueous solution, RSC Adv. 8 (2016) 10783–10791.

[31] S. Moriyana. K. Sasaki, T. Hirajima, Effect of temperature on Mg-Al bimetallic oxides as sorbents for removal of fluoride from aqueous solution, Chemosphere 95 (2014) 597–603.

[32] A.H. Elsayed, M.M. Eldin, A.M. Elsyed, A.H. Alazm, E.M. Younes, H.A. Motaweh, Synthesis and characterization of polyaniline/ferrites nanocomposites, Int. J. Electrochem. Sci. 6 (2011) 206–209.

[33] S.B. Kondawar, S.P. Agrawal, S.H. Nimkar, H.J. Sharma, P.T. Patil, Conductive polyaniline-tin oxide nanocomposites for ammonia sensor, Adv. Mater. Lett. 3 (2012) 393–398.

[34] M. Bhaumik, R.I. McCrindle, A. Maity, S. Agarwal, V.K. Gupta, Polyaniline nanofibers as highly effective re-usable adsorbent for removal of reactive black 5 from aqueous solutions, J. Colloid Interface Sci. 466 (2016) 442–451.

[35] R. Li, Y. Wang, C. Zhou, C. Wang, X. Ba, Y. Li, X. Huang, J. Liu, Carbon-stabilized high-capacity ferroferric oxide nanorod array for flexible solid-state alkaline battery-supercapacitor hybrid device with high environmental suitability, Adv. Funct. Mater. 25 (2015) 5384–5394.

[36] I. Saha, I. Ghosh, D. Nandi, K. Gupta, D. Chatterjee, U.C. Ghosh, β-Cyclodextrin modified hydrous zirconium oxide. Synthesis, characterization and defluoridation performance from aqueous solution, Chem. Eng. J. 263 (2015) 220–230.

[37] E. Vences-Alvarez, L.H. Velazquez-Jimenez, L.F. Chazaro-Ruiz, P.E. Diaz-Flores, J.R. Rangel-Mendez, Fluoride removal in water by a hybrid adsorbent lanthanum-carbon, J. Colloid Interface Sci. 455 (2015) 194–202.

[38] K.Y. Foo, B.H. Hameed, Insights into modelling of isotherm adsorption systems, Chem. Eng. J. 156 (2010) 2–10.

[39] Z. Wen, C. Dai, Y. Zhu, Y. Zhang, Arsenate removal from aqueous solution using magnetic mesoporous iron manganese bimetal oxides, RSC Adv. 5 (2015) 4058–4068.

[40] N.H. Kera, M. Baumik, N. Ballav, K. Pillay, S.S. Ray, A. Maity, Selective removal of Cr(VI) from aqueous solution by polypyrrole/2.5-diaminobenzene sulfonic acid composite, J. Colloid Interface Sci. 475 (2016) 144–157.

UNIVERSITY OF JOHANNESBURG

[41] X. Dou, D. Mohan, C.U. Pittaman Jr, S. Yang, Remediating fluoride from water using hydrous Zirconium oxide, Chem. Eng. J. 198 (2012) 236–245.

[42] J. Wang, W. Xu, L. Chen, Y. Jia, X.J. Huang, J. Lui, Excellent fluoride removal performance by CeO_2 and ZrO_2 nanocages in water environment, Chem. Eng. J. 231 (2013) 195–205.

[43] A. Azari, R.R. Kalantary, G. Ghanizadeh, B. Kakavandi, M. Farzadkia, E. Ahmadi, Iron-silver oxide nanoadsorbent synthesized by co-precipitation process for fluoride removal from aqueous solution and its adsorption mechanism, RSC Adv. 5 (2015) 87377–87391.

[44] B.C. Anderson, P.D. Bloom, K.G. Baikerikar, V.V. Sheares, S.K. Mallapragada, Al-Cu-Fe quasicrystal/ultra-high molecular weight polyethylene composites as biomaterials for acetabular cup prosthetics, Biomaterials 23 (2002) 1761–1768.

[45] E. Kontou, M. Niaounakis, Thermo-mechanical properties of LLDPE/SiO_2 nanocomposites, Polymer 47 (2006) 1267–1280.

[46] T. Kuila, S. Bose, A.K. Mishra, P. Khanra, N.H. Kim, J.H. Lee, Effect of functionalized graphene on the physical properties of linear low-density polyethylene nanocomposites, Polym. Test. 31 (2012) 31–38.

[47] Y. Zhang, M. Yang, X. Huang, Arsenic removal with Ce(VI) doped with Fe oxide adsorbent, Chemophore 51 (2003) 945–852.

[48] Z. Yu, C. Xu, K. Yuan, X. Gan, C. Feng, X. Wang, L. Zhu, G. Zhang, D. Xu, Characterization and adsorption mechanism of ZrO_2 mesoporous fibers for health-hazardous fluoride removal, J. Hazard. Mater. 346 (2018) 82–92.

[49] J. Zhu, X. Lin, P. Wu, Q. Zhou X. Luo, Fluoride removal from aqueous solution by Al(III)-Zr(VI) binary oxide adsorbent, App. Surf. Sci. 357 (2015) 91–100.

[50] A. Dhillon, S.K. Soni, D. Kumar, Enhanced fluoride removal performance by Ce-Zn binary metal oxide: Adsorption characteristics and mechanism, J. Fluorine Chem. 199 (2017) 67–76.

[51] L. Li, Q. Zhu, K. Man, Z. Xing, Fluoride removal from liquid phase by Fe-Al-La tri-metal hydroxides adsorbent prepared by iron and aluminium leaching from red mud, J. Mol. Liq. 237 (2017) 164–172.

[52] H.X. Wu, T.J. Wang, L. Chen, Y. Jin, Y. Zhang, X.M. Dou, The roles of the surface charge and hydroxyl group on a Fe-Al-Ce adsorbent in fluoride adsorption, Ind. Eng. Chem. Res. 48 (2009) 4530–4534.

[53] S.K. Swain, S. Mishra, T. Patnaik, R.K. Patel, U. Jha, R.K. Dey, Fluoride removal performance of a new hybrid sorbent of Zr (IV)-ethylenediamine, Chem. Eng. J. 184 (2012) 72–81.

[54] Q. Ke, C. Tang, Y. Liu, H. Liu, J. Wang, Intercalating graphene with clusters of Fe_3O_4 nanocrystals for electrochemical supercapacitors, Mater. Res. Express, 1 (2014) 025015.

UNIVERSITY OF JOHANNESBURG

[55] E. Binkauskienė, V. Jasulaitienė, A. Lugauskas, Effect of Aspergillus niger Tiegh. L-10 on the physical and chemical properties of a polyaniline coating in the growth substrate, Synth. Met. 159 (2009)1365–1368.

[56] A. Azari, R.R. Kalantary, G. Ghanizadeh, B. Kakavandi, M. Farzadkia, E. Ahmadi, Iron-silver oxide nanoadsorbent synthesized by co-precipitation process for fluoride removal from aqueous solution and its adsorption mechanism, RSC Adv. 5 (2015) 87377–87391.

UNIVERSITY OF JOHANNESBURG

CHAPTER SIX

MAGNETIC ARGININE-FUNCTIONALIZED POLYPYRROLE WITH IMPROVED AND SELECTIVE CR(VI) IONS REMOVAL FROM WATER

6.1 Introduction

In the last two chapters attention has been focused on fluoride removal from water. However, heavy metals ions like hexavalent chromium (Cr(VI)) produced mainly from anthropogenic industrial activities, also pose a serious risk to the ecosystem and humans [1-6]. Cr(VI) toxicity stems from its potential carcinogenic and mutagenic properties [2,7,8]. Hence, the World Health Organisation (WHO) regulates total chromium in water and the recommended concentration of Cr(VI) in surface waters is 0.1 mg/L, while 0.05 mg/L is fixed for drinking water [9,10]. Accordingly, how to efficiently and totally remove Cr(VI) ions from water systems is still an imperative but challenging task. Consequently, a variety of technologies has been developed [7,8,10-14] including adsorption whose merits have already been mentioned in chapter 4 and 5, through utilization of a variety of adsorbents [5,6,15-20]. Besides just adsorption, Cr(VI) water remediation may involve its reduction to the relatively stable and less toxic Cr(III) derivative using doped NH-containing polymers like PPy which has shown many advantages as a host material [19-23]. These have a strong ability to interact with heavy metal ions with relatively high adsorption capacities having been reported [5,13,19-29].

This chapter focusses on the synthesis of a magnetic arginine-functionalized polypyrrole nanocomposite (Fe_3O_4@Arg-PPy) *via in-situ* polymerisation and its application in Cr(VI) remediation from synthetic and wastewater samples. It was hypothesised that doping PPy with arginine bearing four amino groups per molecule would result in a highly improved adsorption capacity. Furthermore, incorporating a magnetic property in the adsorbent would afford ease of isolation from water [30-32] and extensive studies with other materials have been conducted to that effect [17,33-37]. In addition, the performance of adsorbent and adsorption mechanisms may be better understood through quantification and speciation of chromium after adsorption [1,38,39] and an attempt was made to that effect. Various chemical, morphological and physical characteristics of Fe_3O_4@Arg-PPy nanocomposite were studied. Adsorption of Cr(VI) onto the described adsorbent was investigated by varying parameters such as adsorbent dose, pH,

The work presented in this chapter received positive comments from the Journal of Molecular Liquids, MOLLIQ_2018_4103

contact time and temperature in batch experiments. Co-existing ions interference study was conducted to test the Fe_3O_4@Arg-PPy selectivity toward Cr(VI). Wastewater sample treatment was carried out to evaluate the potential applicability of this novel adsorbent. Furthermore, the reusability of this material was assessed through adsorption-desorption study.

6.2 Materials and methods

6.2.1 Materials

Pyrrole (Py), arginine, ammonium persulphate (APS) and iron(II/III) oxide (Fe_3O_4) nanoparticles (50-100 nm) were obtained from Sigma-Aldrich, South Africa. The Py was distilled before use. Other chemicals like hydrochloric acid (HCl), sodium hydroxide (NaOH), potassium dichromate ($K_2Cr_2O_7$) and 1,5-diphenyl carbazide, of analytical grades, were obtained from Sigma-Aldrich, USA.

6.2.2 Synthesis of magnetic Fe_3O_4 arginine doped polypyrrole (Fe_3O_4@Arg-PPy) Nanocomposite

The Fe_3O_4@Arg-PPy nanocomposite was prepared following a modified procedure described elsewhere [5,20]. Arginine 1.3 g was dissolved in 80 mL of deionised water and 0.3 g of Fe_3O_4 nanoparticles (NPs) were then added. The mixture was sonicated for 30 minutes so as to achieve good dispersion of Fe_3O_4 NPs. Next, 1 mL of Py monomer was syringed at once and the solution was vigorously stirred for 30 minutes. Subsequently, APS (3.9 g) was dissolved in 20 mL of deionised water and added dropwise. The solution mixture was continuously stirred for an additional 20 minutes. The resulting solution was left for 12 h at ambient temperature after which 10 mL of acetone was added to stop the polymerisation process. The mixture was filtered, washed with deionised water and acetone, vacuum dried at 60 ^oC for 12 h and finally ground to a fine powder to afford a Fe_3O_4@Arg-PPy nanocomposite.

6.2.3 Characterization of Fe_3O_4@Arg-PPy nanocomposite

The FTIR spectra of the Fe_3O_4@Arg-PPy nanocomposite before and after Cr(VI) ions adsorption were obtained using a Perkin Elmer Spectrum 100 Spectrometer (Perkin Elmer, USA). Each spectrum represented a collection of 32 scans in the range of 500-4000 cm^{-1} with 4 cm^{-1} spectral resolution. The surface morphology and nanostructure of the Fe_3O_4@Arg-PPy nanocomposite were studied by FE-SEM and TEM images, obtained using a Zeiss Auriga Cobra FIB microscope and a high resolution transmission electron microscope (JEOL–JEM 2100, Japan) with LaB6 filament operated at 200 kV, respectively. The BET surface area of pristine PPy and Fe_3O_4@Arg-PPy nanocomposite were assessed with a Micromeritics ASAP 2020 gas adsorption instrument (Micromeritics, USA) using a low-temperature (-195.80 °C) N_2 adsorption-desorption method. A PANalyticalX'Pert PRO-X-ray diffractometer (PANalytical, The Netherlands) using CuKα radiation with a wavelength of 1.5505 Å and adjustable slits at 45 kV/30 mA in the range of $2\theta = 5$ to 90° was used for XRD characterization. XPS spectra were obtained from a Kratos Axis Ultra device with Al monochromatic X-ray source (1486.6 eV). The magnetisation curve of the Fe_3O_4@Arg-PPy nanocomposite before and after Cr(VI) adsorption were acquired at room temperature using a Vibrating Sample Magnetometer (VSM, Quantum design, USA) with a maximum applied magnetic field of 10 kOe. The Cr(VI) concentrations in treated samples were determined using a Lambda 750S UV-Visible spectrophotometer (Perkin Elmer, USA). The chromium speciation in filtered samples was conducted using ion chromatography with inductively coupled plasma-mass spectrometer (IC-ICP-MS) (Thermo Scientific, USA). The pH at point-of-zero charge was determined using a change in pH approach with a Thermo Scientific pH meter.

UNIVERSITY OF JOHANNESBURG

6.2.4 Batch adsorption studies

6.2.4.1 Adsorption Studies

A stock solution containing 1000 mg/L Cr(VI) ions was prepared by dissolving 2.83 g of oven dried $K_2Cr_2O_7$ (Analytical grade) in 1000 mL of deionised water. All experimental solutions for Cr(VI) ions removal studies were prepared by appropriate dilutions from the stock solution. The adsorption studies were carried out by keeping in contact 0.05 g of Fe_3O_4@Arg-PPy adsorbent with 50 mL of 200 mg/L Cr(VI) ions solution and shaking in a temperature-controlled water bath shaker at 200 rpm for 24 h. The experiments were conducted in triplicate. The determination of residual Cr(VI) ions in treated water samples was conducted by

measuring the absorbance of the purple complex of Cr(VI) with 1,5 diphenylcarbazide reagent at 540 nm.

The percentage (%) removal of Cr(VI) ions was calculated using **Equation (6.1):**

$$\% \text{ removal} = \left(\frac{C_o - C_e}{Co}\right) \times 100 \quad (6.1)$$

where C_o and C_e are the initial and the equilibrium concentrations, respectively.

The effect of pH was investigated by adjusting the pH (from 2-12) of 50 mL Cr(VI) ions solutions (200 mg/L) using 0.1M HCl and 0.1M NaOH solutions at 0.05 g adsorbent dosage. The Cr(VI)-adsorbent suspension was shaken for 24 h. The adsorbent dose study was conducted by varying the amounts of adsorbent from 0.05 to 0.1 g under the following conditions: pH 2, 50 mL Cr(VI) ions solutions (200 mg/L) and contact time of 24 h. The equilibrium adsorption capacity is given by **Equation (6.2)**:

$$q_e = \left(\frac{C_o - Ce}{m}\right) V \quad (6.2)$$

where q_e (mg/g), m (g) and V (L) are the equilibrium amount of pollutant per unit mass of adsorbent, mass of adsorbent and the sample volume, respectively.

UNIVERSITY OF JOHANNESBURG

The adsorption isotherms for the removal of Cr(VI) were studied at 15, 25, 35 and 45 °C using a Sep. Sci MRC Refrigerated Shaker Bath, South Africa under the following conditions: adsorbent dose 0.05 g, pH 2, sample volume 50 mL, Cr(VI) concentration range 50-450 mg/L, contact time 24 h. The experiments were conducted in triplicate. The isotherm data were also used to determine the thermodynamic parameters; Gibbs free energy *(Δ$G°$),* enthalpy *(Δ$H°$)* and entropy *(Δ$S°$)* change. Kinetics study was conducted using different initial Cr(VI) concentrations (50, 100, 150 mg/L) at pH 2 and Fe_3O_4@Arg-PPy dose 1 g in 1000 mL solution over 0 to 350 min. Additionally, temperature dependent kinetics were studied at 15, 25, 35 and 45 °C so as to determine the activation energy of the adsorption process. The adsorption capacity of the adsorbent (q_t) at time t was obtained using **Equation (6.3)**:

$$q_t = \left(\frac{C_o - C_t}{m}\right) V \quad (6.3)$$

where q_t (mg/g) and C_t (mg/L) are the amount of Cr(VI) ions adsorbed per unit mass of adsorbent and concentration of the pollutant at time *t*, respectively**.**

6.2.4.2 Effect of co-existing ions

The influence of co-existing ions was performed using the initial Cr(VI) concentration of (100 mg/L) and different concentrations (25, 50, 100 and 150 mg/L) of Zn^{2+}, Cu^{2+}, Ni^{2+}, SO_4^{2-}, NO_3^-, SO_4^{2-}, HCO_3^- and HPO_4^{3-} as well as their mixture. The pH of the resulting solution and other key parameters were kept as follows: pH 2, adsorbent dosage 0.05 g, sample volume 50 mL, contact time 24 h.

6.2.4.3 Regeneration studies

For regeneration studies, five plastic bottles containing 0.05 g of Fe_3O_4@Arg-PPy adsorbent in 50 mL of 200 mg/L Cr(VI) ions solution at pH of 2 were shaken for 24 h. Then, the chromium loaded adsorbent of each experiment was treated with 0.025, 0.05, 0.075, 0.1 and 0.2M NaOH solutions, respectively, and 2M HCl solution for regeneration. It was found that 0.05M NaOH concentration produced the highest desorption ability. This was then used for four successive adsorption-desorption cycles.

UNIVERSITY OF JOHANNESBURG

6.3 Results and discussion

6.3.1 Physico-chemical characterization

6.3.1.1 FTIR spectral analysis

Fig. 6.1A(a) shows the FTIR spectrum of PPy with the characteristic bands at 1527, 1437, and 1280-961 cm^{-1}, corresponding to C=C, C–N, and C−H stretching vibrations, respectively [5,20,22,38]. On the other hand, the FTIR spectrum of Fe_3O_4@Arg-PPy revealed a shift of bands at 1527 and 1437 cm^{-1} to 1554 and 1474 cm^{-1}, respectively as shown in **Fig. 6.1A(b)**. This confirms the incorporation of the arginine dopant on the PPy backbone [5,19,20,21,31]. Moreover, an additional band at 3098 cm^{-1}, corresponding to N–H stretching vibration, owing to the occurrence of $-^+NH_3$ function of the arginine zwitterion is detected. The band at 602 cm^{-1} is attributed to Fe–O vibration of magnetite NPs [3,17]. The band at 1685 cm^{-1} is assigned to carbonyl stretching vibration of the zwiterionic arginine [5,20]. After adsorption, the FTIR

spectrum of Fe_3O_4@Arg-PPy **(Fig. 6.1A(c))** displayed a significant shift of band at 3098 to 3121, certainly as a result of the interaction between $^{+}NH_3$ and Cr(VI) [5].

6.3.1.2 XRD patterns

Fig. 6.1(B) shows the XRD patterns of (a) Fe_3O_4 NPs, (b) pristine PPy, (c) Fe_3O_4@Arg-PPy, and (d) chromium loaded Fe_3O_4@Arg-PPy. A broad peak at 2θ = 24.10, characteristic of amorphous PPy is observed in **Fig. 6.1(B)(b)** [5,21]. The peaks at 2θ = 30.25, 35.69, 43.43, 53.78, 57.27 and 62.83 consistent with Fe_3O_4 lattice parameters (220), (311), (400), (422), (511) and (440), respectively, are evidenced in **Fig. 6.1(B)(a),(c)** and **(d)** [5,21,22]. These interpretations reveal the coexistence of both PPy and Fe_3O_4 in Fe_3O_4@Arg-PPy nanocomposite. With respect to the XRD patterns of Fe_3O_4@Arg-PPy and chromium loaded Fe_3O_4@Arg-PPy, no major characteristic changes could be identified as revealed in **Fig. 6.1(B)(c)** and **(d)**.

6.3.1.3 BET surface area analysis

Fig. 6.1(C) exhibits the N_2 adsorption-desorption isotherms of (a) Fe_3O_4@Arg-PPy nanocomposite and (b) PPy. The BET surface area, average pore diameter and pore volume of Fe_3O_4@Arg-PPy nanocomposite were estimated to be 22 m^2/g, 17.0 nm and 0.1 cm^3/g, respectively. As compared to pristine PPy (8 m^2/g, 37.0 nm and 0.02 cm^3/g), Fe_3O_4@Arg-PPy showed increased surface area and pore volume.

UNIVERSITY OF JOHANNESBURG

6.3.1.4 Magnetic property analysis

Fig. 6.1(D) shows the room temperature magnetic hysteresis loops of (a) Fe_3O_4@Arg-PPy nanocomposite and (b) chromium loaded Fe_3O_4@Arg-PPy with zero coercive force and remanence characteristic of a superparamagnetic material. The saturation magnetisation (*Ms*) before and after adsorption were recorded to be 2.65 and 1.89 emu/g, respectively. Although these obtained *Ms* values were much lower than that of Fe_3O_4, owing to the presence of non-magnetic PPy doped arginine and lower loading of Fe_3O_4, Fe_3O_4@Arg-PPy and chromium loaded Fe_3O_4@Arg-PPy shows strong superparamagnetic material magnetic properties. The latter could therefore be isolated from the treated aqueous solution using an external magnet as shown in Scheme 1 [20,26,39].

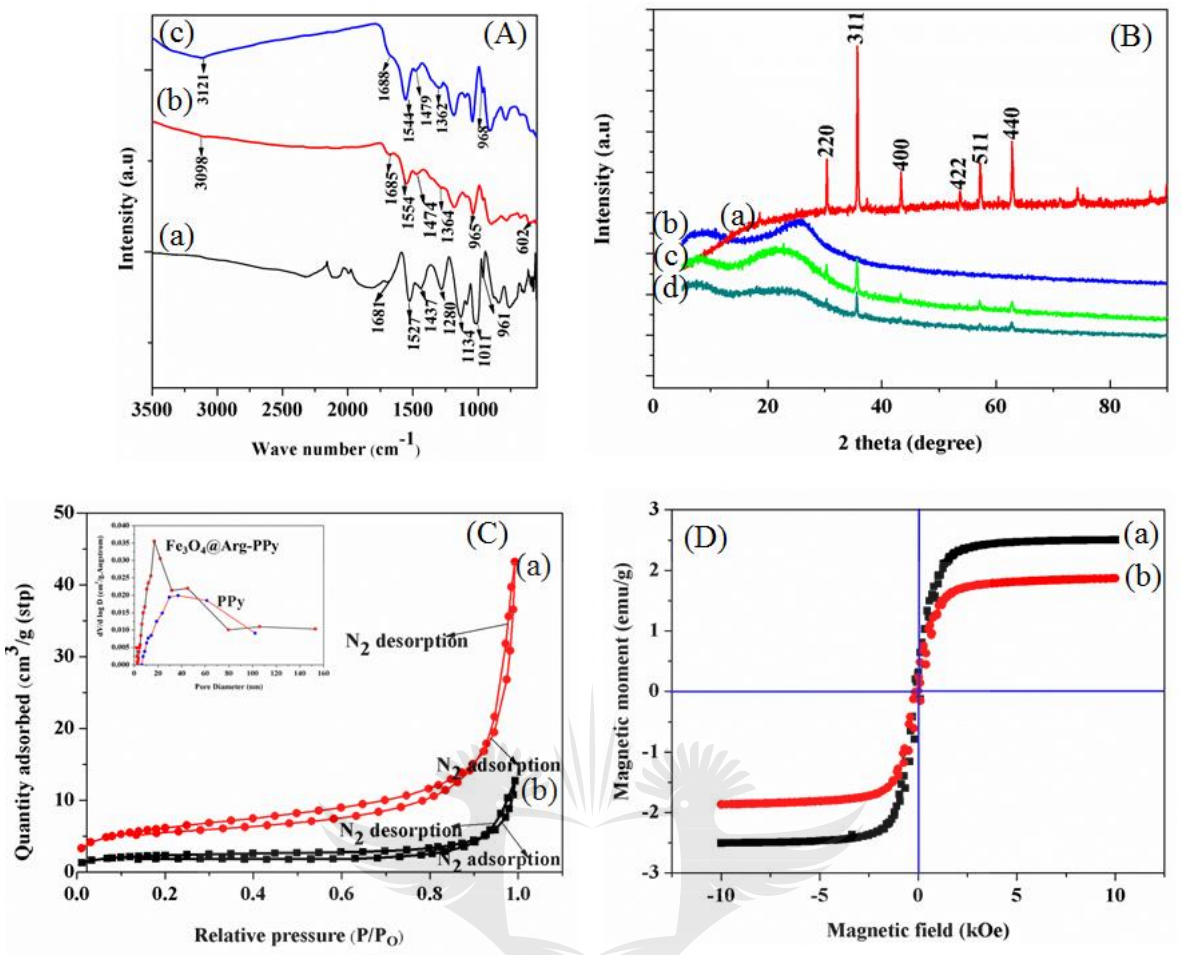

Fig. 6.1: (A) FTIR spectra of (a) PPy and Fe_3O_4@Arg-PPy nanocomposite (b) before (c) after Cr(VI) ions removal. (B) XRD patterns of (a) Fe_3O_4 NPs, (b) PPy, Fe_3O_4@Arg-PPy nanocomposite (c) before and (d) after Cr(VI) ions removal. (C) N_2 adsorption-desorption isotherms of (a) Fe_3O_4@Arg-PPy nanocomposite and (b) PPy. (D) Magnetic hysteresis loop of Fe_3O_4@Arg-PPy nanocomposite (a) before and (b) after Cr(VI) ions removal.

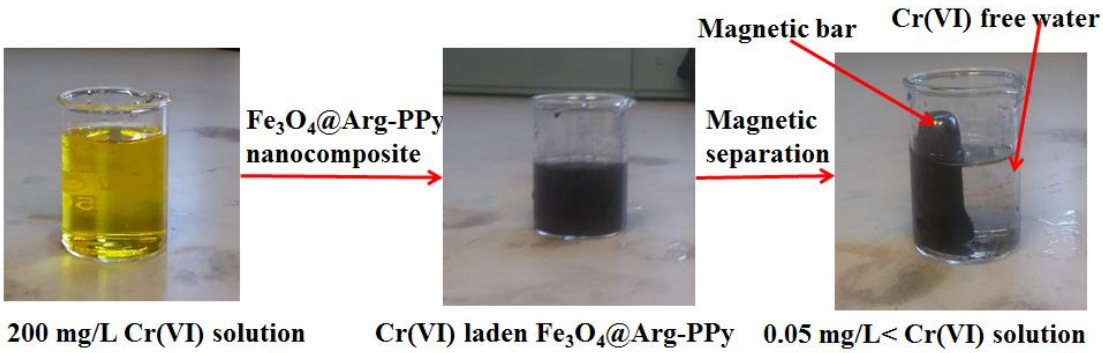

Scheme 6.1: Illustration of Cr(VI) removal from aqueous solution and magnetic isolation of Cr(VI)-loaded Fe_3O_4@Arg-PPy nanocomposite.

6.3.1.5 TEM and SEM

The SEM micrograph of Fe_3O_4@Arg-PPy nanocomposite in **Fig. 6.2(A)** exhibits agglomerated spherical-like particles whilst the TEM image in **Fig. 6.2(B)** exposes several nanoparticles coated by a polymeric material. The HR-TEM image in **Fig. 6.2(C)**, on the other hand, displays a section of Fe_3O_4@Arg-PPy nanocomposite exhibiting lattice fringes with an interfringe distance of about 0.3033 nm, corresponding to inter-planar distance of the (220) planes in the cubic spinel structure of Fe_3O_4 [39,40,41]. This indicates that Fe_3O_4 nanoparticles have been successfully enclosed in the polymeric matrix. The STEM images of chromium loaded adsorbent in **Fig. 6.3** reveal a uniform distribution of C, N, O, Fe and Cr elements on the Fe_3O_4@Arg-PPy surface, thereby confirming chromium uptake onto the developed nanocomposite.

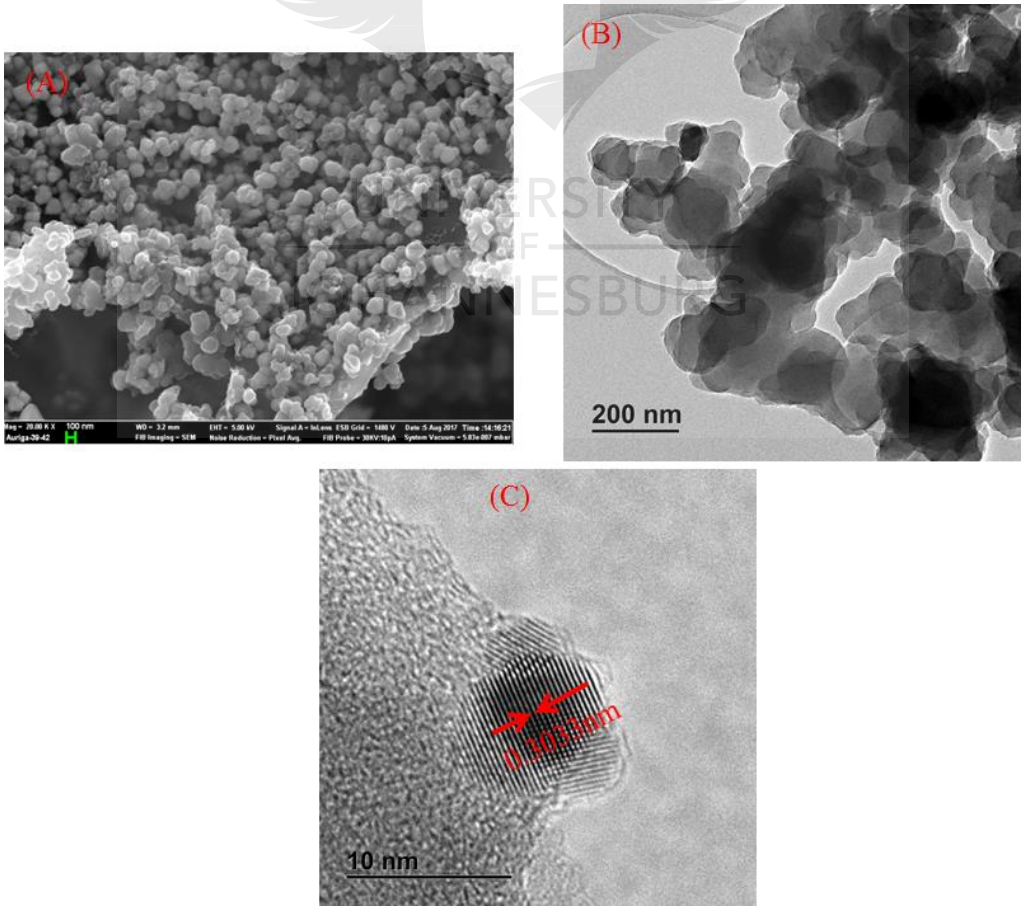

Fig. 6.2: (A) FE-SEM (B) TEM and (C) HR-TEM images of Fe_3O_4@Arg-PPy nanocomposite.

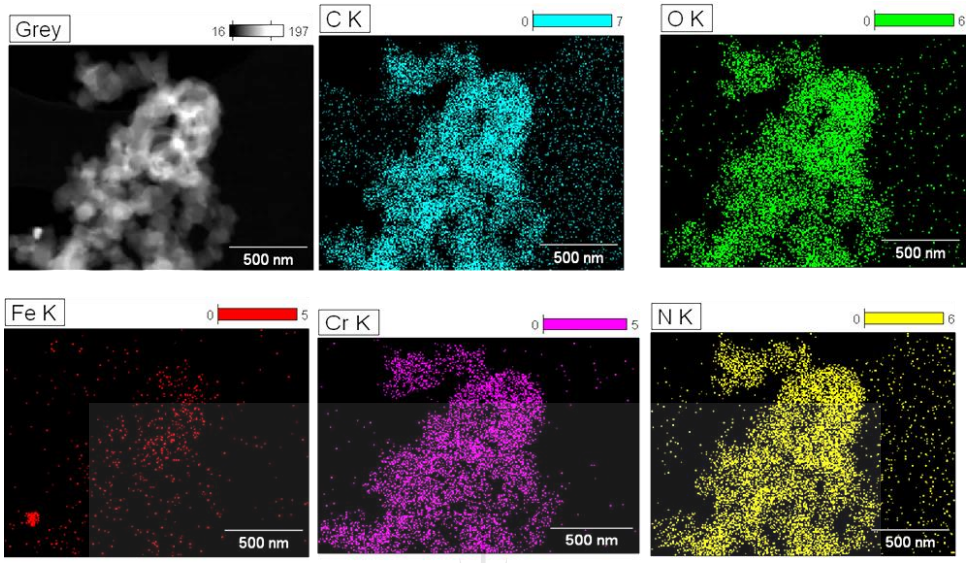

Fig. 6.3: STEM images of Fe_3O_4@Arg-PPy adsorbent after Cr(IV) ions adsorption and elemental mapping.

6.3.1.6 Energy dispersive X-ray spectra

The EDS spectra in **Fig. 6.4(A)** show the elemental constituents of Fe_3O_4@Arg-PPy (a) before and (b) after Cr(VI) ions adsorption. Peaks for C (0.27 keV), N (0.3892 keV, O (0.52 keV), Fe (0.7 and 6.4 keV) are displayed in **Fig. 6.4(A)(a)**. This confirms the incorporation of Fe_3O_4 into the arginine-PPy moiety. After Cr(VI) adsorption **(Fig. 6.4(A)(b))**, additional peaks at 5.41 and 6.4 keV attributed to chromium [39] are detected, confirming their adsorption onto Fe_3O_4@Arg-PPy nanocomposite.

6.3.1.7 XPS analysis

Fig. 6.4(B) shows the wide-scan XPS spectra of the Fe_3O_4@Arg-PPy nanocomposite (a) before and (b) after adsorption of Cr(VI) ions. Energy bands at 284, 531, 400 and 709-724 eV, attributed to Cl 1s, O 1s, N 1s, and Fe 2p core levels, respectively, are observed as presented in **Fig. 6.4(B)(a)**. After adsorption, additional peaks at 576.98 and 586.70 eV corresponding to the binding energies of Cr $2p_{3/2}$ and Cr $2p_{1/2}$, respectively, are revealed (also in **Fig. 6.4(D))** [20,39]. The deconvolution of N 1s core level spectrum produced three peaks at 399.5, 399.9

and 401.1 eV, ascribed to the neutral nitrogen atom within the PPy framework (–NH–), polaron charged species (–NH•+–) and bipolaron charged species (=NH+–), respectively, as shown in **Fig. 6.4(C)** [1,31,38,39].

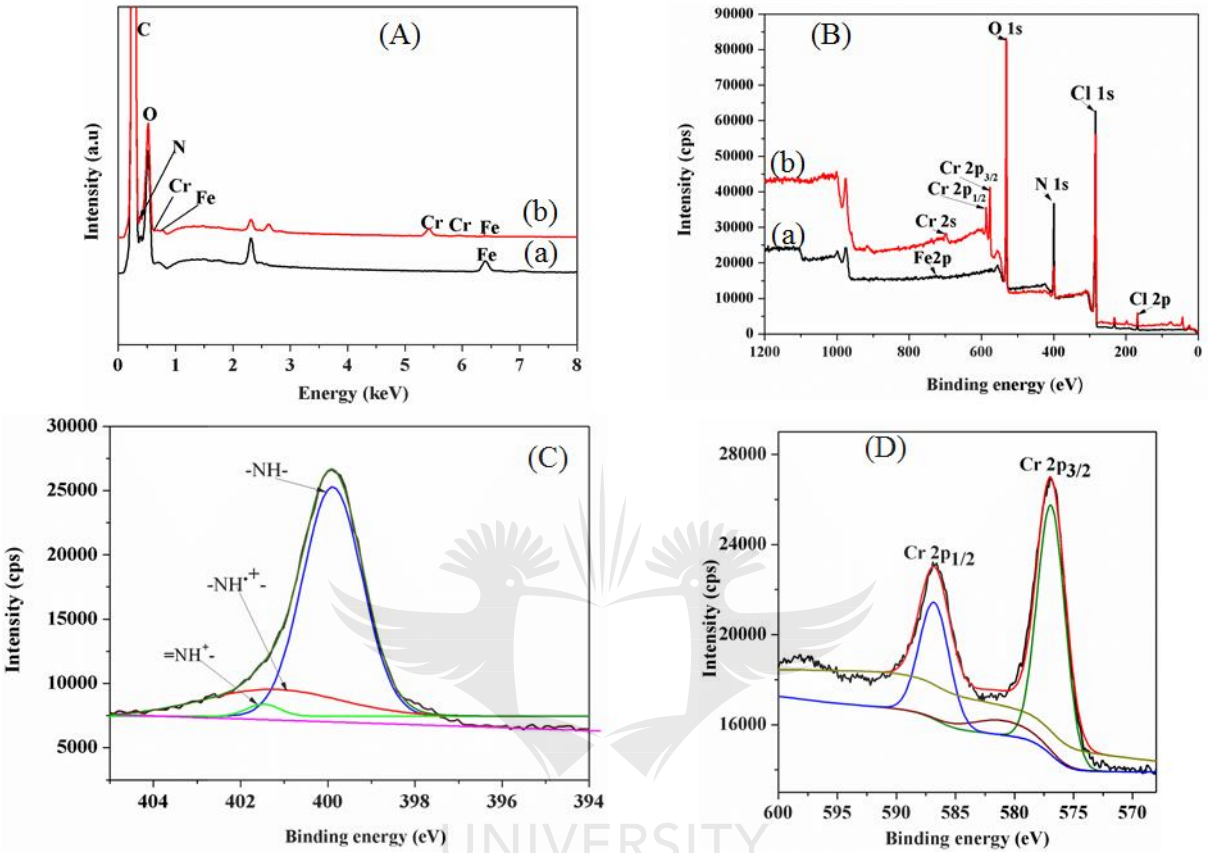

Fig. 6.4: (A) EDS spectra of Fe_3O_4@Arg-PPy nanocomposite (a) before and (b) after Cr(VI) ions adsorption. (B) Wide-scan XPS spectra for Fe_3O_4@Arg-PPy (a) before and (b) after Cr(VI) ions adsorption. (C) N 1s and (D) Cr 2p XPS spectra of Fe_3O_4@Arg-PPy nanocomposite.

6.3.1.8 The point-of-zero charge analysis

The point-of-zero charge (pH_{pzc}) of a material is very important in understanding the process mechanism as well as elucidating the effect of pH. The pH_{pzc} of Fe_3O_4@Arg-PPy nanocomposite was 7.2 as shown in **Fig. 6.5(A)**. Below pH 7.2, the adsorbent surface is positively charged and since Cr(VI) species are negatively charged, their adsorption onto the surface of Fe_3O_4@Arg-PPy nanocomposite takes place by electrostatic attractions. However, above pH_{pzc} deprotonation of the quinoid nitrogen atoms of PPy and arginine dopant is set to

take place and the adsorbent surface is mainly negatively charged. This leads to a decline in the Cr(VI) percentage removal as a result of electrostatic repulsions and competition between hydroxyl and CrO_4^{2-} ions [1,31,20].

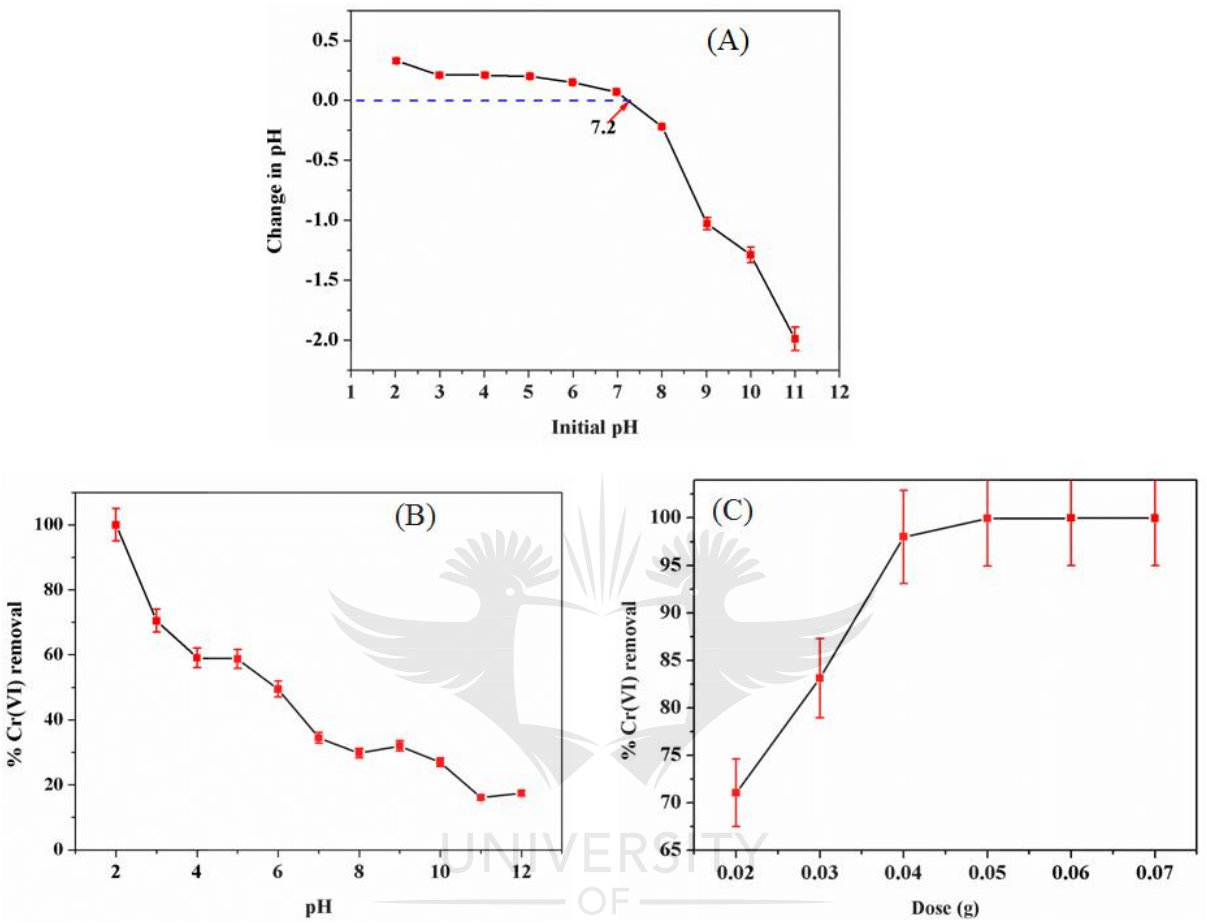

Fig. 6.5: (A) Determination of pH at point-of-zero charge of Fe_3O_4@Arg-PPy. (B) Effect of pH on the % Cr(VI) removal using 200 mg/L Cr(VI) ions solution (adsorbent dose: 0.05 g/50 mL of Cr(VI) ions solution, contact time: 24 h and temperature: 25 °C). (C) Effect of adsorbent dose on adsorption of Cr(VI) ions onto Fe_3O_4@Arg-PPy using 200 mg/L Cr(VI) ions solution at pH 2 and 25 °C.

6.3.2 Adsorption characteristics

6.3.2.1 Effect of pH on the removal of Cr(VI) ions

The effect of pH on Cr(VI) ions removal was studied from pH 2 to 12 using 0.05 g of Fe_3O_4@Arg-PPy adsorbent in 50 mL of 200 mg/L Cr(VI) ions solution and the results are

presented in **Fig. 6.5(B)**. The percentage of Cr(VI) removal drastically decreased from 99.9% at pH 2 to 29.7% at pH 8 and then falls further to 17.4% at pH 11. At low pH (2-6), Cr(VI) exists as H_2CrO_4, $HCrO_4^-$ and $Cr_2O_7^{2-}$ with $HCrO_4^-$ been predominant. On the other hand, at higher pH CrO_4^{2-} dominates [1,4]. At pH 2-6, the nitrogen atoms of PPy and arginine dopant of Fe_3O_4@Arg-PPy nanocomposite are protonated and there is high adsorption of $HCrO_4^-$ through electrostatic attractions [1,28,39]. Besides the electrostatic attractions of $HCrO_4^-$ by the positively charged surface of Fe_3O_4@Arg-PPy adsorbent, $HCrO_4^-$ can also easily undergo reduction to Cr(III) species in the presence of electron rich polymer matrix [1]. At pH above 7.2, the positively charged nitrogen atoms of PPy and arginine dopant become deprotonated and there is electrostatic repulsion between predominant CrO_4^{2-} species and Fe_3O_4@Arg-PPy surface. Moreover, at very high pH (11-12) the solution has more OH^- ions which are likely to compete with the CrO_4^{2-} species for the binding sites [1,28,39]. As a result, all further adsorption experiments were conducted at pH 2 which showed maximum removal of 99.9%.

6.3.2.2 Effect of adsorbent dose

The effect of adsorbent dose was studied at pH 2 using 50 mL of 200 mg/L Cr(VI) ions solution and varying the Fe_3O_4@Arg-PPy dosage from 0.02-0.07 g. From **Fig. 6.5(C)**, it was noted that as the dosage increased from 0.02-0.05 g, the percentage removal also increases up to 99.99%, most likely due to an increase in the number of active sites [21]. Further increase of Fe_3O_4@Arg-PPy dosage to 0.07 g resulted in constant Cr(VI) percentage removal, owing to the overlap of active binding sites [23]. Hence 0.05 g was adopted as the working dose for all further adsorption experiments.

6.3.2.3 Adsorption isotherms

To determine the adsorption capacity of Fe_3O_4@Arg-PPy adsorbent and thermodynamics of its Cr(VI) adsorption, the effect of temperature was investigated. This was conducted by keeping the temperature constant at four different values from 15 to 45 °C at a of pH 2, using 50 mL of 50-500 mg/L Cr(VI) ions solutions and 0.05 g adsorbent dose for 24 h contact time. **Fig. 6.6(A)** shows the nonlinear Langmuir and Freundlich adsorption isotherms model data fit whilst **Figs. 6.6(B)** and **(C)** show the linear fit of data to Langmuir and Freundlich isotherm models, respectively. It is evident from the **Fig. 6.6(A), (B)** and **(C)** that Cr(VI) adsorption onto

Fe_3O_4@Arg-PPy nanocomposite increased with an increase in temperature. Thus, an endothermic adsorption process is supported [5,43].

The linear and nonlinear forms of the Langmuir model are represented by **Equation (6.4)** and **(6.5)** respectively:

$$\frac{C_e}{q_e} = \frac{1}{q_m b} + \frac{C_e}{q_m} \tag{6.4}$$

$$q_e = \frac{b q_m C_e}{1 + b C_e} \tag{6.5}$$

where C_e (mg/L) and q_e (mg/g) are the equilibrium concentration of Cr(VI) ions and the amount adsorbed per unit mass of adsorbent, respectively. q_m and b (L/mg) are the maximum adsorption capacity and the Langmuir constant related to the affinity of the binding sites for chromium ions, respectively [28]. The dimensionless separation factor (R_L) as presented in **Equation (6.6)** gives indication of favourability or non- favourability of the adsorption process.

$$R_L = \frac{1}{1 + b C_o} \tag{6.6}$$

The values of R_L within the range 0 and 1 for each of the different initial Cr(VI) concentrations show favourable adsorption. However, $R_L = 0$, $R_L = 1$, and $R_L > 1$ suggest linear, irreversible and unfavourable process, respectively [28]. For this study, R_L values were found to be between 0 and 1 demonstrating favourable adsorption process (See **Table 1**).The nonlinear [5] and linear [36] forms of Freundlich isotherm, represented by **Equations (6.7)** and **(6.8)**, were equally used to describe the adsorption behaviour of Fe_3O_4@Arg-PPy adsorbent toward Cr(VI) ions:

$$q_e = K_f C_e^{\,1/n} \tag{6.7}$$

$$\ln q_e = \ln K_f + \frac{1}{n} \ln C_e \tag{6.8}$$

where K_f (mg/g) and *1/n* are the Freundlich constants related to the adsorption capacity and intensity of adsorption, respectively [31]. The values of *1/n* are frequently between 0 and 1, and if close to zero, this indicates more surface heterogeneity [36,44]. Moreover, for *n* values

between 1 and 10, stronger adsorbate/adsorbent interaction and the applicability of Freundlich isotherm are endorsed [7,28,36]. In the current investigation, the values of 1/*n* were close to 0 for the linear Freundlich isotherm (See **Table 6.1**). Nevertheless, the Langmuir and Freundlich linear and nonlinear model fit parameters at different temperatures, including, q_m, b, R_L, K_f and *1/n* are shown in **Table 6.1**. Comparing both models, R^2 values for the Langmuir (R^2_{linear} = 0.998-1.000) were higher than those for the Freundlich (R^2_{linear} = 0.9391-0.9816) for all temperatures. As the for the *Sy.x* values, those for Freundlich ranged from 4.623-14.81 with the Langmuir ones being 15.05-28.73 for 15-45 °C. Although the Freundlich model nonlinear fit data shows relatively lower of *Sy.x* values compared to those for Langmuir nonlinear, it is inconclusive that it is a better model to describe the adsorption process even from the linear plot in **Fig. 6.6(C**). *Sy.x* depends on the magnitude of the errors and is biased to fit data obtained at high concentration range [48]. The R^2 values for the Langmuir isotherm model for this temperature range strongly suggest that the experimental data for adsorption of Cr(VI) onto Fe_3O_4@Arg-PPy fitted well to this model with a maximum adsorption capacity of 322.58 mg/g at 25 °C [20,44,47,49]. Furthermore, the values of Langmuir separation factor (R_L) for all the studied temperatures were found to be much less than unity, thus confirming the favourability of adsorption process for all temperatures. R^2 is the most confident criterion for determining the best fitting model in 95% of reported liquid-phase adsorption systems. Therefore overally, the Langmuir model shows the best fit suggesting that the Cr(VI) binding onto Fe_3O_4@Arg-PPy sites is homogeneous, with equivalent adsorption energies and there is monolayer coverage with no interaction between adsorbed species [44]. In cognate studies, magnetic Fe_3O_4-PPy [21], aspartic acid doped PPy [5] and Fe_3O_4@glycine doped PPy [20] exhibited maximum absorption capacities of 169.40 at 25 °C, 176.67 at 30 °C and 238.00 mg/g at 25 °C, respectively. Thus, doping Fe_3O_4-PPy with arginine bearing four hypothetically nitrogen binding sites, significantly improved the adsorption performance. The adsorption capacities of several reported PPy-containing nanocomposites for the removal of toxic hexavalent chromium from water are presented in **Table 6.2** and it can be observed that Fe_3O_4@Arg-PPy adsorbent is relatively superior.

UNIVERSITY OF JOHANNESBURG

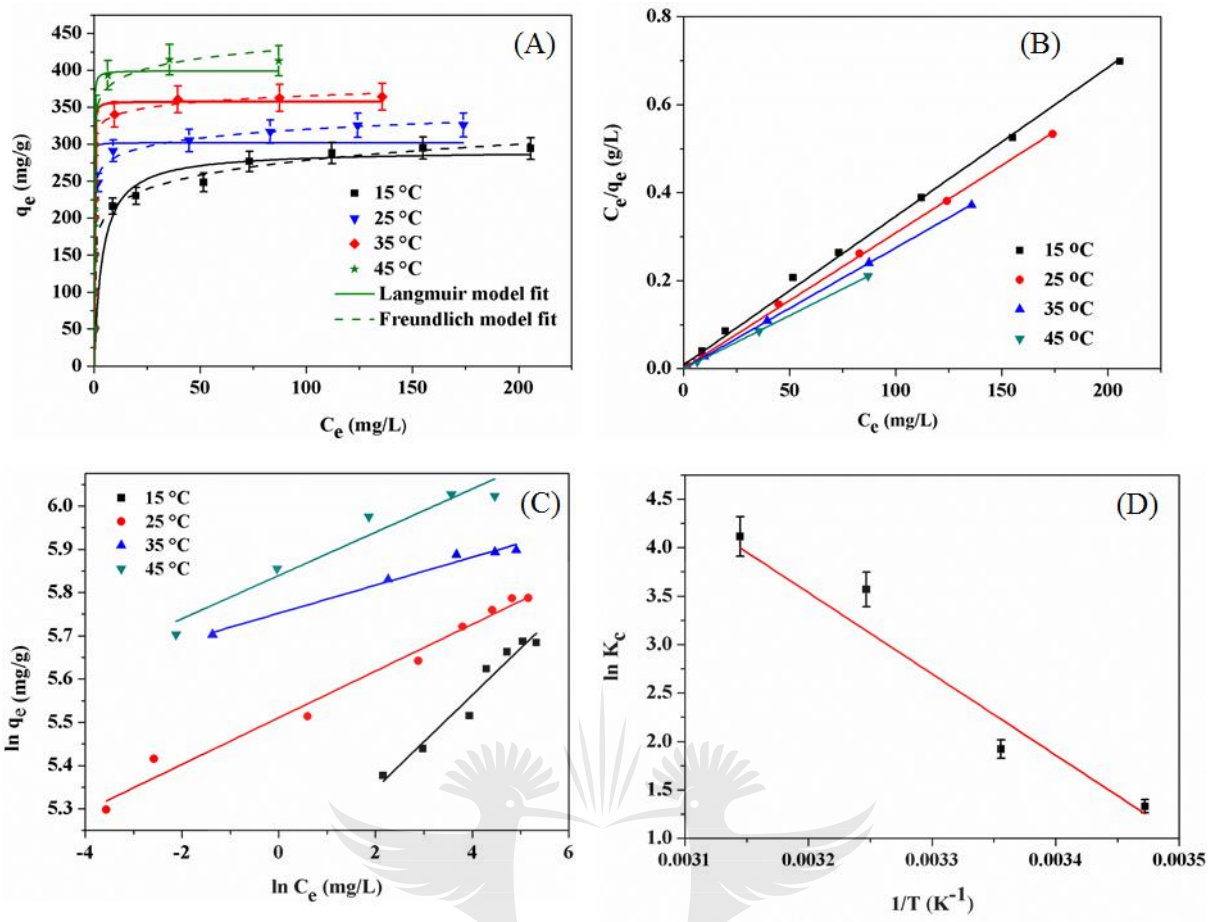

Fig. 6.6: Adsorption equilibrium isotherms for Cr(VI) ions removal by Fe_3O_4@Arg-PPy and fit of data to (A) nonlinear Langmuir and Freundlich models. Linearized (B) Langmuir and (C) Freundlich isotherm models data fit. (D) Van't Hoff's plot.

UNIVERSITY OF JOHANNESBURG

Table 6.1: Langmuir and Freundlich parameters for the sorption of Cr(VI) ions onto Fe_3O_4@Arg-PPy.

Isotherm model	Temperature (°C)			
	15	25	35	45
Langmuir				
Linear				
q_m (mg g^{-1})	303.03	322.58	370.37	416.67
b (L mg^{-1})	0.15	0.78	2.45	6.00
R_L	0.01397	0.00335	0.000636	0.000239
R^2	0.998	0.9997	1.000	1.000
Nonlinear				
Best-fit values				
q_m	291.3	300.3	357.8	399.3
b	0.2656	57.29	20.08	22.97
Std. Error				
q_m	8.473	11.71	5.260	12.27
b	0.07004	21.06	4.665	7.442

95% Confidence Intervals				
q_m	269.5 to 313.1	271.6 to 328.9	341.1 to 374.5	360.3 to 438.4
b	0.08555 to 0.4457	5.752 to 108.8	5.239 to 34.93	0.7072 to 46.66
Goodness of fit				
Degrees of Freedom	6	6	3	3
R^2	0.8195	0.7031	0.8922	0.8353
Absolute Sum of Squares	1133	4951	323.3	1591
Sy.x	15.05	28.73	10.38	23.03
Number of points Analyzed	8	8	5	5
Freundlich				
Linear				
K_f (mg g^{-1})	169.02	249.2	314.91	243.61
1/n	0.1081	0.0545	0.0324	0.0500
R^2	0.9585	0.9797	0.9816	0.9391
Nonlinear				
Best-fit values				
K_f	168.9	247.0	315.3	345.2
n	9.225	18.33	31.27	20.95
Std. Error				
K_f	8.159	2.916	3.355	8.215
n	0.9342	0.9984	2.785	3.396
95% Confidence Intervals				
K_f	147.9 to 189.9	239.9 to 254.2	304.6 to 325.9	319.0 to 371.3
n	6.823 to 11.63	15.89 to 20.77	22.41 to 40.13	10.15 to 31.75
Goodness of Fit				
Degrees of Freedom	6	6	3	3
R^2	0.9550	0.9851	0.9786	0.9319
Absolute Sum of Squares	282.3	248.3	64.12	658.1
Sy.x	7.514	6.433	4.623	14.81
Number of points Analyzed	8	8	5	5

UNIVERSITY OF JOHANNESBURG

Table 6.2: Comparative assessment of Cr(VI) ions adsorption capacity of Fe_3O_4@Arg-PPy with other reported materials.

Adsorbent	Adsorption capacity (mg/g)	Optimised pH	Temp (°C)	Ref.
Aspartic acid doped PPy	176.67	2	30	[5]
Fe_3O_4 glycine doped PPy	238.00	2	25	[20]
PPy/Fe_3O_4	169.40	2	25	[21]
Glycine doped PPy	217.39	2	25	[22]
PPy-PANI fibers	227.00	2	25	[23]
PPy coated hallocyte nanotubes	149.25	2	25	[24]
PPy-rGO/Fe_3O_4	226.80	3	30	[31]
PPy-PANI/Fe_3O_4	303.00	2	25	[39]
PPy/Fe_3O_4/AgCl	111.10	2	30	[45]

Fe_3O_4/PPy	208.77	2	33	[46]
GO/MnO_2/Fe_3O_4/PPy	374.53	2	35	[47]
Fe_3O_4@Arg-PPy nanocomposite	322.58	2	25	**Current study**

6.3.2.4 Thermodynamic parameters for Cr(VI) ions adsorption onto Fe_3O_4@Arg-PPy

The adsorption thermodynamic behaviour was evaluated from the adsorption isotherm data through change in Gibbs free energy ($\Delta G°$), enthalpy ($\Delta H°$) and entropy ($\Delta S°$) using **Equation (6.9)** and **(6.10)**:

$$\Delta G° = -RT\ lnK_c = -RT\ ln\ (m\frac{q_e}{C_e}) \quad (6.9)$$

$$ln\ (m\frac{q_e}{C_e}) = \frac{\Delta S°}{R} - \frac{\Delta H°}{RT} \quad (6.10)$$

where R (J mol^{-1} K^{-1}), T (K) and K_c are the molar gas constant, temperature and equilibrium constant, respectively. The values of $\Delta H°$ and $\Delta S°$ were calculated from the slope and intercept of the plot of $ln\ (mq_e/C_e)$ against $1/T$ as shown in **Fig. 6.6(D)**. The evaluated thermodynamic parameters are displayed in **Table 6.3**. From the calculated adsorption capacities at different temperature, the adsorption efficiency increased with increase in temperature (294.11, 322.58, 370.37 mg/g and 416.67 mg/g at 15, 25, 35 and 45 °C, respectively. The affinity of adsorbate on the adsorbent is higher at high temperatures. Thus, the magnitude and positive value of $\Delta H°$ (+76.16 kJ mol^{-1}) confirms the chemisorption behaviour and endothermic nature of the adsorption process as reported in other studies with PPy-based materials of similar nature [15,20,21,27,31]. At high temperature there is increase in collisions frequency between the Fe_3O_4@Arg-PPy adsorbent and the sorbate ions since the sorbate attain more kinetic energy for diffusion from the bulk phase of solution to the solid phase of the adsorbent. Furthermore temperature can chemically change the adsorbent adsorption sites and activity [25]. The increase in negativity of $\Delta G°$ with temperature indicates feasibility and spontaneity of the adsorption process. This may be due to a greater driving force for adsorption at higher temperatures. Hence, the adsorption process becomes more favourable. At higher temperatures the adsorbate molecules are more mobile in solution or they have more kinetic energy thus their affinity for the adsorbent increases and also adsorbent surface becomes activated leading increased adsorption capacity due favourable interaction [25]. Additionally, the adsorption

took place with increasing randomness at the solid-liquid interface as depicted by the positive value of ΔS° (+0.274 kJ mol^{-1} K^{-1}). The adsorbed solvent molecules/ions which are displaced by the adsorbate species on adsorbent surface, gain more rotational and translational energy which increases with increasing adsorption. This produces positive entropy than is lost by the adsorbate ions/molecules thus permitting for the occurrence of randomness in the system. The positive ΔS° value also relates to an increase in the degree of freedom of the adsorbed species [15,39].

Table 6.3: Thermodynamic data.

Temperature (°C)	Δ*G*° (kJ mol^{-1})	Δ*H*° (kJ mol^{-1})	Δ*S*° (kJ mol^{-1} K^{-1})
15	-3.184	+76.160	+0.274
25	-4.755		
35	-9.133		
45	-10.871		

6.3.2.5 Adsorption kinetics

Adsorption kinetics are valuable in envisioning the adsorption rate controlling step which provides insight into design and modelling for adsorption-based water treatment processes [11,48,49]. The effect of contact time **(Fig. 6.7(A))** for the adsorption of Cr(VI) ions onto Fe_3O_4@Arg-PPy nanocomposite adsorbent was studied for the initial Cr(VI) ions concentrations of 50, 100 and 150 mg/L, and the equilibrium times were found to be 50, 90 and 150 minutes, respectively. The linear and nonlinear pseudo-first-order and pseudo-second-order kinetic models were applied for the adsorption data and these are represented by **Equations (6.11)** to **(6.14)**:

$$q_t = q_e(1 - exp(^{-k_1\, t}) \tag{6.11}$$

$$log(q_e - q_t) = log(q_e) - \frac{k_1}{2.303}\, t \tag{6.12}$$

$$q_t = \frac{k_2 q_e 2\ t}{1 + k_2 q_e t} \tag{6.13}$$

$$\frac{t}{q_t} = \frac{1}{k_2 q_e 2} + \frac{t}{q_e} \tag{6.14}$$

where k_1 (min^{-1}) and k_2 ($g/mg^{-1}.min^{-1}$) are the pseudo-first-order and pseudo-second-order-rate constants respectively. q_e and q_t (mg/g) are the adsorption capacities at equilibrium and time t (min), respectively. The effect of contact time on the adsorption of Cr(VI) ions onto Fe_3O_4@Arg-PPy nanocomposite, nonlinear pseudo-first-order and pseudo-second-order models data fit at different concentrations are illustrated in **Fig. 6.7(A)**. The linearized pseudo-second-order and pseudo-first-order kinetics model data fit are shown in **Fig. 6.7(B)** and (C), respectively. The calculated values for the rate constants and other parameters from linear and non-linear regression plots are presented in **Table 6.4**. The R^2 values obtained from the pseudo-second-order model (R^2_{linear} = 0.9993-0.9999 and $R^2_{nonlinear}$ = 0.8572-0.9625) are higher than those from the pseudo-first-order model (R^2_{linear} = 0.9152-0.9668 and $R^2_{nonlinear}$ = 0.6454-0.8786). Furthermore, the q_e values obtained from the pseudo-second-order model were very close to those obtained experimentally. Thus, Cr(VI) adsorption onto Fe_3O_4@Arg-PPy followed the pseudo-second-order model [39,50].

To understand the nature of the rate controlling step in the adsorption of Cr(VI) ions by Fe_3O_4@Arg-PPy nanocomposite, the Webber-Morris intra-particle diffusion model was engaged, and the equation is as follows:

$$q_t = k_{int}\, t^{0.5} + C_i \qquad (6.15)$$

UNIVERSITY OF JOHANNESBURG

where k_{int} (mg g^{-1} $min^{-0.5}$) denotes the intra-particle diffusion rate constant and C_i (mg/g), a constant linked to the magnitude of the boundary layer thickness. The plots of $t^{0.5}$ against q_t for different initial concentrations of Cr(VI) solutions are shown in **Fig. 6.7(D)**. Several steps affected the adsorption of Cr(VI) on Fe_3O_4@Arg-PPy as depicted by three linear stages. The first stage relates to faster film diffusion, followed by slower adsorption due to intra-particle diffusion. The third region points out the final equilibrium stage [39,48]. Additionally, these plots did not pass through the origin. Based on the above observations, intra-particle diffusion was not the sole rate determining step [39,45,51]. From the slopes of the second linear portion of the curves the value of k_{int} for the three different concentrations were obtained and presented in **Table 6.4**.

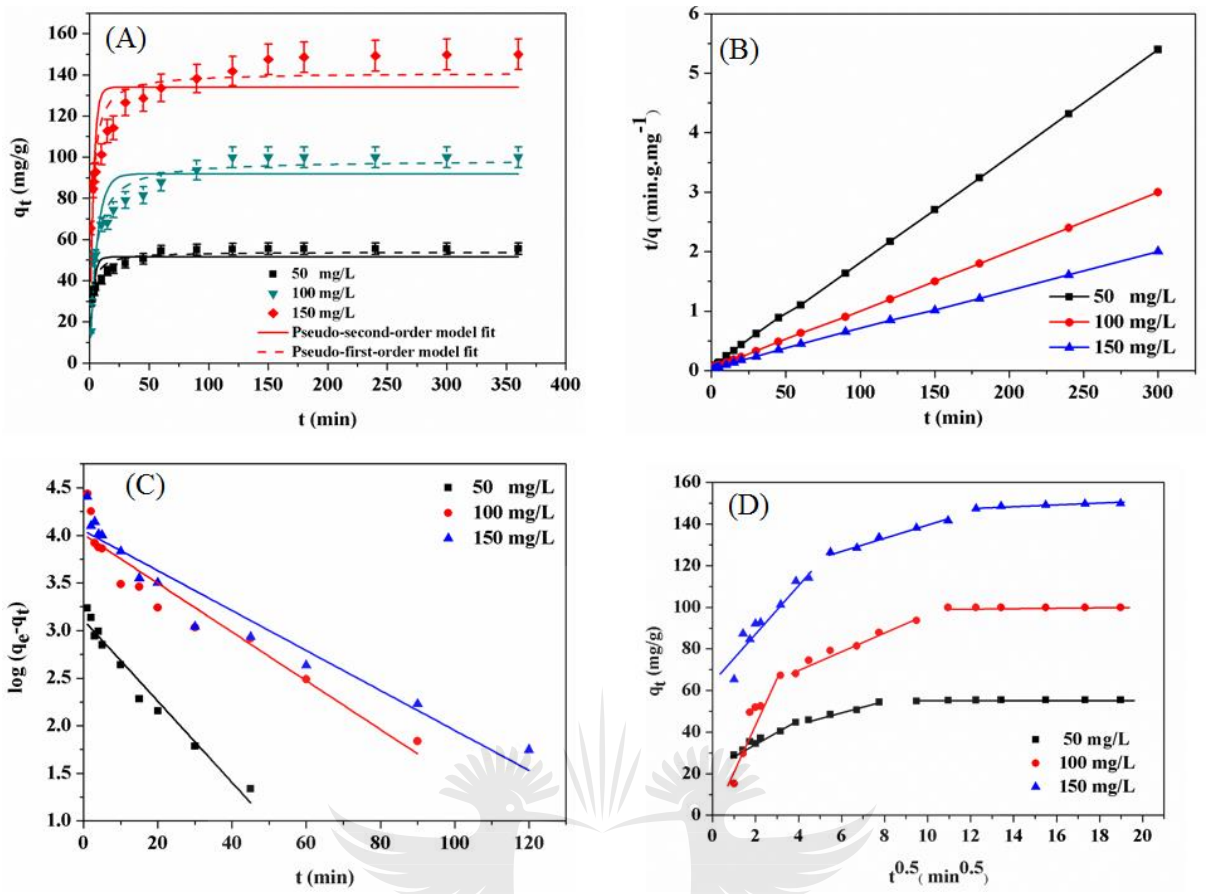

Fig. 6.7: (A) Effect of contact time on the adsorption of Cr(VI) ions onto Fe_3O_4@Arg-PPy, nonlinear pseudo-first-order and pseudo-second-order models fitting (pH = 2, adsorbent dose 0.05 g/50 mL of Cr(VI) ions and temperature 25 °C). Fit of data to linearized (B) pseudo-second-order and (C) pseudo-first-order kinetic models. (D) Intra-particle diffusion model for the Cr(VI) ions adsorption by Fe_3O_4@Arg-PPy nanocomposite

Table 6.4: Kinetics parameters for the sorption of Cr(VI) ions onto Fe_3O_4@Arg-PPy at different concentrations.

Kinetic models	Initial concentration (mg/L)		
	50	100	150
Pseudo-first-order			
Linear			
k_1 (min^{-1})	0.0983	0.05900	0.0463
q_e (mg g^{-1})	54.45	99.97	147.50
R^2	0.9668	0.9152	0.9404
Nonlinear			
Best-fit values			
q_e	51.54	91.89	134.0
k_1	0.3811	0.1666	0.3509
Std. Error			

q_e	1.653	2.869	4.675
k_1	0.06561	0.02498	0.06441
95% Confidence Intervals			
q_e	48.04 to 55.05	85.81 to 97.97	124.1 to 143.9
k_1	0.2420 to 0.5202	0.1137 to 0.2196	0.2144 to 0.4875
Goodness of Fit			
Degrees of Freedom	16	16	16
R^2	0.6454	0.8786	0.6507
Absolute Sum of Squares	555.9	1425	4393
Sy.x	5.895	9.436	16.57
Number of points Analyzed	18	18	18
Pseudo-second-order			
Linear			
k_2 (g m^{-1}.min^{-1})	6.67 x10^{-3}	2.64 x10^{-3}	1.49 x10^{-3}
q_e (mg g^{-1})	54.45	99.97	147.50
R^2	0.9998	0.9999	0.9993
Nonlinear			
Best-fit values			
k_2	0.01121	0.002244	0.003684
q_e	53.90	98.58	141.0
Std. Error			
k_2	0.001848	0.0002701	0.0006601
q_e	1.160	1.919	3.442
95% Confidence Intervals			
k_2	0.00729 to 0.01513	0.001670 to 002817	0.00228 to 0.0050
q_e	51.44 to 56.36	94.51 to 102.6	133.7 to 148.3
Goodness of Fit			
Degrees of Freedom	16	16	16
R^2	0.8656	0.9625	0.8572
Absolute Sum of Squares	210.7	440.1	1796
Sy.x	3.629	5.245	10.60
Number of points Analyzed	18	18	18

Intra-particle diffusion model parameters			
	Cr(VI) ions concentration (mg/L)		
	50	100	150
k_{int} (mg g^{-1}.$min^{-0.5}$)	2.5134	4.2645	3.1863
C_i (mg g^{-1})	34.402	53.982	107.90

UNIVERSITY OF JOHANNESBURG

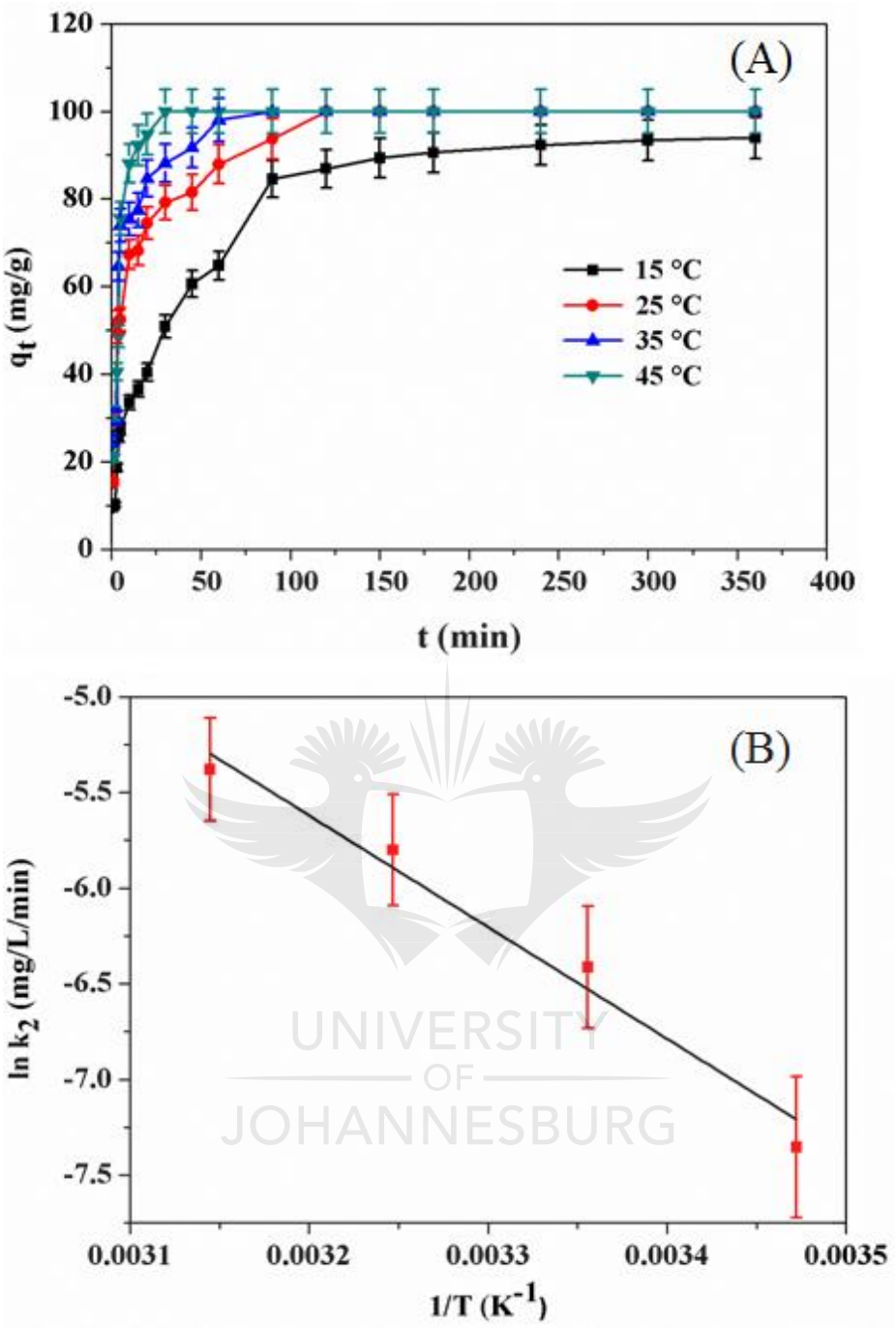

Fig. 6.8: (A) Effect of temperature on the rate of Cr(VI) ions adsorption onto Fe_3O_4@Arg-PPy nanocomposite at 100 mg/L initial Cr(VI) ions concentration (pH = 2, adsorbent dose 0.05 g/50 mL of Cr(VI) ions. (B) Arrhenius plot.

Further, a temperature dependent kinetics investigation was also conducted to determine the activation energy of the Cr(VI) adsorption onto Fe_3O_4@Arg-PPy nanocomposite. **Fig. 6.8(A)** shows a plot of q_t against t at different temperatures (15, 25, 35 and 45 °C). It is clear that the

rate of reaction increases with increase in temperature. The linear pseudo-second-order data fit for temperature dependent kinetics was used to calculate the rate constants k_2 as shown in **Table 6.5** [39,52]. The activation energy, E_A (kJ mol^{-1}) was determined using **Equation (6.16)**:

$$ln\, k_2 = lnA + (-\frac{E_a}{R})\frac{1}{T} \quad (6.16)$$

where k_2 and A (g mg^{-1} min^{-1}) are the pseudo-second-order rate and Arrhenius constants. A plot of lnk_2 versus $1/T$ is shown in **Fig. 6.8(B)**. The activation energy was obtained as 49.91 kJ mol^{-1}, demonstrating chemisorption of Cr(VI) onto Fe_3O_4@Arg-PPy [15,27,39].

Table 6.5: Temperature dependent kinetics.

Temperature (K)	q_t (mg/g)	k_2 (g/mg.min)	ln k_2
288	89.31	6.3 x10^{-4}	-7.35
298	99.67	1.6 x10^{-3}	-6.41
308	99.96	3.0 x10^{-3}	-5.80
318	99.97	4.6 x10^{-3}	-5.38

6.3.2.6 Effect of co-existing ions

Several anions and cations, namely, sulphate (SO_4^{2-}), chloride (Cl^-), copper(II) (Cu^{2+}), zinc(II) (Zn^{2+}), nickel(II) (Ni^{2+}), hydrogen phosphate (HPO_4^{2-}), hydrogen carbonate (HCO_3^-) and nitrate (NO_3^-) may be found along with Cr(VI) ions in natural and wastewater. These ions could have the potential to competitively bind onto Fe_3O_4@Arg-PPy active sites alongside Cr(VI) ions, hence interfering with their uptake. **Fig. 6.9(A)** shows the effect of the above-mentioned ions on the removal of Cr(VI) ions using 0.05 g of Fe_3O_4@Arg-PPy adsorbent. Most of the ions had a negligible effect on the adsorption of Cr(VI) ions except for HCO_3^- ions at high concentration (150 mg/L). For cations, this was expected since at pH 2 the Fe_3O_4@Arg-PPy adsorbent is positively charged and any cations in solution are likely to be repelled [30]. NO_3^- are known to form outer-sphere complexes with binding surfaces [20,21,30,31,39], therefore their adsorption onto Fe_3O_4@Arg-PPy was seen as insignificant. Sulphate ions (SO_4^{2-}), on the other hand, did not also interfere with Cr(VI) ions adsorption in the form of $HCrO_4^-$ at pH 2, probably as a result of favourable hydration (-1080 kJ mol^{-1}) relative to $HCrO_4^-$ (-184 kJ mol^{-1}) [20]. The observed interference of hydrogen carbonate ions (HCO_3^-) at high concentration is certainly ascribed to their ability to undergo hydrolysis and generate OH^- ions which would then compete for binding sites with $HCrO_4^-$ or increase the solution pH [53].

6.3.2.7 Performance on practical industrial waste water samples

The as-prepared Fe_3O_4@Arg-PPy was assessed for applicability in selective adsorption of Cr(VI) ions from chromium ore leachate effluent, sampled from Gweru heavy industrial site wastewater in the Midlands province of Zimbabwe. The initial concentration of Cr(VI) in the effluent was determined to be 78 mg/L and the pH 0.46. The latter was adjusted to be 2 as this value was found to be the optimal pH for Cr(VI) removal using Fe_3O_4@Arg-PPy nanocomposite. Adsorbent dosages of 0.01, 0.025, 0.05, 0.075 and 0.1g per 50 mL sample solutions were used and the suspensions were shaken for 24 h at 25 °C. **Fig. 6.9(B)** shows variation of the adsorbent dose with percentage removal of Cr(VI) ions (red line) and equilibrium concentration of Cr(VI) ions (blue line). It is evident that the removal of Cr(VI) ions increased rapidly with Fe_3O_4@Arg-PPy dosage (0.025 to 0.1 g) from 60.68 to 99.98%. Concurrently, the equilibrium concentration of Cr(VI) ions at dosages greater than 0.05 g fell lower to the detection limit of UV-Visible spectrophotometer. Thus, Fe_3O_4@Arg-PPy adsorbent was able to almost completely remove the Cr(VI) ions contaminant from the collected wastewater sample.

6.3.2.8 Desorption studies

Regeneration and reusability of an adsorbent is necessary to assess its net benefit and cost [54,55]. The removal of Cr(VI) ions from chromium loaded Fe_3O_4@Arg-PPy adsorbent (0.05 g) was conducted using 50 mL of 0.05M NaOH. Then, the desorption of Cr(III) ions and revival of the adsorbent was executed using 50 mL of 2M HCl aqueous solution. Fig. 9(C) shows four consecutive adsorption-desorption cycles of Fe_3O_4@Arg-PPy adsorbent. The observed very low amount of Cr(VI) being desorbed is due to reduction of Cr(VI) to Cr(III) after adsorption as evidenced by XPS Cr 2p spectrum analysis of the chromium loaded nanocomposite. However, there is an increase in the amount of Cr(VI) ions desorbed with the number of cycles, suggesting a decrease in Fe_3O_4@Arg-PPy adsorbent ability to reduce loaded Cr(VI) to Cr(III) after repeated adsorption-desorption procedure. This is probably ascribed to inevitable loss in mass during regeneration/reusability of the adsorbent [56].

UNIVERSITY OF JOHANNESBURG

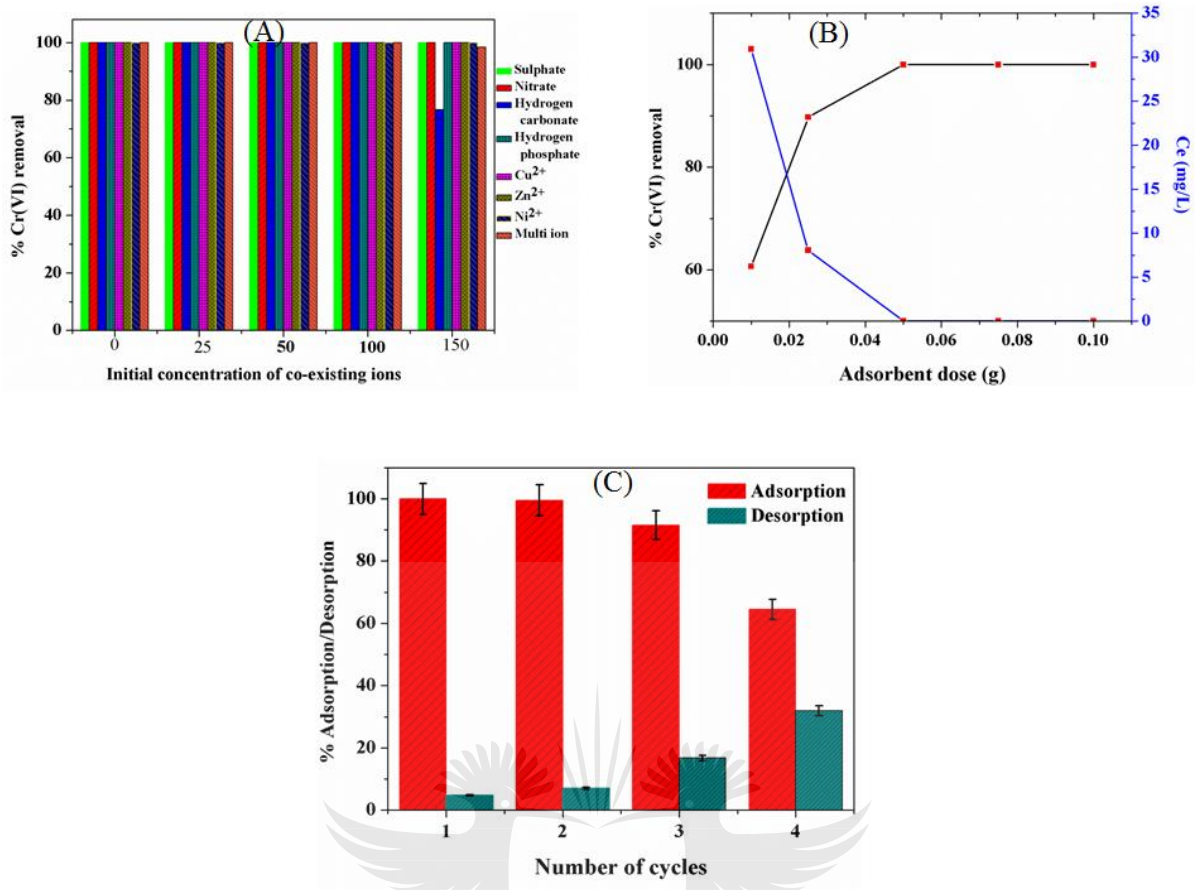

Fig. 6.9: (A) Effect of co-existing ions on Cr(VI) adsorption at pH 2 (adsorbent dose: 0.05 g/50 mL of Cr(VI) ions solution, contact time: 24 h and temperature: 25 °C). (B) Effect of Fe_3O_4@Arg-PPy dose on % Cr(VI) removal and equilibrium concentration in wastewater samples. (C) Adsorption and desorption cycles of Fe_3O_4@Arg-PPy nanocomposite.

6.3.2.9 Adsorption mechanism

Through FTIR and XPS spectra analysis, in conjunction with IC-ICP-MS speciation chromatograms interpretation, a plausible mechanism of Cr(VI) removal was proposed. The FTIR spectrum of Fe_3O_4@Arg-PPy displayed a shift of the band at 3098 cm^{-1} corresponding to NH stretching vibration to 3121 cm^{-1} after Cr(VI) adsorption **(Fig. 6.1(A))**. This shift is certainly caused by the interaction between Cr(VI) ions and protonated and positively charged nitrogen containing substituents of PPy and arginine at low pH. This inferred a possible electrostatic attractions mechanism between Fe_3O_4@Arg-PPy adsorbent and $HCrO_4^-$ species as illustrated by **Equation (6.17)**.

$$Fe_3O_4@Arg\text{-}PPyHN^+ + HCrO_4^- \longrightarrow Fe_3O_4@Arg\text{-}PPyHN^+ \text{----- } HCrO_4^- \quad (6.17)$$

Hexavalent chromium in acidic medium ($HCrO_4^-$) exhibits a high oxidising potential (1.33V) [1,57]. Therefore, in the presence of electron rich polymeric moiety in the nanocomposite, $HCrO_4^-$ easily undergo reduction to afford Cr(III) species as shown by **Equation (6.18)**.

$$HCrO_4^- + 7H^+ + 3e^- \rightleftharpoons 3Cr^{3+} + 4H_2O \quad (6.18)$$

Fig. 6.10(A) shows the XPS N 1s core-level spectrum of Fe_3O_4@Arg-PPy after chromium adsorption with deconvoluted peaks at the binding energies of 399.5, 400.1 and 401.3 eV and their percentages of the total N 1s intensity were 32.1, 67.1 and 29.6%, respectively. As compared to XPS N 1s spectrum of Fe_3O_4@Arg-PPy before treatment **(Fig. 6.4(C))**, a slight shift to the higher binding energies can be observed and a marked reduction in peak intensity [58]. The shift in binding energy and the reduced peak intensity after chromium adsorption indicates the N 1s involvement in binding Cr(VI) ions [58,59]. Furthermore, there was an observed decrease of 44.7% in the proportion of neutral nitrogen atom (–NH–) in the N atom, due to oxidation after Cr(VI) adsorption along with 64.9% increase in the proportion of polaron charged species ($-NH^{\cdot+}-$), owing to the production of the more oxidized state as a result of the Cr(VI) and NH of PPy moiety redox reaction [57,60]. This shows that Cr(VI) is adsorbed electrostatically on protonated –NH– at pH 2 followed by reduction to Cr(III) as illustrated by Eqs.(17) and (18) above. With regard to chromium species, the XPS Cr 2p core level spectra usually show bands from 575.0-580.0 eV (Cr $2p_{3/2}$) and 585.0-588.0 eV (Cr $2p_{1/2}$) for Cr(III). The peaks in the ranges 580.0-580.5 eV (Cr $2p_{3/2}$) and 589.0-590.0 eV (Cr $2p_{1/2}$) are typical for Cr(VI) species [56,60]. In the current investigation, the binding energy of Cr $2p_{3/2}$ and Cr $2p_{1/2}$ were detected at 576.98 and 586.70 eV, respectively **(Fig. 6.4(D))**, consistent with the characteristics of Cr(III). In addition, amino substituents are hard bases that can chelate with hard acid, including, Cr(III) species [13,17,58]. Adsorption behaviours of amino acids using the density functional theory calculations have shown that arginine is capable of binding with metallic compounds at not less than two nitrogen atoms [61].

UNIVERSITY OF JOHANNESBURG

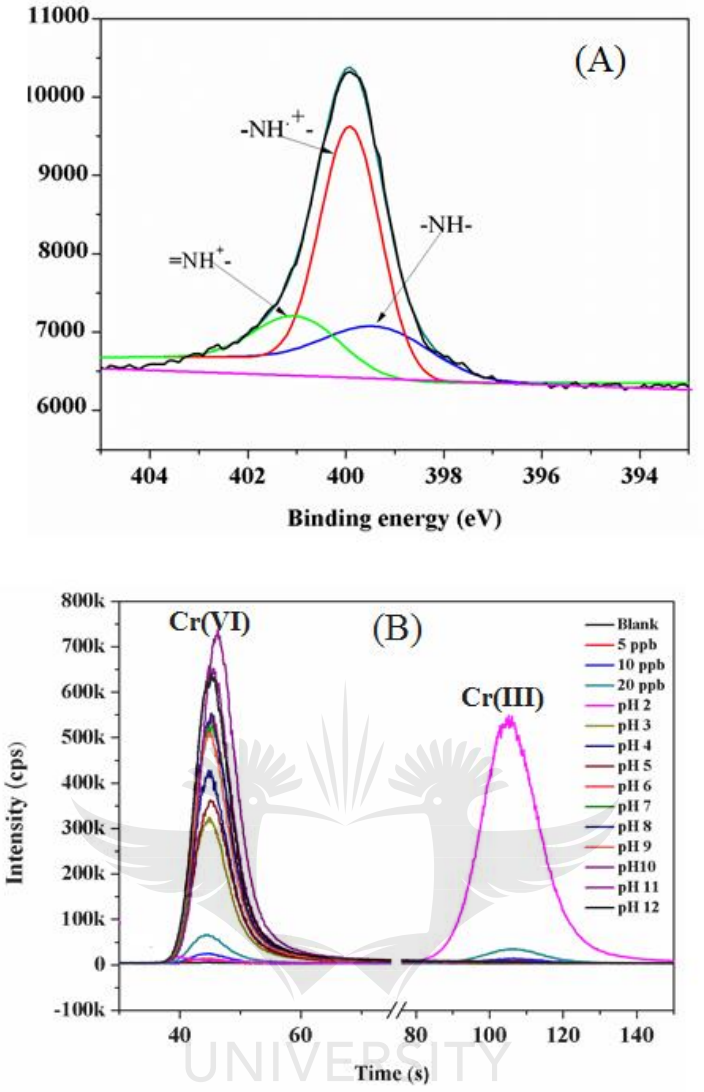

Fig. 6.10: (A) N 1s core-level XPS spectrum of Fe_3O_4@Arg-PPy after treatment. (B) IC-ICP-MS chromatograms of Cr speciation in filtrate samples at various pH values.

The concentrations of Cr(III) and Cr(VI) species in filtrate samples, obtained during pH effect study, were determined using IC-ICP-MS and the speciation chromatograms are shown in **Fig. 6.10(B)**. At pH 2, the concentration of Cr(III) species was found to be 68.90 mg/L in the filtrate and no Cr(VI) ions were detected. However, Cr(III) is well reported to be far less toxic than Cr(VI). On the other hand, at pH 3-12, only Cr(VI) ions ranging from 18.70 to 188.64 mg/L were detected. At higher pH, CrO_4^{2-} dominates and since it has a low redox potential (-0.26 V), it may not be easily reduced to Cr(III). Therefore, pH 2 represents a key parameter for treatment of Cr(VI) contaminated water with Fe_3O_4@Arg-PPy nanocomposite.

The plausible mechanism for Cr(VI) removal using Fe_3O_4@Arg-PPy adsorbent is illustrated in Scheme 6.2 as follows:

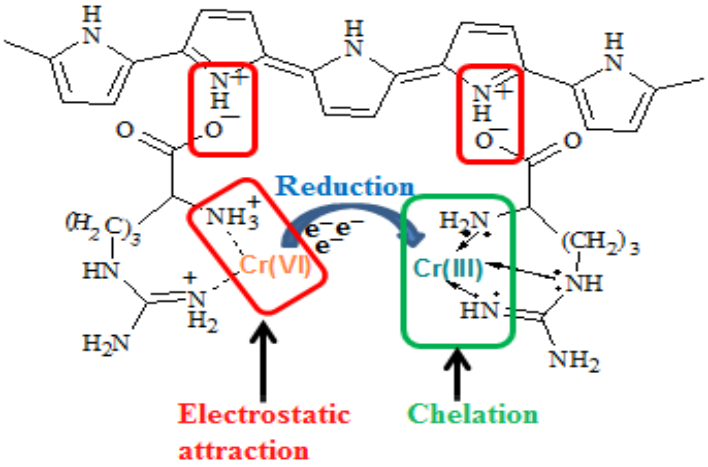

Scheme 6.2: Plausible mechanism for Cr(VI) removal using Fe_3O_4@Arg-PPy adsorbent.

6.4 Conclusion

A highly selective Fe_3O_4@Arg-PPy adsorbent was successfully prepared by a one-pot chemical polymerization of pyrrole with arginine and commercially available Fe_3O_4 NPs. The FTIR, XRD, VSM and TEM analyses of the Fe_3O_4@Arg-PPy nanocomposite established the successful incorporation of arginine and Fe_3O_4 into PPy. The FE-SEM image showed agglomerated spherical-like particles. The specific surface area of the as-described material was measured to be 22 m^2/g, which was much greater than that of pristine PPy. The batch experimental results indicated a highly pH dependent Cr(VI) removal with the optimum pH value of 2. The adsorption process was Langmuir modelled with adsorption capacities of 294.11, 322.58, 370.37 and 416.67 mg/g at 15, 25, 35 and 45 °C, respectively. The kinetics of the Cr(VI) removal using Fe_3O_4@Arg-PPy conformed to the pseudo-second-order model and the determined rate constant was 6.67 $x10^{-3}$ g $m^{-1}.min^{-1}$ at room temperature for the solution of initial Cr(VI) concentration 50 mg L^{-1} and pH 2. The calculated thermodynamic parameters, $\Delta G°$ -4.76 kJ mol^{-1} at 25 °C, $\Delta H°$ +76.16 kJ mol^{-1}, $\Delta S°$ +0.27 kJ mol^{-1} K^{-1} and E_a 49.91 kJ mol^{-1} showed a spontaneous, endothermic and chemisorption process. Field application study using chromium ores leaching water sample revealed the potential effectiveness of Fe_3O_4@Arg-PPy adsorbent. Furthermore, the regeneration and reusability investigation showed that the removal efficiency stabilised at around 64% after four cycles. Co-existing ions had minimal or no effect

on the adsorption process. The results of FTIR, XPS and IC-ICP-MS spectra and chromatograms interpretations exposed Cr(VI) removal through electrostatic attractions, reduction and chelation. Therefore, Fe_3O_4@Arg-PPy has great potential for usage as an adsorbent for hexavalent Cr(VI) remediation from wastewater.

6.5 References

[1] B. Qui, C. Xu, D. Sun, H. Yi, J. Guo, X. Zhang, H. Qu, M. Gueerrero, X. Wang, N. Noel, Z. Luo, Z. Guo, S. Wei, Polyaniline coated ethyl cellulose with improved Hexavalent chromium Removal, ACS Sustain. Chem. Eng. 2 (2014) 2070–2080.

[2] A. Zhitkovich, Chromium in drinking water: sources, metabolism, and cancer risks, Chem. Res. Toxico. 24 (2011) 1617–1629.

[3] S. Fan, Y. Wang, Y. Li, J. Tang, Z. Wang, J. Tang, X. Li, K. Hu, Facile synthesis of tea waste /Fe_3O_4 nanoparticle composite for hexavalent chromium removal from aqueous solution, RSC Adv. 7 (2017) 7576–7590.

[4] X. Sun, L. Yang, H. Xing, J. Zhao, X. Li, Y. Huang, H. Liu, High capacity adsorption of Cr(VI) from aqueous solution using polyethylenimine-functionalised poly(glycidyl methacrylate) microspheres, Colloids Surf. A Physicochem Eng. Asp. 457 (2014) 160–168.

[5] A. Amalraj, M.K. Selvi, A. Rageswari, A. Pius, Preparation and characterization of aspartic acid doped polypyrrole for the efficient removal of Cr(VI) from aqueous solution, J. Water Process Eng. 11 (2016) 162–173.

[6] Y. Zhieng, W. Wang, D. Huang, A. Wang, Kapok fiber oriented-polyaniline nanofibers for efficient Cr(VI) removal, Chem. Eng. J. 191 (2012) 154–161.

[7] Y.Y. Chang, J.W. Lim, J.K. Yang, Removal of As(V) and Cr(VI) in aqueous solution by sand media simultaneously coated with Fe and Mn oxides, J. Ind. Eng. Chem. 18 (2012) 188–192.

[8] M.L. Paul, J. Samuel, N. Chandrasekaran, A. Mukherjee, Preparation and characterization of layer-by-layer coated nano metal oxides-polymer composite film using Taguchi design method for Cr(VI) removal, J. Environ. Chem. Eng. 2 (2014) 1937–1946.

[9] F. Edition, Guidelines for drinking-water quality, WHO chronicle. 38 (2011) 388–389.

[10] M.M. Loock, J.P. Beukes, P.G. Van Zyl, A survey of Cr(VI) contamination of surface water in the proximity of ferrochromium smelters in South Africa, Water SA. 40 (2014) 709–716.

[11] K. Parida, K.G. Mishra, S.K. Dash, Adsorption of toxic ion Cr(VI) from aqueous state by TiO_2-MCM-41: Equilibrium and kinetic studies, J. Hazard. Mater. 241(2012) 395−403.

[12] A.E. Chavez-Guajardo, J.C. Medina-Llanas, L. Maqueira, C.A. Andrade, K.G. Alves, C.P. de Melo, Efficient removal of Cr(VI) and Cu(II) ions from aqueous media by use of polypyrrole and polyaniline magnetic nanocomposites, Chem. Eng. J. 281 (2015) 826–836.

[13] W. Fang, X. Jiang, H. Luo, J. Geng, Synthesis of graphene/SiO_2@ polypyrrole nanocomposites and their application for Cr(VI) removal in aqueous solution, Chemosphere 197 (2018) 594–602.

[14] S. Mandal, S.S. Mahapatra, R.K. Pat, Enhanced removal of Cr(VI) by cerium oxide polyaniline composite: optimisation and modelling using response surface methodology and artificial neural networks, J. Environ. Chem. Eng. 3 (2015) 870–885.

[15] S. Papita, S. Chowdhury, Insight into adsorption thermodynamics, in: M. Tadashi (Ed.), Thermodynamics, InTech, 2011.

[16] B. Kakavandi, R.R. Kalantary, M. Farzardkia, A.H. Mahvi, A. Esrafili, A. Azari, A.R. Yari, A.B. Javid, Enhanced Cr(VI) removal using activated carbon modified by zero valent iron and silver bimetallic nanoparticles, J. Environ. Health. Sci. Eng. 12 (2014) 2–10.

[17] T. Wang, L. Zhang, C. Li, W. Yang, T. Song, C. Tang, Y. Meng, S. Dai, H. Wang, L. Chai, J. Luo, Synthesis of core-shell magnetic Fe_3O_4@poly(m-phenylenediamine) particles for chromium reduction and adsorption, Environ. Sci. Technol. 49 (2015) 5654–5662.

[18] E. Malkovic, Y. Nuhoglu, Potential of tea factory waste for Cr(VI) removal from aqueous solutions: Thermodynamic and kinetic studies, Sep. Purif. Technol. 54 (2007) 291–298.

[19] N.H. Kera, M. Bhaumik, N. Ballav, K. Pillay, S.S. Ray, A. Maity, Selective removal of Cr(VI) from aqueous solution by polypyrrole/2.5-diaminobenzene sulfonic acid composite, J. Colloid Interface Sci. 476 (2016) 144–157.

[20] N. Ballav, H.J. Choi, S.B. Mishra, A. Maity, Synthesis, characterization of Fe_3O_4@ glycine doped polypyrrole magnetic nanocomposites and their potential performance to remove toxic Cr(VI), J. Ind. Eng. Chem. 20 (2014) 4085–4093.

[21] M. Bhaumik, A. Maity, V.V. Srvivasu, M.M. Onyango, Enhanced removal of Cr(VI) from aqueous solution using polypyrrole/Fe_3O_4 magnetic nanocomposite, J. Hazard. Mater. 190 (2011) 381–390.

[22] N. Ballav, H.J. Choi, A. Maity, S.B. Mishra, High efficient removal of Cr(VI) using glycine doped polypyrrole adsorbent from aqueous solution, Chem. Eng. J. 198 (2012) 536–546.

[23] M. Bhaumik, A. Maity, V.V. Srinivasu, M.M. Onyango, Removal of hexavalent chromium from aqueous solution using polypyrrole-polyaniline nanofibers, Chem. Eng. J. 181–182 (2012) 323–333.

[24] N. Ballav, H.J. Choi, S.B. Mishra, A. Maity, Polypyrrole-coated halloysite nanotube clay nanocomposite: synthesis, characterization and Cr(VI) adsorption behaviour, Appl. Clay Sci. 102 (2014) 60–70.

UNIVERSITY OF JOHANNESBURG

[25] V. Manirethan, K. Raval, R. Rajan, H. Thaira, R.M. Balakrishnan, Kinetic and thermodynamic studies on the adsorption of heavy metals from aqueous solution by melanin nanopigment obtained from marine source: Pseudomonas stutzeri, J. Environ Manage. 214 (2018) 315–324.

[26] R. Verma, A. Asthana, A.K. Singh, S. Prasad, An arginine functionalized magnetic nano-sorbent for simultaneous removal of three metal ions from water samples, RSC Adv. 7 (2017) 51079–51089.

[27] R. Kumar, M.O. Ansari, M.A. Barat, DBSA doped polyaniline/multi-walled carbon nanotubes composite for high efficiency removal of Cr(VI) from aqueous solution, Chem. Eng. J. 228 (2013) 748–755.

[28] M. Avila, T. Burks, F. Akntar, M. Göthelid, P.C. Lansåker, M.S. Toprak, M. Muhammed, A. Uheida, Surface functionalised nanofibers for the removal of Cr(VI) from aqueous solution, Chem. Eng. J. 245 (2014) 201–209.

[29] R. Karthik. S. Meenakshi, Removal of hexavalent chromium ions from aqueous solution using chitosan/polypyrrole composite, Desalin. Water Treat. 56 (2015) 1587–1600.

[30] Q. Liang, J. Geng, H. Luo, W. Fang, Y. Yin, Fast and selective removal of Cr(VI) from aqueous solutions by a novel magnetic Cr(VI) ion-imprinted polymer, J. Mol. Liq. 248 (2017) 767–774.

[31] H. Wang, X. Yuan, Y. Wu, X. Chen, L. Leng, H. Wang, H. Li, G. Zeng, Facile synthesis of polypyrrole decorated reduced graphene oxide-Fe_3O_4 magnetic composites and its application for the Cr(VI) removal, Chem. Eng. J. 262 (2015) 597–606.

[32] K. Simeonidis, S. Mourdikourdis, E. Kaprara, M. Mitrakas, L. Polavarapu, Inorganic engineered nanoparticles in drinking water treatment: a critical review, Environ. Sci.: Water Res. Technol. 2 (2016) 43–70.

[33] S. Debnath, A. Maity, K. Pillay, Magnetic chitosan-GO nanocomposite: Synthesis, characterization and batch adsorber design for Cr(VI) removal, J. Environ. Chem. Eng. 2 (2014) 963–973.

[34] X. Lv, X. Xue, G. Jiang, D. Wu, T. Sheng, H. Zhou, X. Xu, Nanoscale zero-valent iron (nZVI) assembled on magnetic Fe_3O_4/graphene for Cr(VI) removal from aqueous solution, J. Colloid Interface Sci. 417 (2014) 51–59.

[35] S.A. Elfeky, S.E. Mahmoud, A.F. Youssef, Applications of CTAB modified magnetic nanoparticles for removal of Cr(VI) from contaminated water, J. Adv. Res. 8 (2017) 435–443.

[36] R. Khosravi, G. Moussavi, M.T. Ghaneian, M.H. Ehrampoush, B. Barikbin, A.A. Ebrahimi, G. Sharifzadeh, Chromium adsorption from aqueous solution using novel green nanocomposite: FAdsorbent characterization, isotherm, kinetic and thermodynamic investigation, J. Mol. Liq. 256 (2018) 163–174.

[37] S. Li, L. Liu, Y. Yu, G. Wang, H. Zhang, A. Chen, Fe_3O_4 modified mesoporous carbon nanospheres: Magnetically separable adsorbent for hexavalent chromium, J. Alloys Compd. 698 (2017) 20–26.

[38] Y. Lei, X. Qian, J. Shen, X. An, Integrated reductive/adsorptive detoxification of Cr(VI)-contaminated water by polypyrrole/cellulose fiber composite, Ind. Eng. Chem. Res. 51 (2012) 10408–10415.

[39] N. Kera, B. Bhaumik, K. Kriveshini, S.S. Ray, A. Maity, Selective removal of toxic Cr(VI) from aqueous solution by adsorption combined with reduction at a magnetic nanocomposite surface, J. Colloid Interface Sci. 503 (2017) 214–228.

[40] Z. Xu, C. Shen, Y. Tian, X. Shi, H.J. Gao, Organic phase synthesis of monodisperse iron oxide nanocrystals using iron chloride as precursor, Nanoscale 2 (2010) 1027–1032.

[41] M.I. Khali, Co-precipitation in aqueous solution synthesis of magnetite nanoparticles using iron(III) salts as precursors, Arab. J. Chem. 8 (2015) 279–284.

[42] K. Parashar, N. Ballav, S. Debnath, K. Pillay, A. Maity, Hydrous ZrO_2 decorated polyaniline nanofibres: Synthesis, characterization and application as an efficient adsorbent for water defluoridation surface, J. Colloid Interface Sci. 50 (2017) 342–358.

[43] A.M. Muliwa, T.Y. Leswifi, M.S. Onyango, A. Maity, Magnetic adsorption separation (MAS) process: An alternative method of extracting Cr(VI) from aqueous solution using polypyrrole coated Fe_3O_4 nanocomposites, Sep. Purif. Technol. 158 (2016) 250–258.

[44] K.Y. Foo, B.H. Hammed, Insights into the modelling of adsorption isotherm systems, Chem. Eng. J. 156 (2010) 2–10.

[45] W. Sun, Y. Zhou, Q. Su, L. Chen, Y. Wang, J. Liu, Y. Sun, H. Ma, Removal of Cr(VI) from aqueous solutions using polypyrrole-based magnetic composites, Polym. Bull.74 (2017) 1157–1174.

[46] U.O. Aigbe, R. Das, W.H. Huo, V. Srinivasu, A. Maity, A novel method for removal of Cr(VI) using polypyrrole magnetic nanocomposite in the presence of unsteady magnetic fields, Sep. Purif. Technol. 194 (2018) 377–387.

[47] W. Liu, L. Yang, S. Xu, Y. Chen, B. Liu, Z. Li, C. Jiang, Efficient removal of hexavalent chromium from water by an adsorption-reduction mechanism with sandwiched nanocomposites, RSC Adv. 8 (2018) 15087–15093.

[48] J.C.Y. Ng, W.H. Cheung, G. McKay, Equilibrium studies of the sorption of Cu (II) ions onto chitosan, J. Colloid Interface Sci. 255 (2002) 64–74.

[49] B. Qui, C. Xu, D. Sun, Q. Wang, H. Gu, X. Zhang, B.L. Weeks, J. Hopper, T.C. Ho, Z. Guo, S. Wei, Polyaniline coating with various substrates for hexavalent chromium removal, Appl. Surf. Sci. 334 (2015) 7–14.

[50] L. Liu, Z. Cui, Q. Ma. W. Cui, X. Zhang, One-step synthesis of magnetic iron-aluminum oxide/graphene oxide nanoparticles as a selective adsorbent for fluoride removal from aqueous solution, RSC Adv. 8 (2016) 10783–10791.

[51] D. Tang, G. Zhang, Efficient removal of fluoride by hierarchical Ce-Fe bimetal oxides adsorbent: thermodynamics, kinetics and mechanism, Chem. Eng. J. 283 (2016) 721−729.

UNIVERSITY OF JOHANNESBURG

[52] X. Liang, X. Fana, R. Li, S. Li, S. Shen, D. Hu, Efficient removal of Cr(VI) from water by quaternized chitin/branched polyethylenimine biosorbent with hierarchical pore structure Bioresour. Techno. 250 (2018) 178–184.

[53] J. Preethi, S.M. Prabhu, S. Meenakshi, Effective adsorption of hexavalent chromium using biopolymer assisted oxyhydroxide materials from aqueous solution, React. Funct. Polym. 117 (2017) 16–24.

[54] Y. Shi, T. Zhang, H. Ren, A. Kruse, R. Cui, Polyethylene imine modified hydrochar adsorption for Cr(VI) and nickel (II) removal from aqueous solution, Bioresour. Technol. 247 (2018) 370–379.

[55] F. Gao, H. Gu, H. Wang, X. Wang, B. Xiang, Z. Guo, Magnetic amine-functionalized polyacrylic acid-nanomagnetite for hexavalent chromium removal from polluted water, RSC Adv. 5 (2015) 60208–60219.

[56] D.M. Guo, Q.D. An, Z.Y. Xiao, S.R. Zhai, Z. Shi, Polyethylenimine-functionalized cellulose aerogel beads for efficient dynamic removal of Cr(VI) from aqueous solution, RSC Adv. 7 (2017) 54039–54052.

[57] M. Bhaumik, S. Agarwal, V.K. Gupta, A. Maity, Enhanced removal of Cr(VI) from aqueous solutions using polypyrrole wrapped oxidized MWCNTs nanocomposites adsorbent, J. Colloid Interface Sci, 470 (2016) 257–267.

[58] D. Zhao, X. Gao, C. Wu, R. Xie, S. Feng, C. Chen, Facile preparation of amino functionalized graphene oxide decorated with Fe_3O_4 nanoparticles for the adsorption of Cr(VI), Appl. Surf. Sci. 384 (2016) 1–9.

[59] L. Chen, D. Zhao, S. Chen, X. Wang, C. Chen, One-step fabrication of amino functionalized magnetic graphene oxide composite for U(VI) removal, J. Colloid Interface Sci. 472 (2016) 99–107.

[60] B. Qiu, C. Xu, D. Sun, H. Wei, X. Zhang, J. Guo, Q. Wang, D. Rutman, Z. Guo, S. Wei, Polyaniline coating on carbon fiber fabrics for improved hexavalent chromium removal, RSC Adv. 4 (2014) 29855–29865.

[61] Z. Fang, J. Wang, X. Yang, Q. Sun, Y. Jia, H. Liu, T. Xi, S. Guan, Adsorption of arginine, glycine and aspartic acid on Mg and Mg-based alloy surfaces: A first-principles study, Appl. Sci. Res. 409 (2017) 149–155.

UNIVERSITY OF JOHANNESBURG

CHAPTER SEVEN

CONCLUSIONS AND RECOMMENDATIONS

7.1 Introduction

This chapter succinctly highlights the major findings of the study. Sufficient consideration is paid to the extent to which the specific objectives of the study were accomplished, inclusive of the feasibility of mixed nano-metal oxides conducting polymer nanocomposites utilization for the removal of fluoride and Cr(VI) ions from aqueous solution. As an ultimate point, the chapter concludes with some prospective recommendations for further studies.

7.2 Conclusions

The major aim of this study was to synthesise and characterize hydrous cerium, magnesium and iron mixed nano-metal oxides and their conducting polymer-based nanocomposites for potential application in the removal of fluoride and Cr(VI) ions from aqueous solution as a mitigating measure for water pollution.

A simple co-precipitation method was used to prepare an environmentally friendly hydrous cerium-magnesium oxides (CeO_2-MgO) adsorbent for fluoride removal from aqueous solution. This involved the dissolution of ($Ce(NO_3)_3.6H_2O$) and ($Mg(NO_3)_2.6H_2O$) salts in deionized water followed by precipitating to pH 10 with a 2M NaOH solution to produce a hydrous binary nano-metal composite (HCeMgO1:1). As an innovative approach, a hydrous cerium–iron oxide (CeO_2-Fe_3O_4) decorated polyaniline fibers composite was synthesized by firstly polymerization production of polyaniline fibers through a rapid mixing technique. This was followed by facile co-precipitation deposition of CeO_2-Fe_2O_4 metal oxides using $FeCl_3$, $FeSO_4.7H_2O$ and 2.17 g $Ce(NO_3)_3.6H_2O$ precursor salts and a 2M NaOH solution on the polyaniline fibers to produce the nanocomposite (HCeFe NFs-2). Lastly, a magnetic arginine-functionalized PPy adsorbent was synthesized by *in-situ* polymerization. This involved mixing a pyrrole monomer, dissolved arginine and sonicated Fe_3O_4 NPs, followed by the addition of ammonium persulphate for polymerization initiation to produce the magnetic arginine-functionalised polypyrrole nanocomposite (Fe_3O_4@Arg-PPy).

The physicochemical characterizations of the as-developed nanocomposites HCeMgO1:1, HCeFe NFs-2 and Fe_3O_4@Arg-PPy were performed by means of numerous techniques such as FTIR, BET, XRD, SEM, TEM, STEM, TGA, XPS, DMA,VSM and pH at point-of-zero charge analysis. The morphological exposition into the structures was obtained through SEM and TEM images. The BET surface area analysis confirmed the realization of the objective of the study in which the as-fabricated adsorbents authenticated a discernible increase in their specific surface areas as compared to their pristines counterparts (hydrous MgO, PANI NFs and PPy). The FTIR, XRD, EDS, STEM and XPS studies confirmed the successful fabrication of nanocomposites by demonstrating the presence of HCeMgO1:1, HCeFe NFs-2 and Fe_3O_4@Arg-PPy. Application of these adsorbents in batch experiments demonstrated their efficiency for the removal of fluoride and Cr(VI) ions from aqueous solution as discussed in chapters 4, 5 and 6. The DMA characterization of HCeFe NFs-2 revealed an improvement in mechanical strength of the as-synthesized adsorbent in comparison to the pristine host polymer. For the HCeMgO1:1 composite, the DMA characterization was not conducted since this is a composite of metal oxides whose mechanical strength is already known to be high and also there was no basis for comparison. For Fe_3O_4@Arg-PPy, it is recommended that future work be conducted on the mechanical strength tests for PPy and Fe_3O_4@Arg-PPy for comparison to confirm an envisaged improvement of the mechanical strength of Fe_3O_4@Arg-PPy relative to PPy. The effects of various adsorption parameters such as adsorbent dose, pH, contact time, temperature and co-existing ions as well as desorption studies were investigated and critically assessed. The effect of pH on adsorption constituted the most critical parameter that governed the adsorption process. Rapid adsorption was revealed for fluoride ions adsorption as highlighted in chapters 4 and 5 whilst for Cr(VI) ions it was moderate as reported in chapter 6. The effect of temperature on adsorption was also found to influence the extent of the adsorption signifying endothermicity or exothermicity of the adsorption processes.

The Langmuir and Freundlich isotherm models were employed to describe the adsorption processes. For all cases in chapters 4, 5 and 6 studies, the Langmuir isotherm model best described the adsorption process, depicting a monolayer process and the pseudo-second-order model best described the kinetics. When the Webber-Morris intra-particle diffusion model was employed, three stages were involved in the adsorption. Firstly, faster reaction controlled by boundary film diffusion, followed by slower reaction due to intra-particle diffusion whilst the third process represented equilibrium stage for all the studies.

UNIVERSITY OF JOHANNESBURG

Most of the ions like chloride (Cl^-), nitrate (NO_3^-), copper (II) (Cu^{2+}), zinc(II) (Zn^{2+}) and nickel(II) (Ni^{2+}) had little or no effect on the adsorption of fluoride and Cr(VI) ions except for phosphate /hydrogen phosphate (HPO_4^{2-}/ PO_4^{3-}), hydrogen carbonate (HCO_3^-) and sulphate (SO_4^{2-}) ions.

Regeneration experiments on HCeMgO1:1, HCeFe NFs-2 and Fe_3O_4@Arg-PPy adsorbents showed three to four successive adsorption-desorption cycles. The fluoride and Cr(VI) ions adsorption mechanisms were established through FTIR, XPS, IC-ICP-MS speciation and point-of-zero charge analyses suggesting ion exchange and electrostatic attractions for fluoride ions with electrostatic attractions, reduction and chelation mechanisms for Cr(VI) ions.

In chapters 4 and 5 the potential of the adsorbents HCeMgO1:1 and HCeFe NFs-2 for the defluoridation of spiked natural fluoride-containing groundwater was evaluated. These nanoadsorbents have the potential to reduce the fluoride concentration to below 1.5 mg/L though more analysis is required in flow through processes. Additionally, in chapter 6, real wastewater application study of Fe_3O_4@Arg-PPy for the removal of Cr(VI) ions from a chromium ore leachate wastewater sample revealed the potential effectiveness of the adsorbent.

In conclusion, the batch adsorption investigations results on the application of HCeMgO1:1, HCeFe NFs-2 and Fe_3O_4@Arg-PPy nanocomposite adsorbents demonstrated a great possibility in water defluoridation and removal of Cr(VI) ions from water. Their adsorption potentials are summarized in **Table 7.1**. From the table, it is revealed that HCeFe NFs-2 is comparatively a better fluoride adsorbent than HCeMgO1:1. This is exposed in its greater surface area, higher adsorption capacity and wider pH range, though fluoride adsorption with HCeMgO1:1 is slightly faster. These attributes can be ascribed to reduced agglomeration of nano-metal oxides when they precipitated on a porous support (PANI NFs), hence minimum loss of activity. This also demonstrates that incorporating inorganic metal oxides onto the matrix of conducting polymers scaffolds and prevents the π-π* aggregation of polymer chains, ensuing increased surface area organic/inorganic hybrid nanocomposites and synergistic interaction leading to improved fluoride adsorption properties as envisaged in the chapter one of this study.

Table 7.1: Summary of physico-chemical characteristics with the fluoride and Cr(VI) adsorption parameters obtained for HCeMgO1:1, HCeFe NFs-2 and Fe_3O_4@Arg-PPy nanocomposites.

Parameter	HCeMgO1:1 (F^- removal)	(HCeFe NFs-2) (F^- removal)	Fe_3O_4@Arg-PPy (Cr(VI) removal)
BET surface area (m^2/g)	34	66	22
pH at point-of- zero charge	5.8	6.6	7.2
Optimum pH range	2.0-8.5	3.0-10.0	2.0
Adsorption capacity, q_{max} at 25 °C (mg/g)	66.23 at pH 5.5 ± 0.2	116.28 at 6.0 ± 0.2	322.58 at pH 2.0 ± 0.05
Equilibrium time (min)	5 (for C_o = 10 mg/L)	10 (for C_o = 10 mg/L)	90 (for C_o = 50 mg/L)

7.3 Recommendations for further studies

7.3.1 Ground water and wastewater applicability

The materials produced in this study showed great potential in removing pollutants in a batch laboratory bench scale. However, more studies on their potential in large scale water treatment as demonstrated in column studies are required. At this level, their appropriateness for real water and wastewater samples in providing safe water for small communities and the environment is assessed more.

UNIVERSITY OF JOHANNESBURG

7.3.2 Multi-functionality of adsorbents and reuse of pollutant-loaded adsorbents

The multifunctionality of the as-developed adsorbents HCeMgO1:1, HCeFe NFs-2 and Fe_3O_4@Arg-PPy need to be evaluated particularly on the effect of co-existing ions, determining the amounts of the other ions Cl^-, NO_3^-, SO_4^{2-}, PO_4^{3-}, HCO_3^- etc the materials can also adsorb. Furthermore, studies on the reuse applications of Cr(VI) and fluoride loaded adsorbents need to be conducted to minimise possible secondary environmental pollution.

7.3.3 Photocatalytic degradation of organic pollutants

The as-synthesized HCeMgO1:1, HCeFe NFs-2 and Fe_3O_4@Arg-PPy may be calcinated and applied in the rapidly emerging and promising technology of photocatalytic degradation of organic pollutants. This is so because nano-metal oxides, especially cerium oxide is quite transparent to visible light and has an excellent UV absorption property due to its wider optical

band gap value. In the as-synthesized materials, ceria is presently doped with other metal oxides hence its catalytic effectiveness in the visible region may be extended.

UNIVERSITY
OF
JOHANNESBURG